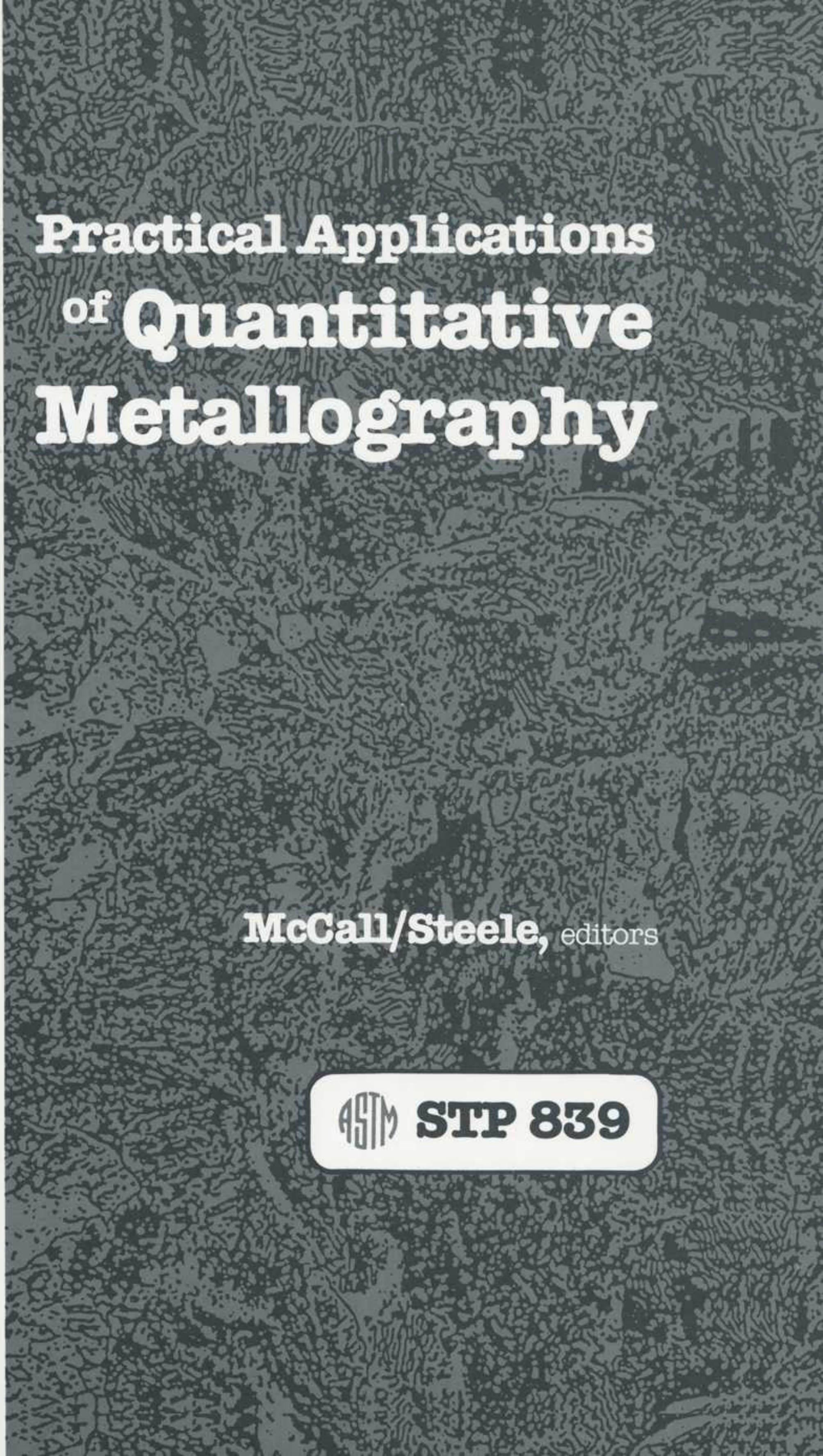

Practical Applications of Quantitative Metallography

McCall/Steele, editors

ASTM STP 839

PRACTICAL APPLICATIONS OF QUANTITATIVE METALLOGRAPHY

A symposium sponsored by
ASTM Committee E-4 on
Metallography and by the
International Metallographic Society
Orlando, Fla., 18–19 July 1982

ASTM SPECIAL TECHNICAL PUBLICATION 839
J. L. McCall, Battelle Columbus Laboratories,
and J. H. Steele, Jr., Armco Inc.,
editors

ASTM Publication Code Number (PCN)
04-839000-28

1916 Race Street, Philadelphia, Pa. 19103

International Metallographic Society

Library of Congress Catalog Card Number: 83-73230

Printed in Ann Arbor, Mich.
July 1984

Foreword

The symposium on Practical Applications of Quantitative Metallography was held 18–19 July 1982 in Orlando, Fla. The event was jointly sponsored by ASTM, through its Committee E-4 on Metallography, and the International Metallographic Society. Chairing the symposium were James L. McCall, Battelle Columbus Laboratories, and James H. Steele, Jr., Armco Inc.; both men also served as editors of this publication.

Related ASTM Publications

MiCon 82: Optimization of Processing, Properties, and Service Performance Through Microstructural Control, STP 792 (1983), 04-792000-28

Metallography—A Practical Tool for Correlating the Structure and Properties of Materials, STP 557 (1974), 04-557000-28

Stereology and Quantitative Metallography, STP 504 (1972), 04-504000-28

Applications of Modern Metallographic Techniques, STP 480 (1970), 04-480000-28

Metals and Alloys in the Numbering System, DS 56B (1983), 05-056002-01

A Note of Appreciation to Reviewers

The quality of the papers that appear in this publication reflects not only the obvious efforts of the authors but also the unheralded, though essential, work of the reviewers. On behalf of ASTM we acknowledge with appreciation their dedication to high professional standards and their sacrifice of time and effort.

ASTM Committee on Publications

ASTM Editorial Staff

Janet R. Schroeder
Kathleen A. Greene
Rosemary Horstman
Helen M. Hoersch
Helen P. Mahy
Allan S. Kleinberg
Susan L. Gebremedhin

Contents

Introduction

Stereology or quantitative metallography is a generalized body of methods for characterizing a three-dimensional microstructure from two-dimensional sections or thin foils. The methods, which are based on geometrical probabilities and specific statistical sampling techniques, provide relationships between measured quantities (on specimen sections) and specific characteristics of the microstructure. Two of the most commonly used stereological relationships are discussed in the ASTM Recommended Practice for Determining Volume Fraction by Systematic Manual Point Count (E 562-83) and ASTM Method for Determining Average Grain Size (E 112-82). Several texts are available[1,2,3] that provide derivations and detailed discussion of this body of methods. A previous ASTM symposium published as *Stereology and Quantitative Metallography, ASTM STP 504* (1972), covered many of the important aspects of these methods.

The present symposium was organized to provide a variety of selected practical applications of the stereological methods. It was presented under joint ASTM and International Metallographic Society (IMS) sponsorship on 18–19 July 1982 in Orlando, Fla., at the 15th Annual IMS Meeting. The papers include general microstructural characterization and problems, as well as in-depth studies describing microstructural changes and correlating microstructure and properties. Each paper provides a unique point of view in applying stereological methods for quantitative characterization of microstructure.

The stereological terminology and notation used by the authors are based on a standard subscripted format. The symbols and parameters are specifically defined by the individual authors and should be interpreted as illustrated by the following typical examples:

1. Microstructural parameters:

V_V = volume of the feature per unit volume of microstructure.
S_V = surface area of the feature per unit volume of microstructure.
N_V = number of the features per unit volume of microstructure.

2. Typical measured parameters:

$\bar{P}_P$ = average point fraction (see ASTM Recommended Practice E 562-83).

---

[1] *Quantitative Microscopy*, F. N. Rhines and R. T. DeHoff, Eds., McGraw-Hill, New York, 1968.

[2] Underwood, E. E., *Quantitative Stereology*, Addison-Wesley, Reading, Mass., 1970.

[3] Serra, J., *Image Analyses and Mathematical Morphology*, Academic Press, New York, 1982.

$\bar{N}_L$ = average number of intersections of the feature boundary per unit length of a test line (see ASTM Method E 112-82).

$\bar{N}_A$ = average number of features intersected per unit area of a two-dimensional section.

These definitions are presented to illustrate the subscripted notation and to indicate the two types of parameters involved in stereological applications. The reader will find throughout the papers a variety of additional terms, which are specifically defined by each author.

James H. Steele, Jr.

Armco Inc., Middletown, Ohio 45043; symposium cochairman and editor.

James L. McCall

Battelle Columbus Laboratories, Columbus, Ohio 43201; symposium cochairman and editor.

Frederick N. Rhines[1] *and Jack E. Lemons*[2]

Grain Boundary Hardening of Alpha Brass

REFERENCE: Rhines, F. N. and Lemons, J. E., "**Grain Boundary Hardening of Alpha Brass,**" *Practical Applications of Quantitative Metallography, ASTM STP 839*, J. L. McCall and J. H. Steele, Jr., Eds., American Society for Testing and Materials, Philadelphia, 1984, pp. 3-28.

ABSTRACT: At fixed temperature and composition, the Brinell hardness of alpha brass is directly proportional to the area of grain boundary in a unit volume of metal. The resistance to deformation in the Brinell test is shown to be the sum of three distinguishable parts. These are, first, the elastic resistance, measured by the Harris strainless indentation technique and found to be independent of the presence of grain boundary. Second is the resistance to plastic deformation of the bodies of the grains, measured as the hardness at zero grain boundary area and found to be constant for grains of all sizes. Third is the resistance of the grain boundaries to the passage of shear through the metal, measured as the ratio of hardness to grain boundary area. The grain boundary contribution to hardness exhibits a sharp maximum in the neighborhood of 25% zinc, where the stacking fault energy of alpha brass is at a minimum. For shear to pass through the grain boundary without causing rupture, it is necessary that the slip be homogeneously distributed. This requires the intervention of cross-slip, which represents an energy requirement beyond that for slip within the grains. The formation of stacking faults opposes cross-slip and greatly increases the energy for the deformation of the boundary. Hardening diminishes with rising temperature. At 600°C, at ordinary speeds of testing, grain boundary hardening is negative, that is, softening occurs. Negative hardening is absent at high speeds of testing, showing that the softening effect is related to diffusion. At high temperature, shearing across the grain boundary gives way to shearing parallel to the grain boundary.

KEY WORDS: quantitative metallography, hardness, Brinell hardness, elastic hardness, grain boundary hardness, impact hardness, plastic hardness, high-temperature hardness, low-temperature hardness, grain boundary, grain boundary deformation, grain boundary energy, grain boundary sliding, grain boundary softening, grain boundary area measurement, grain boundaries cross-slip, grain boundary brittleness, alpha copper/zinc, alpha silver/zinc, alpha brass

---

[1] Distinguished Service Professor Emeritus, Department of Materials Science and Engineering, University of Florida, Gainesville, Fla. 32611.

[2] Professor and chairman, Department of Biomaterials, University of Alabama at Birmingham, Birmingham, Ala. 35294.

A polycrystalline metal is not simply a collection of crystals, but is rather an organization of crystals of different sizes, shapes, and orientations into a space-filling whole, wherein the mutual contact among neighbors forms a continuous network of grain boundary. This factor is of particular importance in plastic deformation, because no crystal of an aggregate is free to deform as a single crystal but must coordinate its plastic behavior with that of its neighbors, of which the average grain has 14, each deforming differently. The resulting complex is the more resistant to deformation the larger the area of grain boundary. Attempts to relate the hardening effect to microstructure have generally followed one of two courses of thought: either that the property change is to be associated with grain size [*1*][3,4,5] as such, or that the change represents the specific resistance of the grain boundary to the passage of shear through the system. The observation that the Brinell hardness is proportional to the area of grain boundary has been offered in support of the latter view [*2*]. In the present research, this relationship has been explored in depth across the composition range of the alpha brasses and over a large span of temperatures, confirming its constancy and providing a basis for understanding its mechanism.

Before proceeding with a presentation of these findings, it will be illuminating to consider the validity of the long-held suspicion that the Brinell test and tension test measure different properties of a metal. It has been shown [*3*] and recently verified [*4*] that only the largest grains of an aggregate participate significantly in the deformation measured in a normal tension test, with the consequence that the yield strength, ultimate tensile strength, and engineering elongation are highly sensitive to the breadth of distribution of grain sizes in the metal [5]. Where there exists a mixture of grain sizes, including relatively large grains, all of the tensile properties tend to have low values, because the plastic response is largely concentrated in a few grains. Thus, the tensile properties of a metal are characterized by a strong dependence upon the grain size distribution.

In contrast to the tension test, the Brinell hardness test is distinguished by a high degree of deformation concentrated in the immediate vicinity of the impression. This forces a nearly universal plastic participation of all of the grains in the affected locality, irrespective of differences among them in grain size. The Brinell test is, therefore, not sensitive to grain size distribution, responding

---

[3] The italic numbers in brackets refer to the list of references appended to this paper.

[4] See also Hall, E. O., *Proceedings of the Physical Society*, Vol. 64B, 1951, pp. 747-753; and Petch, N. J., *Journal of the Iron and Steel Institute*, Vol. 174, 1953, pp. 25-28.

[5] Most frequently cited is the so-called Hall-Petch[4] relationship, in which yield strength is presumed to be related to $l^{-1/2}$, where l is the mean intercept measured by a lineal grain count on a two-dimensional section. It has been pointed out, however, that this parameter is, in fact, one half of the square root of the total area of grain boundary. Hence, in reality, the Hall-Petch relationship is concerned with grain boundary area and not with any measure of grain size; it is emphatically not connected with the grain diameter, which cannot be determined by any two-dimensional measurement.

rather to the totality of all of the grain boundary present in the system. Accordingly, Brinell hardness does, indeed, measure a different property. Moreover, the property that it measures is simpler than the tensile properties and more easily analyzed, as will be demonstrated in this paper.

Experimental Procedure

A series of eight copper/zinc alloys, ranging in composition from 0 to 35% zinc, in intervals of 5%, was prepared by the Anaconda Brass Co. These alloys were made from high-purity copper and zinc and were cast as 5 by 5 by 30-cm (2 by 2 by 12-in.) ingots. The analyses are given in Table 1. Each alloy was cold rolled 33% and annealed 1 h at 650°C in order to produce a standard condition for growing a range of grain sizes. This material, cut into pieces approximately 6 cm (2½ in.) square, was subjected to a series of rolling and annealing treatments wherein the cold rolling was varied from 10 to 50%, and the annealing treatments varied from 1½ to 3 h at 500 to 850°C. In order to avoid loss of zinc from the surface, each specimen was enclosed in an iron capsule, together with chips of the same alloy for each heat treatment performed. The details of these treatments for the several alloys are recorded in Table 2.

The grain boundary area of each specimen was measured by quantitative microscopy, using the relationship $S_V = 2N_L$, where S_V is the total area of grain and twin boundary in a unit of volume of the material, and N_L is the number of intercepts of a test line imposed upon the two-dimensional image of the microstructure. A total of 15 series of measurements was made upon the broad face of each specimen, and occasional check measurements were made on side faces to guard against error due to anisotropy of the grains. The total area of grain and twin boundary is given for each specimen in Table 2, where the maximum error is less than 5% of the reported value. It is to be noted that secondary, as well as primary, twins were present in those alloys containing up to 20% zinc.

The Brinell hardness measurements were made at room temperature (298 K)

TABLE 1—*Spectrographic analysis of alpha brass alloys.*

Nominal Copper Composition, Weight %	Element Analysis, Weight%	
	Copper	Zinc
100	100.00	0.00
95	94.58	5.42
90	89.69	10.31
85	84.60	15.40
80	79.72	20.28
75	74.72	25.28
70	69.80	30.20
65	64.85	35.15

TABLE 2—*Pretreatment, boundary area, and hardness data for copper/zinc alloys.*

Specimen, % Copper-Specimen No.	Cold Work, %	Heat Treatment			Hardness, HB[b]				
		Duration, h	Temperature, °C	S_V[a]	77 K	298 K	573 K	873 K	298 K (Final)
100-1	10	1.5	700	347.0		37.7			
100-2	20	1.5	700	458.6	47.2	39.4	34.9	21.6	
100-3	30	1.5	700	301.2		37.3			
100-4	40	1.5	700	895.4	53.1	40.0	34.9	23.6	
100-5	10	1.5	850	286.4		37.0			
100-6	20	1.5	850	270.9	44.1	37.3			
100-7	30	1.5	850	209.2		38.1			
100-8	40	1.5	841	45.6	43.9	35.5	32.3	20.3	
95-3	25	3	500	759.3		45.2			
95-4	50	3	500	1208.5	59.4	48.9	42.0	31.2	48.0
95-6	15	1	600	507.1	54.8	44.2	39.1	28.7	43.4
95-7	35	1	600	766.2		45.0			
95-8	50	1	600	893.1	57.5	46.6	40.2	30.9	46.9
95-10	10	1	700	284.2		41.6			
95-11	25	1	700	494.5		43.3			
95-12	50	1	700	565.6		44.9			
95-13	10	1	800	280.1		41.7			
95-14	25	1	800	361.5		42.3			
95-15	35	1	800	352.3	52.8	42.2	37.7	28.3	42.4
95-16	50	1	800	367.7		42.4			
90-3	25	3	500	892.8		52.0			
90-4	50	3	500	1618.5	67.7	55.9	48.0	31.5	53.4
90-6	15	1	600	581.0	59.0	48.0	44.4	30.9	47.5
90-7	35	1	600	839.5	60.9	50.9	44.9	30.7	50.3
90-8	50	1	600	964.2		53.1			
90-10	10	1	700	366.6		46.1			
90-11	25	1	700	626.4		48.3			
90-12	50	1	700	635.3		49.3			
90-13	10	1	800	353.8		45.4			

90-14	25	1	800	218.5		44.9			
90-15	35	1	800	383.1	55.4	45.1	40.0	30.0	44.0
90-16	50	1	800	260.3		44.9			
85-3	25	3	500	1562.5		59.6			
85-6	15	1	600	821.1		50.9			
85-7	35	1	600	1402.2		57.0			
85-8	50	1	600	1383.9	70.0	57.2	51.2	31.7	56.8
85-10	10	1	700	646.3		48.0			
85-11	25	1	700	763.8	64.6	53.1	48.0	32.1	51.5
85-12	50	1	700	522.3	61.3	51.3	46.9	32.3	51.8
85-13	10	1	800	310.9		45.4			
85-14	25	1	800	219.0	56.8	45.4	40.2	31.4	44.4
85-15	35	1	800	178.6		45.2			
85-16	50	1	800	205.9		45.1			
80-2	15	1	600	1114.9		54.8			
80-3	35	1	600	1459.5	73.0	59.8	42.5	32.4	58.6
80-4	50	1	600	1046.0	68.2	57.3	51.8	32.8	60.1
80-7	25	3	500	1755.5		61.7			
80-10	10	1	700	489.5		48.2			
80-11	25	1	700	537.1		50.6			
80-12	50	1	700	403.6	60.9	48.6	44.1	31.4	48.3
80-13	10	1	800	158.4		42.7			
80-14	25	1	800	236.3	56.8	43.8	40.2	29.8	43.0
80-15	35	1	800	134.7		43.3			
80-16	50	1	800	161.3		44.6			
75-3	25	3	500	1033.1		61.5			
75-4	50	3	500	1454.0		67.3			
75-7	35	1	600	1047.0	76.2	60.1	53.8	25.9	59.0
75-8	50	1	600	765.8	73.6	58.6	53.8	28.4	57.5
75-10	10	1	700	491.0		47.2			
75-11	25	1	700	374.8		48.6			
75-12	50	1	700	330.7	63.8	46.7	44.9	33.2	50.6
75-13	10	1	800	157.2		42.0			
75-14	25	1	800	172.6	56.8	41.7	37.5	28.4	41.5
75-15	35	1	800	151.7		40.9			
75-16	50	1	800	131.7		41.1			

TABLE 2—*Continued*

Specimen, % Copper-Specimen No.	Cold Work, %	Heat Treatment			Hardness, HB[b]				
		Duration, h	Temperature, °C	S_V[a]	77 K	298 K	573 K	873 K	298 K (Final)
70-3	25	3	500	828.8		56.1			
70-4	50	3	500	1575.4	83.2	67.0	58.6	25.4	62.9
70-6	15	1	600	731.8		51.7			
70-7	35	1	600	826.2		55.1			
70-8	50	1	600	771.6	69.1	54.1	51.8	29.9	50.9
70-10	10	1	700	433.8		46.1			
70-11	25	1	700	365.9	64.6	48.1	42.9	24.1	51.2
70-12	50	1	700	293.2		45.9			
70-13	10	1	800	115.1		40.2			
70-14	25	1	800	126.8		40.9			
70-15	35	1	800	130.1	56.8	40.9	38.3	26.9	39.2
70-16	50	1	800	153.0		41.5			
65-4	50	3	500	1733.4	79.6	64.4	56.8	23.6	61.7
65-5	15	1	600	731.7		52.8			
65-7	35	1	600	717.8	73.6	54.6	52.8	20.9	56.5
65-8	50	1	600	739.9		54.4			
65-10	10	1	700	364.8		47.7			
65-11	25	1	700	155.9		43.8			
65-12	50	1	700	228.8	62.5	47.6	43.6	21.2	46.9
65-13	10	1	800	316.4		50.0			
65-14	25	1	800	463.0	65.9	51.2	46.4	20.5	50.3
65-15	35	1	800	501.8		53.1			
65-16	50	1	800	376.6		51.3			

[a] Reliable to within 5% of the value reported.

[b] Reliable to ±1.0 HB.

and at 77, 573, and 873 K, using a Model UK 300-T Brinell hardness tester, a 500-kg load, and a 10-mL-diameter hardened steel ball with a load duration of 30 s, except at the highest temperature, where a loading time of 3 s was used. At room temperature, four impressions were located at equal distances from the specimen's corners along the diagonals of the principal face of each specimen. A standard brass test block was tested before and after each set of readings to guard against machine error. The results are given in Table 2, where the values are considered reliable to two points HB.

Four grain sizes in each alloy were tested at low and at high temperature. At 77 K both the specimen and the indenter were immersed in liquid nitrogen, while the Brinell impression was made in the usual manner. At higher temperature, a special testing chamber was required in order to maintain a protective atmosphere during the test. This chamber contained the specimen, powdered graphite, and metal chips of the composition of the alloy being tested. The complete chamber, including the specimen and the indenter, was heated to the testing temperature, inserted in the testing machine, loaded, and cooled naturally to room temperature for reading. The results, reported in Table 2, represent a single impression in each case. Subsequently, the hardness was remeasured at room temperature (298 K final), in order to detect any change in the material that might have occurred during hot testing. In general, there was no detectable change, indicating both that the grain size had not increased significantly and that the composition of the alloy had been maintained.

The same materials were used in auxiliary studies that will be described presently. These include (1) a microhardness survey, (2) strainless indentation hardness studies made at Clemson University [*6*] and reported for the first time in this paper, (3) high-velocity hardness experiments carried out by Rhode [*7*], and (4) grain boundary energy measurements made by Bates [*8*]. Similar materials were employed in the studies on the quenching-out of short-range order.

Analysis of the Hardness Versus Grain Boundary Area Relationship

A striking feature of the hardness versus grain boundary area plots (Fig. 1) is their strict adherence to linearity in all cases, over broad ranges of alloy composition, testing temperature, and grain boundary area. This behavior obtains even when increase in grain boundary area is associated with softening, as is illustrated, for example, in the case of the 70Cu-30Zn alloy at 873 K. The linearity of these graphs relates the hardening effect directly to the area of the grain boundary as a *two-dimensional entity*. At the same time it excludes the influence of grain size as a three-dimensional property, because this would have to be expressed as a cubic function, which would introduce curvature into these plots.

More direct evidence of the absence of a role for grain size, as such, is to be obtained through consideration of the grain volume distribution in the specimens tested in this research. It has been shown elsewhere [*9*] that the grain

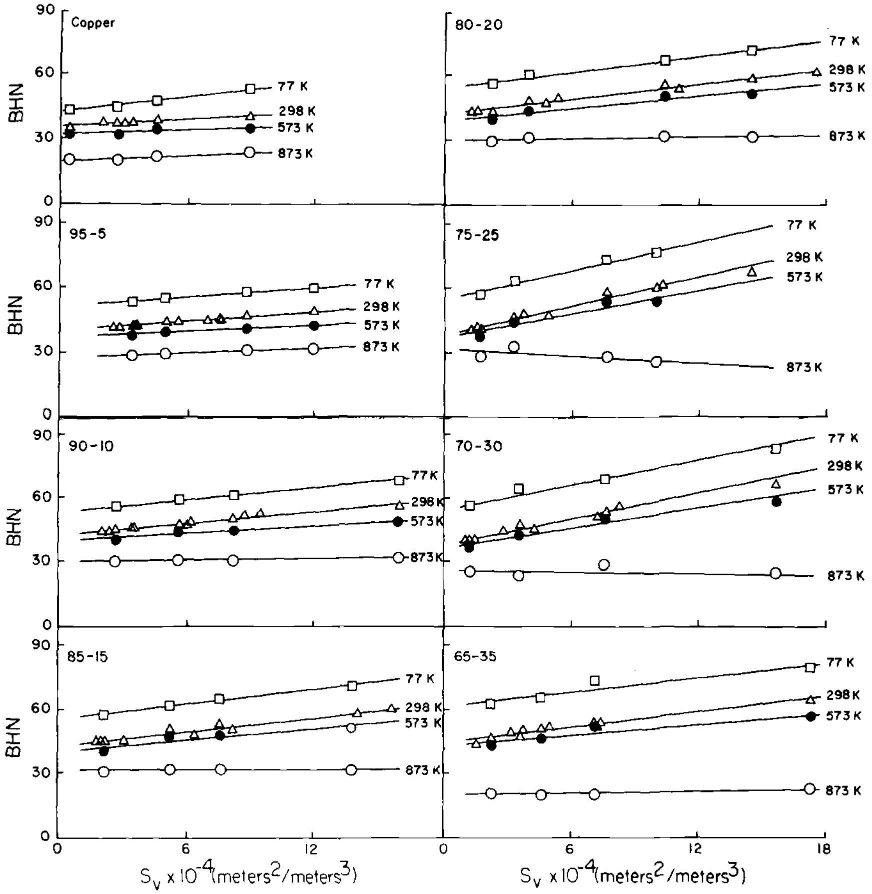

FIG. 1—*Brinell hardness number versus the area of grain plus twin boundary (1/m) for copper and the alpha brasses at 77, 298, 573, and 873 K.*

volume distribution of recrystallized metal is log normal and that the standard deviation of the distribution is a reciprocal function of the degree of cold plastic deformation that has preceded recrystallization. The microstructures analyzed in the present research had been produced by applying different degrees of cold working prior to annealing (Table 2). This factor, which has varied from 10 to 50% of deformation, is expected to produce grain volume distributions with standard deviations ranging from about 1.1 to almost 3. This is a very broad range, and it means that structures having the same grain boundary area can and do differ widely in their grain size distributions. Yet, there is no indication of such variation in the grain boundary area versus hardness relationships.

This point may be understood more fully by reference to a specific example.

Consider the group of three points near the center of the room temperature line (298 K) for the 65Cu-35Zn alloy in Fig. 1. These all have approximately the same grain boundary area and hardness. Reference in Table 2 to Alloys 65Cu-5Zn, 65Cu-7Zn, and 65Cu-8Zn reveals, however, that they had been subjected to very different degrees of cold working prior to annealing, specifically to 15, 35, and 50%. The first of these specimens would have included some very large grains, with others grading down to a very small size, the average being relatively small. The third specimen, worked 50%, would have a fairly homogeneous grain volume distribution. Such a difference would have a large effect upon the tensile properties and would affect the Brinell hardness as well, were it sensitive to the sizes of the individual grains. Clearly, *the observed differences in hardness are not to be associated with differences in grain volume but are related exclusively to the grain boundary area.*

The resistance to deformation in the Brinell test may be regarded as being composed of three additive parts, depicted in the schematic diagram of Fig. 2. First, there is the elastic component, represented in the lower portion of the diagram. Added to this, and represented in the central portion of the diagram, is the plastic resistance of the bodies of the grains. The third component is the contribution of the grain boundary, represented in the upper part of the diagram. Each of these factors has been analyzed and measured separately.

Elastic Contribution to Brinell Hardness

The elastic contribution to hardness, represented in Fig. 2, has been determined by the strainless indentation method of Harris [*10*]. In this method, the Brinell ball is reseated and reloaded repeatedly with intermediate annealing until the impression is one that will support the load without a detectable

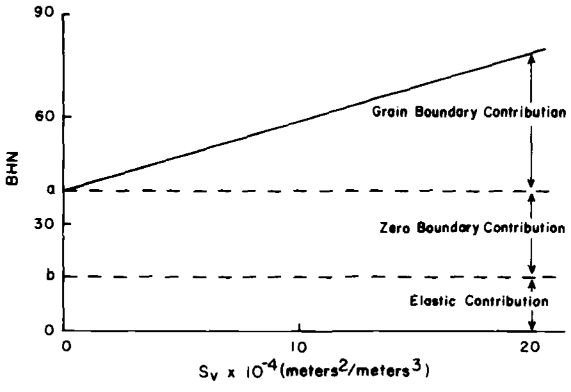

FIG. 2—*Schematic representation of the strainless, zero grain boundary, and grain boundary hardness contributions that make up a polycrystalline hardness number.*

increase in area, that is, the load is being supported elastically by unstrained metal.

Two undergraduate students, Geronimos and Wood, working at Clemson University under the guidance of J. S. Wolf [*6*], have measured the Harris hardness of both 5 and 30% zinc brass as a function of grain boundary area and have found the elastic contribution to be independent of grain boundary area (Fig. 3). This fact is represented in Fig. 2 by drawing a horizontal line through Point *b*, separating the elastic from the plastic contribution to hardness. Since the grain boundary does not contribute to the elastic resistance of the Brinell indentation, it follows that the contribution of the grain boundary is entirely plastic. In other words, ***grain boundary hardening is the resistance of the grain boundary to the passage of plastic deformation from crystal to crystal in the polycrystalline aggregate.***

Resistance to Crystalline Slip Within the Grains

By a short extrapolation of the hardness plots, as at Point *a* in Fig. 2, a value is obtained for the hardness at zero grain boundary area. The zero grain boundary hardness is not that of a single crystal, nor is it an average hardness measured in different directions on a single crystal. Rather, it is the average hardness of grains of assorted shapes, sizes, and orientations as these deform within the constraints of a polycrystalline aggregate, but without the resistance of the grain boundary. A horizontal line is drawn through Point *a* in Fig. 2, in accord with the conclusion that the contribution of the grains themselves to the hardness is the same for all grain sizes,[6] based upon the regularity of the data points in Fig. 1,

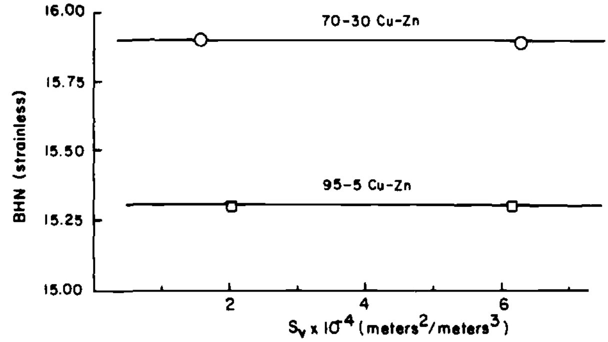

FIG. 3—*Harris strainless indentation hardness versus the grain boundary area,* S_V, *for the 95Cu-5Zn and 70Cu-30Zn alloys, showing an absence of any effect of grain size on the elastic contribution to hardness [6].*

---

[6] This is not in conflict with the observation that only the largest grains participate in tensile yielding, because, where all grains have the same resistance to deformation, those with the least grain boundary per unit volume will deform most easily. These are the largest grains.

which would otherwise display scatter because of diversity in the grain volume distribution, which is known to exist among specimens in the same sequence. The plastic portion of the zero grain boundary hardness is, of course, the difference between the zero grain boundary hardness and the elastic contribution.

Grain Boundary Contribution to Hardness

The slope ($\Delta HB/\Delta S_V$) of the total hardness line in Fig. 2 is the contribution of the grain boundary, in terms of the increase in hardness per unit area. It includes all boundaries, both grain and twin, it having been shown previously [*2*] that the omission of the twin boundary area results in a scatter of the data points. While it is undoubtedly true that the grain boundary differs in its contribution to hardness according to its orientation and that of the crystals that it bounds, it seems that a Brinell test, of the kind under consideration, responds to an average boundary resistance that is highly reproducible. Special orientation situations will not be treated in this paper.

The Brinell Test

The Brinell hardness number (HB) is measured by the spherical area of the indentation produced by a ball of specified diameter, pressed into the metal surface with a specified load, usually in a fixed time. The result is reported in terms of load per unit area. This test has been criticized [*11*][7] in the past on the basis that it does not load the surface of the indentation uniformly. A more generally accepted version of the test is the Meyer [*12*] hardness test, which is based upon a series of indentations made by a sequence of increasing loads and in which the projected area of the indentation is measured. This method involves the use of much larger specimens. An abbreviated survey was made to compare the Brinell and Meyer hardnesses of the alpha brasses. It was found that the two kinds of readings agreed within 1%. In the interest of obtaining a maximum of information from the specimens at hand, this program as a whole was conducted by the use of the Brinell tests.

For the discussions that follow, the Brinell test will be thought of as measuring the force required to displace a specified volume of metal by a fixed total of plastic shear, which could, in turn, be expressed as a fixed total area of offset passed through grain boundary. In passing into and through the metal the dislocation must encounter grain boundary in proportion to the area of boundary present in a unit volume (S_V). The loading force measures the energy required to pass this fixed area of dislocation through the measured area of grain boundary. Thus, *the grain boundary contribution to the Brinell hardness is proportional to both the area of grain boundary and the force required to move the dislocation.*

---

[7] See also Tabor, D., *The Hardness of Metals*, Oxford University Press, Oxford, England, 1951.

Shear Through the Grain Boundary

The geometric problem of passing shear through coincident grain boundaries has been dealt with quantitatively in a previous paper by one of the present authors [*13*]. A dislocation cannot pass "through" a grain boundary because the crystals on either side are differently oriented, providing no common plane of slip. Instead, the dislocation must terminate upon the boundary, producing a ledge, analogous to the slip line that appears on an external surface under like circumstances. This ledge reacts elastically against the conjoint crystal, creating a back-stress that resists the passage of more slip on the same crystal plane, until the boundary becomes flattened again by like slip on adjacent planes. Because the slip on all adjacent planes is in the same direction, the grain boundary is tilted, like the edge of a pack of cards when the pack is slipped. At the same time there is a change in both the area and the shape of the bounding surface of the first crystal, creating a shear stress in the plane of the boundary, between the two crystals. This can be relieved only by suitable slip in the second crystal. New dislocations must emerge from the boundary into the second crystal, generating slip steps that change the area and shape of its surface to match that of the first crystal.

In this way, shear passes from grain to grain without interrupting the integrity of the metal. The boundary has served to transform the slip in one grain to that in its differently oriented neighbor by converting it first into a two-dimensional stress in the plane of the boundary and then back again on the other side. It is particularly to be noted that this process requires a homogeneity of the distribution of slip on essentially all of the crystal planes where they meet the boundary.[8] Ordinarily, slip within a crystal occurs inhomogeneously, that is, in packets. In order to redistribute the slips homogeneously, it is necessary that some dislocations transfer to other planes by the process of cross-slip. This must happen close to the grain boundary under the directing forces of the distorted boundary. It represents an unrecoverable expenditure of energy beyond that which would have been required to deform an unbounded crystal similarly. Thus, *the grain boundary contribution to hardness arises from the extra energy required to produce cross-slip adjacent to the boundary and over its entire area.*

Effects of Composition

Further insight into the foregoing matters will be provided by an examination of the effects of change of composition across the alpha field of the copper/zinc system.

---

[8] It may be recalled that W. Rosenhain, in his first paper on slip in copper, commented on the apparent termination of slip lines short of the grain boundary, implying homogeneous deformation in this zone (*Introduction to Physical Metallurgy*, Constable and Co., London, 1935, pp. 288-289 and Fig. 13, p. 272).

Solid Solution Hardening of Alpha Brasses

Because copper and zinc are adjacent elements in the periodic system (atomic numbers 29 and 30) the solid solution hardening effect is not expected to be large. This expectation is borne out by both the elastic and zero grain boundary plastic contributions to hardness (Fig. 4 and Table 3). The bottom line in this graph is the elastic contribution, measured by Harris [*10*] in 1922. It suggests a solid solution hardness maximum at between 15 and 20% zinc, as do the zero grain boundary plastic contributions measured at 77, 298, 573, and 873 K in the present research. At a corresponding temperature, the elastic and plastic curves are nearly parallel, the elastic portion of the hardening being about two thirds as great as the plastic portion.

At the lower temperatures, all of the plots in Fig. 4 exhibit a rise in hardness at between 30 and 35% zinc. This is ascribed to short-range ordering of the crystals, which, according to Köster and Schüle [*14*] and Clareborough et al [*15*] begins at 20% zinc and increases with rising zinc content. This interpretation is supported by the disappearance of the hardening increase at 873 K, where ordering is reported to be absent. At 873 K the zero grain boundary hardness assumes the classical form of a solid solution in crossing the alpha field.

Confirmatory evidence of the effect of the zinc content on the hardness of the grains, exclusive of boundary area, has been sought through a microhardness survey made on grain centers (Fig. 5). This study was performed with a Kentron machine equipped with a Vickers 136° diamond pyramid indenter, using a 50 g load and a testing time of 30 s. About 25 grains were tested at each composition. The microhardness of the grain centers closely parallels that of the zero grain boundary hardness across the alpha field. The near absence of an effect from making the microhardness readings upon grain boundaries is thought to arise from the shallowness of the microindentation, the deforma-

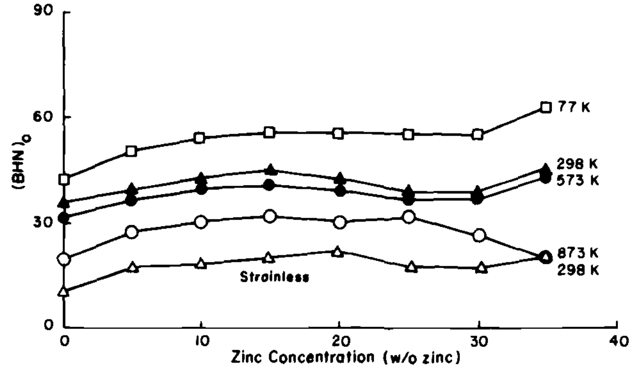

FIG. 4—*Zero grain boundary hardness versus the zinc concentration in alpha brass at 77, 298, 573, and 873 K and* (bottom curve) *the strainless hardness at 298 K.*

TABLE 3—*Zero intercepts and slopes of the lines plotted in Fig. 1.*

Zinc Composition, Weight %	Temperature, K	Intercept	Slope
0	77	42.25 ± 3.41	0.012 ± 0.0032
0	298	36.05 ± 1.28	0.005 ± 0.0014
0	573	32.07 ± 2.91	0.004 ± 0.0273
0	873	19.58 ± 1.78	0.004 ± 0.0167
5	77	50.59 ± 1.93	0.007 ± 0.0008
5	298	39.65 ± 0.62	0.008 ± 0.0004
5	573	36.33 ± 1.50	0.005 ± 0.0006
5	873	27.03 ± 1.93	0.004 ± 0.0008
5	298 final	40.08 ± 2.28	0.007 ± 0.0009
10	77	53.28 ± 1.39	0.009 ± 0.0006
10	298	43.00 ± 1.05	0.009 ± 0.0007
10	573	39.89 ± 4.66	0.005 ± 0.0020
10	873	29.96 ± 0.98	0.001 ± 0.0004
10	298 final	43.23 ± 4.39	0.007 ± 0.0019
15	77	55.13 ± 3.04	0.011 ± 0.0015
15	298	43.31 ± 2.30	0.010 ± 0.0010
15	573	40.40 ± 7.18	0.009 ± 0.0036
15	873	31.83 ± 1.56	0.000 ± 0.0008
15	298 final	44.21 ± 7.25	0.010 ± 0.0036
20	77	54.75 ± 3.07	0.013 ± 0.0014
20	298	42.40 ± 1.59	0.012 ± 0.0011
20	573	42.16 ± 17.2	0.003 ± 0.0080
20	873	30.05 ± 2.68	0.002 ± 0.0012
20	298 final	42.03 ± 11.8	0.013 ± 0.0055
25	77	54.98 ± 7.80	0.022 ± 0.0049
25	298	38.96 ± 1.98	0.021 ± 0.0016
25	573	36.86 ± 10.7	0.018 ± 0.0066
25	873	31.82 ± 8.87	−0.005 ± 0.0055
25	298 final	41.41 ± 11.1	0.019 ± 0.0069
30	77	56.13 ± 4.97	0.017 ± 0.0028
30	298	39.21 ± 1.30	0.018 ± 0.0011
30	573	38.02 ± 6.73	0.014 ± 0.0037
30	873	26.66 ± 7.94	−0.000 ± 0.0044
30	298 final	41.00 ± 11.5	0.014 ± 0.0065
35	77	61.84 ± 8.76	0.011 ± 0.0043
35	298	45.22 ± 1.94	0.012 ± 0.0015
35	573	43.35 ± 7.73	0.008 ± 0.0040
35	873	20.05 ± 1.91	0.002 ± 0.0009
35	298 final	46.53 ± 7.41	0.009 ± 0.0037

tion being discharged through the external surface instead of passing through boundary to any substantial degree.

The essence of all of these observations is that *there is nothing irregular in the effect of composition on the plastic contribution of the bodies of the grains to the Brinell hardness.* In the case of the grain boundary the situation is otherwise.

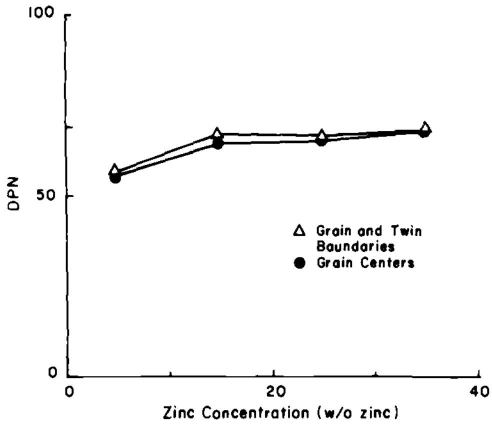

FIG. 5—*Average microhardness number versus the zinc concentration for grain centers and boundaries in annealed alpha brass.*

Effect of Composition on the Grain Boundary Contribution to Hardness

The hardness contribution of the grain boundary per unit of area ($\Delta HB/\Delta S_V$) is summarized as a function of the zinc content at 77, 298, 573, and 873 K in Fig. 6 and Table 3. Considering first the behavior at the lower temperatures (77 and 298 K), the hardening is positive and increases somewhat from 0 to 20% zinc. Thereupon, an abrupt increase in the hardening rate begins, maximizing at around 25% zinc. At 573 K the same pattern is followed, except that the hardening rates are a little smaller. At 873 K, however, the change in rate with added zinc first drops to zero and then becomes strongly negative at a minimum near 25% zinc. The *behavior of the grain boundary hardening rate near 25% zinc is distinctive and differs sharply from*

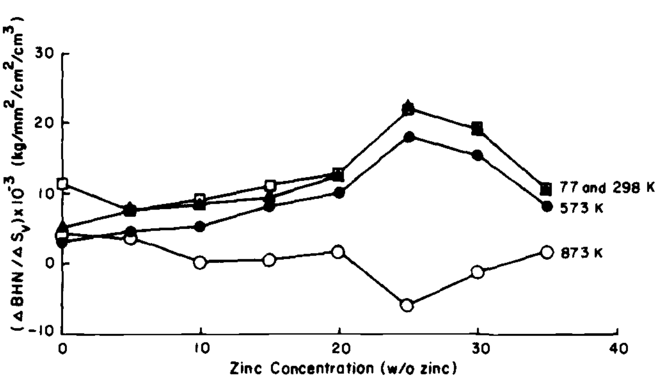

FIG. 6—*Rate of grain boundary hardening versus the zinc concentration in alpha brass at 77, 298, 573, and 873 K.*

the course of change of the elastic and plastic contributions in the same composition range; compare this phenomenon with Fig. 4.

Clearly, there is something unique about alpha brass at the 25% zinc composition, something associated with the passage of plastic shear through grain boundaries and which may shed further light on the mechanism of grain boundary hardening. The properties of the alpha brasses having been a major subject of study for more than a century and by essentially every known means of analysis, it appeared likely that an examination of the literature would identify some aspect in which the 25% zinc alloy is unusual. A thorough search revealed one, and only one, such property—namely, the stacking fault energy, which Thomas [*16*] found to display a sharp minimum in this composition range (Fig. 7). He conjectured that the stacking fault energy would continue to fall at beyond 25% zinc were it not for the onset of short-range order, which opposes the formation of stacking faults. This he demonstrated by measuring the stacking fault energies of brasses containing more than 25% zinc after they had been quenched from 1073 K, when they would be in the disordered state. The result is plotted as a dashed line in Fig. 7. The downward trend of the stacking fault energy continues through higher zinc compositions in the absence of ordering.

Further evidence that the observed abrupt increase in the grain boundary hardening rate is, indeed, to be associated with the low stacking fault energy has been obtained through a set of auxiliary experiments. These results demonstrate that an increase in the hardening rate is similarly suppressed by short-range order at higher zinc content. Three alloys, containing respectively 30, 33, and 35% zinc, were quenched from 873 K in order to decrease their degree of short-range order. Their hardness was measured immediately and then again after an extended period of aging, during which time the ordered

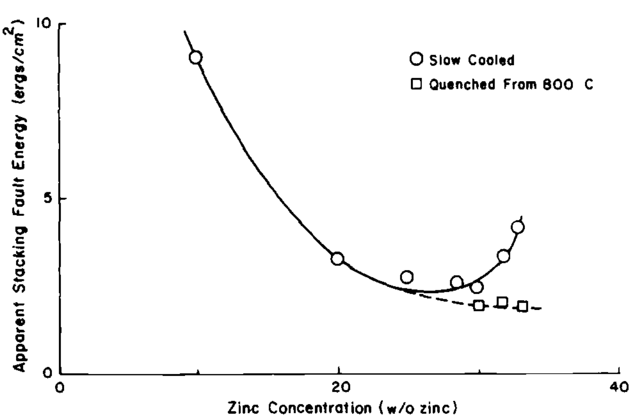

FIG. 7—*Stacking fault energies versus the zinc concentration in slow-cooled and quenched alpha brass [16].*

state was expected to be restored. The two alloys with lower zinc were little affected by this treatment, but the 35% zinc alloy exhibited increased hardness immediately after quenching and then reverted to its normal hardness during aging (Fig. 8). The authors conclude that *the low stacking fault energy is, indeed, responsible for the extra grain boundary hardening in the 25% zinc range.*

Role of Stacking Faults in Grain Boundary Hardening

Where stacking faults occur, the dislocations are split into partials that travel separately across the crystal plane. A partial dislocation, arriving at a grain boundary, is repelled elastically until its matching component arrives, because a split dislocation cannot undergo cross-slip. The lower the stacking fault energy, the greater the separation of the halves of the split dislocations and the larger the elastic resistance to the removal of the fault by closing the split dislocation. Hence, the lower the stacking fault energy, the greater the grain boundary contribution to hardening.

To estimate the energy required to eliminate the stacking faults in a unit volume of metal, it is necessary to know the fault width per dislocation line, the specific fault energy, and the percentage of slip planes that are faulted. Specific fault energies, γ, of the alpha brasses have been measured by Thomas [*16*] (Table 4). The stacking fault energy is related to the fault width per dislocation line through a relationship introduced by Cottrell [*17*]—that is, $r = \mu a^2/24\pi\gamma$, where r = the partial dislocation separation, μ = the shear modulus, a = the atomic spacing, and γ = the stacking fault energy. The stacking fault probability, α, is related to the stacking fault energy through the equation $\alpha = A\epsilon^2/\gamma$, where ϵ^2 = the mean square strain obtained from X-ray analyses of peak shifts, and A is a constant.

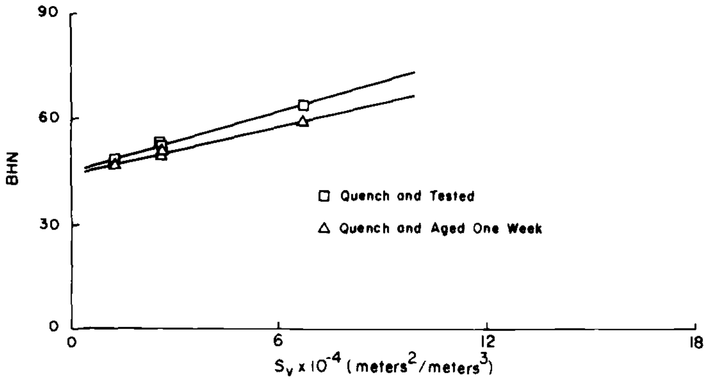

FIG. 8—*Brinell hardness number versus the grain boundary area (1/m) for the quenched and the aged states of 65Cu-35Zn brass.*

TABLE 4—*Stacking fault energy, stacking fault energy ratio, and grain boundary area contribution to the hardness ratio for the alpha brasses.*

Alloy Copper/Zinc Composition, Weight %	γ,[a] J/m^2 × 10^3	γ Copper/ γ Alloy Ratio	(ΔHB/ΔS_V) Alloy/ (ΔHB/ΔS_V) Copper Ratio
100/0	12.2	1.00	1.00
95/5	9.3	1.31	1.46
90/10	7.0	1.74	1.54
85/15	4.8	2.54	1.82
80/20	3.4	3.58	2.48
75/25	2.9	4.20	4.21
70/30	2.7	4.52	3.74
65/35	5.0	2.44	2.08

[a] Stacking fault measurements from Thomas [*16*].

In order to compare the fault energy per unit volume of metal for different compositions of alpha brass, the fault width per slip plane, r, is considered on a unit length basis. Thus the area of fault per slip plane would be $r(1)$. Since the fault energy per unit area is known, the energy per fault may be expressed as $r(1)\gamma$. But, since the percentage of faulting varies with composition, it is necessary to introduce this variable, and the fault energy per unit volume becomes $r(1)\gamma\alpha$, where $r = K/\gamma$ and $\alpha = K'/\gamma$. The parameters K and K' are $\mu a^2/24\pi$ and $A\epsilon^2$, respectively. Using these expressions for r and α, the expression for the fault energy per unit volume becomes $(1)KK'/\gamma$. Using this expression to obtain the ratio between the energy for copper and that for any one of the alloys, the factor $(1)KK'$ is eliminated and the energy ratio becomes $(1/\gamma$ alloy$)/(1/\gamma$ copper$)$. This ratio, which reduces to γ copper/γ alloy is a measure of the energy to eliminate all of the stacking faults per unit volume in the alloy divided by the energy to eliminate the stacking faults in copper. It is given for all of the experimental alloys in Table 4.

Chatterjee [*18*] has shown that Brinell hardness can be expressed in terms of the energy required to deform a unit volume of the metal. Hence, the hardness contribution per unit area of grain boundary is also a measure of the energy required to deform the intercrystalline boundary in a unit volume of metal. Again, this can be expressed as a ratio: (ΔHB/ΔS_V) alloy/(ΔHB/ΔS_V) copper, as in Table 4. A comparison of the stacking fault energy ratio versus composition with the ratios of hardness per unit area is made in Fig. 9. The ratios are essentially identical and show the same maximum of near 25% zinc. Thereby, *the increase in the hardening rate is associated directly with the energy increase required to pass dislocations into the grain boundaries.*

Effect of Temperature and Rate of Loading

As can be verified by reference to the graphs in Fig. 4, the zero grain boundary hardness decreases monotonically with a rise in temperature. Indeed, the

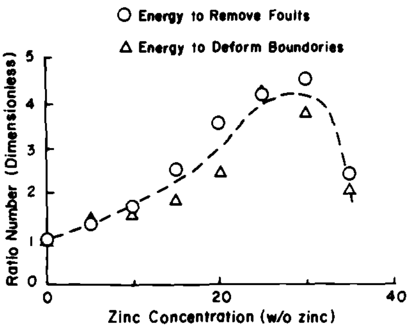

FIG. 9—*Comparison of the energy required to deform intercrystalline boundaries and to remove stacking faults in alpha brasses, divided by similar measurements in pure copper.*

decrease is nearly linear with temperature for pure copper, but becomes less regular with increasing zinc content. In Table 5 a comparison is made between the zero grain boundary hardness at the three higher temperatures (298, 573, and 873 K) and measurements of the dynamic elastic modulus, made by Köster [*19*] at the same temperatures. The parallelism between these sets of data is shown clearly in Fig. 10. From this it can be inferred that *the decrease in the zero grain boundary hardness that occurs with rising temperature is to be ascribed mainly to a reduction in the elastic contribution.*

Since the grain boundary contribution is derived from the transmission of plastic shear, which is now seen to be relatively unaffected by temperature change, it is not surprising that the rate of grain boundary hardening ($\Delta HB/\Delta S_V$) should also be unaffected by temperature (Fig. 6). The plots for 77 and 298 K are virtually superimposed and that for 573 K is only a little lower, although perhaps significantly so. But, at 873 K all is different. With increasing zinc content, the rate first drops to zero and, then, at near 25% zinc becomes strongly negative. The lowered resistance to plastic flow in creep

TABLE 5—*Comparison between the dynamic elastic modulus measurements of Köster and the zero grain boundary hardness for copper/zinc alloys at 298, 573, and 873 K.*

	Alloy			
Temperature, K	95Cu-5Zn	85Cu-15Zn	72Cu-28Zn	67Cu-33Zn
	ELASTIC MODULUS ($E \times 10^{-3}$), kg/mm^2			
298	13.0	12.4	11.5	11.3
573	11.8	11.1	10.2	10.1
873	9.5	8.8	7.9	7.2
	ZERO GRAIN BOUNDARY HARDNESS (HB), kg/mm^2			
298	39.8	44.9	38.6	42.5
573	36.5	40.4	36.5	40.0
873	27.1	31.8	28.5	23.0

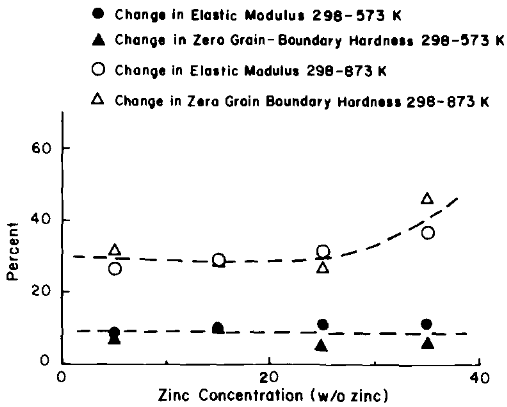

FIG. 10—*Percentage change in the elastic modulus and in the zero grain boundary hardness from 298 to 573 K and from 298 to 873 K as a function of the zinc concentration of the brass.*

in this temperature range is, of course, familiar and has been associated with so-called "sliding" on the grain boundary. Also, it will be recalled, it was necessary to use a shortened loading time at this temperature, because of the effect of creep on the size of the Brinell impression. Evidently, time becomes an important factor in the meaning of hardness in this temperature range.

To investigate further the effect of the time of loading, Rhode [7] reduced the time to 1/8000 s by using a Magniformer to apply the load. Because the magnitude of the load was indeterminate, though reproducible, it was necessary to make measurements at 298 K, as well as at 873 K, in order to obtain a comparison with results taken at normal speed. Also, the high-speed tests were run at room temperature both before and after the high-temperature tests to detect possible effects of grain growth at the high temperature. The results for pure copper and for the 70Cu-30Zn alloy are given in Fig. 11. In comparison with the plots for copper and for the 70Cu-30Zn brass in Fig. 1, the relative differences in the hardness numbers at high and low temperatures are much less in the high-speed tests. While the lineal relationship with the grain boundary area has been preserved, the rate of grain boundary hardening has dropped to zero at both temperatures in the case of copper. In the case of the brass, the rate of hardening at room temperature is reduced to about half that in testing at normal speed, while at 873 K, the rate of hardening has become positive and almost the same as that at room temperature.

The reduction in the grain boundary contribution to hardening in high-speed testing is interpreted to mean that that factor in normal plastic deformation which is special to the passage of shear through grain boundaries has been aborted in some degree. In other words, it is suggested that cross-slip has been restricted by the short duration of the test. The alternative is, of course, that slip packets have penetrated into the grain boundary. This would lead to

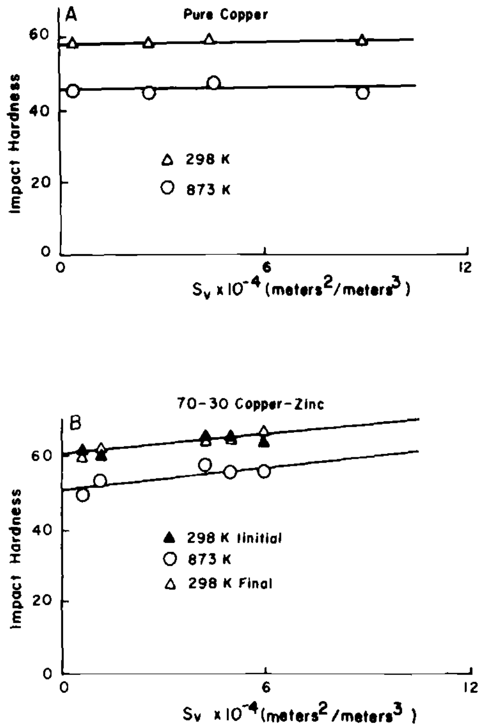

FIG. 11—*Impact hardness versus grain boundary area for pure copper and for the 70Cu-30Zn alloy, at 298 and 873 K [7].*

a higher shear resistance of the grain boundary if the stress were not relieved in some other way. The obvious means of relief is crack formation at overstressed sites on the grain boundary. Not only would this decrease the apparent resistance of the boundary to the passage of shear, but it would lead ultimately to grain boundary fracture at sufficiently high speeds of stressing. This is another familiar behavior of metals, in which the hexagonal metals in particular are noted for their tendency to fracture along grain boundaries in shock loading. The authors propose that *the brittle grain boundary fracture of pure metals under conditions of shock loading is to be ascribed to the failure of cross-slip to develop sufficiently in the time available.*

Grain Boundary Shearing

At slow speeds of deformation, at high temperature, shearing parallel with the grain boundary tends to replace shear across the boundary to a significant extent. In the present case, this process is held to be responsible not only for reducing the resistance of the boundary to plastic deformation, but also for actually reducing the overall resistance to deformation below that required to deform the crystalline matter in the absence of grain boundary.

The principal characteristics of high-temperature grain boundary shearing have been described in a prior publication by one of the present authors [*20*]. It occurs coincidentally with transgranular slip, at relatively low loads, at temperatures in the recovery range, where diffusion processes are rapid. Shear is confined to a thin zone parallel with the grain boundary and is in the direction of the maximum shear stress in the plane of the boundary, irrespective of the orientation of the crystal in which it happens. It occurs locally along the boundary in little bursts that add up to a total displacement of one crystal with respect to its neighbor. The duration of the burst is of the order of 1 s. When a shear ledge is exposed on an external surface, the surface of the ledge is glossy, as though it had been melted. Once shear has occurred across a boundary, a period of dormancy follows, as though the shear zone were pausing for a recharge. Perhaps the most remarkable attribute of grain boundary shearing is that its progress is unaffected by interruptions in loading or by temperature excursions, both to lower and to higher temperatures. When the original testing conditions are restored, grain boundary shearing continues where it left off, as though there had been no interruption.

The mechanism of grain boundary shearing, proposed in the same publication [*20*], is both consistent with and reinforced by the findings of the present research. At elevated temperature, where the rate of diffusion is high, some of the dislocations approaching the grain boundary, instead of undergoing cross-slip and entering the boundary, elect to precipitate as subgrain boundary. In this configuration, the dislocation is locked in place. It can neither cross-slip nor glide away and it is not disturbed by long exposure to high temperature. As plastic deformation of the aggregate continues, more dislocations are trapped in the zone next to the grain boundary, where they tend to distort the thin layer, much as the grain boundary would have been distorted had they penetrated it. The result is a lateral stress parallel with the grain boundary, but contained within the first crystal so that it is not relieved by transmission of its stress into the conjoint crystal. As the density of dislocations becomes higher, the crystalline matter, in a small region, becomes constitutionally unstable and is transformed momentarily into a fluid state, whereupon shear parallel with the boundary relieves the local stress and the fluid reverts to unstrained crystal. This process happening many times at different sites on a grain boundary results in the behavior known as "sliding." As in the case of high-speed deformation, the failure of some of the shear to pass through the grain boundary results in an accumulation of shear at points where grain boundaries meet, that is, at quadruple points of the grain boundary network. This accumulation builds a hydraulic stress at the quadruple point that may initiate a cavity that can spread along the connecting grain boundaries [*21*], leading ultimately to the rupture of the metal. Again, the force required to deform the aggregate is reduced by the opening of cavities and is lowered beneath that needed to deform the crystalline matter alone by the intervention of fluid shear along the grain boundary.

It has long been recognized that brasses in the 25 to 30% zinc range are particularly susceptible to grain boundary shearing. A reason for this can now be proposed. Since stacking faults decrease the tendency for the dislocations to cross-slip, their presence in the brass would tend to increase the fraction of dislocations precipitated as subgrain boundary. *This would increase the ratio of grain boundary shear to shear transmission through the boundary, thereby diminishing the hardness.*

Concerning Grain Boundary Energy

The thermodynamic energy of the grain boundary produces a two-dimensional tensile stress in the plane of the grain boundary. This stress differs from that which develops during the passage of shear through the boundary mainly in that it is a relatively weak force and in that its direction is controlled by crystallographic factors other than the slip systems. Whether these forces interact sufficiently to show an effect on the hardness has not been established. In pursuit of this question, Bates [*8*] undertook the determination of the grain boundary energy as a function of the zinc content of the alloys, using the dihedral angle method of Smith [*22*]. Sample specimens of the alloys were immersed in mercury, which was subsequently evaporated away to permit the measurement of the angle of the groove created at the grain boundaries. The readings contained too much scatter to be useful in any quantitative interpretation. They showed only a general trend toward higher energy with increasing zinc content, but no marked increase corresponding to the 25% zinc composition. The authors conclude that, *whereas it is not possible to rule out a contribution of the grain boundary energy to the hardening, as a whole, the special hardening at 25% zinc is of purely mechanical origin.*

A Note on the Silver/Zinc Alloys

The silver/zinc system is constitutionally very similar to the copper/zinc system and may be expected to exhibit similar mechanical behavior. Jenkins [*23*] undertook a similar study using three silver/zinc alloys containing 20, 25, and 30% zinc and ran hardness versus grain boundary area surveys at 77 and 298 K. He found the same direct relationship between Brinell hardness and grain boundary area, but the grain boundary contribution to hardness was from 10 to 20% less than in the copper/zinc alloys of the same concentrations. There was a distinct, but smaller maximum in hardness near 25% zinc. At the same compositions the silver alloys are considerably harder than their copper counterparts. The hardness difference at between 77 and 298 K is much greater in the silver series, however, indicating that softening with rising temperature sets in at a lower temperature.

Summary

1. The Brinell hardness of the alpha brasses is proportional to the grain boundary area at all compositions and at all temperatures (77 to 873 K), even in the high-zinc, high-temperature range, where an increase in the grain boundary area is associated with a decrease in hardness, even under conditions of shock loading in the Brinell test.

2. Brinell hardness measures a total resistance to deformation arising from three sources, which can be distinguished and measured separately. These are (1) the elastic resistance of the grains, (2) the resistance to plastic deformation of the grains, exclusive of their boundaries, and (3) the additional resistance to shear through the grain boundary.

3. The elastic contribution is measured by the strainless indentation method of Harris. It is not affected by the presence, or the amount, of grain boundary; that is, the grain boundary does not contribute to the elastic properties of the metal.

4. The hardness contribution of plastic shear through the bodies of the grains is measured by extrapolation of the total hardness to the zero grain boundary area and then subtracting the elastic contribution. The plastic resistance is about 50% greater than the elastic resistance. It is also independent of the sizes of the grains, as has been shown by the lack of effect on hardness of the distribution of grain size in the metal.

5. The grain boundary contribution to hardness is measured as the difference between the total hardness and the sum of the elastic and plastic contributions. The rate of grain boundary hardening is expressed as the change in total hardness per unit area of grain boundary.

6. The grain boundary serves to transform shear in one crystal into that in its differently oriented neighbor by first converting the shear that arrives at the grain boundary into a two-dimensional stress in the plane of the boundary. This stress is then relieved by an exactly compensating shear in the conjoint crystal, on a new set of slip planes.

7. The preservation of the integrity of the metal during shear into the grain boundary requires that the shear be homogeneous, in the sense that similar slip occurs on successive planes all across the area of the grain boundary. When a dislocation penetrates the boundary upon one slip plane, further slip on the same plane is resisted elastically until adjacent planes have slipped.

8. Inhomogeneous slip, approaching the grain boundary in slip packets, is redistributed by cross-slip acting in response to the elastic forces in the boundary. It is the energy required to effect cross-slip near the boundary that is detected as grain boundary hardening.

9. The elastic and plastic hardness behavior of the alpha brasses is like that of a simple solid solution series, up to 30% zinc, where short-range order appears. The grain boundary contribution is unique, however, in that a sharp

change in the rate of hardening occurs near 25% zinc. This occurrence is associated with the low stacking fault energy of alpha brass in this composition range.

10. At stacking faults, dislocations are split into partials that cannot cross-slip to enter the grain boundary. An additional energy must be supplied to reunite the partials for shear into the grain boundary. This energy has been calculated and its rate of change with change in composition has been found to be equal to the change in the hardening rate of the grain boundary.

11. Because the stacking fault energy is raised by order in the crystals, grain boundary hardening decreases in the presence of order in the 30% zinc range. When ordering is reduced by quenching from a high temperature, grain boundary hardening increases. Aging to restore order is accompanied by a loss in hardening.

12. At low and moderate temperatures, the reduction in total hardness that accompanies increase in temperature is associated mainly with the elastic contribution to hardness; that is, the plastic properties, including grain boundary shear, are unaffected by temperature in this range.

13. At recovery temperatures and above, shearing through the grain boundary begins to be replaced by shearing parallel to the grain boundary. This is felt as a lowering of hardness which, in the alloys in the 25% zinc range, becomes an actual softening of the metal at 873 K.

14. In the recovery range, some of the dislocations tend to precipitate adjacent to the grain boundary in the form of subgrain boundary, in which form they become immobile. As they gather, they build a shear stress parallel to the grain boundary. When the concentration of immobilized dislocations becomes high, the crystal next to the boundary becomes constitutionally unstable and is transformed momentarily into a fluid state (amorphous perhaps), which has low shear resistance and permits the stress parallel to the boundary to be relieved by sudden shear. Such grain boundary shearing creates cavities at grain quadruple points, disrupting the integrity of the metal and, thereby, decreasing the energy required to produce the Brinell indentation.

15. Under conditions of high-speed loading (that is, a Brinell test at 1/8000 s), shear parallel to the grain boundary is suppressed, because the precipitation of dislocations as subgrain boundary is a diffusion process that requires time. The rate of grain boundary hardening is also diminished at high speed, because the process of cross-slip also requires finite time. In the absence of cross-slip, the grain boundary is overstressed locally and voids are created, leading to possible cracking. This appears to be a mechanism of grain boundary fracture in shock loading.

16. The thermodynamic grain boundary energy seems to play little, if any, part in grain boundary hardening.

17. The alpha silver/zinc alloys behave in much the same way as the alpha brasses in their hardness relationships.

Acknowledgment

The contents of this paper were extracted from a doctoral thesis presented to the University of Florida in 1968 by one of these authors (Lemons).

References

[1] Sylwestrowicz, W. and Hall, E. O., *Proceedings of the Physical Society*, Vol. 64B, No. 6, 1951, pp. 495-502.
[2] Babyak, W. J. and Rhines, F. N., *Transactions of the A.I.M.E.*, Vol. 218, 1960, pp. 21-23.
[3] Boas, W. and Hargreaves, M. E., *Proceedings of the Royal Society, Series A*, Vol. 193, 1948, pp. 89-97.
[4] Rhines, F. N., Ellis, R. A., Jr., and Gokhale, A. B., *Scripta Metallurgica*, Vol. 15, 1981, pp. 783-785.
[5] Rhines, F. N. and Gokhale, A. B., *Microstructural Science*, Vol. 11, 1983, pp. 3-11.
[6] Geronimos, M. G. and Wood, R. O., "Relationship of the Harris Number to the Grain Size of Two Copper Alloys," senior thesis submitted to J. S. Wolf at Clemson University, Clemson, S.C., 29 April 1972.
[7] Rhode, R. C., "Strain Rate and Temperature Effects on Grain Boundary Hardness Contributions in Recrystallized Alpha Brass," senior thesis submitted to F. N. Rhines at the University of Florida, Gainesville, Fla., December 1967.
[8] Bates, S., senior thesis submitted to the University of Florida, Gainesville, Fla., 1965.
[9] Rhines, F. N. and Patterson, B. R., *Metallurgical Transactions*, Vol. 13A, No. 6, 1982, pp. 875-993.
[10] Harris, F. W., *Journal of the Institute of Metals*, Vol. 28, No. 2, 1922, pp. 327-351.
[11] O'Neill, H., *The Hardness of Metals and Its Measurement*, Chapman and Hall, London, 1934.
[12] Meyer, E., *Zeitschrift des Vereins der Deutschen Ingenieure*, Vol. 52, 1908, p. 645.
[13] Rhines, F. N., *Transactions of the A.I.M.E.*, Vol. 1, 1970, pp. 1105-1120.
[14] Köster, W. and Schüle, W., *Zeitschrift für Metallkunde*, Vol. 48, No. 11, 1957, pp. 589-591.
[15] Clareborough, L. M., Hargreaves, M. E., and Loretto, M. H., *Journal of the Australian Institute of Metals*, Vol. 6, No. 2, 1961, pp. 104-114.
[16] Thomas, F., *Journal of the Australian Institute of Metals*, Vol. 8, No. 1, 1963, pp. 80-90.
[17] Cottrell, A. H., *Dislocations and Plastic Flow in Metals*, Oxford University Press, Oxford, England, 1953.
[18] Chatterjee, G. P., *Transactions of the A.I.M.E.*, Vol. 206, 1956, pp. 454-455.
[19] Köster, W., *Zeitschrift für Metallkunde*, Vol. 32, No. 6, 1940, pp. 160-162.
[20] Rhines, F. N., Bond, W. E., and Kissel, M. A., *Transactions of the American Society for Metals*, Vol. 48, 1956, pp. 919-951.
[21] Nemy, A. S. and Rhines, F. N., *Transactions of the Metallurgical Society of A.I.M.E.*, Vol. 215, 1959, pp. 992-998.
[22] Smith, C. S., *Transactions of the A.I.M.E.* (Institute of Metals Division), Vol. 175, 1948, pp. 11-51.
[23] Jenkins, D. A., senior thesis submitted to the University of Florida, Gainesville, Fla., 1967.

Günter Petzow,[1] *Shigeaki Takajo,*[2] *and Wolfgang A. Kaysser*[3]

Application of Quantitative Metallography to the Analysis of Grain Growth During Liquid-Phase Sintering

REFERENCE: Petzow, G., Takajo, S., and Kaysser, W. A., "**Application of Quantitative Metallography to the Analysis of Grain Growth During Liquid-Phase Sintering,**" *Practical Applications of Quantitative Metallography, ASTM STP 839,* J. L. McCall and J. H. Steele, Jr., Eds., American Society for Testing and Materials, Philadelphia, 1984, pp. 29-40.

ABSTRACT: During liquid-phase sintering of iron/copper and various other systems, particle contacts involving grain boundaries with low energy, that is, with large dihedral angles, were frequently observed. By means of electron channeling pattern investigations on a copper/silver system, such low-energy grain boundaries were proved to be low-indexed coincidence boundaries. With the assumption that particle coalescence following the low-energy boundary formation mainly contributes to particle growth, the growth behaviors were treated generally on a statistical basis and then correlated with the special case of iron/copper. Average particle sizes and particle size distributions were calculated and compared with experimental results. It was found that coalescence contributes significantly to particle growth.

KEY WORDS: quantitative metallography, liquid-phase sintering, grain growth, coalescence, iron, copper, grain boundaries, metallography

Diffusion-controlled Ostwald ripening is generally thought to be one of the essential mechanisms of particle growth during liquid-phase sintering of metallic systems. Theoretical work of Lifshitz and Slyozov [*1*][4] and Wagner [*2*] dealing with diffusion-controlled Ostwald ripening postulates a cubic time law for

---

[1] Professor, Max-Planck-Institut für Metallforschung, Institut für Werkstoffwissenschaften, Stuttgart, West Germany.

[2] Senior researcher, on leave from the Kawasaki Steel Corp., Kobe, Japan.

[3] Visiting scientist, Department of Materials Science and Engineering, Massachusetts Institute of Technology, Cambridge, Mass. 02139; on leave from the Max-Planck-Institut für Metallforschung, Stuttgart, West Germany.

[4] The italic numbers in brackets refer to the list of references appended to this paper.

the average particle size. This relationship was verified for liquid-phase sintering of numerous systems, including iron/copper. Quantitative measurements however, showed, larger values for the average particle sizes and broader particle size distributions than those predicted by the theory [*3*]. These discrepancies were attributed to the effect of the volume fraction of solid particles, which is usually >0.5 in sintering experiments, while the theory had treated an infinitely dilute solution. Of the several modified Ostwald ripening theories considering the volume fraction effect, Brailsford and Wynblatt have presented the most plausible treatment [*4*]. Their calculation provides more broadened particle size distributions, yet shows no quantitative agreement with measured distributions of liquid-phase sintered systems like iron/copper.

More recently, microstructural observations [*3*,*5*] have indicated particle coalescence as a possible mechanism of grain growth during liquid-phase sintering of some systems. In a prior theoretical approach, Courtney [*6*–*8*] treated the development of the average particle size by assuming that coalescence may occur by the growth of necks which form when particles come in contact because of random particle movement in the liquid. In the present work, an alternative theoretical approach based on the coalescence mechanism, which will be experimentally determined, provides, in addition, a prediction of particle size distributions and, hence, a conclusive comparison between calculations and experiments.

Experiments

Carbonyl iron powder (average diameter, 3.0 μm) and atomized copper powder (average diameter, 9.5 μm) were mixed to obtain the compositions Fe-30Cu and Fe-60Cu, either packed loosely in a crucible or pressed in a die at 500 MPa and sintered in hydrogen (H_2) at 1150°C for times between 4 and 1017 min. Afterward, sintering chord length distributions of the particles were measured by a linear analyzer. Most particles were single grains. Grains connected by necks with random grain boundaries were counted as separate particles. Grains connected by necks with radii 0.9 times the particle radius, that is, with low-energy grain boundaries, were counted as one particle.

Because of the $\gamma \rightarrow \alpha$ phase transformation in the iron/copper specimens during cooling, the characterization of grain boundaries could not be performed in the system. The characterization of grain boundaries was instead carried out on copper/silver specimens, after heat treatment comparable to that used on the iron/copper specimens. The copper/silver specimens were made from a mixture of electrolytic copper powder (nominal size, 10 μm) and electrolytic silver powder (nominal size, 2.0 to 3.5 μm), which was loosely packed and sintered in H_2 at 800°C for 722 min. The orientation relationships between adjacent grains were determined by the electron channeling pattern (ECP) technique.

Results

The microstructure of a liquid-phase sintered iron/copper specimen is shown in Fig. 1. Austenite grain boundaries that were present during liquid-phase sintering, that is, prior to the $\gamma \rightarrow \alpha$ transformation during cooling, can be identified by coarse grain boundary precipitates and precipitation-free zones along the boundaries. Some of the boundaries show high dihedral angles at triple junctions with the solid/liquid interfaces [Fig. 1 (*left*)], which suggests a low grain boundary energy. In addition, unusual grain boundary configurations, shown in Fig. 1 (*right*), may be attributed to the existence of low-energy boundaries on which grain boundary precipitates did not form during cooling. In Fig. 2 the measured apparent dihedral angle distribution of a specimen section is compared with a distribution curve calculated with the assumption of a unique value for the real dihedral angle of 45° [*9*]. The comparison confirms the nonuniqueness of the real dihedral angles and the considerable excess of grain boundaries with large angles, that is, low energy.

Figure 3 shows the results of the ECP analyses of a sintered copper/silver specimen, which has an analogous microstructure to the iron/copper specimens. The orientation relationship between adjacent grains is characterized by a nearest coincidence site relation, with the inverse of the density of coincidence sites, Σ, up to 19 [*10*] and the deviation from that relation θ_{dev}. Boundaries with large dihedral angles yield small Σ values and small deviations, θ_{dev}, from the ideal orientation relationships [*11*].

The time dependence of the average measured intercept length of iron/copper is shown in Fig. 4. For sintering times over 20 min, the cubic time law is clearly seen. In qualitative accordance with the predictions of prior theoretical treatment [*4,12*], the growth rate increases with increasing solid volume fraction. The deviations from the cubic time law for short sintering times, especially for the Fe-60Cu specimen, may be attributed to an initially inhomogeneous melt distribution in these specimens, yielding excess grain growth rates in regions of low melt content in comparison with the growth rates expected for a homogeneous melt distribution. In Figs. 5*a* and 5*b* the measured normalized intercept length distribution data were plotted for various specimens sintered more than 60 min. As shown in previous studies, a stationary distribution is found which shows no sharp cutoff of frequencies for longer intercepts, but a smooth decreasing frequency that may be described as exponential.

Discussion

The microstructural observations suggest the following coalescence mechanism: particle necks with low-energy grain boundaries grow almost without any retarding influence of the grain boundary until the concave curvature at

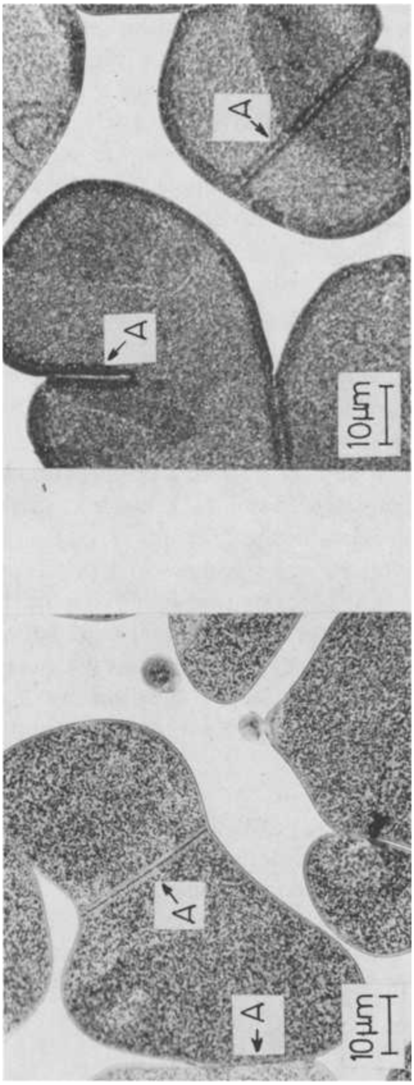

FIG. 1—*Austenite grain boundaries (marked with A) observed in Fe-30Cu (loose powder aggregate, 1165°C):* (left) *sintered for 316 min, cooled at 30 K/min;* (right) *sintered for 1017 min, cooled at 5 K/min.*

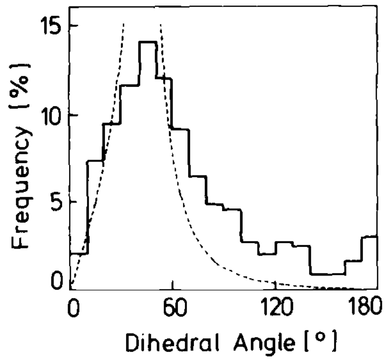

FIG. 2—*Apparent dihedral angle distribution in Fe-30Cu sintered at 1165°C for 315 min. The broken line is calculated for a constant special dihedral angle (45°).*

the neck region is eliminated. Subsequently, the boundaries may migrate away from the former position and the coalescence is completed. Some of the low-energy boundaries remain inside the particles without having an essential effect on the further particle growth.

To compare the suggested mechanism with the quantitative metallographic measurements, basic equations have been derived which describe the growth rate of the average intercept length and the stationary intercept length distribution.

Assuming coalescence as the main contribution to particle growth, an equation for the distribution, $g(v, t)$, for particle volumes, v, at time, t, can be postulated as follows

$$\frac{\partial g(v,t)}{\partial t} = \frac{\eta_c \int_0^v g(v',t)g(v-v',t)dv'}{2\int_0^\infty g(v', t)dv'} - \eta_c g(v,t) \tag{1}$$

where η_c is the frequency of coalescence for any particle in unit time; η_c is assumed to depend on the mean particle volume, $\bar{v}$, at any moment of the sintering. Furthermore, it is assumed that the coalescence process is controlled by the diffusion of the iron atoms in the liquid; therefore, the characteristic time for coalescence, τ_c, is proportional to $\bar{v}$ or $\bar{r}^3$, where $\bar{r}$ is the average particle radius at any time. η_c is expressed as a product of $1/\tau_c$ and the constant coalescence possibility, p_c*[5]

$$\eta_c = p_c/\tau_c \propto \bar{v}^{-1} \tag{2}$$

---

[5] The coalescence possibility, p_c, describes the probability of a particle possessing a neck with a low-energy grain boundary. The coalescence possibility was assumed to be constant during the sintering treatment, without specifying the mechanism of neck formation. The coalescence possibility was defined as the product of the number of necks per particle with low-energy boundaries and the fraction of low-energy boundaries.

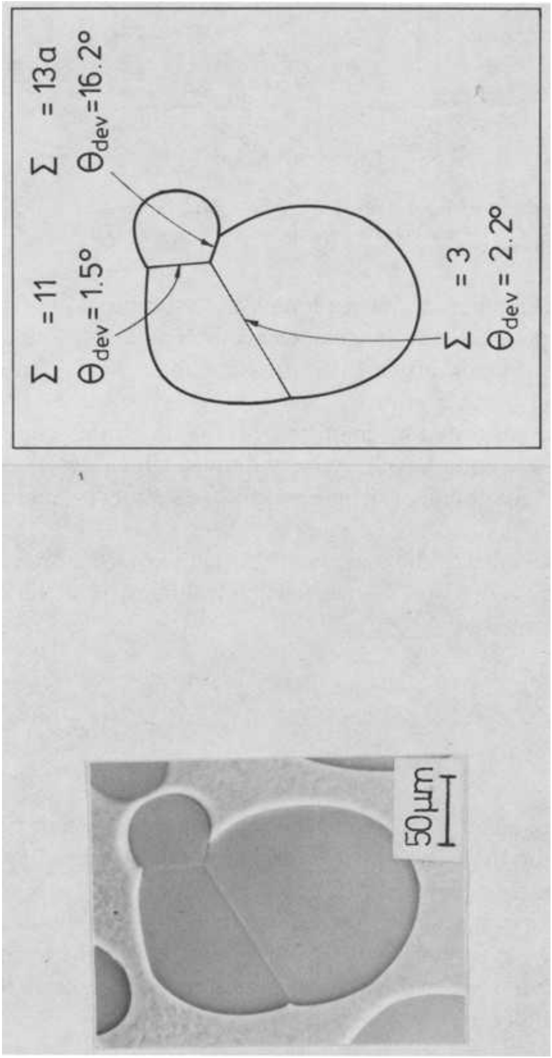

FIG. 3—ECP analyses of a Cu-44Ag specimen sintered at 800°C for 722 min: (left) secondary electron image, (right) characterization of grain boundaries.

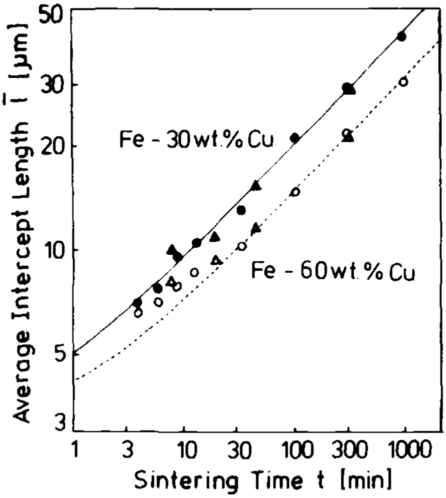

FIG. 4—*Time dependence of the measured average intercept length of particles in iron/copper:* ● ○, *pressed, 1150°C;* ▲ △, *loose powder aggregate, 1165°C;* —, ⋯, *calculated on the basis of the coalescence model.*

It can be shown from Eqs 1 and 2 that the particle growth reaches a steady state after a definite time, where the cubic time law, $\bar{r} \propto \bar{v}^{1/3} \propto t^{1/3}$, holds and the normalized particle volume distribution, $G(w)$, with $w = v/\bar{v}$, has a unique form independent of time: $G(w) = e^{-w}$ [*13*]. The development of the normalized distribution is shown in Fig. 6 in terms of the corresponding particle size distribution, $F(u)$, as a function of $\bar{v}/\bar{v}_0$. A log-normal initial distribution is assumed, where $\bar{v}_0$ is the value of $\bar{v}$ at the beginning of sintering. In Fig. 5 are shown the normalized stationary particle size distributions, $F(u)$, with $u = r/\bar{r}$, for coalescence, which is expressed by

$$F(u) = 2.136u^2 \exp(-0.7121u^3) \tag{3}$$

and for diffusion-controlled Ostwald ripening [*14*] for the solid volume fractions $\rho \rightarrow 0$ and $\rho = 0.8$. In comparison with the others, the distribution calculated on the basis of the coalescence principle is much broader and possesses no cutoff particle size but shows an exponential decrease for large particle sizes.

The particle size distribution function, $F(u)$, was transformed into the intercept length distribution function, $H(z)$, using relations derived by Hillard [*15*]. Expressing his equation in terms of normalized distribution functions, we obtain

$$H(z) = \frac{(\overline{u^3})}{(\overline{u^2})^2} \int_0^\infty uF(u)T\left(\frac{\overline{u^3}z}{\overline{u^2}u}\right)du \tag{4}$$

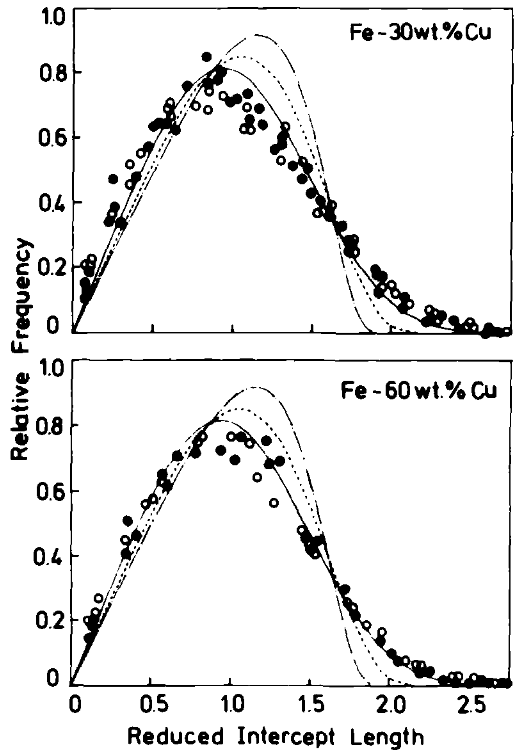

FIG. 5*a*—*The measured intercept length total distribution of particles in Fe-30Cu in comparison with calculations based on the coalescence* (——) *and the diffusion-controlled Ostwald ripening with a solid-phase volume fraction of* ≈ 0 (———) *and 0.8* (---): ○, *pressed, 1150°C;* ●, *loose powder aggregate, 1165°C.*

where $F(u)$ is the normalized particle size distribution as a function of $u = r/\bar{r}$ (r is the particle size, and $\bar{r}$ is the average particle size); $H(z)$ is the normalized intercept length distribution as a function of $z = l/\bar{l}$ (l is the intercept length, and $\bar{l}$ is the average intercept length); $T(L)$ is the normalized intercept length distribution for a single particle as a function of $L = l_l/\bar{l}_l$ (l_l is the intercept length in the particle, and $\bar{l}_l$ is the average intercept length of the particle); and $\bar{u^n}$ is the n^{th} moment of the distribution $F(u)$. For spherical particles, substituting Eq 3 for Eq 4 yields

$$H(z) = 1.208z \exp(-0.403z^3) \tag{5}$$

In Figs. 5*a* and 6 the theoretical normalized intercept length distribution curves for coalescence and diffusion-controlled Ostwald ripening [*4*] are shown, together with the measured distribution. The coalescence curve provides by far the best fit of all the theoretical curves (compare Ref *16*).

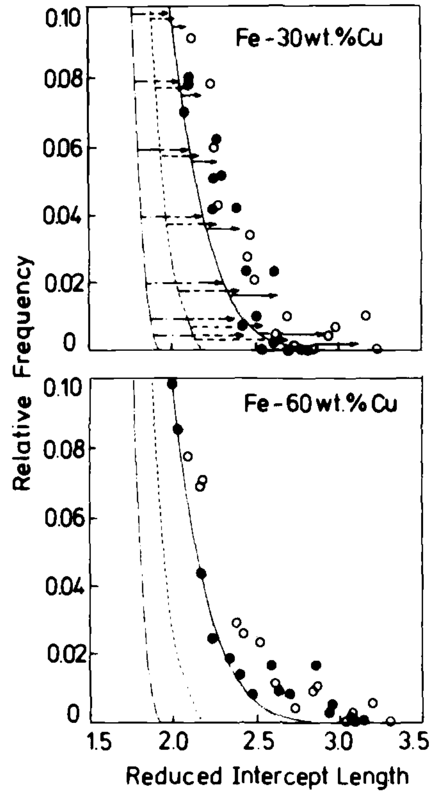

FIG. 5b—*Frequency for large intercepts in Fe-30Cu under the conditions in Fig. 5a. The arrows show the maximal estimated deviation from the calculations due to nonspherical particle shapes.*

For a more detailed comparison between experiment and calculation, the measured data in Fig. 5 are reproduced in Fig. 6 (*top*) as two continuous curves for Fe-30Cu and Fe-60Cu, together with the theoretical curve on the basis of coalescence. Slight discrepancies between experiment and theory can be seen. The main differences between the measured curves and the theory can be characterized by (1) $H(z) \not\rightarrow 0$ for $z \rightarrow 0$ and (2) longer tails [Fig. 6 (*bottom*)]. The latter discrepancy is more marked for Fe-30Cu. The discrepancies may be partly explained by the effect of the nonspherical particle shape. As shown by the microstructure of Fig. 1, the solid particles of liquid-phase sintered iron/copper are not ideally spherical. The deviation from the sphericity may be exaggeratedly modeled by an oblate rotational ellipsoid with an axis ratio of 1:2. Additional effects of the nonsphericity caused by the necks can be modeled by an orthogonally faceted sphere [*17*] with a ratio of the distance between parallel facets to the original sphere diameter of 1:1.1. The geometry of these modeled particle shapes is shown in Fig. 7.

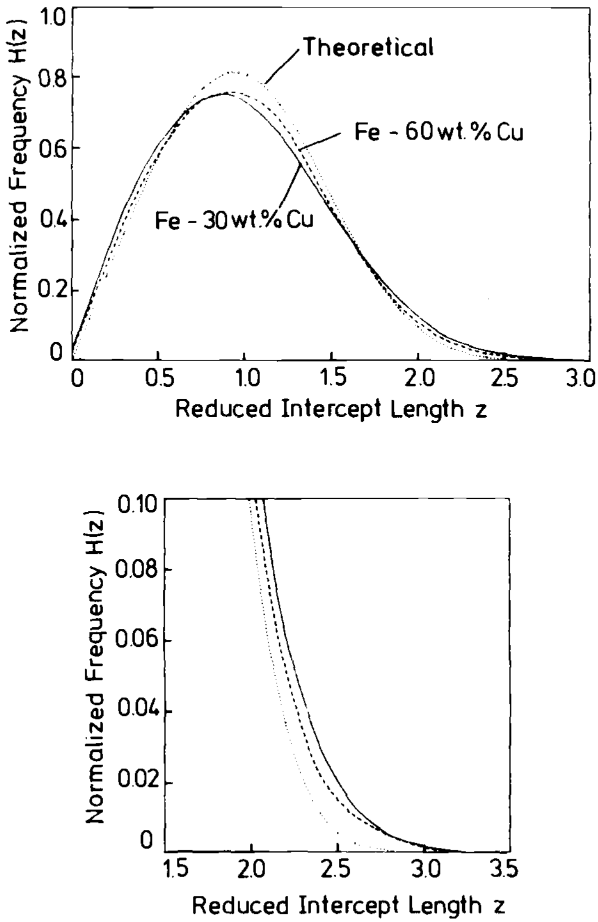

FIG. 6—*Comparison between measured and calculated normalized intercept length distributions:* ——, *measured Fe-30Cu;* ------, *measured Fe-60Cu;* ....., *calculated on the basis of homogeneous coalescence frequency:* (top) *total distribution,* (bottom) *frequency for large intercepts.*

Using the intercept length distributions corresponding to the unit particles [*18*] shown in Fig. 7, we obtain the normalized intercept length distributions on the basis of the coalescence theory (homogeneous coalescence frequency). One of the previously mentioned discrepancies between the measured and the calculated distributions ($H(z) \nrightarrow 0$ for $z \to 0$) is easily explained to be due to the nonspherical but faceted particle shape caused by the necks. The longer tails of the measured distributions may be attributed to the other shape effect.

Nonspherical particle shapes can also broaden the intercept length distribution based on the Ostwald ripening theory. As seen in Fig. 8, however, even as

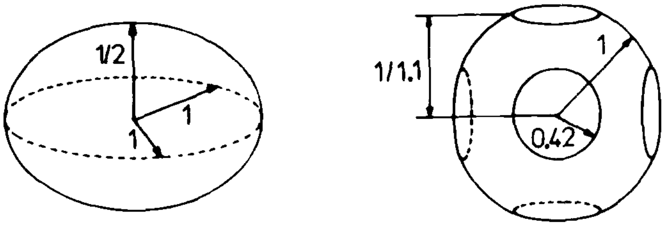

FIG. 7—*Unit particles for modeling realistic particle shapes:* (left) *oblate rotational ellipsoid,* (right) *faceted sphere.*

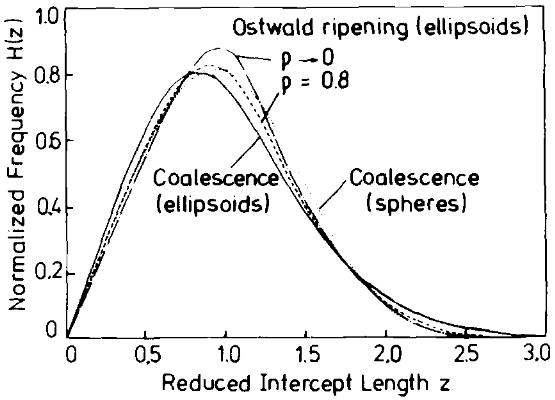

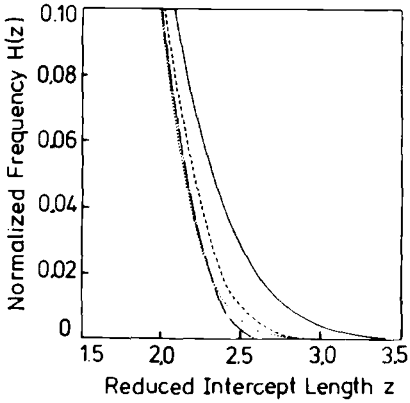

FIG. 8—*Normalized intercept length distributions for ellipsoid-shaped particles calculated on the basis of coalescence and Ostwald ripening:* ——, *homogeneous coalescence frequency;* — — —, *Ostwald ripening with solid phase volume fraction* $\rho \rightarrow 0$; ----, *Ostwald ripening with* $\rho = 0.8$; . . . . ., *homogeneous coalescence frequency for spherical particles:* (top) *total distribution,* (bottom) *frequency for large intercepts.*

exaggerated correction, assuming the ellipsoid in Fig. 7, cannot yield such a long tail as that observed experimentally.

Conclusions

The mechanism of particle coalescence during liquid-phase sintering of iron/copper can be described as contact formation between particles with low-energy grain boundaries, neck growth, and completion of the coalescence by migration of the grain boundary away from the particle neck. Theoretical treatments of the particle growth, assuming coalescence as the main contribution, provide predictions of the time law of the average particle sizes and of particle size distributions which are in good agreement with the experimental results.

References

[1] Lifshitz, I. M. and Slyozov, V. V., *Journal Physics and Chemistry of Solids*, Vol. 19, 1961, pp. 35-50.

[2] Wagner, C., *Zeitschrift für Elektrochemie*, Vol. 65, 1961, pp. 581-591.

[3] Watanabe, S. and Masuda, Y. in *Sintering and Catalysis*, G. C. Kuczynski, Ed., Plenum Press, New York, 1975, pp. 389-398.

[4] Brailsford, A. D. and Wynblatt, R. P., *Acta Metallurgica*, Vol. 27, 1979, pp. 489-497.

[5] Zukas, E. G., Rogers, P. S. Z., and Rogers, R. S., *International Journal of Powder Metallurgy and Powder Technology*, Vol. 13, 1977, pp. 27-38.

[6] Courtney, T. H., *Metallurgical Transactions A*, Vol. 8A, 1977, pp. 671-678.

[7] Courtney, T. H., *Metallurgical Transactions A*, Vol. 8A, 1977, pp. 679-684.

[8] Courtney, T. H., *Metallurgical Transactions A*, Vol. 8A, 1977, pp. 685-689.

[9] Berner, D., Exner, H. E., and Petzow, G. in *Modern Developments in Powder Metallurgy*, H. H. Hausner and W. E. Smith, Eds., Metal Powder Industries Federation, Princeton, N.J., 1974, pp. 237-250.

[10] Pumphrey, P. H., in *Grain Boundary Structure and Properties*, G. A. Chadwick and D. A. Smith, Eds., Academic Press, London, 1976, pp. 139-200.

[11] Kaysser, W. A., Takajo, S., and Petzow, G., *Zeitschrift für Metallkunde*, Vol. 73, 1982, pp. 579-580.

[12] Ardell, A. J., *Acta Metallurgica*, Vol. 20, 1972, pp. 61-71.

[13] Takajo, S., Ph.D. thesis, University of Stuttgart, Stuttgart, West Germany, 1981.

[14] Takajo, S., Kaysser, W. A., and Petzow, G., *Acta Metallurgica*, Vol. 32, in press.

[15] Hillard, J. E., *Transactions of The Metallurgical Society of A.I.M.E.*, Vol. 242, 1968, p. 1373.

[16] Kaysser, W. A., Takajo, S., and Petzow, G., *Acta Metallurgica*, Vol. 32, in press.

[17] Warren, R., *Proceedings*, Fourth International Congress for Stereology, Gaithersburg, Md., September 1975, pp. 25-28.

[18] Naumovich, N. V. and Warren, R. in *Quantitative Analysis of Microstructure in Materials Science, Biology and Medicine*, J. L. Chermant, Ed., Riederer-Verlag, Stuttgart, West Germany, 1978, pp. 161-170.

Setumadhavan Krishnamurthy,[1] *Kuang-Wu Qian,*[2] *and Robert E. Reed-Hill*[3]

Effects of Deformation Twinning on the Stress-Strain Curves of Low Stacking Fault Energy Face-Centered Cubic Alloys

---

REFERENCE: Krishnamurthy, S., Qian, K.-W., and Reed-Hill, R. E., **"Effects of Deformation Twinning on the Stress-Strain Curves of Low Stacking Fault Energy Face-Centered Cubic Alloys,"** *Practical Applications of Quantitative Metallography, ASTM STP 839,* J. L. McCall and J. H. Steele, Jr., Eds., American Society for Testing and Materials, Philadelphia, 1984, pp. 41-64.

ABSTRACT: A quantitative metallographic study of the effects of mechanical twinning on the uniaxial stress-strain curves of Cu-3.1Sn, Cu-4.9Sn, Cu-30Zn, and Co-40Ni has shown that twinning produces identifiable deformation stages in these alloys. These deformation stages are (1) an interval without twinning, (2) twinning on a single crystallographic plane within a grain, (3) twinning on intersecting twinning planes, and (4) dynamic recovery. In Stage 2, in which twins apparently form on the primary slip plane, twinning decreases the work hardening rate, whereas in Stage 3 the development of intersecting twin arrays increases the work hardening rate by progressively decreasing the effective grain size. The increased work hardening in Stage 3 accounts for the unusually high ductility of those alloys that twin heavily. The strength of the effects of the twinning on the stress-strain curve increases with increasing solute concentration and decreasing temperature.

KEY WORDS: quantitative metallography, face-centered cubic (fcc) alloys, stacking fault energy, deformation twinning, tensile stress-strain curves, volume fraction of twins, ductility, strength

While there have been many investigations of mechanical twinning in face-centered cubic (fcc) metals, few have been devoted to determining the effect of

---

[1] Formerly graduate student, Department of Materials Science and Engineering, University of Florida, Gainsville, Fla.; now National Research Council associate, Air Force, Wright Aeronautical Laboratories, Wright-Patterson Air Force Base, Dayton, Ohio 45433.

[2] Visiting professor, Department of Materials Science and Engineering, University of Florida, Gainesville, Fla.; now professor, Fuzhou University, Fuzhou, Fujian, People's Republic of China.

[3] Professor, Department of Materials Science and Engineering, University of Florida, Gainesville, Fla. 32611.

twinning on stress-strain behavior. Furthermore, most of these studies have dealt with single crystals of pure metals deformed at very low temperatures. Thus, research on the effects of twinning on the polycrystalline fcc stress-strain curve at temperatures of commercial interest has been very limited.

In most fcc solid-solution alloys, the twinning stress decreases with increasing solute concentration. This is generally believed to be due to a decrease in the stacking fault energy with increasing solute concentration. The stacking fault energy influences the twinning stress because the work to form a twin includes the energy of the twin boundaries whose surface energy is closely related to the stacking fault energy [*1*].[4]

Deformation twinning and slip can be considered competitive forms of plastic deformation in metals. Twinning differs significantly from slip in a number of ways. Because the motion of a total slip dislocation brings the lattice back into registry behind the dislocation, there is no alteration of the crystal structure caused by the movement of dislocations. This is not true of a twin because the crystal structure inside the twin has a different orientation from that of the original crystal. Although this orientation is twin-related to the matrix, and it can be shown that some dislocations can easily pass through the twin boundary from the matrix to the twin or vice versa, the experimental evidence strongly suggests that a twin boundary can act as a grain boundary. Thus, twins can often be considered to reduce the grain size of a metal by adding additional grain boundaries.

Because slip is normally the more important of the two types of deformation, the effect of mechanical twinning on metal plasticity is perhaps best viewed in terms of how it perturbs the stress-strain behavior expected from slip alone. For example, if the critical stress to form twins is less than that to cause slip, twinning can lower the yield stress. In the low stacking fault energy fcc metals currently under consideration, twinning can influence the yield stress at low temperatures in an alloy such as Cu-4.9Sn, which has a very low stacking fault energy. Normally, however, in these fcc alloys yielding occurs because of slip alone and twinning starts only after a finite critical strain. Thus, the most significant aspect of twinning should be its effect on the work hardening rate. At this point, it should be pointed out that the present discussion is concerned only with very low stacking fault energy fcc alloys, where the greater occurrence of dissociated dislocations should have a strong impact on the work hardening and the competition between slip and twinning.

Currently, there are two divergent views concerning the effect of mechanical twinning on the work hardening rate in low stacking fault energy polycrystalline FCC metals. Vöhringer [*2-5*], who worked with copper alloys using optical microscopy, has proposed that a twin adds an increment to the strain, ϵ, but does not influence the flow stress, σ. This implies a reduction in the work hardening rate once twinning begins. In support of this, Vöhringer has shown

---

[4] The italic numbers in brackets refer to the list of references appended to this paper.

that a sharp increase in $d\epsilon/d\sigma$, the reciprocal of the work hardening rate, occurs on a $d\epsilon/d\sigma$ versus σ plot when the first twin lamellae become visible. On the other hand, Rémy [*6*], who studied twinning in Co-33Ni, takes an alternative stand. He assumes that twins increase the flow stress and the work hardening rate because they decrease the grain size once the twins start to form. Rémy's view is shared by some other investigators [*7,8*]. In a previous paper [*9*], two of the present authors reported on the relationship between twinning and the work hardening rate in Cu-4.9Sn at 298 K. These results suggest that Vöhringer's view is applicable at low strains when the first twins are formed, while Rémy's is valid at higher strains when twin intersections have occurred within many grains. This paper is intended to illustrate the general nature of this twofold effect of twinning on the plastic behavior of low stacking fault energy fcc metals.

Experimental Procedures

Specimen Preparation

Four materials were used in this work: Cu-3.1Sn, Cu-4.9Sn, Cu-30Zn, and Co-40Ni. In each case the alloying element concentration is given in atomic percent. Most of the work involved the copper/tin alloys, which were prepared by the Materials Research Corp., using 99.998% pure elemental materials. As-received 24.4-mm-diameter cast alloy rods were swaged to a diameter of 6.35 mm with one intermediate anneal. The resulting rods were machined into tension and compression specimens. The cold-worked structure was recrystallized to a range of mean grain intercepts between 3.7 and 125 μm, using 0.5-h anneals between 750 and 1150 K. In addition, some Cu-3.1Sn specimens were annealed at 1123 K for 1.5 h to obtain a mean grain intercept of 155 μm. Annealing twin boundaries were counted as well as grain boundaries in determining the mean intercepts.

The commercially pure Cu-30Zn alloy rods were swaged from an initial diameter of 22 mm to a final diameter of 6.35 mm. These specimens were annealed at 923 K for 0.5 h, and a mean grain intercept of 30 μm was obtained.

The Co-40Ni alloy was available in the form of 5.59-mm-diameter swaged rods remaining from an earlier investigation. This alloy was also originally prepared by the Materials Research Corp., using their VP-grade elemental materials. The cobalt/nickel rods were annealed at 1273 K for 0.5 h to obtain a mean grain intercept of 50 μm.

The copper/tin and copper/zinc tension specimens were machined with threaded ends and cylindrical gage sections of 3.8 by 20.3 mm. The corresponding compression specimens were cylinders with a diameter of 6.35 mm and a height of 15.9 mm. The cobalt/nickel tension specimens had 3.5 by 17.3-mm gage sections, while the compression specimens were cylinders with dimensions of 3.5 by 8.33 mm.

The annealed tension specimens were deformed at temperatures between 77 and 900 K on an Instron testing machine, using a base strain rate of 4.2×10^{-4} s^{-1}. True stress versus true strain curves and curves showing the reciprocal of the work hardening rate versus the stress were derived from the load-time charts and plotted only to the maximum load. In all the compression tests Teflon tape was used as a lubricant between the specimen and the loading platens. The compressive stress-strain curves were only plotted to a true strain of about 0.25 because barreling became excessive at strains above this level.

Metallography

The deformed copper/tin alloy specimens were electropolished in a well-stirred solution of 50 g copper nitrate ($Cu(NO_3)_2 \cdot 3H_2O$), 5 mL nitric acid (HNO_3), and 150 mL methanol (CH_3OH) cooled in a mixture of ice and water. They were then etched in a solution containing equal parts of water, nitric acid, and 25% glacial acetic acid. This etching procedure resulted in surfaces responsive to polarized light. The advantage of using polarized light in the metallographic examination of face-centered cubic metals has been discussed in detail earlier [*10*].

The nickel/cobalt microstructures were electropolished in a solution of 60 mL hydrochloric acid (HCl), 15 mL HNO_3, 15 mL glacial acetic acid, and 15 mL water at room temperature. The polished specimens were etched with a solution of 15 drops of 48% hydrofluoric acid (HF) in 20 mL HNO_3.

The volume fraction of mechanical twins was measured on transverse sections of deformed specimens by point counting, using a 5 by 5 square grid ocular. The number of regions used for each measurement was 40 to 45. The statistical errors associated with the averages were estimated using standard techniques.

The traces of twins observed optically on surfaces normal to the stress axis were used to characterize the fiber texture of the specimens. With the aid of measurements of the angles between {111} twin traces, the orientations of individual grains were determined relative to the stress axis, following the analytical method of Drazin and Otte [*11*]. An alternative graphical method [*12*] could also be used.

Results and Discussion

Evidence for a Decrease in Work Hardening Rate Caused by Twinning

The most direct evidence in support of the Vöhringer point of view that twinning acts to decrease the work hardening rate is obtained from plots of $d\epsilon/d\sigma$ against the stress, σ. Metallographic examinations of the specimen structure at the inflection where $d\epsilon/d\sigma$ suddenly rises confirm that the inflection is associated with the initiation of twinning. Thus, when twins begin to appear in the microstructure there is a drop in the work hardening rate.

The effect of twinning in reducing the work hardening rate may also be observed when one compares tensile and compressive stress-strain curves of a low stacking fault energy fcc metal tested under comparable conditions. An example is shown in Fig. 1, where the compressive and tensile stress-strain curves of Cu-4.9Sn specimens tested at 298 K are shown. The compressive curve in this figure was corrected for barreling by using the method of Cook and Larke [*13*], as described elsewhere [*9*]. In Fig. 1 the compressive stress-strain curve is displaced to the right of the tensile curve so that its slope or work hardening rate is smaller. Metallographic studies indicate that the difference between the tensile and compressive stress-strain curves is due to a difference in twinning behavior. Evidence for this is given in Fig. 2, which shows

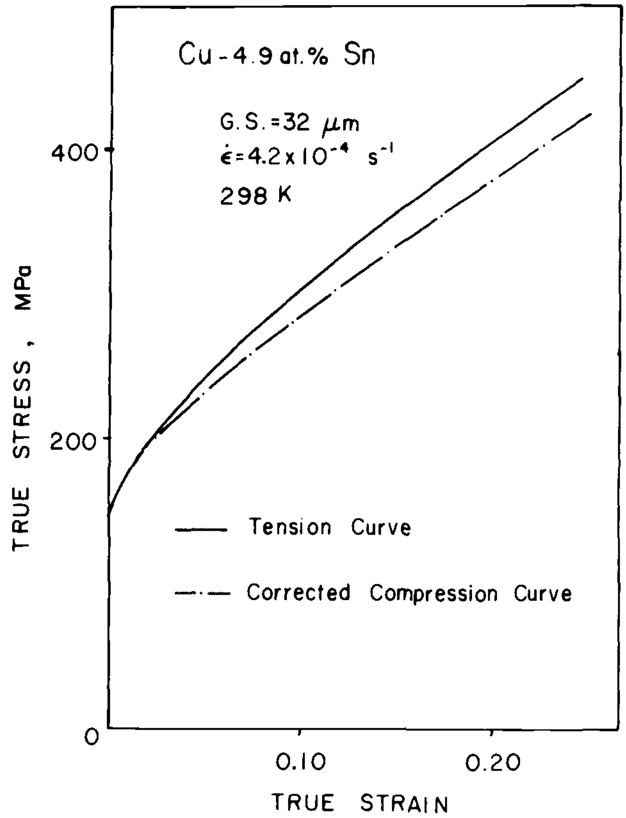

FIG. 1—*A comparison of the 300 K tensile and compressive stress-strain curves for Cu-4.9Sn (that is, copper with 4.9 atomic percent tin). Note: the compressive curve was corrected for barreling.*

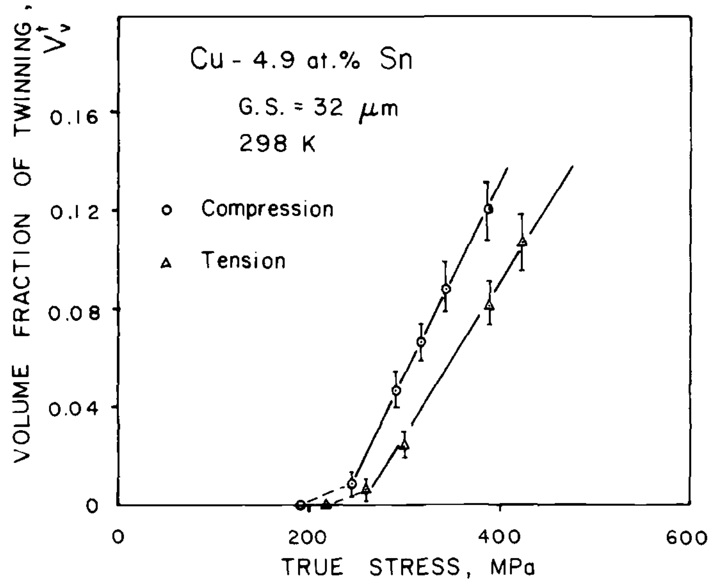

FIG. 2—*The Cu-4.9Sn volume fraction of twins,* V_v^t, *versus the stress,* σ, *for both tension and compression.*

the volume fraction of the twins, V_v^t, as a function of the stress for both tension and compression specimens deformed to strains less than about 0.2. Note that at any given stress level the twinning is greater in the compression specimens. On the assumption that, in this region of the stress-strain curve, twinning does not increase the stress level, while it does increase the strain, one is easily able to rationalize the difference between the tensile and compressive curves. In fact, as demonstrated in Ref *9*, it is possible to compute the strain contribution due to twinning and subtract it from the total strain so as to obtain corrected tensile and compressive stress-strain curves due to slip alone. If this is done, the tensile and compressive stress-strain curves coincide within the experimental error. The difference in the twinning behavior in tension and compression, evident in the plots of the volume fraction of twins in Fig. 2, can also be explained as shown in Ref *9*.

That the effect of twinning on the tensile and compressive stress-strain curves is not restricted to the Cu-4.9Sn material alone is shown in Figs. 3 and 4. These compare the 298 K tensile and compressive stress-strain curves of Cu-30Zn and Co-40Ni specimens, respectively. Both figures show a difference between the tensile and compressive curves similar to that in the Cu-4.9Sn specimens. Although the compressive stress-strain curves in both Figs. 3 and 4 were not corrected for barreling, this is not deemed significant. The barreling correction only increases the difference between the two curves [*9*].

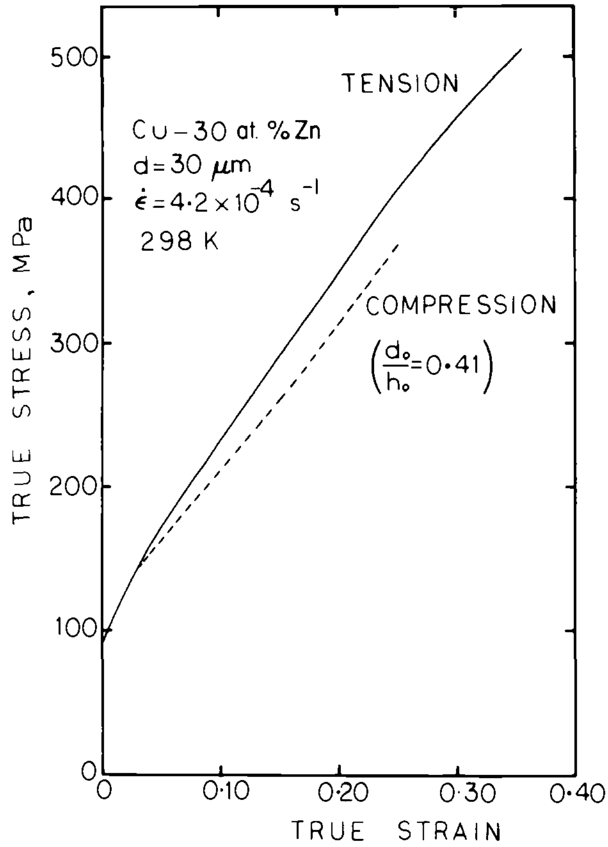

FIG. 3—*The 298 K tensile and compressive stress-strain curves for Cu-30Zn.*

Evidence for an Increase in Work Hardening Rate Caused by Twinning

Evidence for an increase in the work hardening rate caused by twinning can be furnished by a set of tensile stress-strain curves of a low stacking fault energy fcc metal obtained over a range of temperatures. Figure 5 shows such a set for Cu-3.1Sn specimens plotted on true stress and true strain coordinates. Note that with decreasing test temperature both the maximum true strain and the ultimate true stress increase. This combination of an increase in both strength and ductility represents a very desirable combination of mechanical properties. However, it does not represent the normal state of affairs, as pointed out by Zackay et al [*14*], who have stated, "A major part of both the theoretical and experimental evidence accumulated to date suggests that strength and ductility are inversely related." This inherent tendency for strength and ductility to be inversely related can be explained qualitatively on

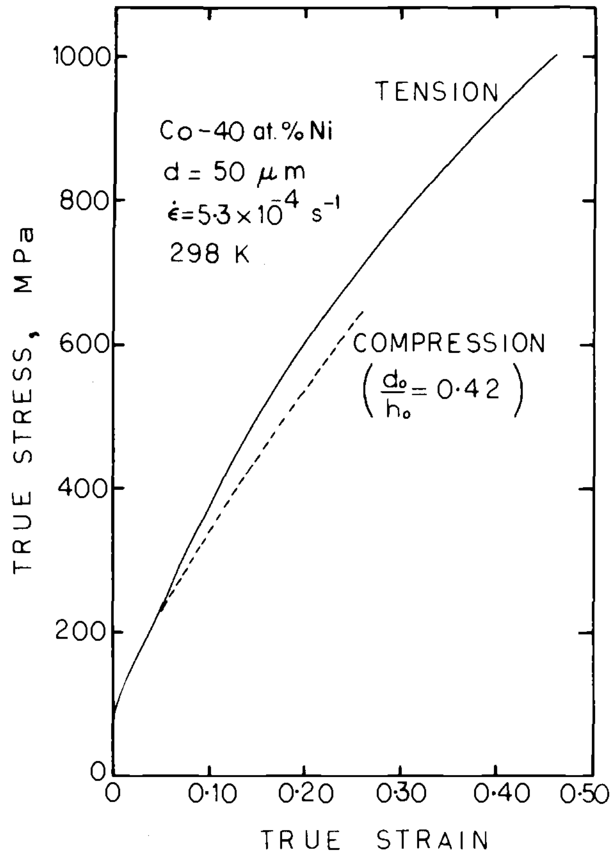

FIG. 4—*The 298 K tensile and compressive stress-strain curves for Co-40Ni.*

the basis that many of our better known strengthening mechanisms do not significantly change in the way that the work hardening rate, $d\sigma/d\epsilon$, varies with the strain, ϵ. The strengthening mechanism merely raises the level of the stress-strain curve without significantly altering its shape. As a result, Considére's criterion for necking ($d\sigma/d\epsilon = \sigma$) is satisfied at smaller and smaller strains the higher the stress level [*15*]. That the reverse is true in the Cu-3.1Sn specimens is clearly shown in Fig. 5. In these specimens, the work hardening rate tends to fall off less rapidly with strain the lower the temperature, so that Considére's criterion is satisfied at larger and larger strains the lower the temperature. As a result, both the ultimate true stress and the maximum uniform strain increase as the temperature is decreased.

The relationship between twinning and the phenomenon just described is apparent when one plots the maximum uniform strain versus the volume fraction of twins at this strain, as in Fig. 6 for Cu-3.1Sn specimens deformed at

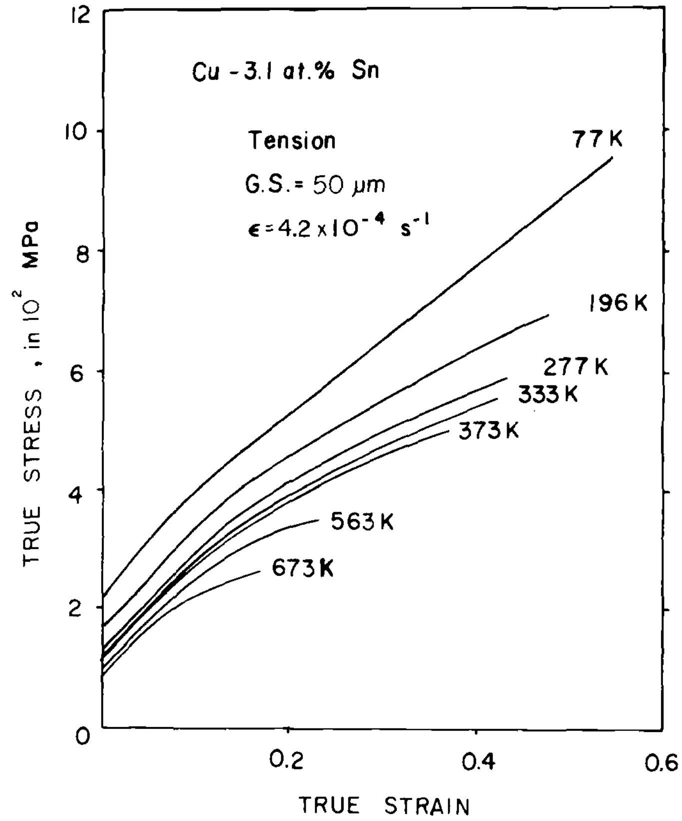

FIG. 5—*The Cu-3.1Sn stress-strain curves, demonstrating that, in this fcc metal, both the strength and ductility increase with decreasing temperature.*

various temperatures at the same strain rate. Note that the uniform strain increases monotonically with the volume fraction of the twins. A close connection between the uniform strain and the volume fraction of twins is also shown in Fig. 7. Here both the uniform strain, ϵ_u, and the corresponding volume fraction of twins at the uniform strain, V_v^t, are plotted versus the test temperature. Note that the uniform strain drops precipitously just above 500 K at the same time that the volume fraction of twins falls to near zero.

Rationalization of the Opposing Points of View

The two opposing points of view on the effect of twinning on the work hardening of a low stacking fault energy fcc metal can be rationalized [*9*]. Figure 8 shows the volume fraction of twins versus the true strain for 32-μm-grain-size Cu-4.9Sn specimens deformed at 298 K with a strain rate of 4.2×10^{-4} s^{-1}. The microstructures of these specimens were examined [*9,10*] at the points

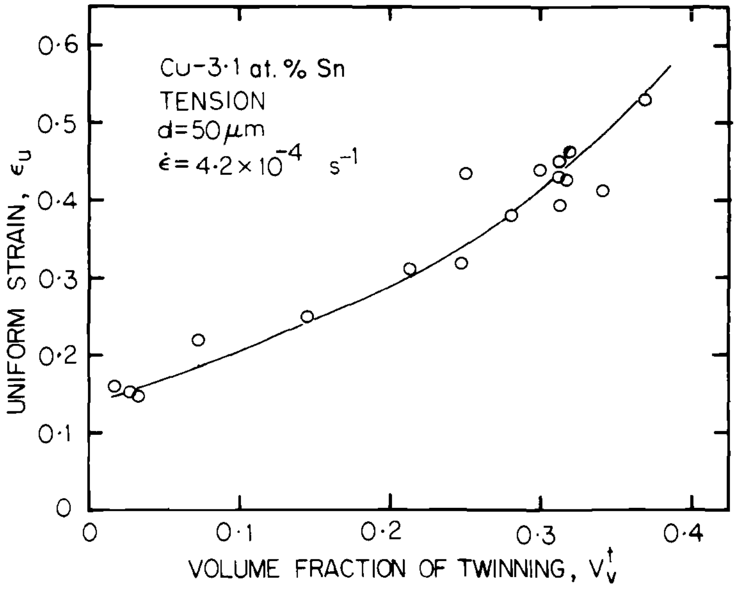

FIG. 6—*This figure shows that the uniform strain,* ϵ_u, *increases with an increase in the volume fraction of twins,* V_v^t.

marked *a* to *e* (Fig. 8) on this curve. Thus, a tension specimen deformed to 0.04 strain (Point *a*) failed to show any evidence of twinning. One deformed to 0.07 strain (Point *b*) had a 0.01 volume fraction of twins that were largely parallel to each other. At 0.10 strain (Point *c*) the twins were still parallel to each other in most grains. However, at 0.20 strain (Point *d*) the microstructure showed that, in the majority of the grains, twinning had occurred on intersecting twinning systems, and the twin volume fraction was about 0.11. Finally, at 0.40 true strain (Point *e*) the structure was heavily twinned on more than one twinning plane with a volume fraction of twins of 0.47. In summary, during the 298 K straining of this Cu-4.9Sn specimen, deformation starts by slip alone, then there is an interval in which twins form in the grains of the specimen on a single twinning plane, and, finally, this is followed by local twinning on intersecting twinning planes. These variations in the deformation behavior are reflected in the stress-strain curve itself. They lead to stages in the deformation behavior analogous to those in the stress-strain curve of a fcc single crystal with an orientation near the center of a standard stereographic triangle. The polycrystalline stages, however, are normally not as pronounced as those in a single crystal and may often not be readily detected on the stress-strain curve itself. The various stages, however, are readily observed if the reciprocal of the work hardening rate is plotted versus the stress, as in Fig. 9. Five points are marked on this figure to indicate, as in Fig. 8, the places where the microstructures described earlier were observed. Note the inflection of the curve between Points *a* and *b* (Fig. 9) marking the start of twinning. This inflection of

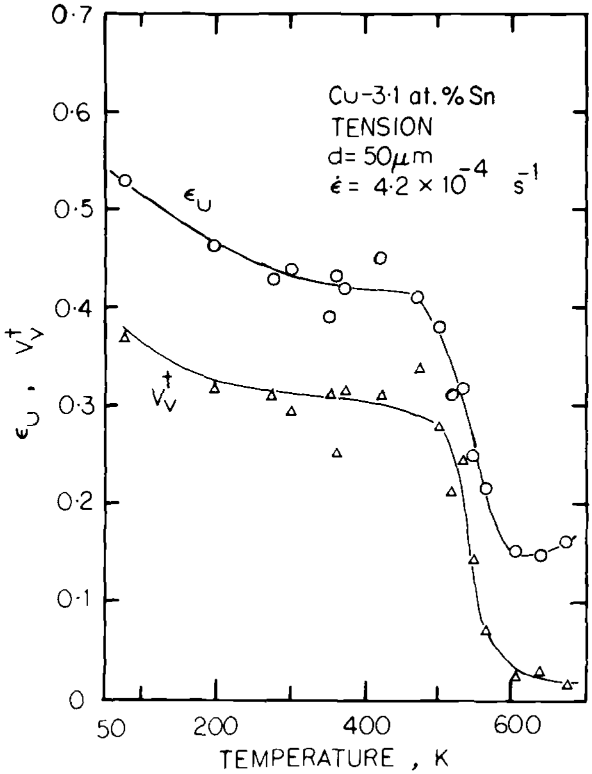

FIG. 7—*The maximum uniform strain,* ϵ_u, *and the volume fraction of twins,* V_v^t, *plotted as functions of the temperature for Cu-3.1Sn specimens.*

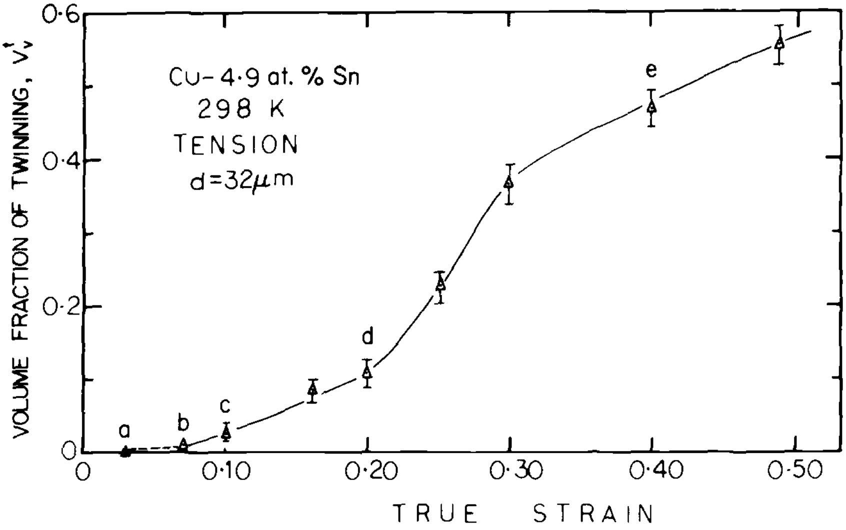

FIG. 8—*The volume fraction of twins,* V_v^t, versus the true strain, ϵ, *for Cu-4.9Sn at 298 K.*

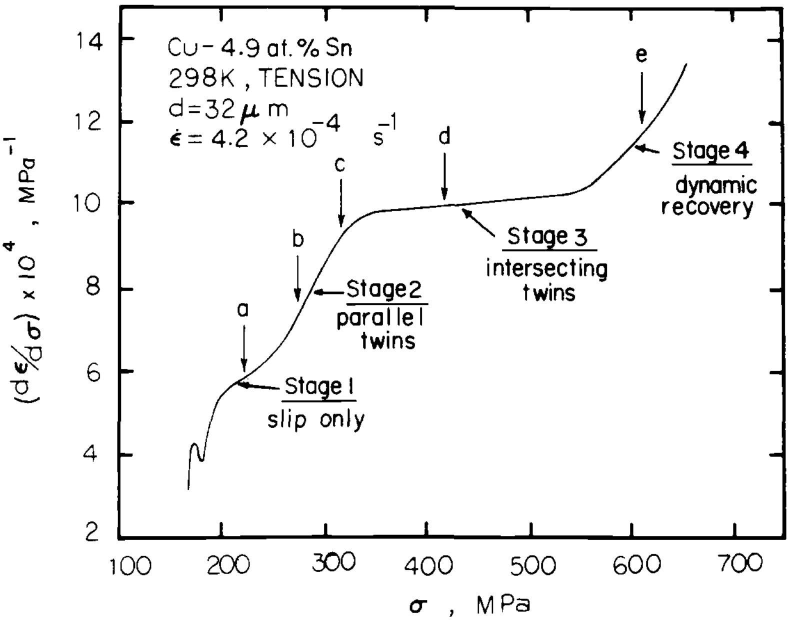

FIG. 9—*The variation of* $d\epsilon/d\sigma$*, the reciprocal of the work hardening rate, with the true stress,* σ*, for Cu-4.9Sn at 298 K.*

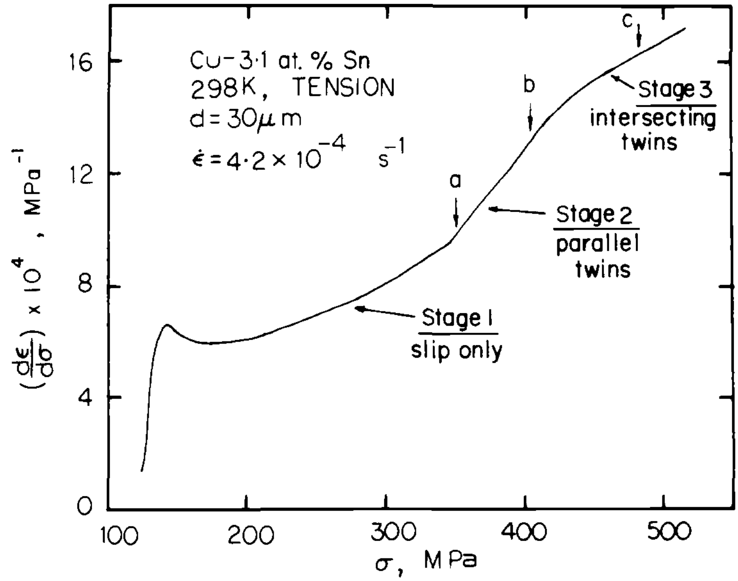

FIG. 10—*The Cu-3.1Sn* $d\epsilon/d\sigma$ *versus* σ *curve at 298 K.*

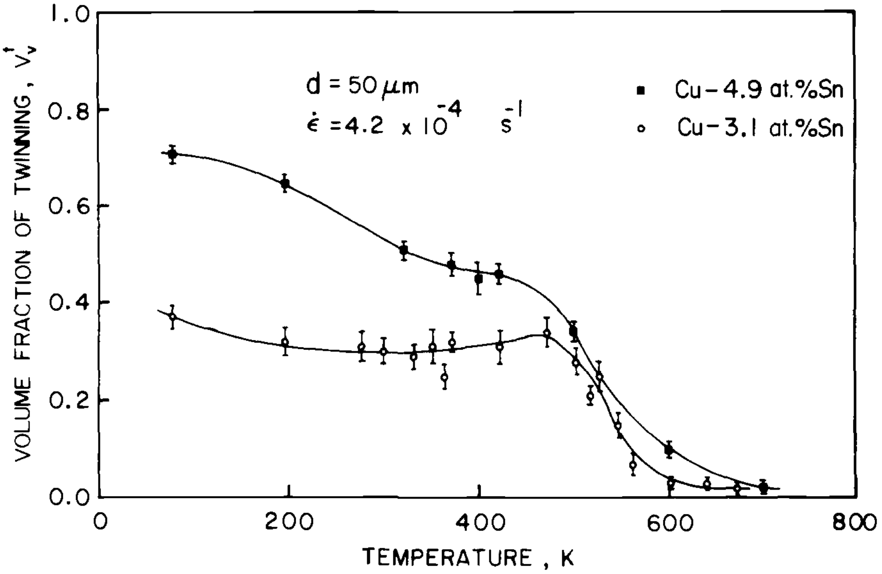

FIG. 11—*The temperature dependence of the volume fraction of twins,* V_v^t, *for both Cu-3.1Sn and Cu-4.9Sn.*

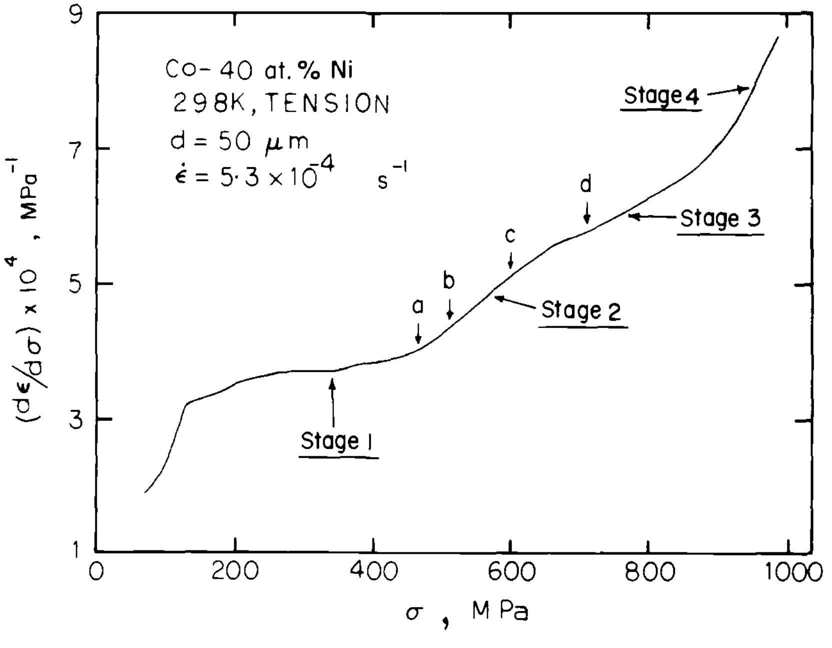

FIG. 12—*The Co-40Ni* $d\epsilon/d\sigma$ *versus* σ *curve at 298 K.*

FIG. 13*a*—*The microstructure at Point* a *in Fig. 12.*

the reciprocal work hardening curve is in complete agreement with Vöhringer's observations. Attention is also called to the second inflection between Points *c* and *d* (Fig. 9), where the slope of the $d\epsilon/d\sigma$ versus σ curve drops sharply to become close to zero, indicating a region of nearly constant work hardening rate. This second inflection correlates with a shift from initial twinning on a single twinning place to twinning on a number of intersecting twinning systems within a grain. The fourth stage appears at a true stress of approximately 550 MPa. Here there is a sharp upward inflection in the $d\epsilon/d\sigma$ versus σ curve that now becomes progressively steeper the larger the strain. This phenomenon corresponds to a progressively decreasing work hardening rate with increasing strain—a type of behavior at large strains normally con-

FIG. 13*b*—*The microstructure at Point* b *in Fig. 12.*

sidered to be due to dynamic recovery. Thus, the Cu-4.9Sn 298 K stress-strain curve shows the following stages: Stage 1, an interval of deformation by slip alone; Stage 2, an interval in which the twins are parallel within a grain; Stage 3, an interval in which twins form intersecting arrays; and Stage 4, dynamic recovery superimposed on the intersecting twins.

The curve in Fig. 9 supports Vöhringer's conclusion that twinning decreases the work hardening rate (that is, it increases $d\epsilon/d\sigma$) as the specimen moves from Stage 1 to Stage 2. However, on entering Stage 3, in which intersecting twins form, there is a sharp drop in $d\epsilon/d\sigma$ or a rise in the work hardening rate. Thus Stage 3 is the point at which Rémy's concept that twinning can act to increase the work hardening rate begins to be valid. It is easy to rationalize this

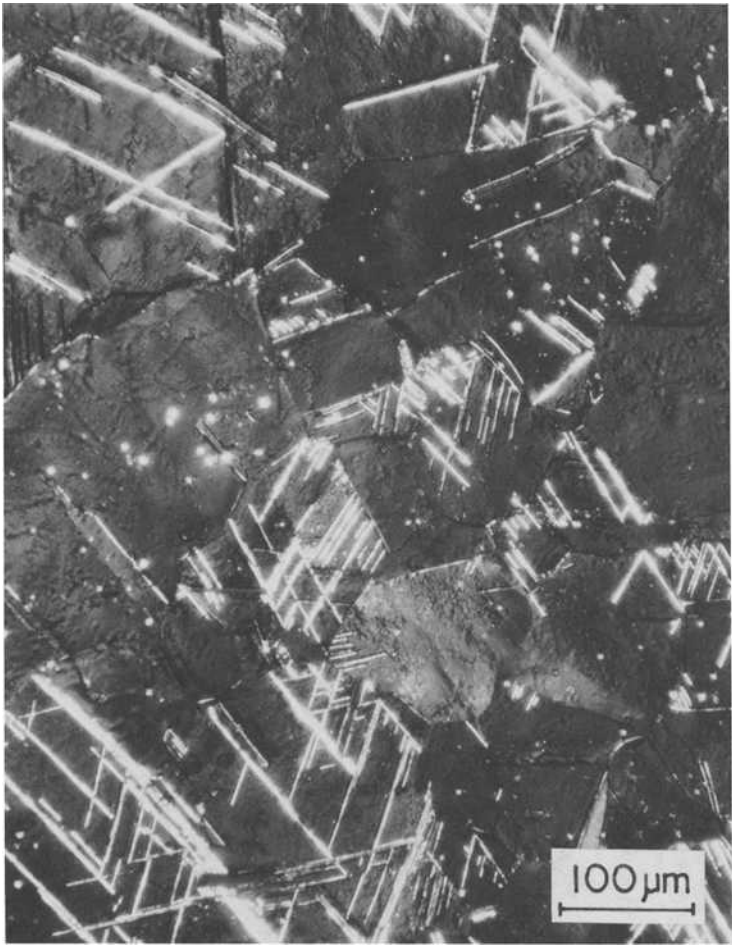

FIG. 13c—*The microstructure at Point* c *in Fig. 12.*

twofold effect of twinning on the stress-strain behavior. The microstructures obtained at strains of 0.07 and 0.10, respectively, show that twins initially form largely on one crystallographic plane of a grain. Previous investigations [*16-19*] involving single crystals have shown a strong correlation between the most active slip plane and the twinning plane in face-centered cubic alloys. Thus, initially twinning should not strongly influence slip and work hardening. On the other hand, at larger strains twins form on intersecting planes. This development of an intersecting twin structure should have a strong effect on the slip process. The twins are no longer all parallel to the primary slip plane. Rather the twins now thoroughly subdivide the microstructure and so

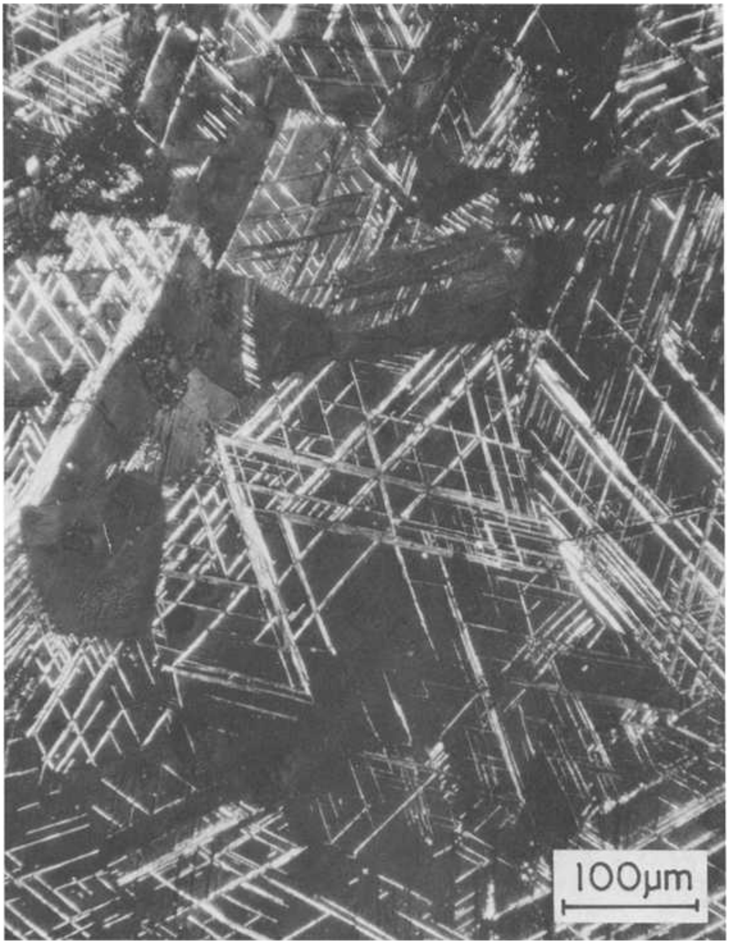

FIG. 13*d—The microstructure at Point* d *in Fig. 12.*

reduce the grain size. This decrease in grain size can easily account for the hardening effect of twinning at larger strains.

The Cu-3.1Sn Stress-Strain Curve

It is also possible to identify stages in a stress-strain curve of a Cu-3.1Sn specimen analogous to those that occur in the curve of the Cu-4.9Sn specimen. This is demonstrated in Fig. 10, a $d\epsilon/d\sigma$ versus σ curve of a 30-μm-grain-size Cu-3.1Sn specimen tested at 298 K. Stage 4 does not appear in this drawing only because the curve was not plotted far enough to show it. With a lower

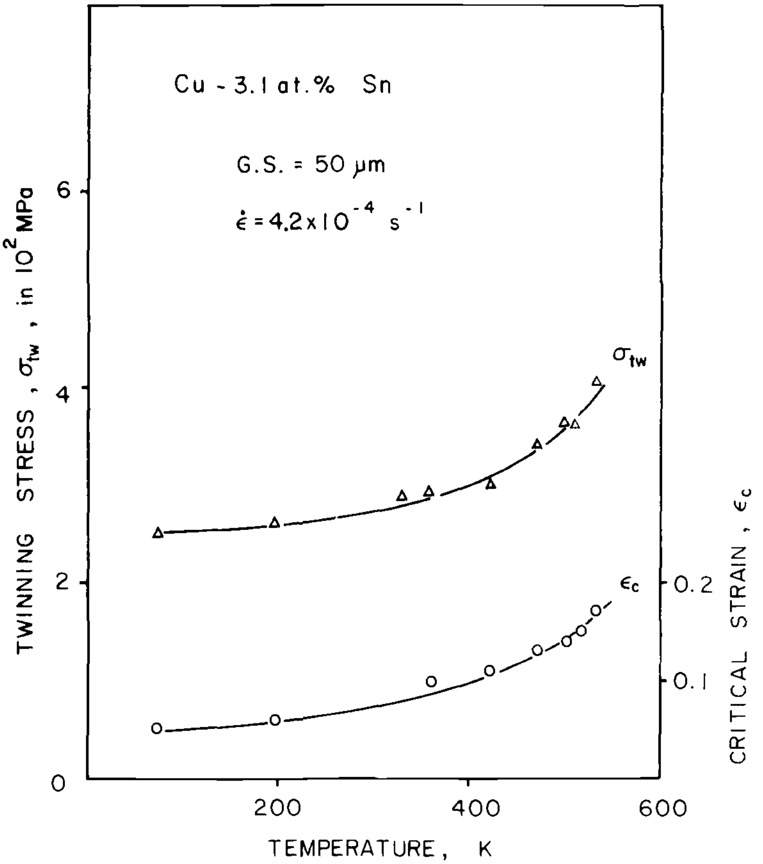

FIG. 14—*The twinning stress,* σ_{tw}, *and the critical strain to form twins,* ϵ_c, *versus the temperature for Cu-3.1Sn.*

concentration of the solute and a consequently higher stacking fault energy, the twinning phenomenon in the Cu-3.1Sn specimen is weaker. Stage 1 is much longer in Fig. 10 than in Fig. 9, indicating a larger critical strain before twinning occurs. As in the Cu-4.9Sn tests, the microstructures reveal that at Point *a* (Fig. 10) twin nucleation occurred, at Point *b* the twins were largely parallel inside a grain, and at Point *c* twin intersections were the rule. The differences between the stages are also less pronounced in Fig. 10 than in Fig. 9, particularly the transition from Stage 2 to Stage 3. Whereas, in the Cu-4.9Sn specimen, $d\epsilon/d\sigma$ becomes almost constant in Stage 3, signifying a nearly constant work hardening rate, in the Cu-3.1Sn specimen there is only a moderate decrease in the slope of the $d\epsilon/d\sigma$ curve between Stage 2 and Stage 3. As a result, the large third-stage slope corresponds to a significant decrease in the work hardening rate with increasing deformation.

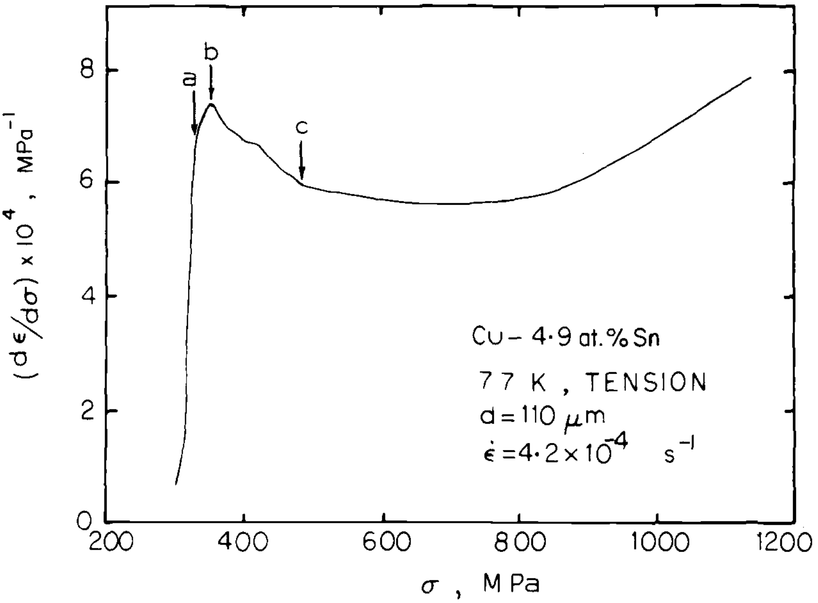

FIG. 15—*The Cu-4.9Sn* $d\epsilon/d\sigma$ *versus* σ *curve at 77 K.*

Quantitative twin volume measurements confirmed that the twinning was greater in the specimen with the higher tin concentration. This can be seen in Fig. 11, a plot of the twin volume fractions, at the uniform strain, against the temperature for both the Cu-3.1Sn and the Cu-4.9Sn specimens. These curves show that the volume fraction of twins is lower in the Cu-3.1Sn alloy over the entire range of temperatures investigated. At 298 K, the temperature currently being considered, the volume fraction of twins at the end of the uniform strain was about 0.52 in the Cu-4.9Sn specimen, while in the Cu-3.1Sn specimen it was only about 0.30. This difference is consistent with the difference in the stress-strain behavior of the two alloys.

The Co-40Ni Stress-Strain Curve

The Co-40Ni $d\epsilon/d\sigma$ versus σ curve of Fig. 12 is similar to data obtained for the Cu-3.1Sn alloy. This similarity may be due to their having nearly equivalent stacking fault energies (24 mJ/m^2, roughly twice that of the Cu-4.9Sn alloy) [*4,20*].

The photomicrographs in Fig. 13 support the relation of the stages in the Co-40Ni alloy to its twinning phenomena. Figure 13*a*, corresponding to Point *a* in Fig. 12, near the start of the change from Stage 1 to Stage 2, shows a num-

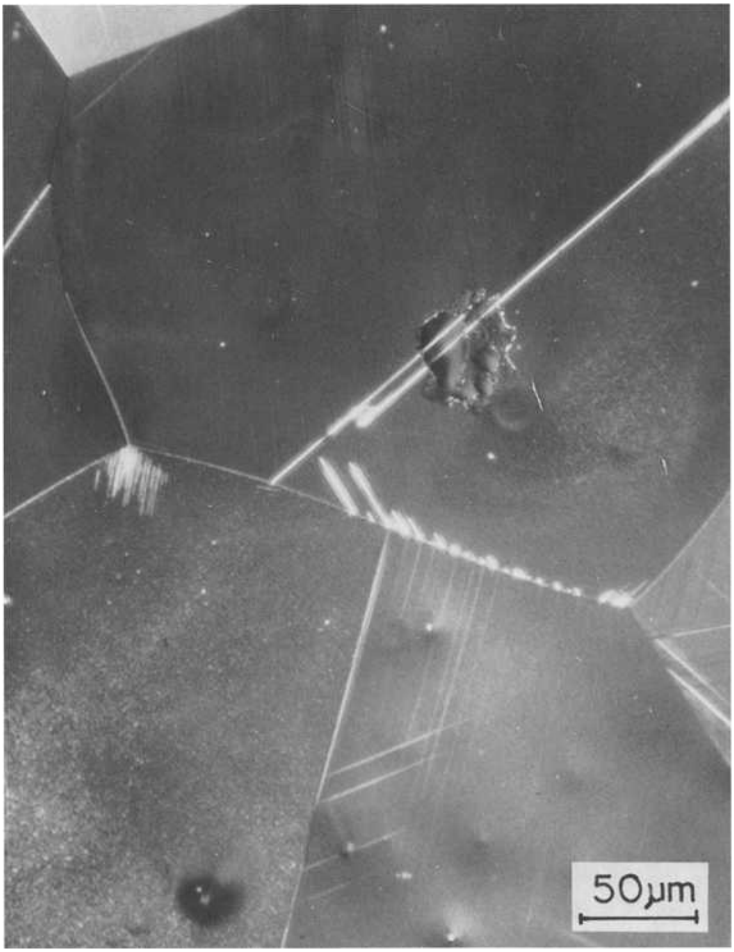

FIG. 16*a*—*The microstructure at Point* a *in Fig. 15.*

ber of very thin short twins and represents the initial stages of twinning. At Point *b* (Fig. 12), corresponding to Fig. 13*b*, the twins, while still thin, are longer and largely parallel inside a given grain so that the structure is still typical of Stage 2. Figure 13*c* shows the structure at Point *c* (Fig. 12) near the beginning of Stage 3. Here some twin intersections are visible. The number of twins and their volume fraction have increased. Finally, a structure well into Stage 3 is illustrated in Fig. 13*d*. Here twin intersections are commonplace. These photographs confirm that the four stages in the Co-40Ni stress-strain curve are related to changes in the twinning behavior analogous to those in the copper/tin specimens.

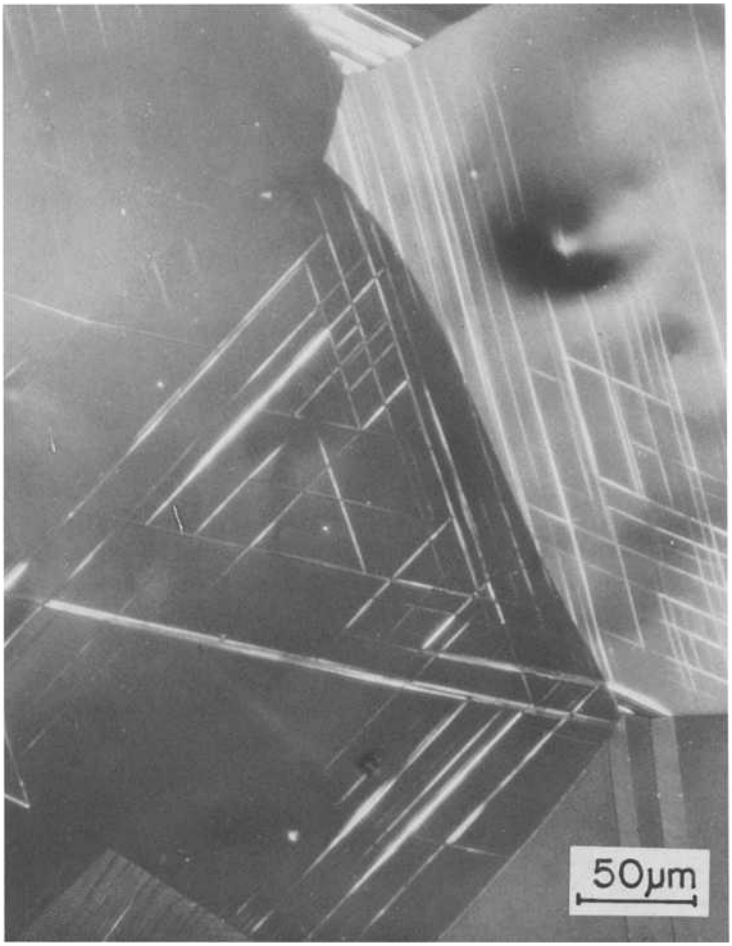

FIG. 16*b—The microstructure at Point* b *in Fig. 15.*

The Relation of the Polycrystalline Results to Earlier Single Crystal Studies

The present observations are supported by the work of Mori and Fujita [*19*] on Cu-8Al single crystals. During the deformation of crystals with an axis near [011], they found that twinning occurred along the primary slip plane before the appearance of the conjugate slip bands. They also observed that the activation of the primary twinning alone gave rise to a reduction of the work hardening rate, as seen by a downward inflection on the stress-strain curve. After the work hardening rate had decreased by more than 30%, a new increase in work hardening was observed that coincided with the appearance of conjugate twins.

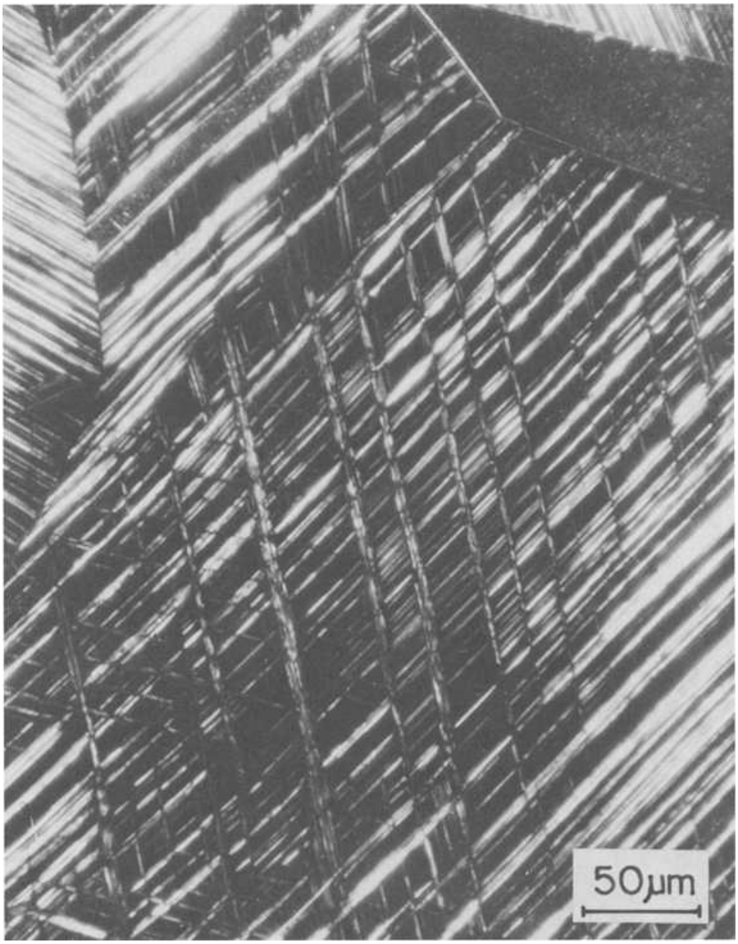

FIG. 16c—*The microstructure at Point* c *in Fig. 15.*

The Effect of Deformation Temperature

The $d\epsilon/d\sigma$ versus σ curves in Figs. 9 and 10 reveal a strong effect of the solute concentration on the shape of the copper/tin stress-strain curves. This is probably due to a decrease in the stacking fault energy with increasing solute concentration, which causes the amount of twinning to be greater in the Cu-4.9Sn alloy than in the Cu-3.1Sn alloy. This difference is shown in Fig. 11, where the volume fractions of twins in the two alloys, at the maximum uniform strain, are plotted versus the temperature. According to Barrett and Massalski [*21*], the deformation temperature may also affect the stacking fault energy in fcc alloys. A decrease in the stacking fault energy with decreasing temperature could thus account for the increase in the twin volume fraction with decreasing temperature shown in Fig. 11. Figure 14 shows that the twinning stress, σ_{tw}, the stress needed to form the first twins, and the critical strain, ϵ_c, the strain at the point of twin nucleation, in the Cu-3.1Sn specimens both decrease as the temperature is lowered. The drop in the stress to form twins as the temperature is lowered is interesting because the stress needed to start slip normally increases as the temperature is decreased. This unusual feature of the twinning stress, however, is consistent with a decrease in the stacking fault energy with decreasing temperature.

As can be seen in Fig. 14, the critical strain needed to start twinning in the Cu-3.1Sn specimens is only about 0.05 at 77 K. In the Cu-4.9Sn alloy, with its increased susceptibility to twinning, the critical strain is much smaller than 0.05. This lowering of the critical strain implies that the initial stages of the deformation should be drastically affected. Proof is given in the $d\epsilon/d\sigma$ versus σ curve for a Cu-4.9Sn specimen deformed at 77 K, shown in Fig. 15. Photographs of the structures observed at Points *a*, *b*, and *c* in Fig. 15 are shown in Fig. 16. Figure 16*a* (Point *a* in Fig. 15) indicates that even at 0.01 strain twinning had already started. There is also evidence of twin intersections at this small strain. Thus, Stage 1, the stage in which there is no twinning, is effectively missing and Stage 2 is also reduced to the point where it is no longer significant. This is confirmed in Fig. 16*b*, where the microstructure at Point *b* in Fig. 15 is revealed. Here at a strain of 0.05, one can see that intersecting twins are the rule. Finally, at Point *c* in Fig. 15, at 0.11 strain, a highly twinned structure is visible (Fig. 16*c*) involving twins on intersecting twinning planes. Thus, after a small inflection, the stress-strain curve enters Stage 3, and the degree of twinning is high enough between Point *b* and Point *c* that $d\epsilon/d\sigma$ decreases with increasing deformation. This, therefore, represents a region in which the work hardening rate actually increases as the specimen is strained. A large interval then follows of nearly constant $d\epsilon/d\sigma$, in which the work hardening is nearly constant. Finally, $d\epsilon/d\sigma$ rises sharply in what amounts to the fourth stage, in which dynamic recovery causes the reciprocal work hardening rate to increase.

Summary and Conclusions

1. The effect of mechanical twinning on the uniaxial stress-strain curves of low stacking fault energy fcc metals was investigated using quantitative microscopy techniques.
2. It was deduced that, in the alloys investigated, twinning was largely responsible for producing four stages in the stress-strain curves.
3. Stage 1 is an interval without twinning. In Stage 2 twins form on a single crystallographic plane within a given grain. Intersecting twins develop in Stage 3, and dynamic recovery occurs in Stage 4.

4. Both composition and temperature have strong effects on the twinning phenomenon and the related stage behavior.

Acknowledgment

The financial support for this research by the National Science Foundation, under Contract No. DMR 77-22654, is gratefully acknowledged.

References

[*1*] Hirth, J. P. and Lothe, J., *Theory of Dislocations*, McGraw-Hill, New York, 1968, p. 764.

[*2*] Vöhringer, O., *Materials Science and Engineering*, Vol. 3, 1968/1969, pp. 299-302.

[*3*] Vöhringer, O., *Proceedings*, Second International Conference on Strength of Metals and Alloys, American Society for Metals, Metals Park, Ohio, 1970, pp. 294-298.

[*4*] Vöhringer, O., *Zeitschrift für Metallkunde*, Vol. 67, 1976, pp. 518-524.

[*5*] Vöhringer, O., *Metall*, Vol. 30, 1976, pp. 1150-1160.

[*6*] Rémy, L., *Acta Metallurgica*, Vol. 26, 1978, pp. 443-451.

[*7*] LaRouche, S. and Mikkola, D. E., *Scripta Metallurgica*, Vol. 12, 1978, pp. 543-548.

[*8*] Murr, L. E., Moin, E., Greulich, F., and Staudhammer, K. P., *Scripta Metallurgica*, Vol. 12, 1978, pp. 1031-1036.

[*9*] Krishnamurthy, S. and Reed-Hill, R. E., *Metallurgical Transactions A*, Vol. 11A, 1980, pp. 565-572.

[*10*] Reed-Hill, R. E., Smeal, C. R., and Lee, L., *Transactions of the American Institute of Mining, Metallurgical, and Petroleum Engineers*, Vol. 230, 1964, pp. 1019-1024.

[*11*] Drazin, M. P. and Otte, H. M., *Tables for Determining Cubic Crystal Orientations*, Harrod Co., Baltimore, Md., 1964.

[*12*] Reed-Hill, R. E., *Transactions of the American Institute of Mining, Metallurgical, and Petroleum Engineers*, Vol. 236, 1966, pp. 1283-1285.

[*13*] Cook, M. and Larke, E. C., *Journal of the Institute of Metals*, Vol. 71, 1945, pp. 371-390.

[*14*] Zackay, V. F., Parker, E. R., Fahr, D., and Busch, R., *Transactions of the American Society for Metals*, Vol. 60, 1967, pp. 252-259.

[*15*] Reed-Hill, R. E., *Physical Metallurgy Principles*, D. Van Nostrand, New York, 1973, pp. 837-840.

[*16*] Narita, N. and Takamura, J., *Philosophical Magazine*, Vol. 29, 1974, pp. 1001-1028.

[*17*] Venables, J. A., *Deformation Twinning*, Gordon and Breach Science Publishers, New York, 1964, pp. 77-116.

[*18*] Fujita, H. and Mori, T., *Scripta Metallurgica*, Vol. 9, 1975, pp. 631-636.

[*19*] Mori, T. and Fujita, H., *Transactions of the Japanese Institute of Metals*, Vol. 18, 1977, pp. 17-24.

[*20*] Köster, E. H., Thölen, A. R., and Howie, A., *Philosophical Magazine*, Vol. 10, 1964, pp. 1093-1095.

[*21*] Barrett,, C. S. and Massalski, T. B., *Structure of Metals*, McGraw-Hill, New York, 1966, pp. 555-558.

Joseph Gurland[1]

Application of Quantitative Microscopy to Cemented Carbides

REFERENCE: Gurland, J., "**Application of Quantitative Microscopy to Cemented Carbides,**" *Practical Applications of Quantitative Metallography, ASTM STP 839,* J. L. McCall and J. H. Steele, Jr., Eds., American Society for Testing and Materials, Philadelphia, 1984, pp. 65–84.

ABSTRACT: Among the cemented carbides, the tungsten carbide/cobalt (WC-Co) alloys are the most studied. Four parameters are used to characterize their microstructures: the binder volume fraction, binder mean free path, carbide grain size, and carbide contiguity. Some success has been achieved in relating these variables empirically and theoretically to mechanical properties relevant to performance, such as hardness and toughness. Current research is directed towards the possibly significant effects of the fine substructures—specifically, those of solutes, precipitates, stacking faults, and other defects in the binder—and those of the binder metal concentration and dislocation arrays at the grain boundaries of the tungsten carbide.

This review briefly describes the use of microscopy in quality evaluation, microstructural characterization, and alloy development.

KEY WORDS: quantitative metallography, cemented carbides, tungsten carbide/cobalt alloy, stereology, quantitative microscopy, quality evaluation

Commercial cemented carbide grades generally consist of two constituents: the carbide [tungsten carbide (WC), titanium carbide (TiC), tantalum carbide (TaC), vanadium carbide (VC), niobium carbide (NbC), and so forth, and their solid solutions] and the binder (cobalt, nickel, or iron, with or without additives and containing dissolved elements of the carbide). In principle, their simple microstructures, consisting of chemically and physically well-defined phases, lend themselves to quantitative characterization, and, in fact, light microscopy and electron microscopy are widely used in production control, quality evaluation, and alloy development. The basic methods of microscopic evaluation of cemented carbides merit their own ASTM and International Organization for Standardization (ISO) standards, and active international interaction is taking place to refine and expand the scope of these methods.

---

[1] Professor of engineering, Division of Engineering, Brown University, Providence, R.I. 02912.

The application of microscopic methods to interpretation of the microstructure of cemented carbides has been reviewed from time to time, most recently by Exner [*1*][2] and Cherniavsky [*2*]. The present review will first describe the use of standard stereological concepts for quality control and alloy development and then briefly discuss and illustrate some of the less common approaches and methods used for research purposes.

Qualitative Comparative Examination for Quality Evaluation

The user of carbide tools might start by examining the fracture surface of a piece of questionable quality: the piece would have been either broken in use, crushed for the purpose by a hammer blow, or broken in a fracture test. Inspection through a low-power lens (×15 to ×40) often reveals qualitative evidence of porosity, excess carbon, and contamination. A very smooth fracture surface, with a characteristic "river" pattern, indicates cleavage and, generally, brittleness [Fig. 1 (*top*)]. Often the large pores and other defects from which the fracture started can be detected. The degree of brittleness to be expected depends, of course, on the grade or alloy. A tougher piece or grade has a dull, satiny, or rough surface associated with greater fracture resistance [Fig. 1 (*bottom*)].

The next step usually is the metallographic determination of the apparent porosity by low-power light microscopy [ASTM Test for Apparent Porosity in Cemented Carbides (B 276-79)]. The surface preparation consists of grinding and polishing a flat section with successively finer diamond powder or paste, finishing with diamond grit of 3-μm particle size. The term apparent porosity refers to the microstructure, observed on the polished but unetched surface and associated not only with the true inherent porosity but also with uncombined carbon and foreign inclusions, all of which generally appear as dark specks on the shiny background of the polished metallic surface (Fig. 2). The pattern of the apparent porosity is compared visually with the photomicrographs of the ASTM standard at a specified magnification of ×100 or ×200 and is classified as to type (porosity or uncombined carbon), size of pores, and area fraction of pores. Good-quality commercial products are generally found to be at the low end of the porosity scale.

Determination of the apparent porosity is often teamed with measurements of the density (ASTM Test for Density of Cemented Carbides [B 311-58(1979)], hardness (ASTM Hardness Testing of Cemented Carbides [B 294-76(1982)]), and transverse rupture strength (ASTM Test for Transverse Rupture Strength of Cemented Carbides [B 406-76(1982)]) to provide the basic "first echelon" input for quality evaluation.

For the purposes of alloy identification and defect characterization, the actual microstructure is examined at higher magnification, typically at ×1500,

---

[2] The italic numbers in brackets refer to the list of references appended to this paper.

in the light microscope (Fig. 3). The ASTM Method for Metallographic Determination of Microstructure in Cemented Carbides (B 657-79) provides instructions for surface preparation and etching procedures. The standard etching solutions are Murikami's reagent [a mixture of equal amounts of 10% aqueous solution of potassium ferricyanide ($K_3Fe(CN)_6$) and potassium or sodium hydroxide] and dilute hydrochloric acid. The various phases are labeled as follows: tungsten carbide (α phase), binder metal (β phase), and cubic carbides, TiC, TaC, NbC, and other carbides, individually or as mixed carbides in solution (γ phase). Also looked for is the presence of free carbon in the microstructures of high-carbon alloys or of the η-type phase (eta), an intermetallic compound of carbides and binder metal typically found in carbon-deficient materials (Fig. 4) [*3*]. The presence of the η phase in appreciable amounts is always deleterious and indicates low fracture strength. Carbide grain sizes are evaluated by ASTM Method B 657-79 and the ASTM Recommended Practice for Evaluating Apparent Grain Size and Distribution of Cemented Tungsten Carbides [B 390-64(1982)].

The visual identification of the constituents is sometimes supplemented by X-ray diffraction and X-ray fluorescence analysis. Also at this stage of quality evaluation, additional physical properties are commonly measured, namely, coercive force and magnetic saturation, which give indications of the amount and distribution of the binder, the carbon content of the binder, and, indirectly, the grain size and grain size distribution of the carbide phase. The total carbon content and the amount of free, uncombined carbon are also determined by chemical analysis.

Stereological Methods for the Quantitative Characterization of Microstructures for Alloy Development

In order to correlate mechanical properties with microstructural parameters, the latter need to be established quantitatively and precisely. What feature or, more likely, what combination of features controls specific properties or performance is still a matter of controversy, but there is general agreement that the alloy composition, carbide grain size, and binder ligament width are of primary practical relevance.

Because of the fine dispersion of carbide and binder in cemented carbides, the resolution of the light microscope is often insufficient, and electron microscopy is required for accurate and precise measurements of volume fractions and sizes. In electron microscopy, the older surface replica method [*4*] has been replaced by scanning electron microscopy with backscattered electrons or secondary electron emission. Various chemical and electrolytic etching procedures are described in the literature [*5*] but, generally, the same etching solutions can be used as for light microscopy (Fig. 5).

By alloy composition is meant the volume fractions of the constituents, that is, the carbide and binder phases. ASTM provides the recommended practice

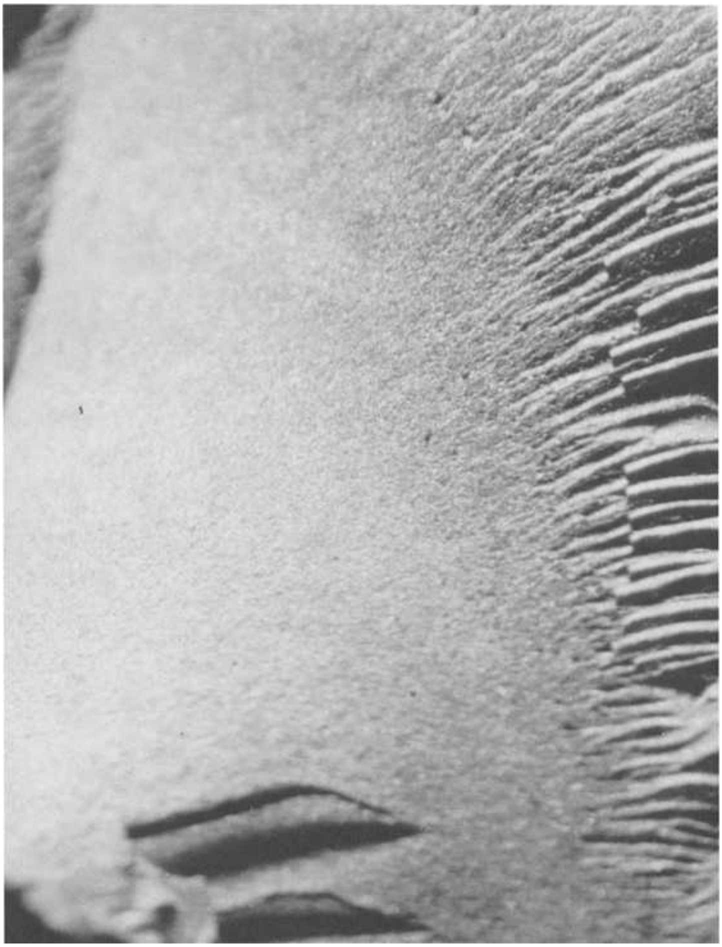

FIG. 1—*Fracture surfaces of commercial grades of WC-Co at* ×*40:* (top) *6% cobalt by weight,* (bottom) *16% cobalt by weight.*

FIG. 2—*Typical porosity of commercial grade WC-Co, unetched surface,* ×*200.*

for estimation of the area fraction of a phase in a multiphase alloy by systematic point counting on a planar test section [ASTM Recommended Practice for Determining Volume Fraction by Systematic Manual Point Count (E 562-76)] (Fig. 6). The point fraction, $(P_P)_\alpha$, intercepted by the α phase, statistically interpreted, provides an estimate of the volume fraction, $(V_V)_\alpha$, area fraction, $(A_A)_\alpha$, and line fraction, $(L_L)_\alpha$. For statistically random microstructures or statistically random measurements

$$(P_P)_\alpha = (L_L)_\alpha = (A_A)_\alpha = (V_V)_\alpha \tag{1}$$

Further structural information is obtained from boundary intercepts with test lines on planar sections. The test lines might be the lines of a transparent grid superimposed upon the microstructure. In the case of tungsten carbide/cobalt (WC-Co) alloys, for instance, one determines the average number of intercepts per unit length of test line with traces of the carbide/cobalt interface, $(N_L)_{\alpha\beta}$, and carbide/carbide grain boundaries, $(N_L)_{\alpha\alpha}$, respectively (Fig. 6). The following parameters can then be calculated:

1. The tungsten carbide mean linear intercept grain size

$$(\bar{L}_3)_\alpha = \frac{2(V_V)_\alpha}{2(N_L)_{\alpha\alpha} + (N_L)_{\alpha\beta}} \tag{2}$$

where $(V_V)_\alpha$ is the volume fraction of the carbide phase.

2. The contiguity of tungsten carbide

$$C_\alpha = \frac{2(N_L)_{\alpha\alpha}}{2(N_L)_{\alpha\alpha} + (N_L)_{\alpha\beta}} \tag{3}$$

3. The binder mean linear intercept distance, that is, the mean free path

$$\bar{L}_\beta = \frac{2(V_V)_\beta}{(N_L)_{\alpha\beta}} \tag{4}$$

where $(V_V)_\beta$ is the volume fraction of the binder phase. Similar measurements can be carried out on the cubic carbides (γ phase), if present.

The mean linear intercept grain size of WC is identical with the mean carbide particle size. It is the particle intercept length averaged over all directions

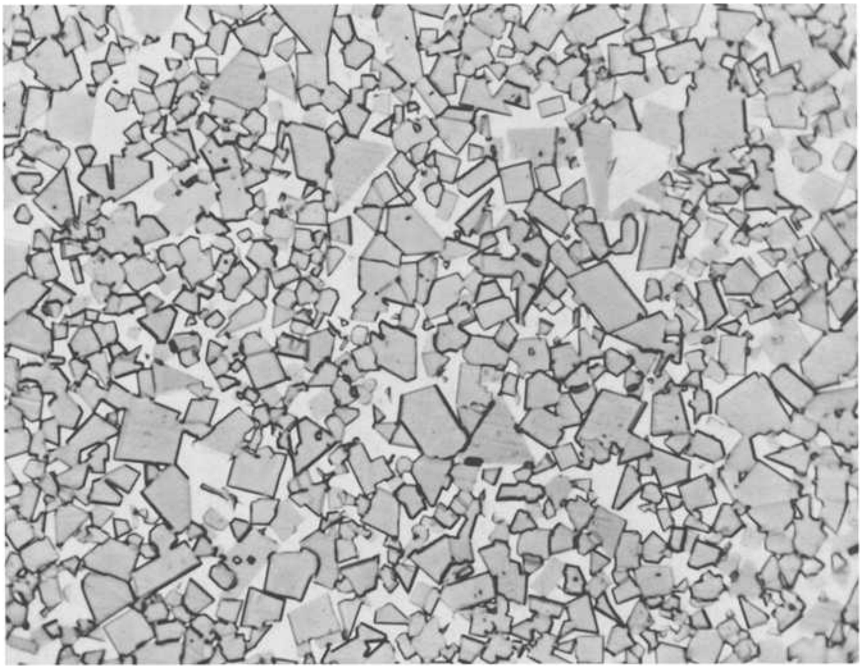

FIG. 3—*Microstructure of commercial grade WC, 16% cobalt by weight, etched with Murikami's reagent, light microscope photomicrograph,* ×*1500.*

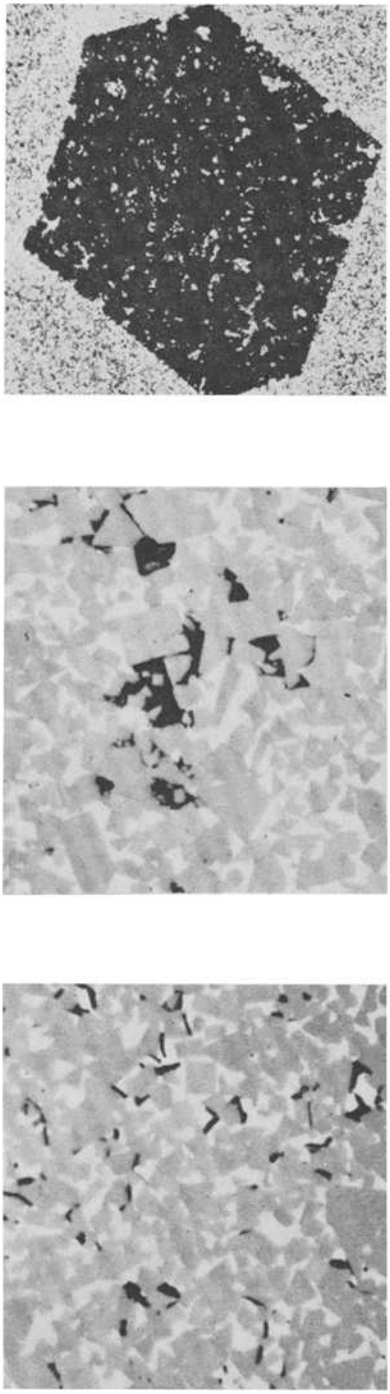

FIG. 4—*Graphite and* η *phase in WC-Co [3]:* (left) *graphite in a carbon-rich specimen, 16% cobalt, unetched,* ×*1500;* (middle) η *phase in a carbon-deficient specimen, 16% cobalt, etched 10 s with Murikami's reagent,* ×*1500;* (right) *abnormally large* η *phase grain resulting from long-time decarburization,* ×*125.*

and all particles. It is directly related to the total surface area of the carbide grains per unit volume, $(S_V)_\alpha$, since

$$(S_V)_\alpha = \frac{4(V_V)_\alpha}{(L_3)_\alpha} \tag{5}$$

where $(S_V)_\alpha$ includes the tungsten carbide (WC)/cobalt interfaces and WC/WC grain boundaries. The mean free path in the binder is a measure of the average thickness of the binder layers and also of the total area of the WC/cobalt interface per unit volume

$$(S_V)_\beta = \frac{4(V_V)_\beta}{\bar{L}_\beta} \tag{6}$$

The grain boundaries of the binder are ignored in these calculations since, in general, the grain size of the binder is very much larger than the mean free path between carbide particles. The contiguity is a measure of the degree of contact between carbide particles. It is defined as the ratio of the WC/WC grain boundary area to the total surface area of the carbide, the latter consisting of WC/WC grain boundaries and WC/cobalt interfaces.

The evaluation of these basic stereological parameters is independent of shape and size, but the structure parameters discussed so far are not independent of each other, as shown by their interrelation

$$\bar{L}_\beta = (\bar{L}_3)_\alpha \frac{(V_V)_\beta}{[1-(V_V)_\beta]\,(1-C_\alpha)} \tag{7}$$

According to Eq 7, any three of the four parameters are sufficient to characterize fully the degree of dispersion of the carbide phase in WC-Co alloys. The theories and practices relevant to these stereological parameters are discussed in detail by Underwood [*6*].

Considerable effort has been expended in attempting to replace the tedious manual point and intercept counting by automatic scanning procedures. Not only can these give the average values of the parameters quickly and easily, but they also lend themselves to further exploitation of the accumulated data, specifically, by supplying information on size distribution, shape factors, and orientation. Unfortunately, the required gray-level distinction is particularly difficult to achieve in cemented carbides because of the fineness of the structure and poor contrast between phases. While automatic methods have not yet generally established themselves in the industry, two interesting approaches are worth mentioning. Nidikom and Davies [*7*] used a special double-etching procedure to increase the contrast between binder and carbide in WC-Co sufficiently to allow scanning by an image analyzing computer. Werlefors and

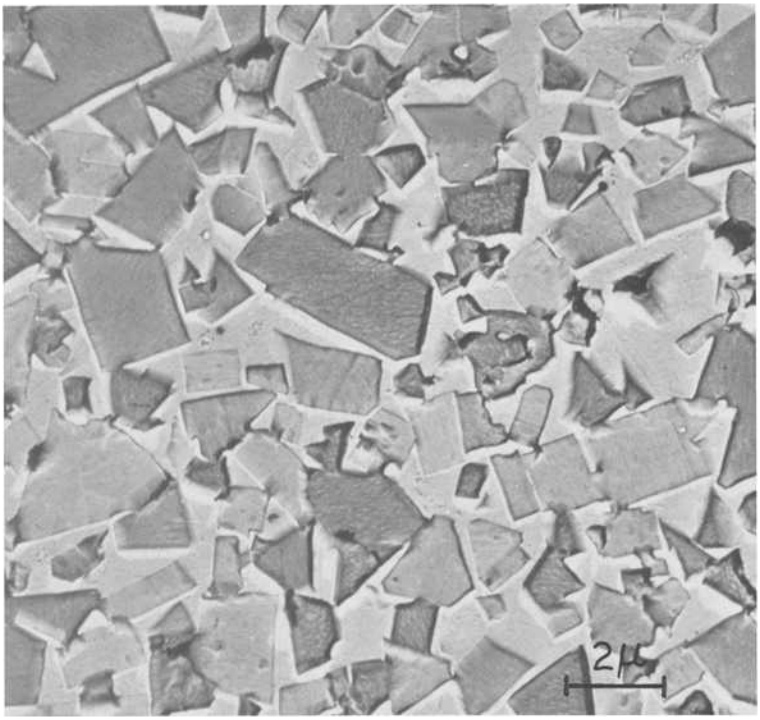

FIG. 5—*Electron photomicrographs of WC-Co, electrolytic etch, replica TEM [10]:* (a) *15% cobalt by weight.*

Eskilsson [*8*] supplemented on-line computer analysis of electron microscope scans by interactive manual tracing of WC/WC grain boundaries by the operator. Other semiautomatic devices, requiring hand tracing of the grain and interphase boundaries on an electronic planimeter (digitizer tablet), with on-line data storage and analysis by computer, are commercially available. Their application to cemented carbides is described by Exner [*1*].

The empirical effects on properties of the aforementioned parameters are well established. High porosity affects density, of course, but even very low porosity may influence fracture strength in a way that is out of proportion to its amount because of the role of critically sized or critically spaced flaws in fracture nucleation.

The overall effects of the cobalt content and WC grain size on the hardness, transverse rupture strength, and fracture toughness are perhaps best summarized by showing the variation in these properties as a function of the binder mean free path (Fig. 7). In general, the hardness decreases and the fracture toughness increases with an increasing mean free path, that is, with increasing cobalt content or increasing WC grain size. The shape of the transverse

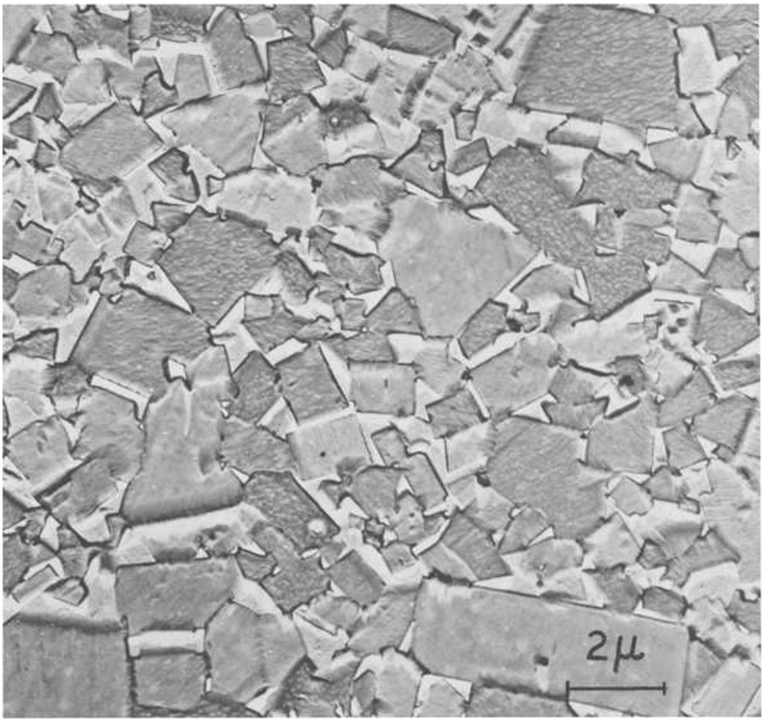

FIG. 5—*Continued:* (b) *4% cobalt by weight.*

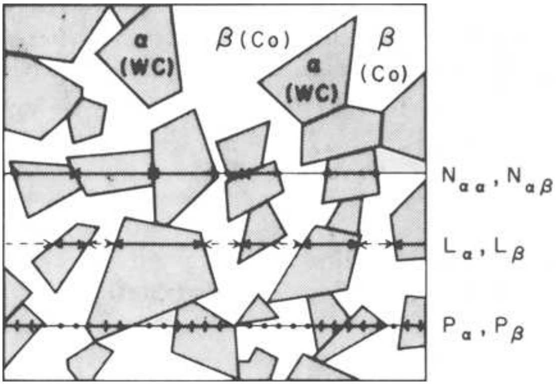

FIG. 6—*Schematic illustration of point counting (*P_α, P_β*), intercept counting (*$N_{\alpha\alpha}$, $N_{\alpha\beta}$*), and linear intercept lengths (*L_α, L_β*).*

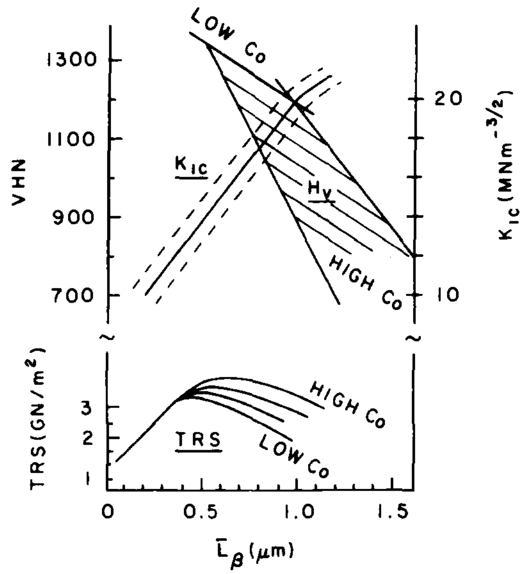

FIG. 7—*Schematic diagram showing trends of transverse rupture strength (TRS), indentation hardness (VHN), and fracture toughness, (K_{Ic}), as a function of the binder mean free path, (L_β) (after Ref 9 and Footnote 3).*

rupture strength versus mean free path curve reflects a transition between brittle and ductile fracture initiation. On the left side, the fracture strength is controlled by the largest defects and the fracture propagation resistance of the material. On the right side, fracture is associated with plastic deformation and crack nucleation at WC particles, and therefore the fracture strength is related to the yield strength. The inverse relationship between hardness and fracture strength in the brittle grades lies at the root of the basic quandary of alloy design. The carbide manufacturers and users are continuously striving for the optimum compromise between maximum hardness and adequate fracture strength.

Very little is known about the effects of contiguity as an independent variable. A tentative interpretation [*9*] of the data available appears to show that there is increasing hardness [*10*] and decreasing transverse rupture strength [*11*] with increasing contiguity. A practical difficulty is that of separating the effects of contiguity from those of the other variables contained in Eq 7.

Microscopy Applied to Research Problems

The apparent simplicity of the microstructures of cemented carbides may be misleading in suggesting that the obvious microstructural parameters (binder volume fraction, binder mean free path, and carbide grain size) exert exclusive control over the mechanical properties. It has become painfully apparent, as the result of recent and current research, that neither is the structure quite as simple as it looks in the light microscope or in the electron microscope at moderate magnifications, nor is it always possible to predict precisely the properties of a phase mixture, such as WC-Co, even if the structure could be regarded as consisting only of hard WC particles embedded in a ductile binder matrix.

For these reasons, much of the current basic research on cemented carbides is concerned with the development of the microstructure during sintering, the deformation processes at the microstructural level, and the relation between structure and properties. Some aspects of these research topics are briefly discussed in this section.

Stereology of Multiphase Materials Applied to Cemented Carbides

Simple cemented carbides, such as WC-Co, belong to the general class of two-phase alloys or phase mixtures of coarse microstructure. Other examples of this class of alloys are dual-phase steels (ferrite-martensite), cast aluminum/silicon (Al-Si) alloys and dual-phase copper/aluminum (Cu-Al) alloys (α-β), among others. The study of the interrelationships between the microstructure and properties of phase mixtures requires stipulation of the relevant microstructural parameters. For instance, in order to consider the effects of second-phase particles on such field properties of a material as the thermal and electrical conductivity, dielectric constant, and magnetic permeability, Ondracek [*12*] identifies five parameters required to define the microstructure: (1) the number of phases implicitly present, (2) a factor relating to the geometrical arrangement of the added phase, that is, the connectivity, and (3) the concentration, (4) shape, (5) orientation of the particles. Together with the properties of the individual phases, these microstructural parameters allow calculation of the upper and lower bounds of a field property as a function of the composition of the mixture. The extreme limits of the properties of the mixture are those corresponding to the parallel and series arrays, respectively, of the phases. Closer bounds are obtained if the parameters are more precisely defined and correspond better to the geometry of the actual structure. Similar considerations apply to linear elastic properties. Closely spaced upper and lower bounds have been calculated for the elastic modulus of phase mixtures [*13,14*] and, as a matter of fact, with first application to WC-Co alloys (Fig. 8).

The theory of nonlinear mechanical behavior of phase mixtures is not nearly as well developed. The plasticity of coarse-grained two-phase alloys has been reviewed by Fischmeister and Karlsson [*15*], including the limited work done on WC-Co alloys. References to, and discussion of, the influences of microstructural features on properties are found in Exner's survey paper [*1*], with particular attention to hardness, transverse rupture strength, and fracture toughness. In general, the dominant microstructural variable in both empiri-

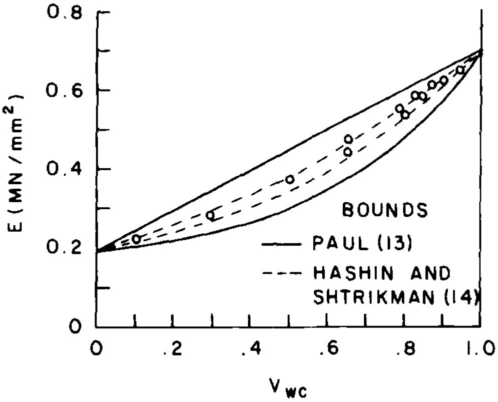

FIG. 8—*Schematic diagram of upper and lower bounds of the elastic modulus, (*E*), of WC-Co as a function of the volume fraction of WC [*$V_{WC} = (V_V)_\alpha$*] (after Fischmeister and Karlsson [15]).*

cal correlations and theoretical models is the binder mean free path, but the prediction of the strength properties from first principles requires a deeper understanding of the deformation mechanisms than is now available and further identification of the relevant microstructural features and variables. Some of the important factors are being revealed by current research, in particular the use of fractography in studying deformation and failure mechanisms and the application of transmission electron microscopy (TEM) to the fine details of the microstructure.

Quantitative Fractography

Detailed study of the fracture surface reveals the contribution of the various features of the microstructure to the fracture process. Luyckx [*16*] and Almond and Roebuck [*17*] called attention to the role of defects, such as pores, inclusions, or large WC grains, which in some cases can be located and identified on the fracture surface. The presence of defects of various sizes may account for the observed scatter of fracture strengths in bending of the more brittle alloy grades [*17,18*].

The local microstructural fracture processes in WC-Co observed on the fracture surface are (1) transgranular cleavage fracture of WC grains, (2) WC grain boundary fracture, (3) WC/cobalt interface decohesion, and (4) rupture of the binder (cobalt) ligaments (Fig. 9) [*19,20*].[3] Quantitative measurements of the lengths of fracture segments in each phase have been carried out (Fig. 10) [*19,20*].

---

[3] Pickens, J. R. and Gurland, J., *Materials Science and Engineering*, Vol. 33, 1978, pp. 135-142.

The plastic deformation of the binder has been studied in some detail on fracture surfaces of WC-Co [*19*]. In addition, the relative areas of the fracture surface occupied by the various microstructural types of fracture were determined by quantitative metallographic methods applied through scanning electron microscopy (SEM) and replica techniques [*21*], and the area fraction of the binder phase on the fracture surface was measured by Auger electron spectroscopy [*22*] and ion spectroscopy [*23*]. In general, it has been shown that the binder area fraction on the fracture surface is appreciably larger than the area fraction of the binder phase on a random planar section. These findings are in agreement with and relevant to the major role that the plastic deformation and ductile rupture of the binder is believed to have in the fracture process. However, fractography has also shown that the properties of the interfaces between carbide and binder, and between carbide grains, may have considerable influence on the fracture sequence and, perhaps, on the fracture strength.

Fine Structure of Sintered WC-Co by TEM

The electron microscope has exposed details of the microstructure which could not have been seen by light microscopy, with the most interesting results obtained by transmission electron microscopy (TEM) of thin films prepared by electrolytic etching or, preferentially, by ion milling. For instance, it has been shown by TEM that WC may contain a complex dislocation network structure, the nature of which is affected by deformation [*24–27*], and that the room temperature crystal structure of the binder is mostly face-centered cubic (fcc) with a high density of hexagonal close-packed (hcp) stacking faults arising during deformation [*25*].

Some attention is currently focused on the structure of the grain boundaries between WC particles in the sintered alloys. Using scanning transmission electron microscope (STEM) analysis, Sharma et al [*28*] have shown that the cobalt/tungsten atomic ratio is more than three times larger in the grain boundaries than in the grain interior. They interpret their results as providing evidence for the presence of a thin film of cobalt (~ 20Å) in the grain boundaries, thereby reopening the old controversy over whether WC forms a continuous skeleton or whether each WC grain is separated from its neighbors by a continuous cobalt film.

There is strong evidence that at least some of the grain boundaries provide a direct transition between contiguous WC crystals. Hagège et al [*29*], using TEM, observed and analyzed in detail the structure of one particular grain boundary with relatively good coincidence of the two crystals' lattices, although the grains were rotated by 90° approximately relative to each other across a common prismatic boundary plane. A small mismatch of low-index atomic planes and an additional small twist component were accommodated

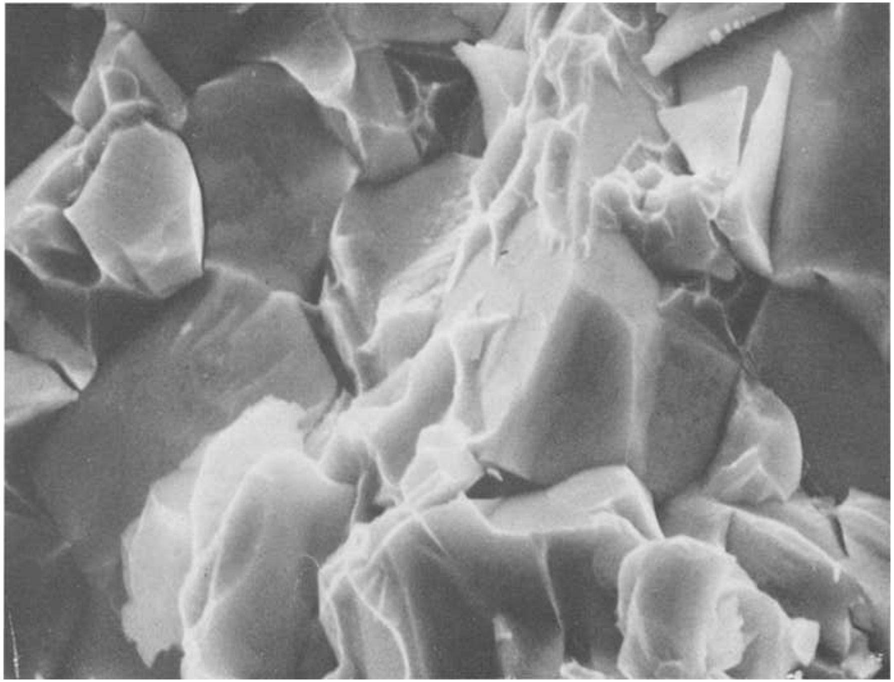

FIG. 9—*Illustration of local fracture processes in WC-Co:* (top) *transgranular cleavage of a large WC grain in 6% cobalt alloy, replica TEM,* ×*13 000 (photomicroscopy by J. Pickens);* (bottom) *WC/WC grain boundary decohesion, showing a WC face with ruptured cobalt ligaments, SEM,* ×*10 000 (photomicroscopy by J. Hong.)*

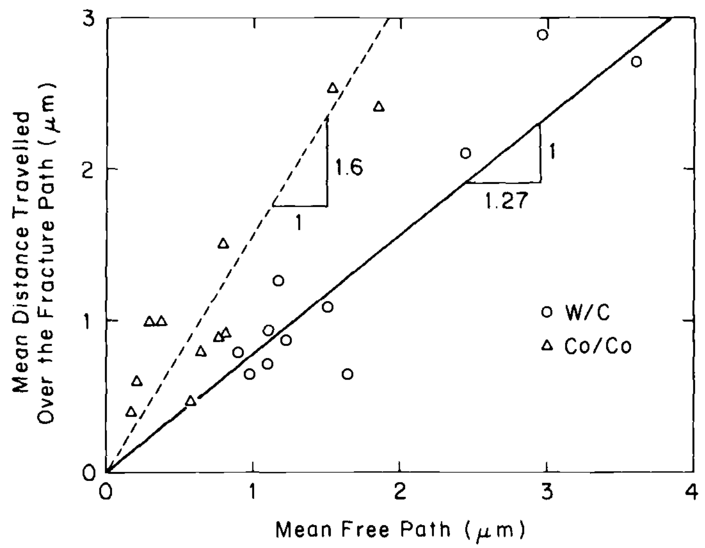

FIG. 10—*Mean fracture segment lengths in carbide (W/C) and in binder (Co/Co) as a function of mean free path [19].*

by the defect structure in the grain boundary. These results are not compatible with the presence of a cobalt film in the boundary.

The distribution of dihedral contact angles between contiguous WC grains, measured by Gurland [*30*] and Deshmukh and Gurland,[4] show pronounced peaks at 60° and 90° (Fig. 11). Such results appear to indicate a geometrical influence on the contact configuration, although they do not necessarily prove a tendency towards a unique preferred orientation across contact planes. Dihedral angles of contact measured in cubic carbide/binder systems [*31*] are a function of the relative values of the carbide/binder interface energy and carbide/carbide grain boundary energy and are generally independent of orientation.

The structure and properties of the WC grain boundaries may well be important factors in the deformation and fracture processes. Reference is made in the literature to a number of observations regarding the role of these boundaries in transmitting plastic deformation through the WC skeleton [*32,33*] and providing primary sites of crack initiation and propagation [*19-22,34*].

General Conclusions and Remarks

The producers and users of cemented carbides have greatly benefited from the development of quantitative microscopy. It is employed at all levels of ob-

---

[4] Work in progress.

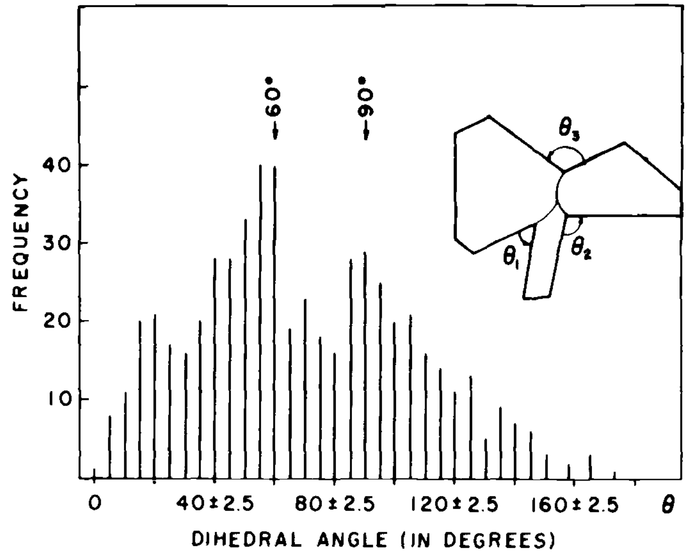

FIG. 11—*Dihedral angles between WC grains, WC-25Co, sintered ½ h at 1450°C in hydrogen (after Deshmukh and Gurland, from work in progress).*

servation, from the counting of pores at ×100, to the measurement of grain size at ×2000 and the examination of stacking faults at ×10 000. It is used for quality evaluation, alloy development, and research. The benefits are greatly improved and consistent grades of carbides.

The current trend in quality control is towards automation of inspection methods, including microscopy. In research, the recent past has seen the application of sophisticated scanning and diffraction instruments to progressively smaller features of the microstructure, and, no doubt, this trend will continue in the near future.

As a final note, it might be mentioned that an initial interest in the specific metallography of cemented carbides has more than once spawned a lasting and fruitful association between that field and the field of stereology at large, as seen, for example, in the contributions of Exner [*1,4,9*], Fischmeister [*4,15*], Chermant [*20,21*], and their co-workers to both the metallography of cemented carbides and theoretical stereology. In that sense, one can expect that the cemented carbides will continue to be a proving ground for further stereological advances.

Acknowledgment

The writing of this review was supported by the Materials Research Laboratory, funded at Brown University by the U.S. National Science Foundation.

References

[*1*] Exner, H. E., "Qualitative and Quantitative Interpretation of Microstructures in Cemented Carbides," *Science of Hard Materials*, Plenum Press, New York, 1983, pp. 233-262.

[*2*] Cherniavsky, K. S., "Stereological Methods in Studying the Cemented Carbides," *Contemporary Stereology, Stereologia Jugoslavica*, Vol. 3, Supplement 1, 1981, pp. 299-308.

[*3*] Gurland, J., *Transactions of the A.I.M.E.*, Vol. 200, 1954, pp. 285-290.

[*4*] Exner, H. E. and Fischmeister, H. F., *Archiv für Eisenhuettenwesen*, Vol. 37, 1966, p. 410.

[*5*] Peter, W., Kohlhaas, E., and Fischer, A., *Praktische Metallographie*, Vol. 5, 1968, p. 115.

[*6*] Underwood, E. E., *Quantitative Stereology*, Addison Wesley, Reading, Mass., 1970, Chapter 4.

[*7*] Nidikom, B. and Davies, T. J., *Planseeberichte für Pulvermetallurgie*, Vol. 28, 1980, pp. 29-38.

[*8*] Werlefors, T. and Eskilsson, C., *Metallography*, Vol. 12, 1979, p. 153.

[*9*] Exner, H. E. and Gurland, J., *Powder Metallurgy*, Vol. 13, 1970, p. 13.

[*10*] Lee, H. C. and Gurland, J., *Materials Science and Engineering*, Vol. 33, 1978, pp. 125-133.

[*11*] Gurland, J., *Transactions of The Metallurgical Society of A.I.M.E.*, Vol. 236, 1966, p. 642.

[*12*] Ondracek, G., *Acta Stereologica*, Vol. 1, 1982, pp. 5-21.

[*13*] Paul, B., *Transactions of the A.I.M.E.*, Vol. 218, 1960, pp. 36-41.

[*14*] Hashin, Z. and Shtrikman, S., *Journal of the Mechanics and Physics of Solids*, Vol. 11, 1963, pp. 127-140.

[*15*] Fischmeister, H. and Karlsson, B., *Zeitschrift für Metallkunde*, Vol. 68, 1977, pp. 311-327.

[*16*] Luyckx, S. B., *Acta Metallurgica*, Vol. 23, 1979, pp. 109-115.

[*17*] Almond, E. A. and Roebuck, B., *Metal Science*, Vol. 11, 1977, pp. 458-461.

[*18*] Amberg, S. and Doxner, H., *Powder Metallurgy*, Vol. 20, 1977, No. 1, pp. 1-10.

[*19*] Hong, J. and Gurland, J., "A Study of the Fracture Process and Fracture Toughness of WC-Co Alloys," *Science of Hard Materials*, Plenum Press, New York, 1983, pp. 649-670.

[*20*] Chermant, J. L. and Osterstock, F., *Journal of Materials Science*, Vol. 11, 1976, pp. 1939-1951.

[*21*] Chermant, J. L., Coster, M., and Osterstock, F., *Metallography*, Vol. 9, 1976, pp. 503-523.

[*22*] Viswanadham, R. K., Sun, T. S., Drake, E. F., and Peck, J. A., *Journal of Materials Science*, Vol. 16, 1981, pp. 1029-1038.

[*23*] Otsuki, E. and Masudo, Y., *Nippon Kinzoku Gakkaishi*, Vol. 44, 1980, No. 2, pp. 117-123.

[*24*] Johannesson, T. and Lehtinen, B., *Physica Status Solidi (B)*, Vol. 16, 1973, pp. 615-622.

[*25*] Sarin, V. K. and Johannesson, T., *Metal Science*, Vol. 9, 1979, pp. 472-476.

[*26*] Gottschall, R. J., Williams, W. S., and Ward, I. D., *Philosophical Magazine A*, Vol. 41, 1980, pp. 1-7.

[*27*] Hagège, S., Vicens, J., Nonet, G., and Delavignette, P., *Physica Status Solidi (A)*, Vol. 61, 1980, pp. 675-687.

[*28*] Sharma, N. K., Ward, I. D., Fraser, H. L., and Williams, W. S., *Journal of the American Ceramic Society*, Vol. 63, 1979, pp. 194-196.

[*29*] Hagège, S., Nonet, G., and Delavignette, P., *Physica Status Solidi (A)*, Vol. 61, 1980, pp. 97-107.

[*30*] Gurland, J., *Metallography*, Vol. 10, 1977, p. 461.

[*31*] Warren, R. and Waldron, M. B., *Powder Metallurgy*, Vol. 15, 1972, pp. 166-201.

[*32*] Arndt, R., *Zeitschrift für Metallkunde*, Vol. 63, 1972, pp. 274-280.

[*33*] Liu, H. C. and Gurland, J., *Materials Science and Engineering*, Vol. 33, 1978, pp. 125-133.

[*34*] Luyckx, S., "Contiguity and the Fracture Process of WC-Co Alloys," *Proceedings*, Fifth International Conference on Fracture, Cannes, France, 1981, D. Francois, Ed., Pergamon Press, New York.

George F. Vander Voort[1]

Grain Size Measurement

REFERENCE: Vander Voort, G. F., "**Grain Size Measurement,**" *Practical Applications of Quantitative Metallography, ASTM STP 839,* J. L. McCall and J. H. Steele, Jr., Eds., American Society for Testing and Materials, Philadelphia, 1984, pp. 85-131.

ABSTRACT: Methods used to measure planar grain size, either manually or by image analysis, are reviewed based on their historical development and their relationship to basic stereological concepts. The methods discussed include comparison techniques employing standard charts or the Shepherd fracture grain size standards; measurement techniques based on determination of the number of grains per unit area (Jeffries method), the number of triple points per unit area, or the number of grains intercepted or grain boundaries intersected per unit length of a test line (Heyn method); and correlations based on grain shape assumptions for estimating spatial grain size characteristics. Specific procedures for measuring the grain size of nonequiaxed, duplex, or multiphased grain structures are also discussed. Examples of these techniques are given, along with information about the accuracy of grain size measurements.

KEY WORDS: grain size, grain size distribution, grain shape, grain boundaries, quantitative metallography, etching, automatic image analysis

Of the many measurements performed by metallographers, determination of the grain size is probably the single most important and most common. The importance of grain size measurements stems from the influence of grain size on the properties and behavior of metals. Although grains are three-dimensional features, their size is normally estimated by one- or two-dimensional measurements on planar surfaces through the specimen volume. If the grains are equiaxed in shape, any randomly oriented sectioning plane will suffice. For routine work, a single average value is used to define the grain size. While this value provides no information about the range and distribution of sizes present, it is a useful value. Development of the grain size distribution and determination of the spatial size of the grains within the specimen volume are difficult tasks. This paper presents the various techniques used to measure grain size and concentrates on the practical problems encountered.

---

[1] Supervisor, Applied Physics Research and Development, Carpenter Technology Corp., Reading, Pa. 19603.

Grain Shape

Grain shapes must be space filling and grain surfaces must conform to laws regarding minimum surface area and surface tension. Spheres exhibit minimum surface area and tension but are not space filling, while cubes are space filling but do not meet surface tension requirements. In 1887, Lord Kelvin showed that the optimum space-filling grain shape with minimum surface area and surface tension is a polyhedron, known as a tetrakaidecahedron, which has 14 faces, 24 corners, and 36 edges. Fifty-nine tetrakaidecahedra with faces having four to six edges have been identified [*1*].[2] This shape model fulfills the surface tension requirements, described by Plateau in 1873, that no more than three grains can meet at an edge and no more than four edges can meet at a corner. However, it does not fulfill the requirement of 120° dihedral angles between grain boundaries where three adjacent grains meet at an edge [*2,3*], unless the faces exhibit curvature. The pentagonal dodecahedron, although not a space-filling grain shape, does correlate well with measurements of actual grains [*4*]. This polyhedron has twelve five-sided faces. Measurement of actual grains shows that they exhibit a wide variety of sizes, shapes, and number of faces.

In a three-dimensional structure, the grains are in contact with each other at their faces, edges, and corners. Grain faces meet in pairs of touching grain surfaces; edges result where three grain faces meet and corners arise where four edges, six faces, and four grains meet. For the "average" grain, equal interfacial energies produce face angles of 109.5° and dihedral angles of 120°. When such conditions are obtained [*3*], the average number of edges per face is 5.1043, the average number of faces per grain is 13.394, the average number of edges per grain is 34.195, and the average number of corners per grain is 22.789.

Desch [5] was the first to study actual grain shapes by separating beta brass grains by immersing the bulk specimen into mercury. Liquid metal embrittlement causes the specimen to fracture intergranularly, thus freeing the individual grains. Measurement of the isolated grains revealed that the number of faces per grain varied from 11 to 20, with an average of 14.5. The larger grains were more complex in shape, with most faces curved and with double curvature frequently observed. The number of sides per face varied from three to eight, as shown here.

	Beta-Brass Grains					
Sides per face, No.	3	4	5	6	7	8
Observations, No.	11	88	190	123	20	3

---

[2] The italic numbers in brackets refer to the list of references appended to this paper.

Five-sided (pentagonal) grains were most frequently observed, and the average number of edges per face was 5.14, which is close to the theoretical predictions.

Williams and Smith [*6*] studied grain shapes using stereomicroradiography and found that the average number of edges per face was 5.06 [*3*], and the average number of faces per grain was 12.48. These measurements compare closely with those of the pentagonal dodecahedron. The larger grains had more faces than the smaller grains, as might be expected.

For the case of a three-dimensional single-phase grain structure cut by a sectioning plane, topology predicts [*2,3*] that the average grain will have six sides; that is, the average planar grain shape is a hexagon. Using one of the ASTM grain size chart illustrations, Smith [*2,3*] determined the number of grains with three to nine sides and found that the average number of sides per grain was six. In any such structure, grains with fewer than six sides are balanced by the presence of grains with more than six sides.

Revealing Grain Structure

In order to obtain an accurate measurement of grain size, the grain structure must be properly delineated. The techniques used to reveal the grain boundaries fully vary with the type of grain structure being examined. For austenitic or ferritic grain structures, standard etchants are utilized to reveal the austenitic or ferritic grain structure (Figs. 1 and 2). For martensitic steel structures, special etching procedures are utilized, but with much greater difficulty, to reveal the prior austenite grain boundaries, as in Fig. 3. For those cases in which the grain growth behavior of hardenable steels is to be studied, special heat treatment practices can be employed to decorate the prior austenite grain boundaries selectively with a second phase. After such a process, for example, the McQuaid-Ehn carburizing method [*7*], simple etchants can be used to reveal the grain structure. Such methods are described in the ASTM Method for Estimating the Average Grain Size of Metals (E 112-82).

In low-carbon steels, such as sheet steels, the parent austenite grain boundaries can be revealed only in rare cases. Hence, the grain size of the transformation product, which is ferrite, is measured. The relationship between the parent austenite grain size and the daughter ferrite grain size is difficult to assess and has been studied only infrequently [*8, 9*]. The results of Carpenter and Robertson' [*8*] indicate that a greater number of ferrite grains are formed from large austenite grains than from fine ones. However, the total number of ferrite grains per unit area is greater when formed from fine austenite grains than when formed from coarse austenite grains. In a study of carbon/manganese steels, Cochrane and Morrison [*9*] showed that the ratio of the austenite-to-ferrite grain size decreased with decreasing austenite grain size and that this ratio was influenced by the carbon content and transformation temperature.

In austenitic metals, measurement of the grain size is more difficult when annealing twins are present (Fig. 1). Not all austenitic metals exhibit annealing twins. Aluminum and its alloys rarely exhibit annealing twins, while they are commonly observed in copper, nickel, and austenitic stainless steels. When measuring the grain size of austenitic metals, annealing twins are ignored. In a few instances, special etching procedures can be employed that will not attack the annealing twins but will produce excellent grain boundary delineation. If structure-property correlations are contemplated, twin boundaries should not be ignored. The best correlations are obtained when both types of boundaries are counted. Such a measurement, however, should not be referred to as grain size.

In any measurement of grain size, it is imperative that all of the grain boundaries be revealed irrespective of the nature of the measurement technique. Hence, the metallographer must select the etchant or technique that produces the highest degree of grain boundary delineation. This is not a trivial task, even for commonly encountered metals and alloys. For example, while nital is widely used to reveal ferrite grain boundaries in sheet steels, it is sensitive to orientation and will not clearly reveal all of the grain boundaries. This is a serious problem if image analysis is performed. The use of Marshall's reagent (Fig. 2) will generally produce a very high degree of boundary delineation in ferritic low-carbon steels.

Etchants that produce grain contrast attack may be quite suitable for comparison-chart grain size ratings, provided that the chart selected has a similar etch appearance. However, grain contrast etchants are less satisfactory for manual measurements and useless for image analysis. Even with etchants that produce grain-boundary attack, the image must be edited for image analysis measurements. If a second phase can be made to decorate the grain boundaries by aging treatments, the grain-boundary etching response will be simplified.

Grain Size Definitions

The ASTM Method for Estimating the Average Grain Size of Non-Ferrous Metals, Other Than Copper, and Their Alloys (E 91 T) (discontinued and replaced by ASTM Method E 112) introduced the basic equation used to define the ASTM grain size scale

$$n = 2^{G-1} \tag{1}$$

where n is the number of grains per square inch at ×100,[3] and G is the ASTM (Timken) grain size number. This relationship can also be expressed as

$$G = \frac{\log n}{\log 2} + 1 \tag{2}$$

---

[3] Note that 1 in.^{2} = 6.4516 cm^2.

FIG. 1—Photomicrograph of an austenitic alloy, alpha brass, containing annealing twins, etched with Klemm's I reagent (saturated aqueous sodium thiosulfate plus 2% potassium metabisulfite), at ×100 magnification.

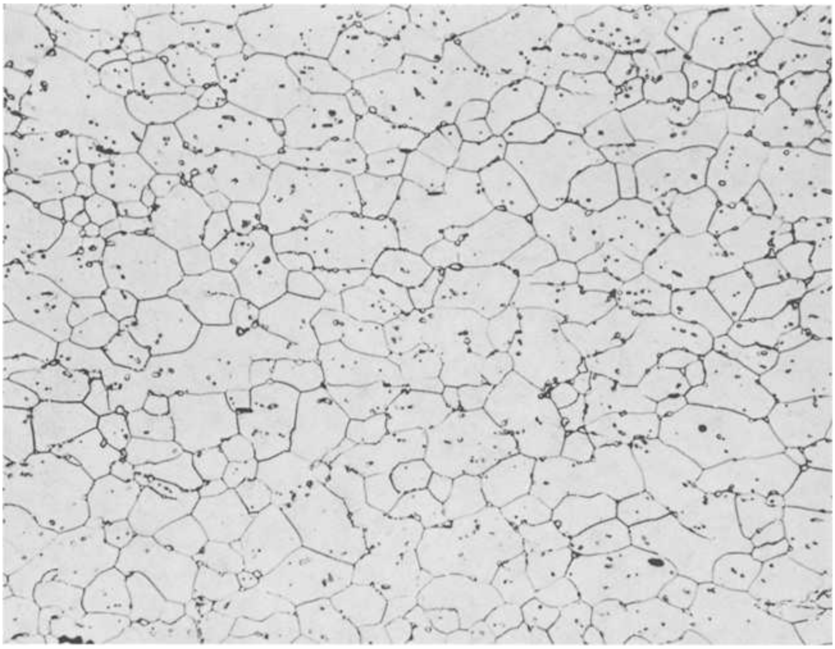

FIG. 2—*Photomicrograph of ferrite grains in a low-carbon sheet steel specimen etched 3 s with Marshall's reagent [one part 30% hydrogen peroxide (H_2O_2) and one part stock solution—5 mL sulfuric acid (H_2SO_4), 8 g oxalic acid, and 100 mL water] followed by a 20-s etch with 2% nital, at ×500.*

Table 1 lists the relationships in ASTM Method E 112-82 among the ASTM grain sizes (Column 1), the average grain diameter (Column 2), the average intercept length (Column 4), the number of grains per square millimetre at ×1 (Column 8), and the number of grains per square inch at ×100 (Column 9). Note that, although ASTM now has a metric base for its standards, grain size was originally defined as the number of grains per square inch at ×100. This is still carried over in ASTM Method E 112-82 (Column 9 in Table 1 of this paper). Column 8 of Table 1, which has the metric equivalent at ×1 (number of grains per square millimetre), has always been part of this standard.

Other countries established their grain size scales using the metric system from the beginning, basing grain size on the number of grains per square millimetre at ×1. The Swedish (SIS 11 11 01), Italian (UNI 3245), Russian (GOST 5639), French (NF A04-102), and International Organization for Standardization (ISO) (R643) standards define the grain size number, G_m, according to

$$m = 8(2^{G_m}) \qquad (3)$$

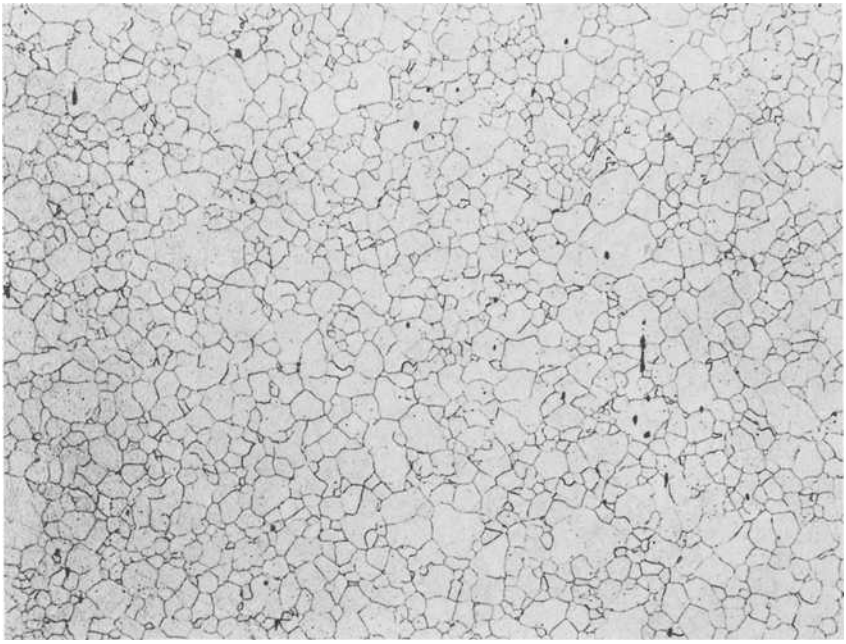

FIG. 3—*Photomicrograph showing prior austenite grains in a heat-treated alloy steel etched with aqueous saturated picric acid plus a wetting agent, sodium tridecyl benzene sulfonate, at ×100.*

where m is the number of grains per square millimetre at ×1. This relationship can also be expressed as

$$G_m = \frac{\log m}{\log 2} - 3 \qquad (4)$$

The grain size numbers calculated by the metric standards are about 4.5% higher than the values calculated by the ASTM system for the same specimen, that is

$$G = G_m - 0.045 \qquad (5)$$

German Standard SEP 1510 also uses the metric system, but the calculation method chosen yields numbers equivalent to those of the ASTM system. In the German method, the photomicrograph serial number, K, is calculated based on the average number of grains per square centimetre at ×100, Z, by the following formula

$$K = 3.7 + 3.33 \log Z \qquad (6)$$

TABLE 1—*Grain size relationships, taken from ASTM Method E 112-82.*

ASTM Micro-Grain Size Number G	"Diameter" of Average Grain Section[B]		Average Intercept Distance[C] $\bar{l}$, mm	Intercept Count, n/l per mm	Area of Average Grain Section, $\bar{a}$, mm^2	Calculated Number of Grains per mm^3, n/v[D]	Average	
	Nominal d_n, mm	Feret's d_f, mm					Grains per mm^2 at 1×,[E] n/a	Grains per in.^{2} at 100×, N/A
00[A]	0.51	0.570	0.453	2.210	0.258	6.11	3.88	0.250
0	0.36	0.403	0.320	3.125	0.129	17.3	7.75	0.500
0.5	0.30	0.339	0.269	3.716	0.0912	29.0	11.0	0.707
1.0	0.25	0.285	0.226	4.42	0.0645	48.8	15.50	1.000
1.5	0.21	0.240	0.190	5.26	0.0456	82	21.9	1.414
(1.7)[F]	0.200	0.226	0.177	5.64	0.0400	100	25.0	1.613
2.0	0.18	0.202	0.160	6.25	0.0323	138	31.0	2.000
2.5	0.15	0.170	0.135	7.43	0.0228	232	43.8	2.828
3.0	0.125	0.143	0.113	8.84	0.0161	391	62.0	4.000
(3.2)[F]	0.120	0.135	0.106	9.41	0.0144	463	69.4	4.480
3.5	0.105	0.120	0.095	10.51	0.0114	657	87.7	5.657
(3.7)[F]	0.100	0.113	0.089	11.29	0.0100	800	100	6.452
	μm	μm	μm		mm^2 × 10^{-3}			
4.0	90	101	80.0	12.5	8.07	1105	124	8.000
4.5	75	85	67.3	14.9	5.70	1859	175	11.31
(4.7)[F]	70	79	62.0	16.1	4.90	2331	204	13.17
5.0	65	71	56.6	17.7	4.03	3126	248	16.00
(5.2)[F]	60	68	53.2	18.8	3.60	3708	278	17.92
5.5	55	60	47.6	21.0	2.85	5258	351	22.63
(5.7)[F]	50	56	44.3	22.6	2.50	6400	400	25.81
6.0	45	50	40.0	25.0	2.02	8842	496	32.00
(6.4)[F]	40	45	35.4	28.2	1.60	12 500	625	40.32
6.5	38	42	33.6	29.7	1.43	14 871	701	45.25
(6.7)[F]	35	39	31.0	32.2	1.23	18 659	816	52.67
7.0	32	36	28.3	35.4	1.008	25 010	992	64.00
(7.2)[F]	30	34	26.6	37.6	0.900	29 630	1111	71.68
7.5	27	30	23.8	42.0	0.713	41 061	1403	90.51
(7.7)[F]	25	28	22.2	45.1	0.625	51 200	1600	103.23

	µm	µm	µm		mm^2 × 10^{-6}	×10^6	×10^3	
8.0	22	25	20.0	50.0	504	0.0707	1.98	128.0
(8.4)^F	20	23	17.7	56.4	400	0.1000	2.50	161.3
8.5	19	21	16.8	59.5	356	0.1190	2.81	181.0
9.0	16	18	14.1	70.7	252	0.200	3.97	256.0
(9.2)^F	15	17	13.3	75.2	225	0.237	4.44	286.7
9.5	13	15	11.9	84.1	178	0.336	5.61	362.0
10.0	11	13	10.0	100	126	0.566	7.94	512.0
(10.3)^F	10	11.3	8.86	113	100	0.800	10.00	645.2
10.5	9.4	10.6	8.41	119	89.1	0.952	11.22	724.1
(10.7)^F	9.0	10.2	7.98	125	81.0	1.097	12.35	796.5
11.0	8	8.9	7.07	141	63.0	1.600	15.87	1024
(11.4)^F	7.0	7.9	6.20	161	49.0	2.332	20.41	1317
11.5	6.7	7.5	5.95	168	44.6	2.692	22.45	1448
(11.8)^F	6.0	6.8	5.32	188	36.0	3.704	27.78	1792
12.0	5.6	6.3	5.00	200	31.5	4.527	31.7	2048
(12.3)^F	5.0	5.6	4.43	226	25.0	6.40	40.0	2581
12.5	4.7	5.3	4.20	238	22.3	7.61	44.9	2896
13.0	4.0	4.5	3.54	283	15.8	12.80	63.5	4096
13.5	3.3	3.7	2.97	336	11.1	21.54	89.8	5793
(13.8)^F	3.0	3.4	2.66	376	9.0	29.6	111.1	7168
14.0	2.8	3.2	2.50	400	7.88	36.2	127	8192
(14.3)^F	2.5	2.8	2.22	451	6.25	51.2	160	10323

[A] The use of "00" is recommended instead of "minus 1" to avoid confusion.

[B] Feret's diameter = height between tangents; $d_f = \bar{a}/\bar{l}$. Values of d_n and d_f rounded to digits shown.

[C] Value of Heyn intercept or mean free path.

[D] Computation of n/v based on grains averaging to spherical shape for which $n/v = 0.5659\,(n/l)^3$.

[E] To obtain grains per mm^2 at 100×, multiply by 10^{-4}.

[F] The G values shown in parentheses are calculated to one decimal place and correspond to some of the nominal "diameter" sizes, (d_n) customarily used in reporting average grain size by the copper and brass industry.

For example, for a chart rating of $K = 5$, there are 2.5 grains/cm^2 at ×100, which translates into 16 grains/in.^{2} at ×100, or ASTM 5.

Japanese Standards JIS G0551 and JIS G0552 are also based on the metric system, but the equation used produces grain size numbers equal to the ASTM numbers. The formula used is

$$m = 2^{G+3} \tag{7}$$

where m is the number of grains per square millimetre at ×1.

Measurement Methods

Measurements on planar polished and etched sections are used to quantify the planar or spatial grain size. A wide variety of parameters is used to describe grain size:

(*a*) average grain "diameter," $\bar{d}$,
(*b*) average grain area, $\bar{A}$,
(*c*) average number of grains per unit area, N_A,
(*d*) average intercept length, $\bar{L}_3$,
(*e*) average number of grains intercepted by a line of fixed length, $\bar{N}$,
(*f*) average number of grains per unit volume, $\bar{N}_V$, and
(*g*) average grain volume, $\bar{V}$.

Of these descriptors of grain size, only the last two spatial parameters provide a measure of the true grain size. The planar parameters are based on measurements of various geometrical parameters of the microstructure, which change as the spatial grain size is altered. They provide a single number estimate of the grain size, which is useful for structure-property correlations, but gives no information about the nature of the grain size distribution. Spatial grain size estimation can be done by direct measurement (serial sectioning) or by indirect methods based on grain shape models. Estimation of the spatial grain size is a tedious procedure, generally only performed in research studies.

To measure or estimate the grain size, several procedures have been used:

(*a*) comparison chart estimates [*10-18*],
(*b*) fracture grain size estimates [*19-22*],
(*c*) planimetric (Jeffries) measurements [*23-25*],
(*d*) intercept (Heyn) measurements [*26-28*],
(*e*) Snyder-Graff intercept counts [*29,30*], and
(*f*) grain size distribution methods [*31-41*].

Reviews of grain size measurement methods are listed in Refs *42-46*.

Comparison Charts

Interestingly enough, measurement procedures preceded comparison chart methods by many years. When what is now the ASTM Method of Preparation of Micrographs of Metals and Alloys (Including Recommended Practice for Photography as Applied to Metallography) [E 2-62 (1974)] was first proposed in 1917, it included both the planimetric and intercept measurement methods, although the latter was not described in depth. Use of these methods, particularly the planimetric method, prompted requests for a simpler method for rating grain size. Consequently, a comparison chart was added in the 1930 revision of ASTM Method E 2. This chart was designed for copper and its alloys and consisted of ten photomicrographs at ×75. A grain contrast etch of ammonium hydroxide-hydrogen peroxide (NH_4OH-H_2O_2) was depicted with the average diameter expressed in millimetres, as determined by the Jeffries method. The ASTM grain size scale (Eq 1) was not established at this time. This chart was subsequently criticized as being poorly graded.

Grain size methods were deleted from ASTM Method E 2 in 1941 and a revised chart for copper with twelve photomicrographs was incorporated in a new standard, the ASTM Method for Estimating the Average Grain Size of Wrought Copper and Copper-Base Alloys (E 79-49 T), issued in 1949. This standard was discontinued in 1963 when all the grain size methods were incorporated into a single standard, ASTM Method E 112. A new chart with 14 photomicrographs was incorporated as Plate III of Method E 112. The average grain diameter is still expressed in millimetres and the photomicrographs are still at ×75.

In 1933, the ASTM Classification of Austenite Grain Size in Steels (E 19-33 T) was adopted, which included a standard chart for rating grain sizes in steels treated by the McQuaid-Ehn carburizing method. The chart contained eight photomicrographs, each depicting both the hypereutectoid and hypoeutectoid case structures. While the chart listed the range of grains per square inch at ×100 applicable for each picture, the grain size numbers, G, were not included. In the 1938 revision of ASTM Classification E 19, a stylized grain size chart was added; the McQuaid-Ehn chart in the earlier version (1933) was criticized because many of the photomicrographs depicted grain structures finer than the stated ranges. ASTM Classification E 19 was discontinued in 1961 when ASTM Method E 112 was developed. Plate IV of this method (E 112-82) is now used to rate McQuaid-Ehn specimens.

McQuaid-Ehn specimens are most commonly etched deeply with nital to reveal the unetched (white) cementite grain boundary phase against the darkly etched pearlite grain interiors, as depicted in Plate IV of ASTM Method E 112-82. This etching procedure does not, however, produce optimum visibility of the grain structure. The grain structure can be more vividly revealed if the specimen is etched with alkaline sodium picrate, either boiling or electrolytically, as illustrated in Fig. 4 (Parts *b* and *c*). French Standard NF A04-102 contains a chart for rating McQuaid-Ehn specimens, in which the photomicrographs illustrate specimens of different grain sizes etched with alkaline sodium picrate.

In 1950, ASTM introduced the ASTM Method for Estimating the Average Ferrite Grain Size of Low-Carbon Steels (E 89-50 T), which contained a chart

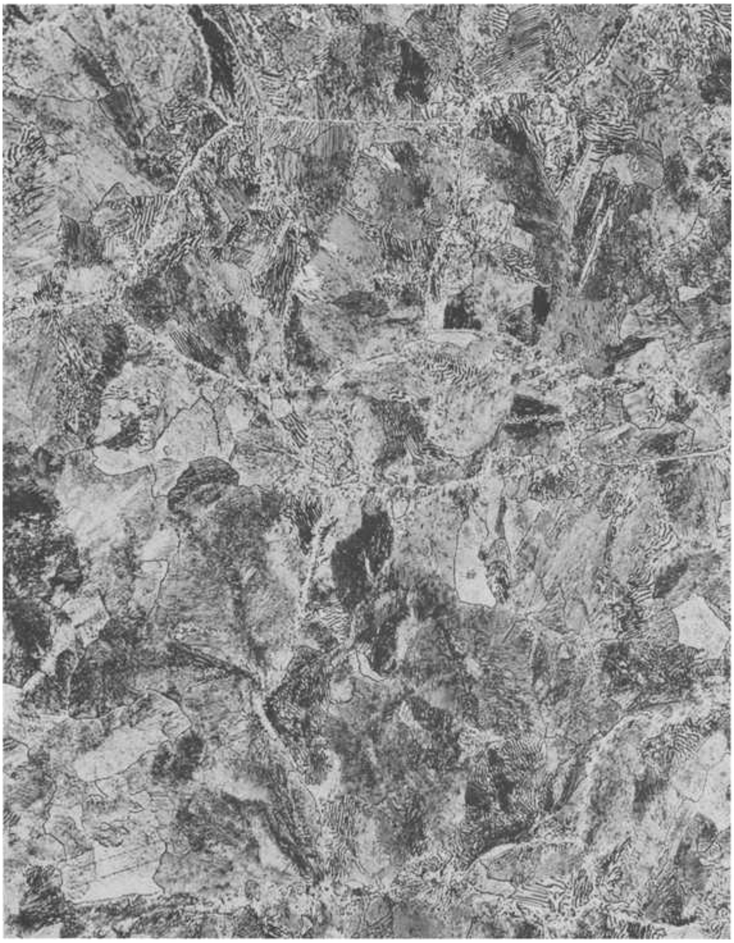

FIG. 4—*Photomicrographs illustrating the use of alkaline sodium picrate to delineate cementite grain boundary networks in a McQuaid-Ehn carburized specimen, at* ×*200:* (a) *this photomicrograph was etched with 2% nital, which faintly reveals the white (unetched) grain boundary network (compare with Parts* (b) *and* (c) *of this figure).*

depicting ferrite grains with sizes from ASTM 1 to 8. This chart was reasonably accurate, except for grain sizes 2, 4, and 5, which were slightly coarser than stated. However, the grain structures depicted were developed by using nital etching, and numerous poorly developed or undeveloped grain boundaries were present. ASTM Method E 89 was discontinued in 1961 when ASTM Method E 112 was prepared. The present version, ASTM Method E 112-82, does not include a similar chart. Instead, a stylized chart (Plate I) is used for rating untwinned grain structures with a grain-boundary etch.

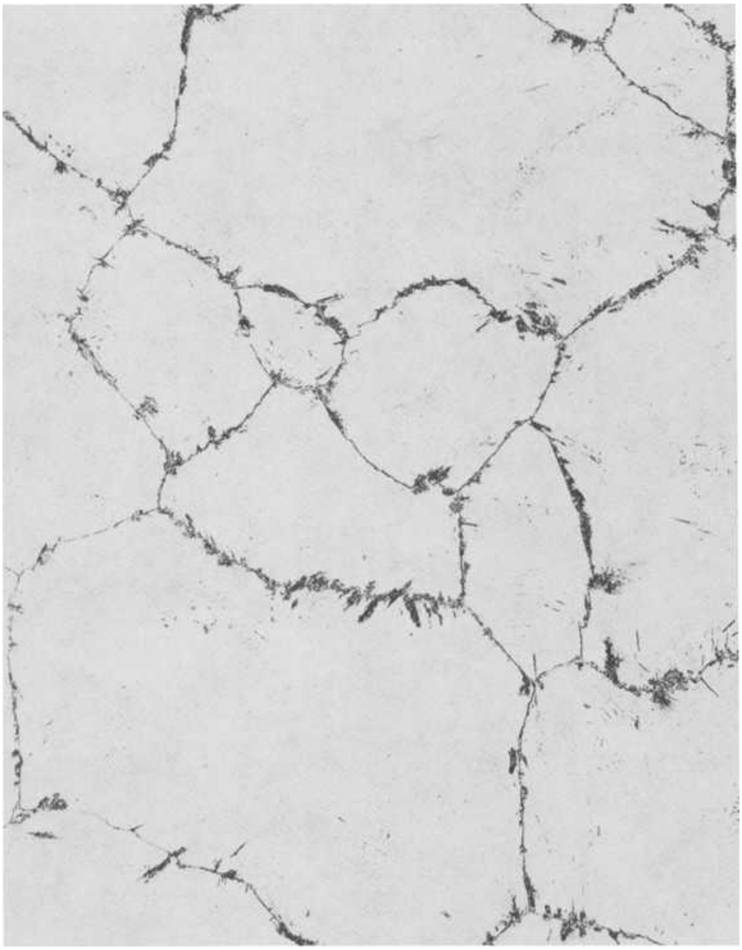

FIG. 4—*Continued:* (b) *photomicrograph of the specimen in Fig. 4, Part* a, *after etching with boiling alkaline sodium picrate.*

In 1947, ASTM initiated a study of grain size rating for nonferrous metals other than copper. ASTM Method E 91, adopted in 1951, contained two charts, one for twinned alloys and the other for untwinned alloys. Method E 91 was discontinued when ASTM Method E 112 was adopted, and neither of the Method E 91 charts was continued. Instead, Plate I of ASTM Method E 112-82 is used for untwinned specimens and Plate II is used for twinned specimens. Both charts illustrate specimens with a grain boundary etch attack.

Other countries and the International Organization for Standardization (ISO) have developed their own charts or adopted ASTM charts. Besides the previously mentioned French chart, the German SEP 1510 standard contains

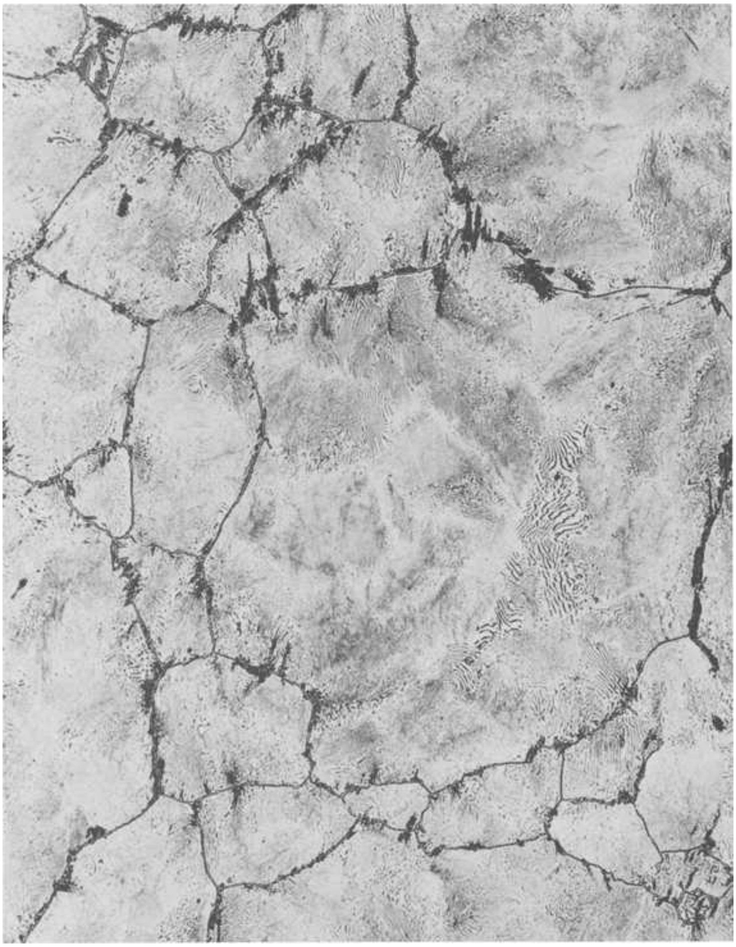

FIG. 4—*Continued:* (c) *photomicrograph of the specimen in Fig. 4, Part* a, *after electrolytic etching with alkaline sodium picrate, 6 V dc, 0.15 A/cm^2, for 1 min.*

a chart worth discussion. This chart illustrates untwinned grains that are either equiaxed or elongated (2 to 1 and 4 to 1) by cold working.

To employ the chart comparison method, the specimen is polished and etched in a manner consistent with the chart to be used. Each specimen should be rated at a number of blindly chosen locations (the fields are selected without viewing the image to prevent bias; the fields are spaced systematically around the specimen surface), at least five, and the average is computed and rounded to the nearest whole number. The operator should not attempt to choose "typical" fields for rating. Unbiased, blind field selection always produces the best results. If the structure is not uniform, the number of fields rated is increased.

Estimates are made by viewing the microstructure through the microscope eyepieces or on a projection screen, with views of the chart interspersed. First impressions of the equivalent chart photomicrograph or drawing are usually the best. Some of the charts may be available as eyepiece reticles so that the specimen and the standard can be viewed simultaneously. Plate I of ASTM Method E 112-82 can be obtained from ASTM as transparencies. These can be held next to the projected image or superimposed over the image, thus producing excellent ratings.

In general, the structure should be viewed at the same magnification as the chart. However, in the case of rather fine structures, higher magnifications can be used to advantage. If the grain structure is viewed at a magnification, M, where M is greater than the chart magnification, M_b, the true grain size number will be greater by a factor, Q, than the apparent grain size rating. The opposite is true if M is less than M_b, a situation that might be encountered when very coarse structures are rated. As an example of this procedure, suppose that the structure is viewed at ×500 and the apparent grain size is ASTM 5. To determine the correct grain size, the following relationship is employed

$$G = G_{\text{estimated}} + Q = G_{\text{estimated}} + 6.64 \log \frac{M}{M_b} \tag{8}$$

In our example, M is ×500 and M_b is ×100 (for most charts). Hence, Q is 4.64 and the ASTM grain size is 5 + 4.64 or 9.64 (rounded to 9.5 or 10).

Some laboratories use the comparison method to describe the distribution of grain sizes within a specimen—even in cases in which the structure is not duplex. In the case of a uniform grain structure, the sectioning plane produces an apparent spread of grain areas that will cover the average areas of three to four grain size numbers. If the structure is truly duplex, the amounts of each grain area and its grain size can be estimated by the use of comparison charts, although the accuracy of such estimates is dubious. For example, a certain structure exhibiting duplex grains might be rated as 70% ASTM grain sizes 7 to 8 and 30% ASTM 2 to 4. Apparent grain size distributions of this type cannot be converted by weighing procedures [*42*] to produce a meaningful average grain size number.

Fracture Grain Size Comparison Method

For evaluation of the prior austenite grain size in high-hardness, relatively brittle martensitic steels, particularly tool steels, the Shepherd fracture grain size comparison method can be utilized. In this method, a fractured specimen is compared with a set of ten standard graded fractures that correspond numerically to ASTM grain sizes 1 to 10. The technique was introduced by Arpi

[*19*] in 1931, but his set of five standard fractures was enlarged to ten by Shepherd [*20*] in 1934.

While the literature claims that all ten fractures are intergranular, only those of ASTM grain sizes 1 to 6 are intergranular. For fractures of the finer grain sizes, the amount of intergranular fracture decreases to zero as the grain size decreases, and is replaced by cleavage.

The Shepherd method cannot rate specimens with grain sizes finer than ASTM 10, as visual examination lacks the necessary sensitivity required to discern differences that may be present. Grain sizes coarser than ASTM 1 could be rated by extrapolation, but the need to do so for tool steels is rare. For best results, a flat fracture is needed; hence, a certain degree of brittleness in the material is necessary. Only martensitic structures can be rated by this method, as the fractures, when other structures are present (except for retained austenite), will yield coarser grain size estimates. Likewise, if the martensite is tempered sufficiently to increase its ductility, lower ratings will be obtained.

To use the method, as-quenched or lightly tempered tool steel specimens measuring about 7.6 cm (3 in.) long by 2.5 cm (1 in.) thick (size is not too critical) are fractured transversely. Longitudinal test fractures will produce acceptable results as long as inclusions, carbides, or alloy banding do not substantially alter the fracture appearance. Lightly tempered specimens may require notching and, perhaps, refrigeration to obtain a flat, featureless, brittle fracture.

To illustrate the method, Fig. 5 shows a series of fractured AISI 01 tool steel specimens austenitized at the recommended 802°C (1475°F) temperature and at 871, 982, and 1093°C (1600, 1800, and 2000°F) and oil quenched. Figure 5 shows the fractures at ×2¼ and ×500, lists the hardnesses and fracture grain size ratings, and shows the microstructures at ×500. Note that the specimen austenitized at 982°C (1800°F) has a partly intergranular fracture, while the specimen austenitized at 1093°C (2000°F) has a completely intergranular fracture.

If the test is applied to tempered specimens, the fracture grain size ratings will be reduced if the temper has noticeably increased ductility. For most tool steels, tempering at 204°C (400°F) will not impair the ratings, while somewhat higher tempering temperatures can be tolerated with the more highly alloyed grades.

Jeffries Planimetric Method

The planimetric method, suggested originally by Sauveur [*23*] and refined by Jeffries [*24,25*], has been used for many years to determine the number of grains per unit area. The method is generally employed by drawing a circle 79.8 mm in diameter (5000 mm^2) on a photomicrograph or on a transparency placed on the projection screen. The magnification is adjusted to provide at least 50 grains within the test area. A count is made of the number of grains completely within the area, n_1, and the number of grains intersecting the test circle, n_2. The total of $n_1 + n_2/2$ is multiplied by the Jeffries factor, f, for the magnification employed with the 79.8-mm-diameter circle to obtain an estimate of the number of grains per square millimetre.

$$N_A = f\left(n_1 + \frac{n_2}{2}\right) \tag{9}$$

The value of f for any magnification, M, is found by

$$f = \frac{M^2}{5000} \tag{10}$$

The average grain area, $\bar{A}$, is obtained from

$$\bar{A} = \frac{1}{N_A} \qquad \text{(in square millimetres)}$$

or

$$\bar{A} = \frac{10^6}{N_A} \qquad \text{(in square millimetres)} \tag{11}$$

while the mean grain "diameter," $\bar{d}$, is obtained from

$$\bar{d} = \bar{A}^{1/2} = \frac{1}{N_A^{1/2}} \qquad \text{(in millimetres)} \tag{12}$$

Note that the average grain "diameter," $\bar{d}$, is the length of a side of a square of average grain area, $\bar{A}$. Because the average planar grain shape is a hexagon [2,3] rather than a square, $\bar{d}$ is smaller than the caliper diameter of a hexagon of average grain area, $\bar{A}$, by about 19%.

The ASTM grain size number, G, can be found by using the data in Table 1 or by the following calculation

$$G = (3.322 \log N_A) - 2.95 \tag{13}$$

Values of $\bar{d}$, $\bar{A}$, and N_A as a function of G are listed in Columns 2, 6, and 8 of Table 1 (taken from ASTM Method E 112-82). Figure 6 illustrates the Jeffries method.

Figure 6 is a photomicrograph of an austenitic manganese steel specimen that was solution annealed at 1038°C (1900°F) and water quenched. The specimen was polished and etched with 2% nital for 5 s and then with 20%

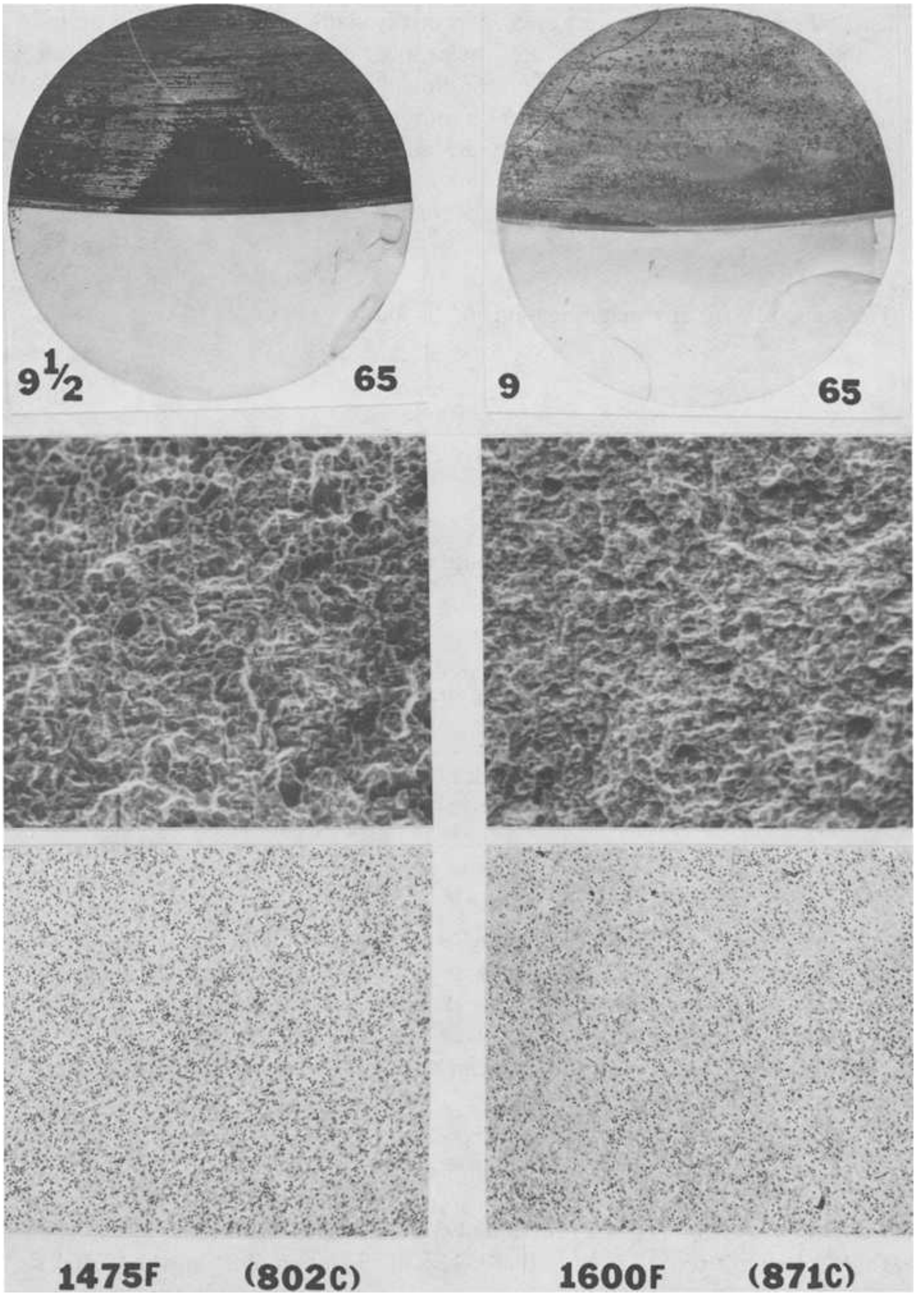

FIG. 5—*Illustration of fracture grain size ratings of oil-quenched AISI 01 tool steel (the ratings fracture appearance and microstructure after different austenitizing temperatures:* (top) *at*

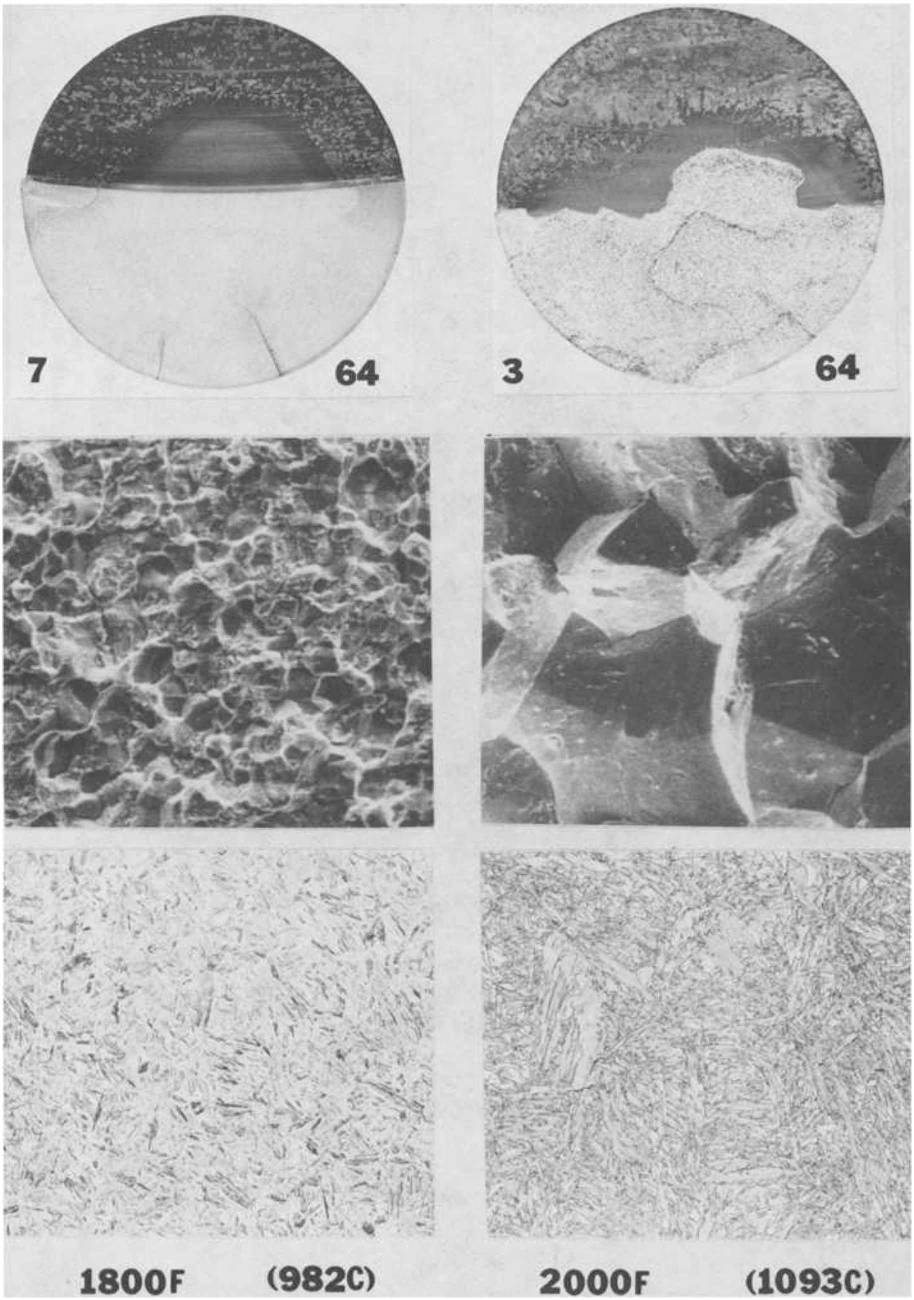

are at the left, and the HRC hardnesses are at the right under the fractures) showing the change in ×2¼; (middle) *at ×500;* (bottom) *at ×500, etched with 2% nital.*

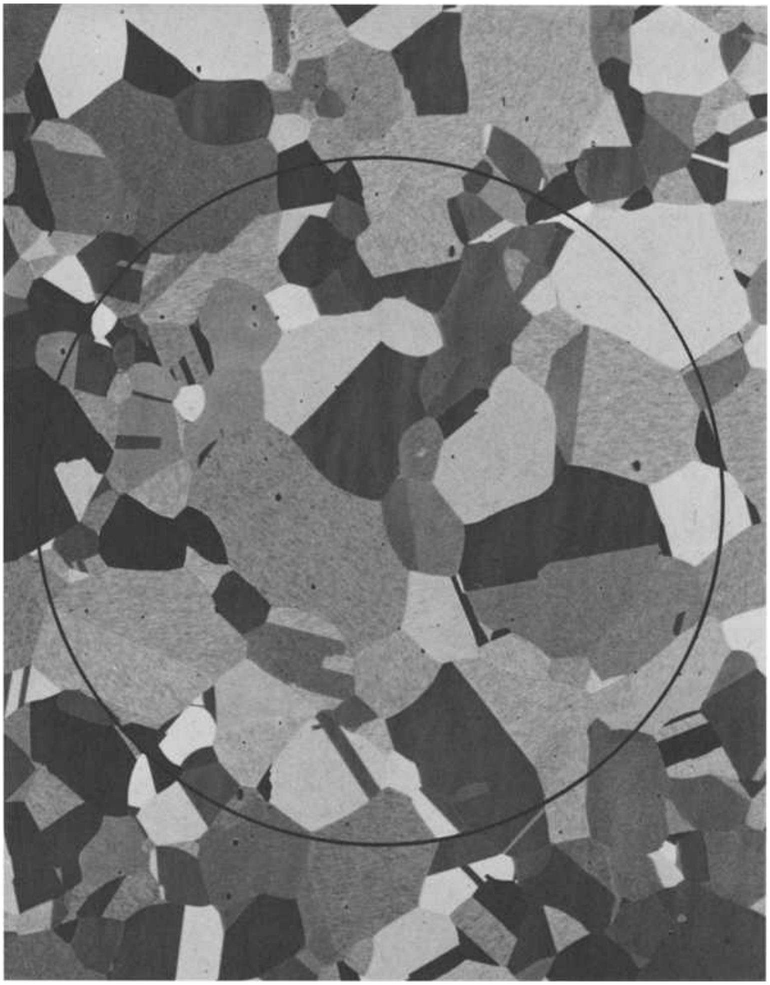

FIG. 6—*Photomicrograph illustrating grain size measurement using the Jeffries planimetric method. The method is described in the text.*

aqueous sodium metabisulfite for 20 s. The grains completely within the circle, n_1, were counted (43 in number), and the grains intersecting the circle, n_2, were counted (32 in number). The number of grains per square millimetre at ×1 was determined by using Eq 9, where f is 2 for the ×100 photomicrograph, and a 79.8-mm circle.

$$N_A = f\left(n_1 + \frac{n_2}{2}\right) = 2\left(43 + \frac{32}{2}\right) = 118\ \text{mm}^{-2} \quad \text{at} \times 1$$

Then, the ASTM grain size, G, was calculated using Eq 13

$$G = (3.322 \log N_A) - 2.95 = (3.322 \log 118) - 2.95$$

$$G = 3.9\ (\text{round to } 4)$$

To obtain good results, the grains must be marked off as they are counted to prevent miscounts. In most work, G is rounded to the nearest one-half unit.

Gokhale [46] has shown that the number of grains per unit area, N_A, is directly related to L_V, the total length of grain edges per unit volume by

$$L_V = 4N_A \tag{14}$$

Thus the ASTM grain size number, G, computed by the Jeffries procedure is related to the total grain edge length per unit volume.

An idea of the degree of grain size uniformity can be obtained by measuring the area of the largest observed grain, A_{max}, and dividing it by the average grain area, $\bar{A}$. For the tetrakaidecahedron grain shape model, the ratio of $A_{\text{max}}/\bar{A}$ is 1.856 for a uniform grain size distribution [45]. Hull and Houk [4] concluded that for actual grain shapes in metals, the ratio of $A_{\text{max}}/\bar{A}$ for a uniform grain size distribution is in the range of 1.8 to 2. The greater the degree of nonuniformity, the higher the ratio of $A_{\text{max}}/\bar{A}$.

Triple-Point Count Method

Although infrequently used, G can be estimated through the use of Euler's law [2]. A circle of known size, as in the Jeffries method, is drawn on a photomicrograph or on a transparency. The number of grain-boundary triple points, P, within the test area is counted. If a four-ray junction is observed (which is rare), it is counted as 2. The number of grains per unit area, N_A, is calculated from

$$N_A = \frac{\frac{P}{2} + 1}{A_T} \tag{15}$$

where A_T is the test area at ×1. An example of the use of this method is given in Fig. 7.

Figure 7 is a photomicrograph of an austenitic manganese steel specimen that was solution annealed at 1038°C (1900°F), water quenched, and then aged at 560°C (1040°F) for 1 h to decorate the grain boundaries with pearlite. (This is a companion specimen to the one shown in Fig. 6.) The number of grain boundary triple points within the test circle was counted and found to be 95. The photomicrograph is at ×100 magnification, and the circle has a diameter of 79.8 mm. Hence, the circle's true area is 0.5 mm². The number of grains per unit area, N_A, is

$$N_A = \frac{\frac{P}{2} + 1}{A_T} = \frac{\frac{95}{2} + 1}{0.5} = 97\ \text{mm}^{-2} \quad \text{at } \times 1$$

Next, the ASTM grain size, G, can be calculated using Eq 13

$$G = (3.322 \log N_A) - 2.95 = (3.322 \log 97) - 2.95$$

$$G = 3.7 \text{ (round to 4)}$$

As with the Jeffries method, this measure of grain size is dependent on L_V [*46*].

Heyn Intercept Method

The Jeffries method and the triple-point count method both require marking a photomicrograph or a plastic overlay to obtain accurate counts. Hence, both methods are rather slow. Greater speed with nearly equal accuracy can be obtained by using the intercept method [*26-28*], suggested by Heyn [*26*]. Because the test element is a line rather than an area, marking is not necessary for accurate counting. Grid overlays or reticles are perfectly suitable for use; hence, one does not need to work on photomicrographs.

In practice, a good grain size measurement can be made with this method in slightly more time than is required for a comparison chart rating, but with much greater accuracy. Nonequiaxed grains can also be evaluated to produce a measure of the elongation or to provide an average value. To measure elongation, straight test lines are used parallel and perpendicular to the deformation axis, while to determine an average value, the anisotropy can be averaged using circular test lines. The number of intercepts per unit length, N_L, is directly related to the ratio of the grain surface area to the volume, S_V, by

$$S_V = 2N_L \tag{16}$$

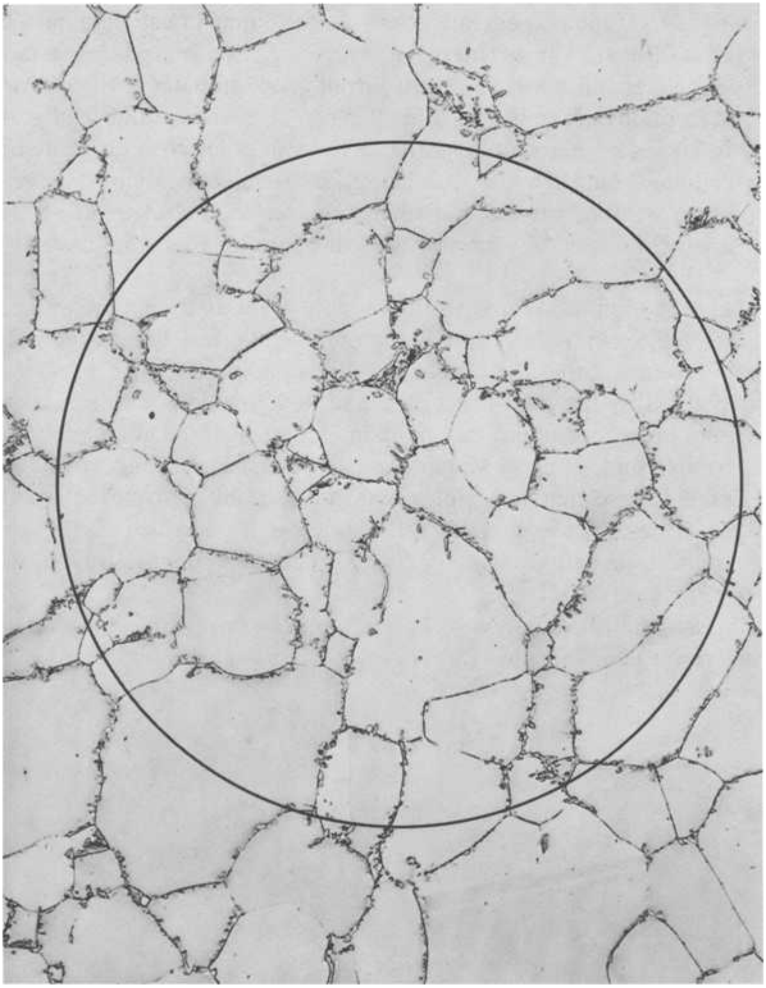

FIG. 7—*Photomicrograph illustrating the triple-point count method for measurement of grain size (etched with 2% nital). The method is described in the text.*

To use this method, a straight or curved line of a known length, L, is drawn on the photomicrograph, a clear plastic overlay, a ground glass projection screen, or an eyepiece reticle. The magnification is adjusted so that the grain boundary intersections with the test line are clearly visible. Either the number of grains intercepted by the line, N, or the number of grain boundary intersections with the line, P, can be counted. For single-phase structures, the latter count is preferred, while, for multiphased alloys, the former is easier. The total test line length (500 mm is generally used) and the magnification should be chosen so that 70 to 150 grain interceptions, N, or grain boundary intersections, P, per field are obtained. This will permit good estimates of the number of grain interceptions per unit of test line length, N_L, or the number of grain boundary intersections per unit length, P_L. The values for N_L and P_L are obtained by dividing N and P by L/M, where M is the magnification. If a circular test pattern is used, the circle diameter should be several times greater than the largest grains within the test area to minimize bias from a circular test line.

If parallel or randomly oriented straight test lines are used, and the number of grain interceptions, N, is counted, the ends of the test lines usually fall within grain interiors rather than exactly at a grain boundary. The number of grains intercepted by the lines is counted and, if a line ends within a grain, each end point is counted as one half of an interception. If the grain boundary intersections are counted using straight or curved test lines, tangent hits are counted as one intersection and triple-point intersections are counted as two. Multiphased structures are counted differently, as is described further on. For a single-phase structure, counting N or P yields equivalent results, differing, at most, by one.

For a single-phase structure, $N_L = P_L$ and either counting procedure can be used to determine G. The values for N_L and P_L are calculated by

$$N_L = \frac{N}{\frac{L_T}{M}}$$

and

$$P_L = \frac{P}{\frac{L_T}{M}} \tag{17}$$

where L_T is the total test line length, and M is the magnification. The mean lineal intercept (mean intercept length), $\bar{L}_3$, is determined by

$$\bar{L}_3 = \frac{1}{N_L} = \frac{1}{P_L} \tag{18}$$

These relationships are valid for single-phase grain structures but not for multiphased structures. Columns 4 and 5 of Table 1 show the relationship between $\bar{L}_3$ and N_L and G (Column 1). Note that for each unit increase in G, $\bar{L}_3$ decreases by $1/(2)^{1/2}$, a geometric progression. G may also be calculated from

$$G = (-6.6457 \log \bar{L}_3) - 3.298 \tag{19}$$

where $\bar{L}_3$ is in millimetres. The average grain "diameter," $\bar{d}$, is about 12.5% greater than the mean lineal intercept, $\bar{L}_3$, for the same grain size. If enough fields are measured, G can be estimated to the nearest one tenth of a unit.

By combining Eqs 16 and 18, we obtain

$$\bar{L}_3 = \frac{2}{S_V} \tag{20}$$

Thus the ASTM grain size, G, calculated from the mean lineal intercept, $\bar{L}_3$, is related to the total grain boundary surface area per unit volume, S_V. Hence, in this measurement, G is based on a different geometric microstructural characteristic than is used in the Jeffries and the triple-point count methods [*46*]. Some difference may be expected in the values of G determined by these different methods.

An idea of the grain size uniformity can be obtained by dividing the diameter of the largest observed grain, $L_{\max}$, by the mean lineal intercept, $\bar{L}_3$. For the tetrakaidecahedron grain shape model, the theoretical ratio of $L_{\max}/\bar{L}_3$ is 1.872 for a uniform grain size distribution [*45*]. The greater the degree of nonuniformity in the grain size distribution, the greater this ratio.

The relationship between G and $\bar{L}_3$ was first shown in ASTM Method E 89. This standard suggested making intercept counts on two sets of perpendicular test lines to yield two estimates, N_{L1} and N_{L2} (in this case at Magnification M rather than at ×1), to calculate the number of grains per square inch at ×100 (the line lengths were in inches)[3] from

$$N_A (\text{at} \times 100, \text{in.}^2) = 0.8 \left(\frac{M}{100} \right)^2 N_{L1} N_{L2} \tag{21}$$

This relationship was stated in ASTM Method E 112 when it was first issued, but the current procedure used in that standard to relate $\bar{L}_3$ to G is based on the average intercept width of a circular grain of average area, $\bar{A}$, calculated from Eq 11. The relationship between $\bar{L}_3$ and $\bar{A}$ for a circular grain section is

$$\bar{L}_3 = \left(\frac{\pi}{4} \bar{A} \right)^{1/2} \tag{22}$$

The mean lineal intercept of polygonal grains is slightly larger than this value (0.52%) and is decreased by grain anisotropy and increased as the range of section sizes increases. The difference between $\bar{L}_3$ calculated using Eq 21 and that using Eq 22 is very small.

To develop an average grain size, a circular test line is preferred, as was first suggested by Hilliard [*27*] and later expanded to three concentric circles by Abrams [*28*]. This latter test grid has been adopted by ASTM Method E 112 and is now the preferred referee method for grain size measurements. The three circles have diameters of 79.58, 53.05, and 26.53 mm for a total circumference of 500 mm. Tick marks are placed at the north pole of each circle for reference in counting. This template can be obtained from ASTM. If the number of grain interceptions or intersections is low, the circular test grid will overestimate $\bar{L}_3$. Hence, the magnification should be adjusted to provide from 70 to 150 P or N counts per field. Again, the field selection should be done blindly to prevent bias. Five fields, or a total of about 500 intercepts or intersections, generally provides reasonable statistical accuracy unless the grain structure is nonuniform. The standard deviation of five field measurements is an indicator of the uniformity. Additional fields can be measured if greater accuracy is required. Figure 8 illustrates the intercept method of grain size measurement.

Figure 8 is a photomicrograph of a specimen of austenitic AISI 304 stainless steel etched using the method of Bell and Sonon to suppress the annealing twins (60% aqueous nitric acid, platinum cathode, 0.6 V dc, 20°C, 2 min) at ×100. The ASTM three-circle intercept test grid is shown, for which the total line length is 500 mm. The grain boundary intersections have been counted and found to be 75 in number. The number of intercepts per unit length, N_L, is determined by using Eq 17

$$N_L = \frac{N}{\dfrac{L_T}{M}} = \frac{75}{\dfrac{500}{100}} = 15\,\mathrm{mm}^{-1} \quad \text{at} \times 1$$

Then, the mean lineal intercept, $\bar{L}_3$, is calculated using Eq 18

$$\bar{L}_3 = \frac{1}{N_L} = \frac{1}{15} = 0.067\mathrm{mm}$$

The ASTM grain size, G, is found using equation 19

$$G = (-6.6457 \log \bar{L}_3) - 3.298 = (-6.6457 \log 0.067) - 3.298$$

$$G = 4.5$$

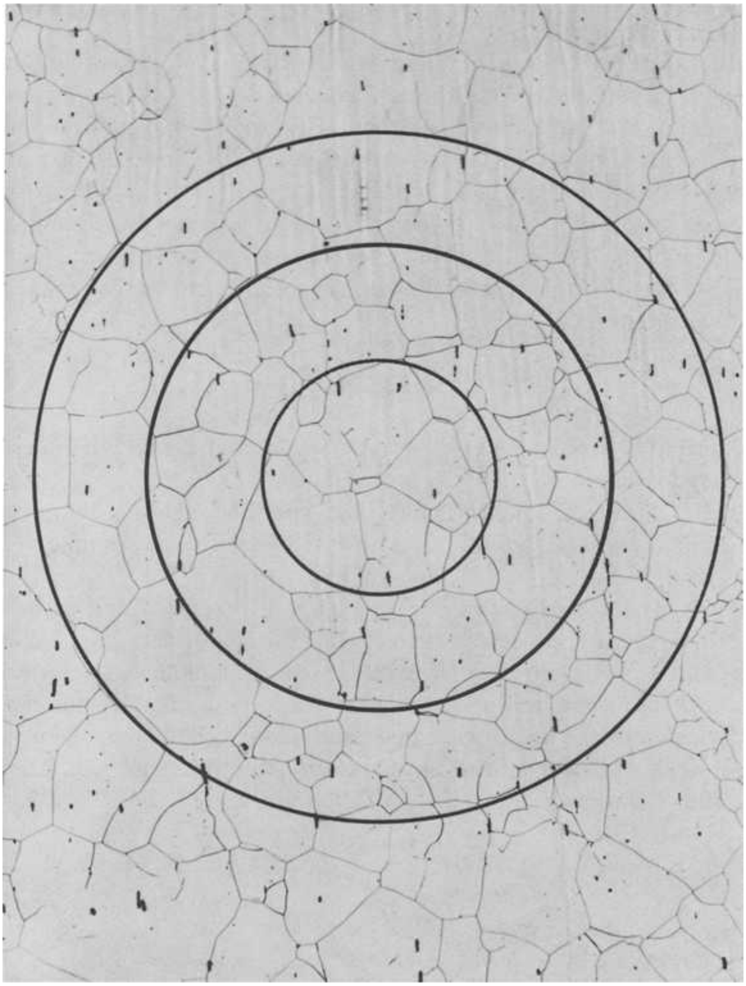

FIG. 8—*Photomicrograph illustrating the intercept method of grain size measurement. The method is described in the text.*

Snyder-Graff Intercept Count Method

The prior austenite grain size of high-speed tool steels is generally in the range of ASTM 9 through 13, for which the fracture grain size method is insensitive. Over this range, the number of grains per unit area changes by a factor of 16, while the mean lineal intercept is reduced from 14.1 to 3.54 μm. To obtain greater measurement sensitivity, Snyder and Graff [*29*] developed a modified intercept method in 1938.

The prior austenite grain boundaries of many high-alloy tool steels can be revealed with nital (2 to 10%) in the as-quenched or lightly tempered conditions. The addition of 10% hydrochloric acid (HCl) to 3% nital has been shown to improve grain boundary delineation. In this test, the structure is usually viewed at ×1000. A 127-mm (5-in.) test line is drawn on a ground glass projection screen and used as the test element. A count is made of the number of grains intercepted by the line, N, and the average of ten such counts, $\bar{N}$, is the Snyder-Graff intercept grain size number. The equivalent ASTM grain size number can be determined from

$$G = (6.635 \log \bar{N}) + 2.66 \qquad (23)$$

The relationship between $\bar{N}$ and G shown by Snyder and Graff [*29*] is in error. To convert $\bar{N}$ to a mean lineal intercept length, multiply $\bar{N}$ by 7.874 to give $\bar{N}_L$ as the number of interceptions per millimetre, and then take the reciprocal of $\bar{N}_L$ to obtain $\bar{L}_3$, and calculate G using Eq 19 or Table 1. An example of this method is given in Fig. 9.

Figure 9 is a photomicrograph of a specimen of quenched and tempered AISI M2 high-speed tool steel etched with nital at ×1000. Two 127-mm (5-in.) test lines have been drawn on the photomicrograph to illustrate the method. In actual work, ten measurements would be used. The number of grains intersected by the lines was counted and found to be 13 on one line and 14 on the other line. Hence, the Snyder-Graff intercept grain size number would be 13.5. To find the equivalent ASTM grain size, G, Eq 23 is used

$$G = (6.635 \log S\text{-}G) + 2.66 = (6.635 \log 13.5) + 2.66$$

$$G = 10.2 \text{ (round to 10)}$$

Nonequiaxed Grain Structures

If the grains have been noticeably deformed by processing, measurements should be made on transverse, longitudinal, and planar (rolling plane) surfaces in relation to the deformation axis. Either the planimetric or the intercept method may be employed, although the latter is preferred because it provides additional information. If the Jeffries method is used to obtain N_A on each of

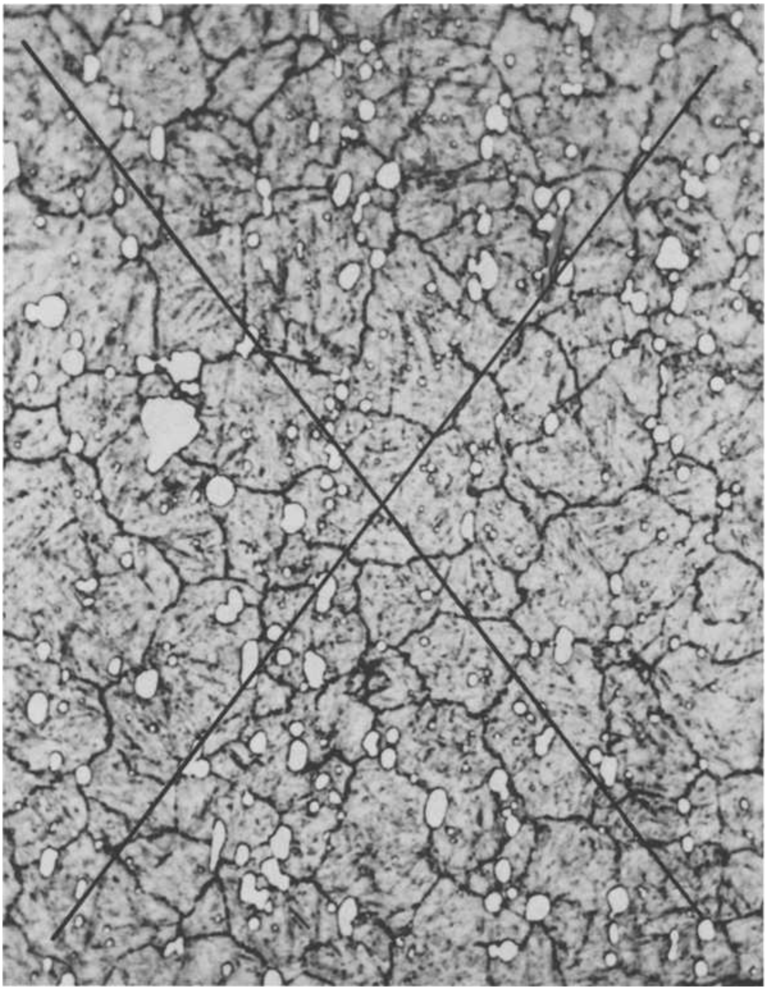

FIG. 9—*Photomicrograph illustrating the Snyder-Graff intercept method for measurement of the grain size of high-speed tool steels.*

the three principal planes, N_{At} (transverse), N_{Al} (longitudinal), and N_{Ap} (planar), the grain size is obtained by computing an average of these three values, $\bar{N}_A$

$$\bar{N}_A = (N_{At} \cdot N_{Al} \cdot N_{Ap})^{1/3} \tag{24}$$

and G is determined from Eq 13 or Table 1.

If the intercept method is employed, straight test lines are recommended with their orientations mutually perpendicular to each other on the three principal planes:

(*a*) N_{Lt}, perpendicular to the spread, that is, in the short-transverse direction,

(*b*) N_{Ll}, parallel to the deformation direction, and

(*c*) N_{Lp}, perpendicular to the deformation direction.

To determine the grain size, an average intercept value, $\bar{N}_L$, is calculated

$$\bar{N}_L = (N_{Lt} \cdot N_{Ll} \cdot N_{Lp})^{1/3} \tag{25}$$

and used to obtain $\bar{L}_3$ (Eq 18) and G (Eq 19 or Table 1).

Duplex Grain Structures

Duplex grain structures (a mixture of two grain size distributions) are occasionally observed in partially recrystallized specimens or at the onset of rapid grain growth. Such structures exhibit a bimodal distribution of grain areas, diameters, and intercept lengths. Two types of duplex structures may be encountered. One type exhibits agglomerations of small grains within a matrix of large grains, or vice versa, while the other type exhibits a more continuous dispersion of coarse or fine grains throughout the structure.

If the duplex condition is agglomerated, analysis is rather straightforward. The percentage of fine and coarse grains is determined by point counting [ASTM Recommended Practice for Determining Volume Fraction by Systematic Manual Point Count (E 562-83)]. Then, the grain size within each distinct region is determined by intercept measurements. The magnification and test grid size or type must be adjusted to permit grain size measurements within the areas (chosen selectively rather than blindly). The percentage and grain size of each distinct region can be expressed in this way.

Analysis is more difficult when the duplex structure is well dispersed throughout the specimen. The duplex condition can only be revealed by developing the distribution of grain areas, diameters, or intercept lengths. This type of measurement is tedious when done manually but can be automated. ASTM Committee E-4 on Metallography is currently developing a procedure for such measurements. Underwood[4] (unpublished research) has suggested an intercept frequency distribution that can be done manually or with semiautomatic tracing devices. For this measurement, a grid consisting of a number of parallel straight test lines spaced 5 mm apart is superimposed over the structure using four orientations: 0, 45, 90, and 135°. The intercept lengths are measured and summarized for each orientation according to class intervals of length.

This method is illustrated for the duplex nickel-base superalloy grain structure shown in Fig. 10, a rather extreme example of a duplex structure. Two such fields were enlarged about two times (×106). The grids were applied at the four orientations and the measurements were grouped into 5-mm class intervals, as shown in Table 2. The data for each orientation were averaged, as listed in Column 6 of Table 2. Next, the intercept length per class interval was calculated, as shown in Column 7. Then, the percentage of intercept length per class was calculated (Column 8). These data were separated into two regions, coarse and very coarse, after inspection of the frequency data.

In each region, the number of intercepts and the intercept length were calculated. The volume fractions of the coarse and very coarse regions were determined by dividing the intercept length in each region by the total intercept length. The intercept length in each region was divided by the magnification to obtain the true total intercept length in each region. The number of intercepts in each region was divided by the true intercept length in each region to give N_L for each region. Then, $\bar{L}_3$ and G were calculated for each region. For the data in Table 2, the results are as follows:

Parameter	Coarse Grain Region	Very Coarse Grain Region
Volume fraction, %	85.4	14.6
N_L, mm^{-1}	14.1	1.95
$\bar{L}_3$, mm	0.0709	0.513
ASTM grain size, G	4.3	~00

The data in Table 2 have been plotted in Fig. 11 to illustrate the distribution of intercepts. This illustration provides an example of one possible way to handle duplex grain structures. More work on this problem is required before a practice can be standardized.

---

[4] Underwood, E. E., Georgia Institute of Technology, "Procedure to Estimate Parameters of a Duplex Grain-Size Microstructure," personal communication to ASTM Subcommittee E04.08 on Grain Size, a subcommittee of ASTM Committee E-4 on Metallography, 16 August 1980.

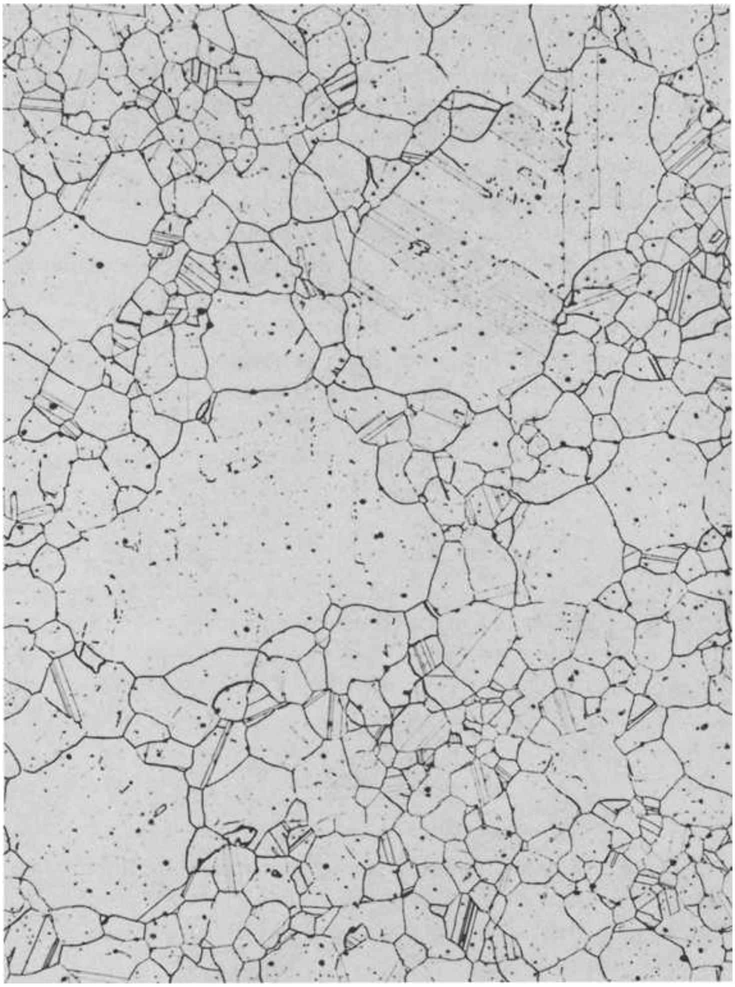

FIG. 10—Photomicrograph showing a duplex grain structure in Pyromet 31 nickel-base superalloy etched with Kalling's No. 2 etchant, at ×50 (one of two areas analyzed).

TABLE 2—*Data and analysis of a duplex grain size specimen.*[a]

Class Interval, mm	Counts per Orientation					Intercept Length/ Class, mm	Intercept Length/ Class, %
	0°	45°	90°	135°	Average		
			COARSE GRAINS				
0 to 5	144	148	153	160	151.25	378.125	7.83
5 to 10	180	199	209	203	197.75	988.75	20.46
10 to 15	115	109	107	114	111.25	1112.5	23.02
15 to 20	48	46	51	55	50	750	15.52
20 to 25	24	23	25	15	21.75	435	8.8
25 to 30	9	11	12	11	10.75	268.75	5.56
30 to 35	3	1	4	6	3.5	105	2.17
35 to 40	4	2	2	2	2.5	87.5	1.81
			VERY COARSE GRAINS				
40 to 45	4	6	1	1	3	120	2.48
45 to 50	2	2	3	1	2	90	1.86
50 to 55	2	4	3	2	2.75	137.5	2.85
55 to 60	2	1	1	1	1.25	68.75	1.42
60 to 65	0	2	1	0	0.75	45	0.93
65 to 70	3	0	1	0	1	65	1.35
70 to 75	0	0	2	1	0.75	52.5	1.09
75 to 80	0	0	0	2	0.5	37.5	0.78
80 to 85	0	0	0	0	0	0	0
85 to 90	0	0	0	2	0.5	42.5	0.88
90 to 95	0	0	1	0	0.25	22.5	0.47
95 to 100	0	0	0	0	0	0	0
100 to 105	0	0	0	1	0.25	25	0.52
Total	540	554	576	577	561.75	4831.875	99.8

[a] Measurement data:

Coarse grain region:

L_T = 4125.625 mm at ×106 = 38.91 mm
$\bar{N}_L$ = 548.75/38.91 = 14.1 mm^{-1}
$\bar{L}_3$ = 1/14.1 = 0.07093 mm
G = 4.3
V_V = (4125.625/4831.875) · 100 = 85.4%

Very coarse grain region:

L_T = 706.25 at ×106 = 6.663 mm
$\bar{N}_L$ = 13/6.663 = 1.951 mm^{-1}
$\bar{L}_3$ = 1/1.951 = 0.513 mm
G ≈ 00
V_V = (706.25/4831.875) · 100 = 14.6%

Intercept data:

	Number of Intercepts, mm	Sum of Intercept Lengths, mm
Coarse region	548.75	4125.625
Very coarse region	13	706.25
Total	561.75	4831.875

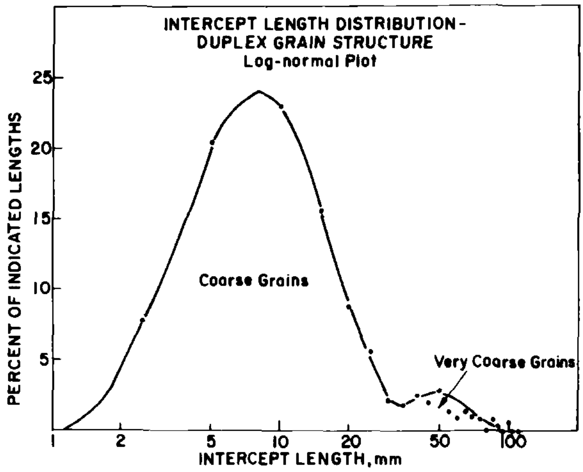

FIG. 11—*Semilogarithmic frequency distribution curve of the intercept lengths in the duplex austenitic superalloy photomicrograph shown in Fig. 10 (plus another field not shown).*

Multiphased Structures

If a specimen contains more than one phase, the previously described methods must be modified. For such specimens, the matrix phase, one particular phase, or several phases may be measured for grain size, as desired. If the amount of the second phase is less than a few percentage points and the second phase is confined to the grain boundaries of the matrix phase, the methods just described can be used without appreciable error. However, when more than a few percentage points of a second phase is present, the previous methods must be modified. The Jeffries method could be employed for such measurements, but manual implementation of this technique is inconvenient, although the method is adaptable to image analysis. The number of grains of interest within the test area and those intersecting the test perimeter are counted as before, but the percentage of the test area covered by the phase must be determined.

The intercept method can be readily used with both manual and automated measurements. First, the volume fraction of the phase of interest, $V_{V\alpha}$, is determined by point counting (ASTM Recommended Practice E 562-83) or by other methods. Next, the three-circle test grid is used to determine the number of matrix grains intercepted by the test lines, N_α. Alternatively, a count can be made of the number of α-α and α-β grain and phase boundaries to obtain P_L, which is twice N_L for multiphase structures. The mean lineal intercept length of the matrix (α) phase, $\bar{L}_{3\alpha}$, is calculated from

$$\bar{L}_{3\alpha} = \frac{V_{V\alpha} \cdot \frac{L_T}{M}}{N_\alpha} \tag{26}$$

where L_T is the total test line length, and M is the magnification. G is then found in Table 1 or by the use of Eq 19. An example of this measurement is given in Fig. 12.

Figure 12 is a photomicrograph of annealed AISI 4140 alloy steel containing ferrite and pearlite. Three concentric circles with a total line length of 500 mm have been drawn on the photomicrograph for intercept counting. The amount of ferrite was first determined by point counting and found to be 49.4%. Then, the number of ferrite grains intercepted by the three lines was counted and found to be 96. The mean lineal intercept of the ferrite phase, $\bar{L}_{3\alpha}$, is calculated using Eq 26

$$\bar{L}_{3\alpha} = \frac{V_{V\alpha} \cdot \frac{L_T}{M}}{N_\alpha} = \frac{0.494 \frac{500}{200}}{96} = 0.0129\text{mm}$$

The ASTM grain size, G, is calculated using Eq 19

$$G_\alpha = (-6.6457 \log \bar{L}_{3\alpha}) - 3.298 = (-6.6457 \log 0.0129) - 3.298$$

$$G_\alpha = 9.3 \text{ (round to 9)}$$

Grain Size Distributions

Development of the three-dimensional, spatial grain size distribution to obtain N_V and $\bar{V}$ is a very tedious procedure if done manually but rather straightforward if done with the aid of image analyzers. Most of the methods developed [*31-39,44,47-49*] assume some simple grain shape, such as a sphere, and a uniform grain size to simplify calculations. A few methods have been based on other grain shape models, such as the tetrakaidecahedron. The grain size (planar) distribution is developed by measurements of grain areas, diameters, or chords (intercept lengths). The data are grouped into size classes, and corrections are applied to account for the sectioning plane influence. This permits calculation of the spatial grain size distribution, that is, N_{Vi}, for each size class, which is totalled to obtain N_V, the number of grains per unit volume. The average grain volume, $\bar{V}$, is the reciprocal of N_V. One can then calculate either an arithmetic mean grain diameter or a geometric mean grain diameter. The latter is preferred, since the grain size distribution is log normal.

These indirect methods, because of the assumptions made regarding grain shape, grain size uniformity, and the sectioning plane corrections, are not precise estimators of N_V. Intercept methods are less reliable than grain area methods, and the number of class intervals influences the results [*34*]. The serial sectioning method [*40,41*] provides a method for direct determination of N_V. Application of this method requires considerable skill and is exceptionally challenging for fine-grained structures.

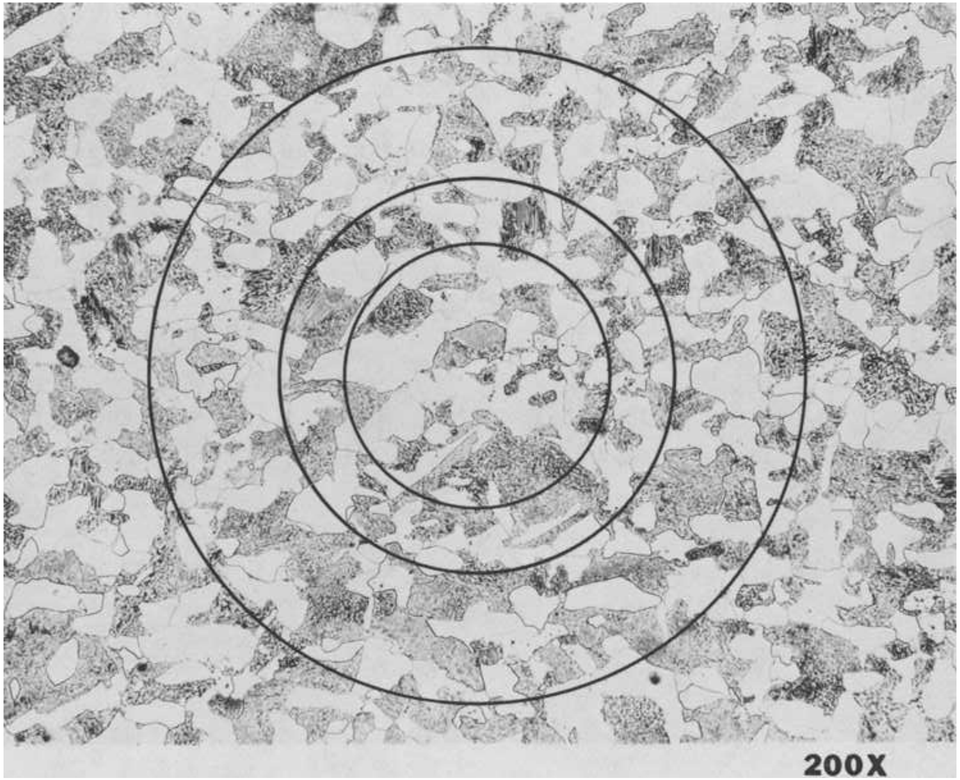

FIG. 12—*Photomicrograph illustrating the grain size measurement of a specimen containing two constituents, using the intercept method combined with point counting. The method is described in the text.*

Estimation of $\bar{D}$

Several studies have developed simple relationships between the mean lineal intercept, $\bar{L}_3$, and the mean true volumetric grain diameter, $\bar{D}$. These conversions are based on grain shape models, for example, spheres or tetrakaidecahedra. Fullman [*50*], using spheres of uniform size in a microstructure, showed that $\bar{D} = 1.5\,\bar{L}_3$. ASTM Method E 112-82 has based its N_V data (Table 1) on this relationship. For this relationship, the average grain volume, $\bar{V}$, is $1.7671\,\bar{L}_3$, and N_V is calculated from the relationship

$$N_V = 0.5659\,N_L^3 \tag{27}$$

Derivations in which the tetrakaidecahedron is used for the grain shape model have produced several similar equations: $\bar{D} = 1.68\,\bar{L}_3$ [*51*], $\bar{D} = 1.74\,\bar{L}_3$ [*52*], and $\bar{D} = 1.776\,\bar{L}_3$ [*45*]. The differences arise because of the assumptions made by each researcher. The reliability of such correlations has not been proven and they should be viewed as approximations subject to error.

Estimation of N_V

In addition to the derivations just described, several experimenters have shown that measurements of N_A and N_L can be used to estimate N_V for equiaxed single-phase grain structures. Rutherford et al [*53*] estimated N_V as a function of G using the Kelvin truncated octahedron grain shape model. Their values of N_V were about 8% lower than the current values listed in ASTM Method E 112-82 (Table 1), calculated by Eq 27. Underwood [*49*] has used this grain shape model to equate N_V with N_A and N_L measurements

$$N_V = 0.744\,\frac{N_A^2}{N_L} \tag{28}$$

Hanson [*54*] developed an equation by computer modeling that produces estimates of N_V similar to (slightly higher than) those from Eq 28. His equation is

$$N_V = \left[\frac{2.4150}{N_A^{1/2}} - \frac{1.4552}{N_L}\right]^{-3} \tag{29}$$

Warren and Durand [*39*] developed a general equation for estimating N_V by computer modeling structures of different types and shapes. Their equation is

$$N_V \approx \frac{\pi N_A^2}{4N_L} + \left(\frac{\pi N_A^3}{6V_V}\right)^{1/2} - \frac{16N_L^3}{9\pi V_V^2} \tag{30}$$

This equation produces estimates of N_V for single-phase grain structures that are somewhat lower than those obtained by Eqs 28 and 29. The accuracy of these equations has not been proven and they should be viewed as approximations.

Grain Size by Image Analysis

Grain size can be determined by using image analyzers and semiautomatic tracing devices in most of the techniques that have been described. However, greater attention must be given to specimen preparation than is necessary for manual analysis; that is, the quality of grain boundary delineation must be very high. Grain contrast etchants, such as those used in Fig. 6, cannot be employed. When measuring the grain size of austenitic alloys that contain annealing twins, such as those shown in Figs. 1 and 10, the etching of twin boundaries must be suppressed by special etching techniques, as shown in Fig. 8. Such etching techniques do not exist for all alloys. Complete grain boundary delineation in austenitic alloys, irrespective of twin etching, is difficult to obtain. In some cases, the alloy can be aged to precipitate a second phase at the grain boundaries, as shown in Fig. 7, which makes the grain boundaries more easily revealed by etching.

In many instances, it is necessary to edit the image in order to obtain complete grain boundary delineation and to delete other detected features that would alter the measurement. After image cleaning, the detected image, that is, either the grain boundaries or the grain interiors, can be measured. Depending on the technique employed, the grains intersecting the live frame border can influence the measurement accuracy. If N_A is to be measured, the grains touching the live frame should be deleted from the image so that only whole grains are counted. The area that these grains (those within the live frame) occupy can be found by combining the detected and undetected images. If two phases are present, the volume fraction of the grains of interest is determined and this value is multiplied by the number of grains in the measurement area and then divided by the measurement area. The lowest magnification at which the grains can be clearly separated should always be used to ensure the best statistical data.

Intercept techniques can also be employed by counting the number of grain boundary intersections with scan (horizontal) lines of known length and number. To eliminate anisotropy effects, the image should be rotated or scan lines of several orientations can be used. Alternatively, for single-phase grain structures, one can measure the length of the grain boundaries per unit area, L_A, and divide by $\pi/2$ to obtain P_L and then $\overline{L}_3$.

Another technique is to detect only the grain interiors of the phase of interest and measure chord lengths. The average chord length is equal to $\overline{L}_3$. Again, it is best to rotate the image or the scan lines and to delete those grains intersecting the live frame border (to prevent undersizing of these grains). This type of procedure can be employed with two-phase structures without the need to correct for the volume fraction.

Accuracy of Grain Size Estimates

Hilliard [*42*] described three types of errors that can influence grain size estimates. The first arises from experimental limitations, for example, limited resolution, poor grain boundary delineation, overetching, inaccurate test line length measurement, miscounting, and so forth. It is difficult to assess the extent of these errors except by replication of the tests at different times and by different operators. Rigorous attention to technique is needed to control the sources of these errors. Resolution problems become more acute as the grain size decreases. The second error type is due to improper sampling. All the fields should be chosen blindly to prevent operator bias. The third error type arises from the representativeness of the chosen areas and the specimens to the entire material. The last two error types are usually the greatest sources of error [*42*].

To obtain the best estimate of the grain size, the most efficient method must be chosen, that is, the technique that gives the best accuracy for the least effort. The most efficient method can be determined from the magnitude of the errors and the analysis time. Errors of the first type are difficult to determine; however, sampling errors can be assessed from the standard deviation of the field measurements on the specimen and from comparisons with data from other specimens from the same material. While the population standard deviation, σ, cannot be determined, the standard deviation of the observations, s, approaches that of the population as the number of measurements, N, increases. As N increases, s decreases.

The standard deviation of the observations, s, is calculated by

$$s = \left[\frac{\Sigma (X_i - \bar{X})^2}{N - 1} \right]^{1/2} \tag{31}$$

where $\bar{X}$ is the mean value of the individual measurements, X_i. The standard deviation is an absolute measure of the data dispersion, but if the mean values of different measurements differ significantly, it is difficult to compare standard deviations. The standard deviation can be normalized by dividing by the mean value and expressing this ratio as a percentage. This ratio, the coefficient of variation (CV) is

$$\text{CV} = \frac{s}{\bar{X}} \cdot 100 \tag{32}$$

Many workers prefer to calculate the 95% confidence limit and the percentage of relative accuracy of the measurements to assess accuracy. The 95% confidence limit (CL) is calculated by

$$95\%\ \text{CL} = \frac{t \cdot s}{(N - 1)^{1/2}} \tag{33}$$

where t varies with the number of measurements and the confidence level chosen. Table 3 lists values of t for computing the 95% confidence limit as a function of N. The data are expressed by citing the mean value followed by plus or minus (±) the confidence limit.

The percentage of relative accuracy, (RA) is obtained by dividing the 95% CL by the mean and multiplying by 100. For most work, a 10% relative accuracy is adequate. If the initial measurement produces a value substantially higher, it is a good practice to make additional measurements. In general, to reduce the relative accuracy by half, four times as many measurements must be made.

Hilliard [*42*] examined the accuracy of the lineal analysis method. If N is the number of "events," that is, counts, and $s(N)$ is the standard deviation of the counts made on different fields, the ratio of $s(N)/\bar{N}^{1/2}$ will be constant if the counts are independent of each other. Hilliard found that this ratio was 0.62 if the diameter of the test circle used for the intercept count was several times as large as the average grain diameter. Hilliard showed that the average number of intercepts counted determined the relative error

$$\frac{s(\bar{L}_3)}{\bar{L}_3} = 0.62 \frac{1}{\bar{N}^{1/2}} \tag{34}$$

The standard deviation of the grain size number, based on the average number of intercepts, was calculated from

$$s(G) \approx \frac{1.8}{\bar{N}^{1/2}} \tag{35}$$

TABLE 3—*List of* t *values for calculating the 95% confidence limits.*

n'^a	t	n'^a	t
1	12.706	18	2.101
2	4.303	19	2.093
3	3.182	20	2.086
4	2.776	21	2.080
5	2.571	22	2.074
6	2.447	23	2.069
7	2.365	24	2.064
8	2.306	25	2.060
9	2.262	26	2.056
10	2.228	27	2.052
11	2.201	28	2.048
12	2.179	29	2.045
13	2.160	30	2.042
14	2.145	40	2.021
15	2.131	60	2.000
16	2.120	120	1.980
17	2.110	∞	1.960

[a] The degrees of freedom, n', is $N - 1$.

If plus or minus twice the standard deviation is to be less than half a G unit, about 200 intercepts must be counted. This relationship applies to equiaxed structures.

Pereira da Silva [45] and Woodhead [55] performed a similar study of the accuracy of the Jeffries method. For grain counts, the ratio of $s(N)/\bar{N}^{1/2}$ was 1.03 ± 0.06, that is

$$\frac{s(\bar{N}_A)}{\bar{N}_A} = 1.03\frac{1}{\bar{N}_A^{1/2}} \tag{36}$$

The standard deviation of G [55] is

$$s(G) \approx \frac{1.49}{\bar{N}_A^{1/2}} \tag{37}$$

For the same coefficient of variation, about three times as many grains must be counted as intercepts, but the standard deviation of G is smaller.

Hilliard [42] has shown that for a single measurement field, the Jeffries method produces a lower standard deviation than the intercept method. However, because the Jeffries method is much slower, for equal measurement accuracy, about 60% more time is required for it than for the intercept method. Consequently, the intercept method is more efficient than the Jeffries method.

As an example of an error specific to image analysis, the influence of grains intersecting the frame border was assessed using the measurement of chord lengths in the grain interiors to calculate an average chord length, equivalent to $\bar{L}_3$. If the grains intersecting the frame are not deleted from the measurement field, $\bar{L}_3$ will decrease with increasing magnification. To illustrate this problem, the austenitic stainless steel specimen shown in Fig. 8 (only one field was measured in this specimen; the grain size was rather variable) was measured without deleting the grains touching the border. Three different microscope objectives were used. The grain size of this specimen was rather coarse, and the use of such a procedure produced an error which increased as the number of grains in the measurement field decreased. The following results were obtained:

Objective	$\bar{L}_3$, μm	G
×8	48.3	5.45
×16	45.1	5.65
×32	40.7	5.94

The same specimen was analyzed manually with the ASTM three-circle test grid at different magnifications. The results agree fairly well with the ×8 objective image analysis results at all of the magnifications employed, as shown here:

Screen Magnification	Number of Fields	Mean Number of Intercepts	Relative Accuracy, %	$\bar{L}_3$, μm	G
×100	5	97.4	7.6	51	5.3
×200	10	46.6	8.6	54	5.1
×500	20	18.8	11.1	53	5.2
×1000	40	10.4	13.1	48	5.5

Because of the field-to-field measurement variability at high magnifications, the number of fields measured was increased to keep the relative accuracies reasonably similar. The agreement in G at the higher magnifications is good despite the fact that the number of intercepts counted per field was lower than that recommended in ASTM Method E 112-82. To offset this, triple-point intersections are counted as two.

Another approach was used to measure the grain size of this specimen by image analysis. The grain boundaries were displayed and the length of the grain boundaries per unit area, L_A, was measured to determine $\bar{L}_3$. The number of fields was increased as the magnification was raised. The results were as follows:

Objective	Number of Fields	$\bar{L}_3$, μm	Relative Accuracy, %	G
×16	10	57	8.8	5.0
×32	40	47	6.2	5.5
×50	50	51	15.8	5.3

These results are similar to, and in agreement with, the manual data, irrespective of the magnification. With this method, care must be exercised when setting the threshold, and the image must be cleaned to eliminate inclusion interfaces.

Strict attention must be given to the etch quality, regardless of the measurement method used. To illustrate this problem, a specimen similar to the one shown in Fig. 2 was etched for different times, up to 30 s, with 2% nital. The ferrite grain size was measured using a program designed to detect grain interiors and measure chord lengths. Because this specimen was fine grained, little error was introduced by undersizing of the grains at the perimeter of the live frame when a relatively low magnification was used. Figure 13 shows how the mean lineal intercept, $\bar{L}_3$, and the ASTM grain size, G, vary with the etch time. The same fields exactly could not be retested each time, but the grain size in this specimen was fairly uniform. As the etch time increased, the mean lineal intercept length decreased from about 66 μm to about 17 μm, that is, from ASTM grain size 4.5 to 8.5. After about a 20-s etch, the grain size could be measured with accuracy. Also shown are two different measurements of the same specimen after it had been etched with Marshall's reagent followed by nital. These measurements were made after minor image cleaning. The ASTM grain size was slightly lower, 8.3, as a result of removal of some features that were not grain boundaries but had been detected previously. This same specimen was also analyzed at higher magnification, using chord sizing without deleting those grains touching the frame. The results were the following:

Objective	$\bar{L}_3$, μm	G	
×16	18	8.3	(Fig. 13)
×32	12	9.5	
×50	9	10.3	

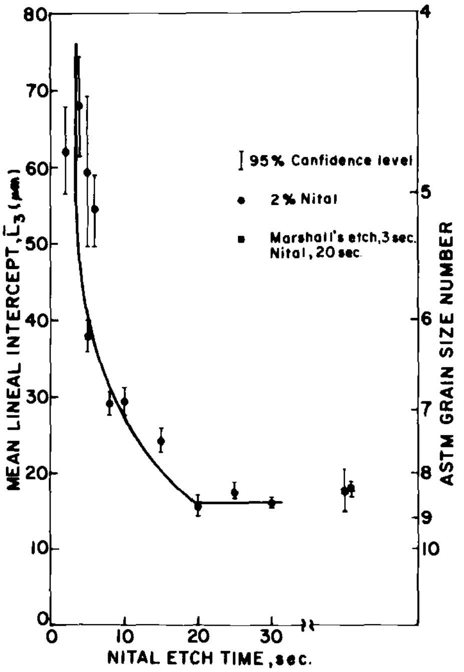

FIG. 13—*Influence of the etch time with 2% nital on the measurement of ferrite grain size, and results using Marshall's reagent.*

Note that a fine-grained specimen is influenced more by this effect than a coarse-grained specimen.

Summary

Measurement of grain size is complicated by the variety of grain sizes that can be measured on both single-phase and multiphased grain structures, which may be equiaxed, elongated, or duplex in nature. Each of these conditions requires a specific measurement approach. Also, one can measure the austenite grain size (with or without twins), prior austenite grain size, or ferrite grain size, depending on the specimen. If annealing twins are present in austenitic alloys, they are ignored in determining grain size, which can make the analysis quite difficult. If structure-property correlations are to be made on twinned alloys, the twin boundaries should not be ignored. In this situation, $\bar{L}_3$ for grain and twin boundaries should be measured, but this value should not be converted to a grain size number.

The specimen chosen must be representative of the bulk sample. Heterogeneous materials require additional sampling to obtain a meaningful grain size. The plane of polish can be chosen at random in testing an equiaxed specimen, while the three principal planes must be measured in specimens with elongated grains. In either case, the field selection must be done blindly, with the fields spaced systematically around the specimen's surface. The etching must delineate the grain boundaries completely without overetching. This can be a difficult task for many materials.

Comparison chart ratings may be adequate for simple screening, that is, for determining whether the specimen is fine or coarse grained. The accuracy of chart ratings is adequate for such purposes so long as the grain size is not close to the division point between fine and coarse grains, ASTM 5. The specimens should be etched to produce an appearance similar to that of the chart photomicrographs or drawings. Use of clear plastic overlays of Plate I of ASTM Method E 112-82 will produce the best accuracy by this method.

Greater accuracy is obtained by measurement of the actual grain sizes. The intercept method is generally preferred to the Jeffries method because of its greater speed. Grain elongation can also be measured using straight test lines parallel and perpendicular to the elongation, or it can be averaged out using circular test lines. The mean lineal intercept is directly related to the grain surface-to-area ratio, S_V, which is useful in structure-property correlations.

The Jeffries and the triple-point count methods provide a measure of the number of grains per unit area, N_A, which is directly related to the total length of grain edges per unit volume, L_V. The intercept method provides a measure of the number of grains intercepted per unit length of test line, N_L, which is inversely proportional to the mean lineal intercept and directly proportional to the grain boundary surface area per unit volume, S_V. Hence, these measures of grain size are based on two different geometrical characteristics of the grain structure and some difference in results may be expected when estimating the planar grain size by these methods.

In the Jeffries method, N_A is used to compute the average grain area, $\bar{A}$, and then the average grain "diameter," $\bar{d}$. In this calculation, $\bar{d}$ is the side of a square of area $\bar{A}$. Because the average planar shape of grains is hexagonal, not square, $\bar{d}$ has no physical significance. The mean lineal intercept length is more realistically related to the planar grain size, but it is smaller than the caliper diameter of the average grain.

These grain size measurements produce an average value for the grain size but say nothing about the range of grain sizes present or the grain size uniformity. The standard deviation of $\bar{L}_3$ gives an idea of the uniformity. Grain size uniformity can also be qualitatively assessed by using the ratios $A_{\max}/\bar{A}$ or $L_{\max}/\bar{L}_3$.

Grain size analysis is one of the most important microscopic measurements because of the influence of the grain size, and the grain size distribution, on the properties and behavior of materials. The methods are easy to apply manually or by image analysis and do not require effort substantially greater than that needed to obtain a good comparison chart rating. Knowledge of the potential sources of error will reduce their influence.

References

[1] Hucher, M. and Grolier, J., *Journal of Microscopy*, Vol. 111, December 1977, pp. 329-337.

[2] Smith, C. S., "Grain Shapes and Other Metallurgical Applications of Topology," *Metal Interfaces*, American Society for Metals, Cleveland, 1952, pp. 65-113.

[3] Smith, C. S., *Metallurgical Reviews*, Vol. 9, 1964, pp. 1-48.

[4] Hull, F. C. and Houk, W. J., *Transactions of the A.I.M.E.*, Vol. 197, April 1953, pp. 565-572.

[5] Desch, C. H., *Journal of the Institute of Metals*, Vol. 22, 1919, pp. 241-276.

[6] Williams, W. M. and Smith, C. S., *Transactions of the A.I.M.E.*, Vol. 194, July 1952, pp. 755-765 and Vol. 197, May 1953, pp. 741-743.

[7] McQuaid, H. W. and Ehn, E. W., *Transactions of the A.I.M.E.*, Vol. 67, 1922, pp. 341-391.

[8] Carpenter, H. C. H. and Robertson, J. M., *Journal of the Iron and Steel Institute*, Vol. 123, No. 1, 1931, pp. 345-394.

[9] Cochrane, R. C. and Morrison, W. B., "The Relationship Between Ferrite and Austenite Grain Size in Normalized Fine-Grained Steels," *Phase Transformations*, Series 3, No. 11, Vol. 2, April 1979, The Institute of Metallurgists, London, pp. 77-79.

[10] Berglund, T., Hultgren, A., and Phragmén, G., *Jernkontorets Annaler*, Vol. 121, No. 9, 1937, pp. 579-602.

[11] Mahoney, C. H. and Tarr, A. L., *A.S.T.M. Bulletin*, October 1944, pp. 15-20.

[12] Hull, F. C., *Transactions of the A.I.M.E.*, Vol. 172, 1947, pp. 439-451.

[13] Saller, H. A., Dickerson, R. F., and Lind, G. E., "Grain Size Chart for Uranium," Battelle Memorial Institute, Report BMI-66, 1 June, 1951.

[14] Berglund, T., *Jernkontorets Annaler*, Vol. 137, No. 11, 1953, pp. 767-784 (BISI No. 1171).

[15] Stahl-Eisen Prufblatt 1510-61, "Microscopic Test of Steels for Grain Size by Comparison with Standard Charts" (BISI No. 12452 British Industrial and Scientific International Translation Service), Verlag Stahleisen mbH, Dusseldorf, West Germany.

[16] ASTM Standard Methods for Estimating the Average Grain Size of Metals (E 112-82), *1982 Annual Book of ASTM Standards, Part 11*, American Society for Testing and Materials, Philadelphia, 1982.

[*17*] Brandis, H. and Wiebking, K., *D.E.W. Technische Berichte*, Vol. 7, No. 4, 1967, pp. 215-226 (BISI No. 6536).

[*18*] Brandis, H. and Wiebking, K., *D.E.W. Technische Berichte*, Vol. 8, No. 3, August 1968, pp. 124-127.

[*19*] Arpi, R., *Metallurgia*, Vol. 11, No. 65, March 1935, pp. 123-127.

[*20*] Shepherd, B. F., *Transactions of the American Society for Metals*, Vol. 22, December 1934, pp. 979-1016.

[*21*] Enlund, B. D., *Jernkontorets Annaler*, Vol. 134, No. 11, 1950, pp. 553-555 (HB No. 3207).

[*22*] Grossman, M. A., *Transactions of the A.I.M.E.*, Vol. 167, 1946, pp. 39-79.

[*23*] Sauveur, A., *Transactions of the A.I.M.E.*, Vol. 22, 1894, pp. 546-557.

[*24*] Jeffries, Z., Kline, A. H., and Zimmer, E. B., *Transactions of the A.I.M.E.*, Vol. 54, 1916, pp. 594-607.

[*25*] Jeffries, Z., *Transactions of the Faraday Society*, Vol. 12, 1916, pp. 40-56.

[*26*] Heyn, E., *The Metallographist*, Vol. 5, 1903, pp. 39-64.

[*27*] Hilliard, J., *Metal Progress*, May 1964, pp. 99-100, 102.

[*28*] Abrams, H., *Metallography*, Vol. 4, 1971, pp. 59-78.

[*29*] Snyder, R. W. and Graff, H. F., *Metal Progress*, April 1938, pp. 377-380.

[*30*] Brandis, H. and Wiebking, K., *D.E.W. Technische Berichte*, Vol. 8, No. 1, 1968, pp. 41-45.

[*31*] Scheil, E., *Zeitschrift für Metallkunde*, Vol. 27, 1935, pp. 199-209; and Scheil, E. and Wurst, H., *Zeitschrift für Metallkunde*, Vol. 28, 1936, pp. 340-343.

[*32*] Johnson, W. A., *Metal Progress*, January 1946, pp. 87-92, 92B.

[*33*] Kostron, H., *Archiv für Metallkunde*, Vol. 3, June 1949, pp. 193-203, and July 1949, pp. 229-242.

[*34*] Aaron, H. B., Smith, R. D., and Underwood, E. E., "Spatial Grain-Size Distribution from Two-Dimensional Measurements," First International Congress of Stereology, Vienna, 18-20 April, 1963, pp. 16-1 to 16-8.

[*35*] Saltykov, S. A., "The Determination of the Size Distribution of Particles in an Opaque Material from Measurement of the Size Distribution of their Sections," *Stereology*, Springer-Verlag, New York, 1967, pp. 163-173.

[*36*] Exner, H. E., *International Metallurgical Reviews*, Vol. 17, 1972, pp. 25-42.

[*37*] Okazaki, K. and Conrad, H., *Transactions of the Japanese Institute of Metals*, Vol. 13, May 1972, pp. 198-204.

[*38*] Bodyako, M. N., Kasichev, V. P., and Naumovich, N. V., *Practical Metallography*, Vol. 17, May 1980, pp. 232-237.

[*39*] Warren, R. and Durand, M. C., "Computer Synthesis of Microstructures in Stereological Analysis," Swedish Symposium on Non-Metallic Inclusions, Sodertalje, Sweden, 1981, pp. 269-284.

[*40*] Rhines, F. N., Craig, K. R., and Rouse, D. A., *Metallurgical Transactions*, Vol. 7A, November 1976, pp. 1729-1734.

[*41*] Patterson, B. R. and Rhines, F. N., "Serial Section Estimate of Number Per Unit Volume," *Microstructural Science*, Vol. 7, Elsevier North-Holland, New York, 1979, pp. 457-462.

[*42*] Hilliard, J. E., "Grain-Size Estimation," Report No. 62-RL-3133M, General Electric Research Laboratory, Schenectady, N.Y., December 1962.

[*43*] "Standard Method for Measuring the Austenite Grain Size in Steel," Special Report No. 5, Japanese Society for the Promotion of Science, Tokyo, 4 Nov. 1965.

[*44*] Schuckher, F., *Acta Polytechnica Scandinavica*, 1966, pp. 1-102 (see also Ref *48*, pp. 201-265).

[*45*] Pereira da Silva, P. S. C., "Grain Size Measurement," M.S. thesis, University of Sheffield, England, September 1966.

[*46*] Gokhale, A. M., *Transactions of the Indian Institute of Metals*, Vol. 35, December 1982, pp. 595-600.

[*47*] Saltykov, S. A., *Stereometric Metallography*, 2nd ed., Metallurgizdat, Moscow, 1958 (rough draft translation AD 267-700 and 267-701, Armed Services Technical Information Agency); 3rd ed., 1970.

[*48*] De Hoff, R. T. and Rhines, F. N., Eds., *Quantitative Microscopy*, McGraw-Hill, New York, 1968.

[*49*] Underwood, E. E., *Quantitative Stereology*, Addison-Wesley, Reading, Mass., 1970.

[50] Fullman, R. L., *Transactions of the A.I.M.E.*, Vol. 197, March 1953, pp. 447-452.
[51] Miller, G. A., Avery, D. H., and Backofen, W. A., *Transactions of the A.I.M.E.*, Vol. 236, December 1966, pp. 1667-1673.
[52] Thompson, A. W., *Metallography*, Vol. 5, 1972, pp. 366-369.
[53] Rutherford, J. J. B., Aborn, R. H., and Bain, E. C., *Metals and Alloys*, Vol. 8, December 1937, pp. 345-348.
[54] Hanson, K. L., *Acta Metallurgica*, Vol. 27, April 1979, pp. 515-521.
[55] Woodhead, J. H., "The Statistical Errors in Grain Size Measurement," *Quantitative Analysis of Microstructures in Medicine, Biology and Materials Development*, Riederer-Verlag, Stuttgart, 1975, pp. 265-276.

W. Brian James[1]

Use of Image Analysis for Assessing the Inclusion Content of Low-Alloy Steel Powders for Forging Applications

---

REFERENCE: James, W. B., "**Use of Image Analysis for Assessing the Inclusion Content of Low-Alloy Steel Powders for Forging Applications,**" *Practical Applications of Quantitative Metallography, ASTM STP 839,* J. L. McCall and J. H. Steele, Jr., Eds., American Society for Testing and Materials, Philadelphia, 1984, pp. 132-145.

ABSTRACT: The extensive porosity present in pressed and sintered ferrous materials masks the effects of inclusions on the mechanical properties of these materials. In contrast, the properties of material powder forged to near theoretical density are strongly influenced by the composition, size distribution, and location of nonmetallic inclusions.

A method is therefore required for assessing the cleanliness of iron and low-alloy steel powders intended for powder forging applications. Automatic image analysis techniques are preferred for use in this application, as they are not subject to operator sensitivity and can be used routinely to obtain a wider range of data. However, many of the inclusions found in water-atomized low-alloy powders have a relatively open, "lacy" appearance. In order to count such inclusions as single entities rather than numerous smaller particles, a special image analysis technique has been developed. This involves amendment of the detected video image using various combinations of image dilation, erosion, and reconstruction.

KEY WORDS: quantitative metallography, steels, image analysis, image amendment, nonmetallic inclusions, powder forging, low-alloy steel powders

Powder forging competes directly with casting and drop forging as a forming method. The relative isotropy of mechanical properties and the better surface finish of powder-forged parts can result in superior component performance [*1*].[2]

The powder forging process is illustrated schematically in Fig. 1. Metal powder is cold compacted to form a preform, which is subsequently heated

---

[1] Manager, Product Development, Hoeganaes Corp., Riverton, N.J. 08077.

[2] The italic numbers in brackets refer to the list of references appended to this paper.

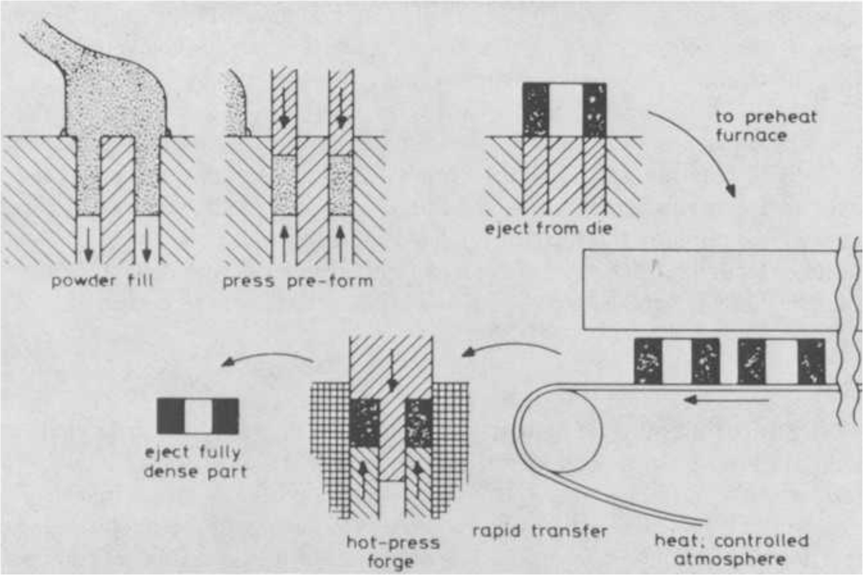

FIG. 1—*Schematic illustration of the powder forging process.*

and then forged in a single blow to full or near full density, using closed dies. The flash typically produced during drop forging is absent from powder forgings. Powder forging, therefore, represents a high degree of material utilization.

The mechanical properties of powder-forged materials are strongly influenced by the number, size distribution, and type of nonmetallic inclusions present [*2-6*]. Improvements in the cleanliness of water-atomized low-alloy steel powders have led to their use in inner and outer bearing race applications [*7*]. As part of a program aimed at ensuring consistent powder properties, a method has been developed for assessing the inclusion content of water-atomized low-alloy steel powders intended for forging applications. The technique described in this paper is a refinement of one previously developed for the same application [*8*].

During the water atomization process, which is used to produce low-alloy steel powders for forging applications, high-pressure water jets are employed to disintegrate a controlled stream of molten metal. The molten metal, therefore, comes into intimate contact with water and some oxidation occurs. Although the atomized powder is subsequently annealed in order to reduce its oxygen content and improve its compressibility, the processing temperature is insufficient for reduction of the relatively stable oxides of such elements as chromium, manganese, silicon, and aluminum. Commercially available low-alloy steel powders are therefore based on nickel/molybdenum alloys.

In comparison with wrought steels, only a limited amount of material flow is present in powder-forged components. Inclusion stringers common to wrought steel are therefore not found in powder-forged materials. Figures 2 through 4 illustrate some of the inclusion types generally encountered in powder-forged low-alloy steels. The fragmented nature of these inclusions makes size determination by image analysis more complex than is the case with solid exogenous inclusions, such as that shown in Fig. 5. Basic image analysis techniques tend to count the inclusions shown in Figs. 2 through 4 as numerous small particles rather than as a single larger entity. Amendment of the detected video image is required to classify such inclusions correctly.

Procedure

A Leitz Texture Analyse System (TAS) plus unit has been used to develop an inclusion assessment procedure for powder-forged low-alloy steels.

In essence, an image analyzer consists of a good-quality metallurgical microscope, a video camera, a display console plus keyboard, a microprocessor, and hard copy printout facilities. The video image is assessed in terms of its gray level characteristics, black and white being extremes on the available scale. The detection level can be set to differentiate between oxides and sulfides.

Exogenous refractory inclusions, such as that shown in Fig. 5, present no problem to the average image analyzer. They are easily detected and their relatively solid appearance permits accurate measurement of such parameters as area fraction, perimeter, projected length, and maximum Feret diameter. Lacy sulfides, spotty particle oxides, and lacy, partially reduced complex oxides, illustrated in Figs. 2 through 4, are much more of a challenge. Some of the spotty particle oxides are occasionally so faint that they are barely discernible through the eyepiece of the microscope. Even when such inclusions are detected, the image analyzer measures the individual particles rather than the inclusion cluster as a whole. The video image amendment capabilities of the more sophisticated image analyzers are necessary for correct classification of such inclusions.

The basis of the technique is to transform the detected image by combinations of image dilation, erosion, and reconstruction into a form in which these fragmented inclusions are measured as individual particles without distorting the other particles within the field of view. This is made possible by feature-localized operations carried out under microprocessor control.

The image amendment procedure is illustrated in Figs. 6 through 11 for a typical spotty particle oxide inclusion. Figure 6 represents the initial live video image as it appears on the display console and Fig. 7 the detected image, that is, the bright features shown. (These can vary depending on the gray level threshold set for detection.) The bright lines on the photomicrographs denote the limits of the measuring field.

FIG. 2—*"Spotty particle" oxide inclusion, magnification ×800.*

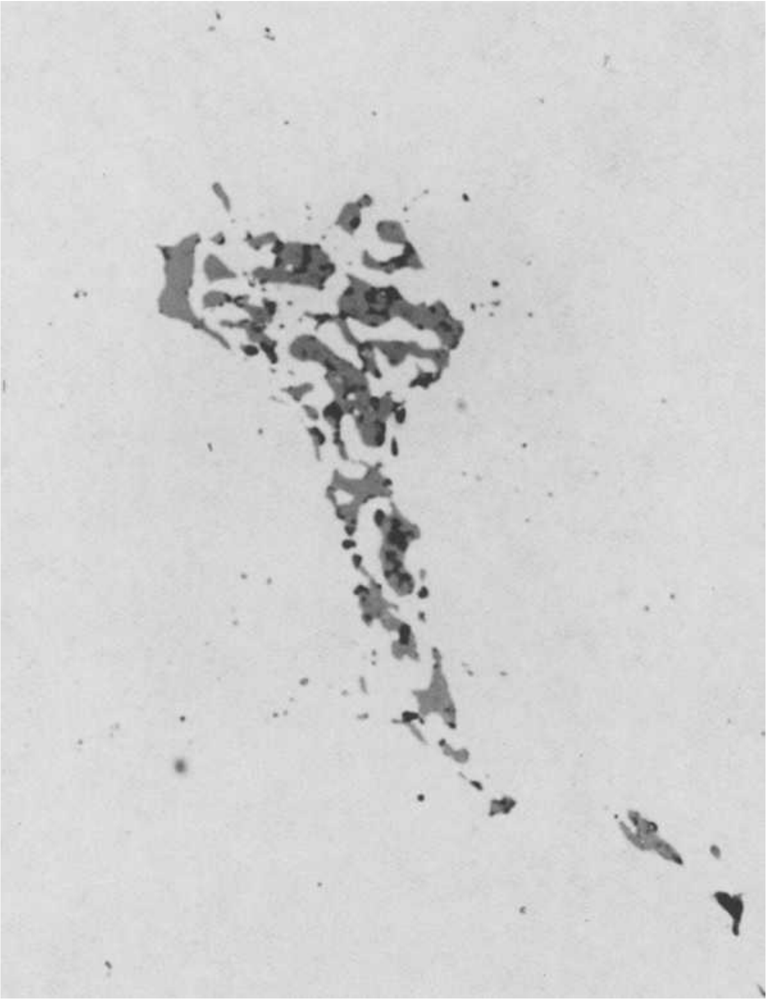

FIG. 3—*"Lacy" sulfide inclusion, magnification ×800.*

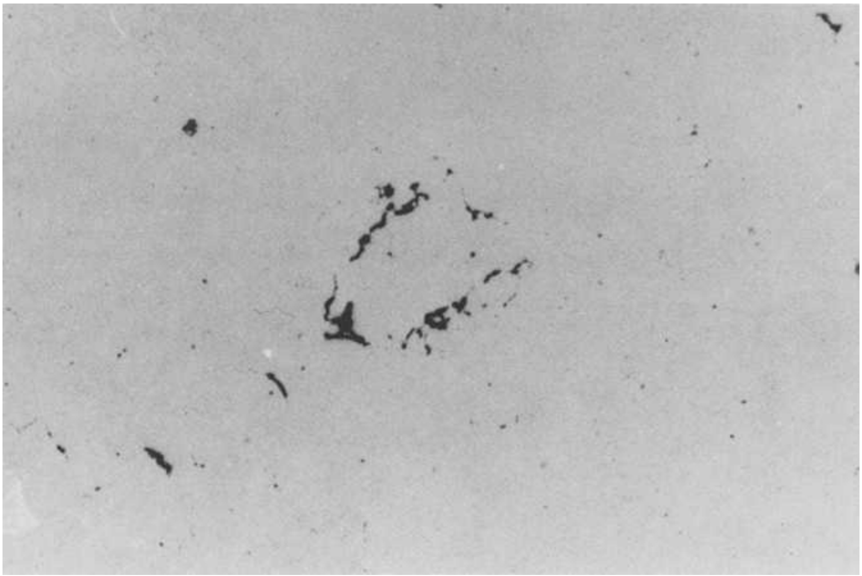

FIG. 4—*Particle boundary oxide inclusion, magnification ×400.*

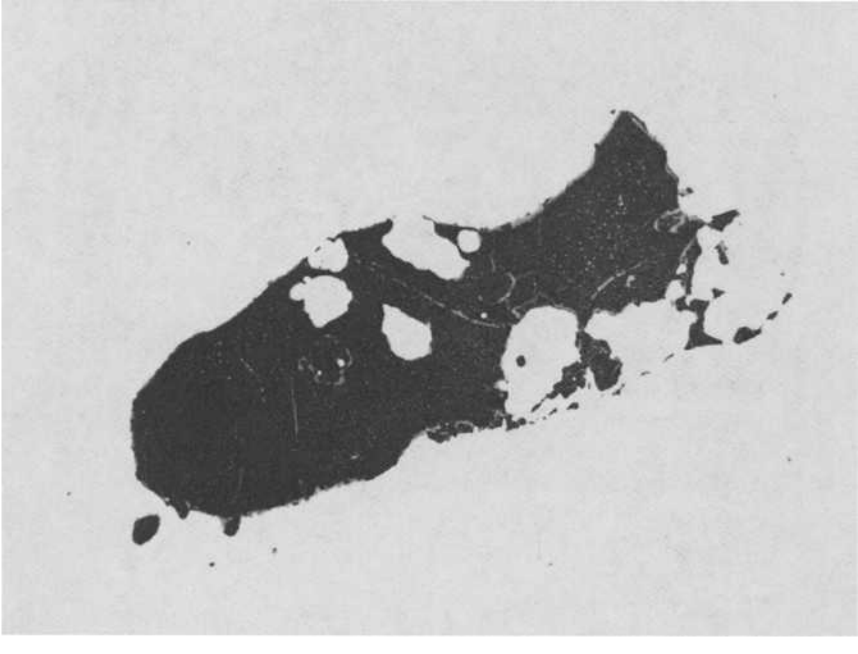

FIG. 5—*Exogenous slag inclusion, magnification ×800.*

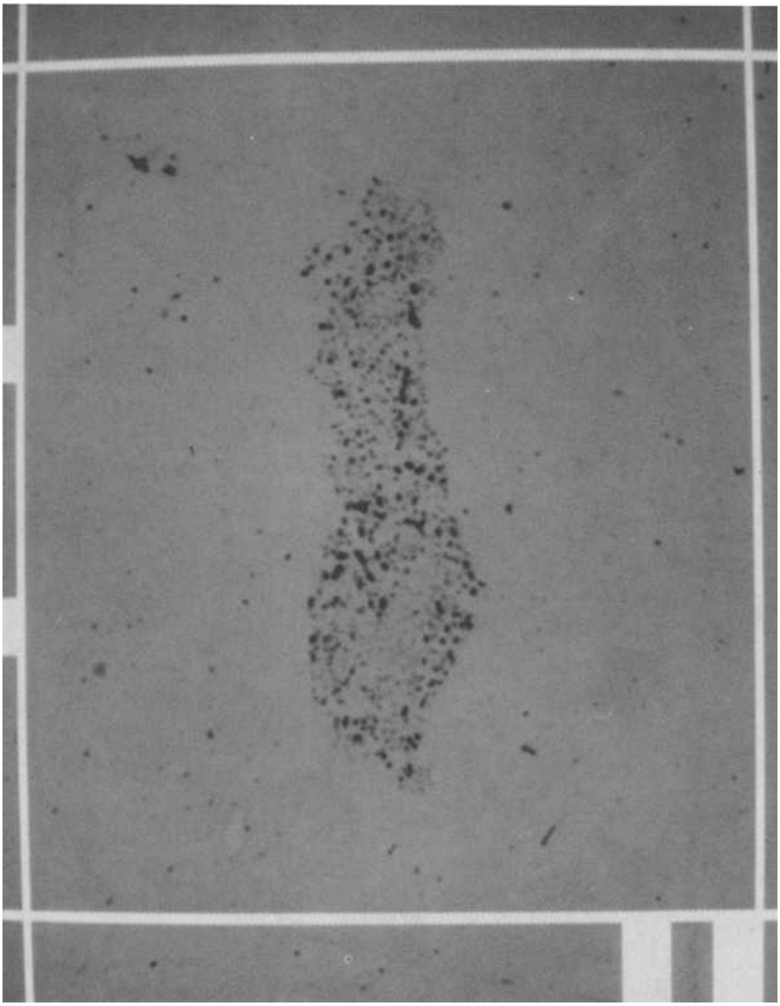

FIG. 6—*Initial live video image.*

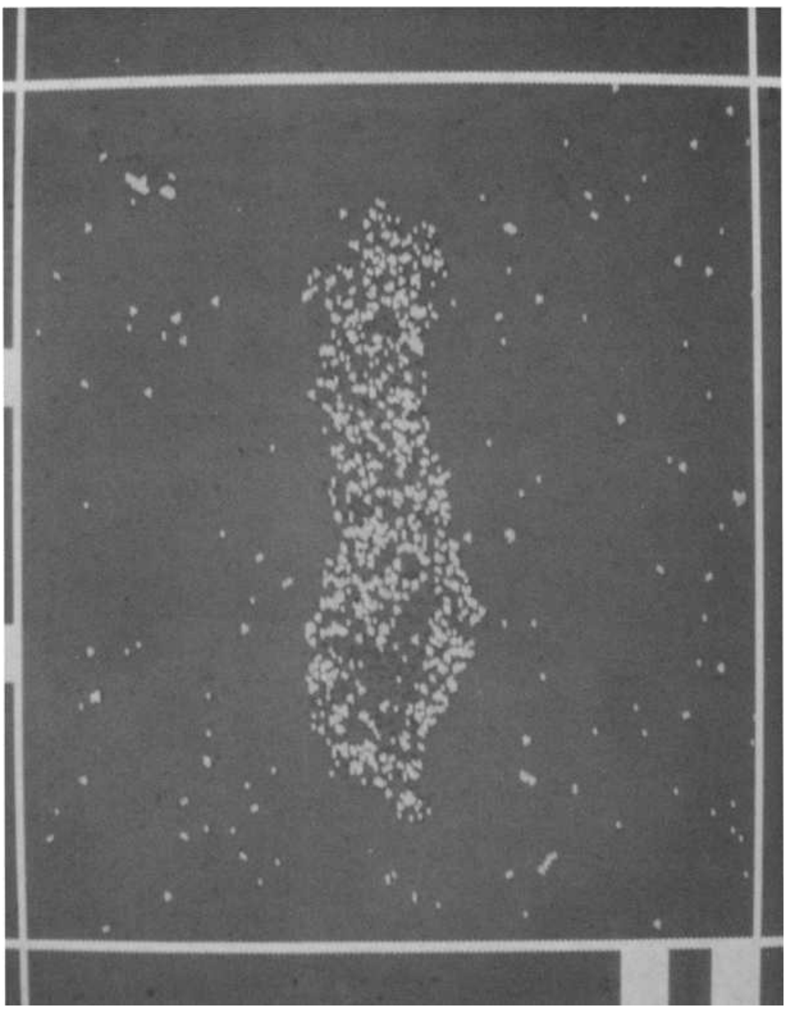

FIG. 7—*Original detected image.*

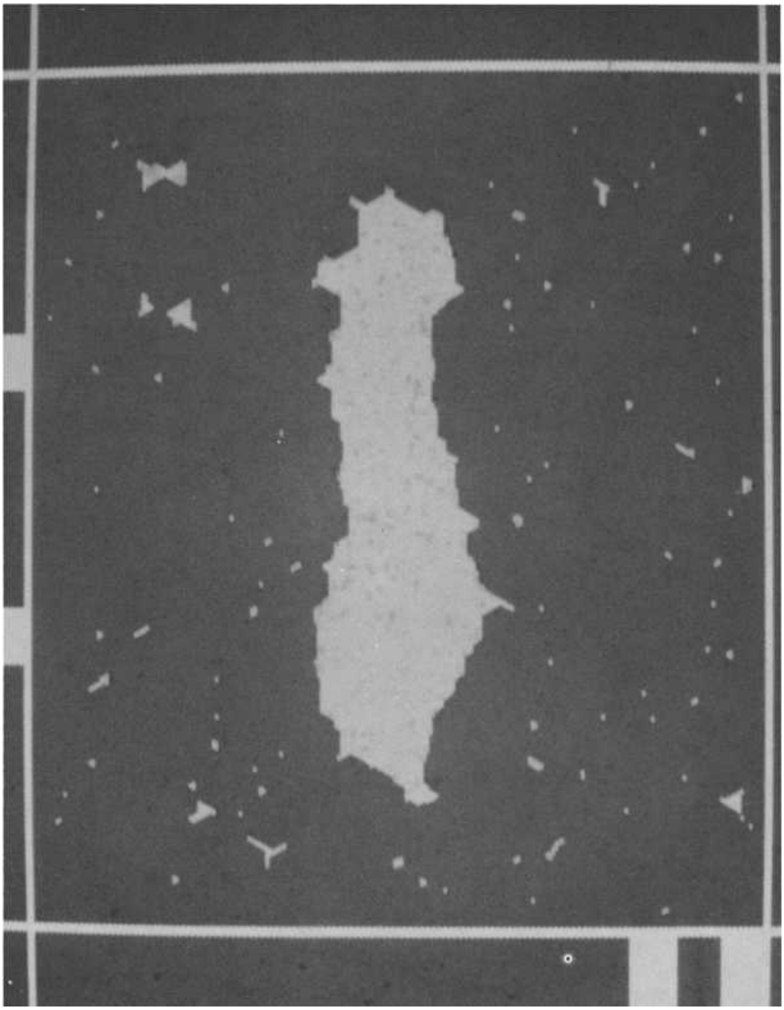

FIG. 8—*Detected image in Fig. 7 subjected to five dilations followed by five erosions.*

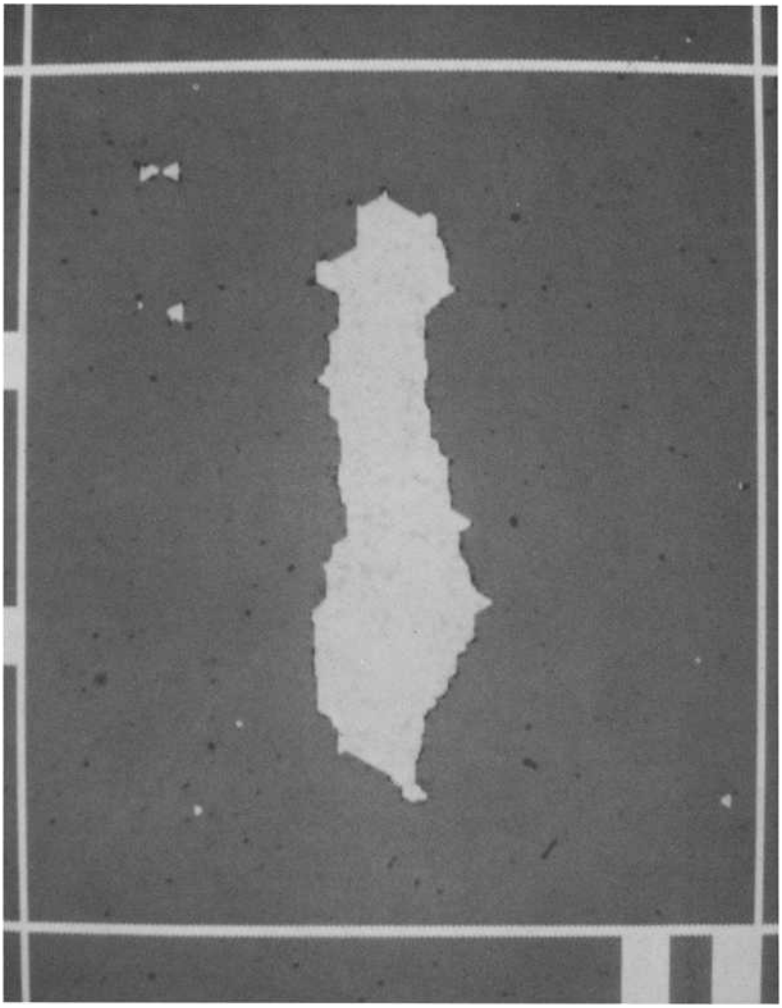

FIG. 9—*Detected image in Fig. 8 plus one further erosion.*

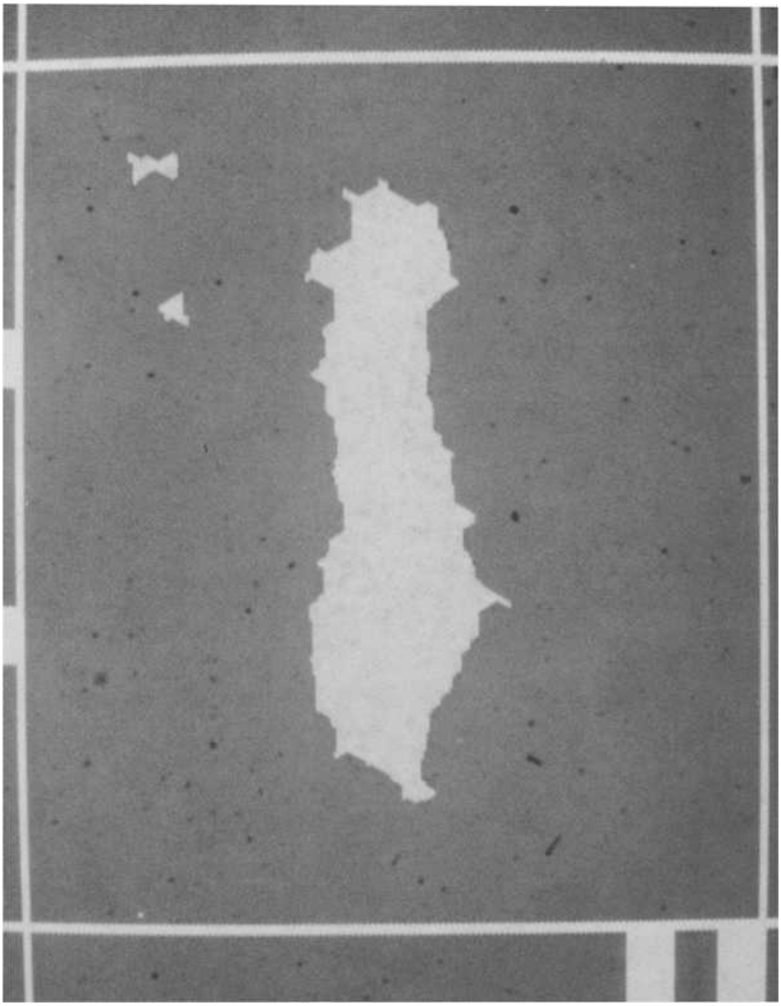

FIG. 10—*Detected image in Fig. 8 plus two erosions followed by reconstruction.*

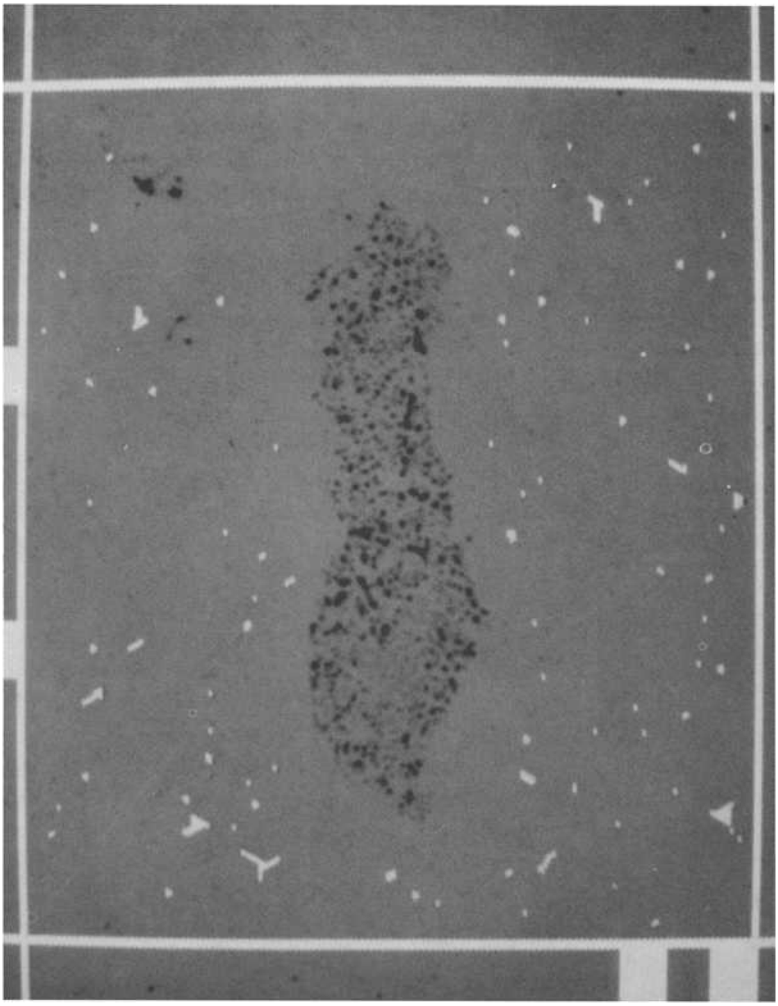

FIG. 11—*An illustration of the inclusions eliminated by the "sizing out" process.*

In Fig. 8 the detected image of Fig. 7 has been subjected to a total of five dilations, based on the hexagonal measuring raster system used in the TAS, plus five erosions. The fragmented nature of the originally detected image has been transformed and the spotty particle oxide inclusion has been "filled in." The dilation process has joined the near neighboring features, and separation has not occurred during the erosion stage.

However, in comparison with the original detected image in Fig. 7, some of the smaller discrete inclusions are now somewhat enlarged. The next sequence of image amendment sizes out those inclusions smaller than a given size. This is done by a process of erosion and reconstruction of the detected image. Figure 9 illustrates the effect of one erosion. Notice how many of the smaller inclusions detected in Fig. 8 have now been eliminated. Figure 10 shows what happens when two erosions plus a reconstruction are applied to the detected image shown in Fig. 8. The two erosions have eliminated or "sized out" those inclusions smaller than a given size, and the reconstruction step has returned the remaining detected image to the dimensions it had in Fig. 8, that is, to its true size. Those inclusions eliminated by the sizing out process are shown as the bright features in Fig. 11.

The actual sequence and the required numbers of dilations and erosions followed by erosions and reconstruction depend on the nature of the inclusions to be evaluated.

A comparison of the area percentage measurements on detected images, such as those shown in Figs. 7 and 10, gives an indication of how fragmented the inclusions are. Exogenous inclusions, such as that illustrated in Fig. 5, would show little difference.

In addition to the aforementioned area percentage measurements, the image analyzer can, for example, provide a complete histogram of the full size distribution of inclusions, a sizing of all particles greater than a given size maximum Feret diameter on an individual basis, and automatic return and sequencing through such inclusions at the end of the run. Such inclusions can also be checked at two gray level settings to establish whether they are based predominantly on oxides or sulfides.

The technique described in this paper or a slight variant of it is intended to be used for the following applications:

(*a*) for routine cleanliness checks on low-alloy powders,

(*b*) for determination of the influence of powder production process changes on powder cleanliness, and

(*c*) for relating the inclusion content of low-alloy steel powders to the mechanical property performance of powder-forged material.

Acknowledgments

The author wishes to acknowledge the assistance of Jim Golden of Leitz Inc. and of Tom Murphy of Hoeganaes Corp. in developing the procedure described in this paper.

References

[1] James, W. B., *Metal Powder Report*, Vol. 37, No. 5, 1982, pp. 251-253.

[2] Brown, G. T. and Steed, J. A., *Powder Metallurgy*, Vol. 17, No. 33, 1974, pp. 157-177.

[3] Bastian, F. L. and Charles, J. A., *Powder Metallurgy*, Vol. 21, No. 4, 1978, pp. 199-208.

[4] Lindskog, P. and Grek, S. E. in *Modern Developments in Powder Metallurgy*, Vol. 7, Metal Powder Industries Federation, Princeton, N.J., 1974, pp. 285-301.

[5] Bockstiegel, G. and Blande, C. A., *Powder Metallurgy International*, Vol. 8, No. 4, 1976, pp. 155-160.

[6] Saritas, S., James, W. B., and Davies, T. J., *Powder Metallurgy*, Vol. 24, No. 3, 1981, pp. 131-140.

[7] *Production*, October 1981, pp. 106-108.

[8] James, W. B. in *Modern Developments in Powder Metallurgy*, Vol. 14, Metal Powder Industries Federation, Princeton, N.J., 1981, pp. 541-560.

Robert T. DeHoff[1]

Insights Provoked by Surprises in Stereology

REFERENCE: DeHoff, R. T., "**Insights Provoked by Surprises in Stereology,**" *Practical Applications of Quantitative Metallography, ASTM STP 839,* J. L. McCall and J. H. Steele, Jr., Eds., American Society for Testing and Materials, Philadelphia, 1984, pp. 146-159.

ABSTRACT: Surprising results and their implications are reviewed for five studies that focus stereological methodology upon recrystallization, grain growth, mechanical properties and grain size, sintering, and austenitization of an eutectoid steel.

KEY WORDS: stereology, quantitative metallography, recrystallization, grain growth, grain size, sintering, austenitization, aluminum, silicon, iron

Application of stereological methods frequently yields results that are unexpected. This paper reviews five examples of experimental studies that gave surprising results. In each case the results were surprising in the context of existing views of the behavior involved. Explanations of these unexpected results required significant modification of the preexisting notion of the phenomenon under study, so that an alternate, or more sophisticated, understanding had to be developed.

The five examples deal with studies in the following areas:

(*a*) recrystallization,
(*b*) grain growth,
(*c*) mechanical properties,
(*d*) sintering, and
(*e*) austenitization of a spheroidized steel.

For each case the relevant experiment will be briefly described, and this will be followed by a presentation of the surprising result and a discussion of the insight that this result evoked. The resulting insights are not necessarily fully de-

---

[1] Professor, Department of Materials Science and Engineering, University of Florida, Gainesville, Fla. 32611.

veloped, nor are they crystal clear or necessarily the final word on the subject; materials science continues to evolve, and stereological information continues to accumulate, along with all other kinds of experimental observations. Nonetheless, this collection of examples serves to demonstrate the utility of stereology as a research tool.

Recrystallization

During the past two decades a number of researchers have applied stereology to the study of recrystallization [*1-4*].[2] A program carried out by Speich and Fisher [*4*] is reviewed here as an example of the strategy typical of such studies; the results of these researchers are also typical of the form of results found by others, although the programs and results differ in important details.

Speich and Fisher studied the isothermal recrystallization behavior of a 3.27% silicon, silicon/iron alloy over a very wide range of temperatures, from 500 to 1000°C. At each temperature they followed the course of the process stereologically, measuring the volume fraction, V_V, and the surface area per unit volume, S_V, of the growing recrystallized regions at each of a series of times. With this information, it was possible to compute the Cahn-Hagel growth rate, $\bar{v}_S$, [*5*] by

$$\bar{v}_S \equiv \frac{\int\int v\,ds}{\int\int ds} = \frac{1}{S_V} \cdot \frac{dV_V}{dt} \tag{1}$$

(where v is the local velocity of the element of a boundary area, ds), which is the average velocity of the moving boundary of the recrystallized regions.

The surprising result of this study is shown in Fig. 1. A plot of the growth rate versus annealing time on a log-log scale is a straight line with a slope of -1. By itself, this observation is not particularly eye-catching, but in these experiments, all of the results for all temperatures fall on a single straight line. Thus, the growth rate, v, in this system is described by the equation

$$v = \frac{a}{t} \tag{2}$$

where a is a constant, independent of temperature. Evidently the average interface velocity depends only upon time, t—how long the sample had been in the annealing furnace; it does not depend upon the temperature. Surely grain boundary migration is a thermally activated process, so that this result is unexpected.

This result can be explained if it is assumed that the recrystallization process occurs by nucleation and growth and that the growth is two-dimensional [*6*].

---

[2] The italic number in brackets refer to the list of references appended to this paper.

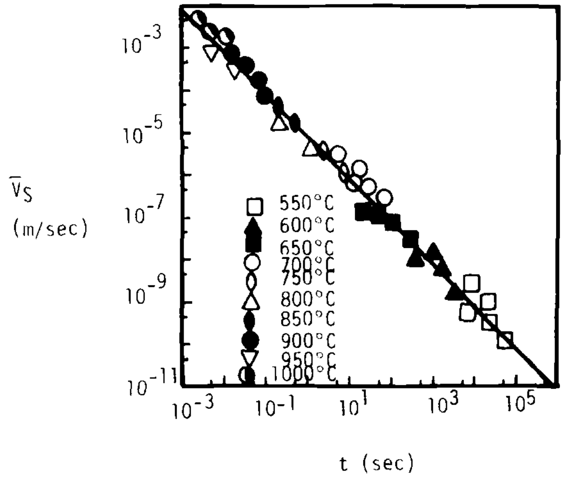

FIG. 1—*Variation of the average interface velocity with annealing time for a specimen series of cold-worked 3.27% silicon/iron alloy annealed at temperatures from 500 to 1000°C (after Speich and Fisher [4]).*

Some support for this view is provided by Vandermeer's detailed study of the early stages of recrystallization in aluminum [*1*], in which he demonstrates that, under the conditions used in his study, recrystallization begins by forming colonies of grains along grain edges, which subsequently grow radially, that is, two-dimensionally. Consider a simple model in which the grain edges per unit volume, N_V, each of a length, l, activate to initiate recrystallization. Assume the grains then grow radially, with a constant growth rate, G. After some time, t, the radius, R, grows to $R = Gt$, and the volume fraction recrystallized is

$$V_V = N_V \pi \ell G^2 t^2 \tag{3}$$

The surface area of recrystallized zones per unit volume of structure is

$$S_V = N_V \pi G^2 t^2 + N_V 2\pi \ell G t \tag{4}$$

In the range of the process, where $\ell \ll Gt$, at long times

$$S_V \cong N_V G^2 t^2 \tag{5}$$

Under these conditions, the Cahn-Hagel growth rate may be computed by substituting these expressions into its definition in Eq 1

$$\bar{v}_S = \frac{1}{N_V \pi G^2 t^2} N_V \pi \ell G^2 (2t)$$

$$\bar{v}_S = \frac{2\ell}{t} \tag{6}$$

which may be compared with Eq 2. If the growth is two-dimensional, the numerator and denominator of the Cahn-Hagel growth rate expression have the same dependence upon G, the radial growth rate. These dependences cancel, and with them the dependence of v upon temperature.

Thus, one insight provided by this exercise is that the recrystallization process may occur by two-dimensional growth of colonies. Equally important is the observation that, although the Cahn-Hagel growth rate is a rigorously defined velocity average, that average may contain no information about "growth rates," which are usually defined as the rate of change of some characteristic dimension of the growing particle. This geometric distinction is emphasized for one-, two-, and three-dimensional growth in a variety of models in Ref *6*.

Grain Growth

In the most common usage of this term, grain growth means the coarsening of a space-filling aggregate of grains, characterized by a decrease in grain boundary area, a decrease in the number of grains in the system, and an increase in the average grain size. The last element of the description may be ambiguous, since "grain size" may be measured and reported in a variety of ways [*7*]. The most common measure of grain size is the mean grain intercept, $\bar{l}$, determined from a count of the number of times a test line crosses grain boundary traces on a representative section through the structure.

The rate of grain growth is usually described in terms of the time rate of change of the "grain diameter," which is computed from the mean grain intercept on the assumption that the grains are spheres of uniform size [*8*]. Theories of the kinetics of grain growth attempt to relate this rate to the rate of grain boundary migration, as determined in basic bicrystal experiments. The rate of change of the average grain diameter is assumed to be simply related to the average of the local velocity of grain boundaries in the structure.

In a two-dimensional grain structure, for example, in a sheet specimen, it is possible to observe the motions of the grain boundaries directly during grain growth. A simple stereological relationship permits the evaluation of the true average interface velocity, $\bar{v}_L$, in such a structure

$$\bar{v}_L \equiv \frac{\int v\,d\ell}{\int d\ell} = \frac{1}{L_A} \cdot \frac{dA_A}{dt} \tag{7}$$

where L_A is the total length of grain boundary per unit area, and A_A is the area fraction swept out by moving grain boundaries. Thus, in such a system, it is possible to make a direct assessment of the validity of the geometric assumption that underlies theories that connect grain growth with grain boundary observations.

Such an assessment has yet to be made on a real grain structure; however, an experiment of this kind has been carried out on a soap film model of a sheet grain structure [9]. Two Plexiglas sheets were machined to form a thin disk-shaped cavity between them. A small amount of soap solution was introduced into the cavity, and the pressure was reduced somewhat. When this kind of apparatus is shaken, a soap froth develops which coarsens into a soap film network. The configuration of this sheet-like network is governed by surface tension forces and takes a form that is a good analogue of a two-dimensional grain structure. With time, this network coarsens; its length decreases, the number of cells decreases, and its average "size" increases.

As the structure evolved, a time series of photographs was taken. The total length of the boundary area, L_A, was measured with the line intercept count, and the mean cell intercept was computed from this value. An average grain diameter, $\bar{D}$, was computed from this value, modeling the grains as uniform circles. Then sequential pairs of photographs were carefully superimposed, and the areas swept by the moving segments of boundary were colored. The area fraction swept out by the moving boundary, A_A, during each time interval was then determined by applying a point count to these shaded areas.

The surprising results of these experiments are shown in Figs. 2 and 3. Figure 2 compares the true average interface velocity computed from Eq 7 with the rate of change of the average grain diameter. These two quantities are clearly not proportional to each other; they are not even qualitatively similar. The dD/dt decreases with time, while $\bar{v}_L$ remains essentially constant, or perhaps increases slightly with time. Figure 3 demonstrates that the area fraction swept out is essentially proportional to the number of grains annihilated. From this figure it is possible to compute that the total area is swept by moving grain boundaries once for every 40 grains annihilated.

These observations suggest that dD/dt is a misleading measure of the true average interface velocity in cell coarsening, and hence in grain growth. If it is assumed that the local velocity of grain boundaries behaves as is observed in

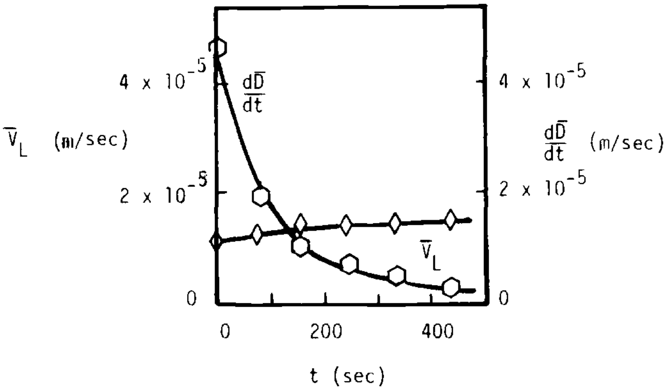

FIG. 2—*Comparison of the true average rate of boundary migration with the rate of change of the average cell "diameter" (after DeHoff and Cone [9]).*

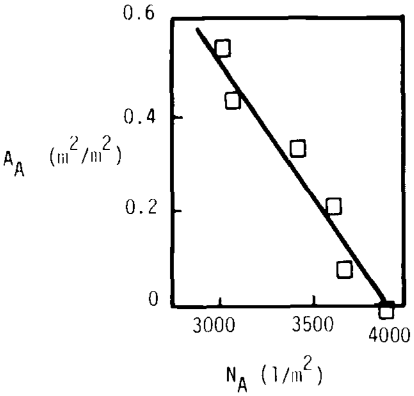

FIG. 3—*Variation of the area fraction swept out by moving boundaries with the number of cells remaining during cell growth (after DeHoff and Cone [9]).*

bicrystal experiments, where the geometry is simple, then $\bar{v}_L$ is a proper measure of the kinetics of grain growth. The observation that this quantity does not decrease with time, as is commonly inferred from measurements of dD/dt, suggests a need for a new point of view for the process. Smith [*10*] has suggested that grain growth requires the occurrence of specific topological processes in the grain boundary network: annihilation of grains (which contributes to grain growth by decreasing the number of grains, and thus their average area), and grain encounter reactions (which do not change the number of grains or their average size, but modify the distribution). Rhines and Craig [*11*] and Steele [*12,13*] have extended these ideas to three-dimensional grain structures. Description of the kinetics in terms of the rates of occurrence of these topological events, rather than the rate of change of the average grain diameter, might provide a more realistic and sophisticated understanding of this geometrically complex process.

Grain Size and Mechanical Properties

A primary goal of thermomechanical processing of nominally single-phase materials is the control of grain size to control properties. There exists extensive literature dealing with such correlations [*14-17*], highlighted by the classic papers of Hall [*14*] and Petch [*15*]. Indeed, the fundamental, most widely accepted theoretical analysis of such correlations bears their names—the familiar Hall-Petch relation [*16*].

Recent studies by Gokhale and Rhines [*18*] and by Rhines and his students [*19*] explored this connection in greater depth. Specimens of high-purity aluminum (99.998%) were cold worked to a range of prestrains and heat treated to develop annealed structures. Besides measuring the grain size (mean grain intercept, which is related to the surface area of the grain boundary per unit volume [7]), these investigators also measured the grain size distribution. To avoid uncertainties associated with stereological size distribution measurements, the size distribution of grain volumes was measured directly. The polycrystalline specimens were infiltrated with gallium, which penetrates the grain boundaries, and disintegrated into an aggregate of separate grains. The volumes of larger grains in the distribution were determined by weighing the grains; the volume distribution of smaller grains was determined with a Coulter counter.

The size distributions could be described as log normal [20]; this is demonstrated in Fig. 4, which shows that the distribution functions are linear when plotted on normal probability paper with a logarithmic size axis. It can be shown that the slope of such a plot is related to the coefficient of variation of the

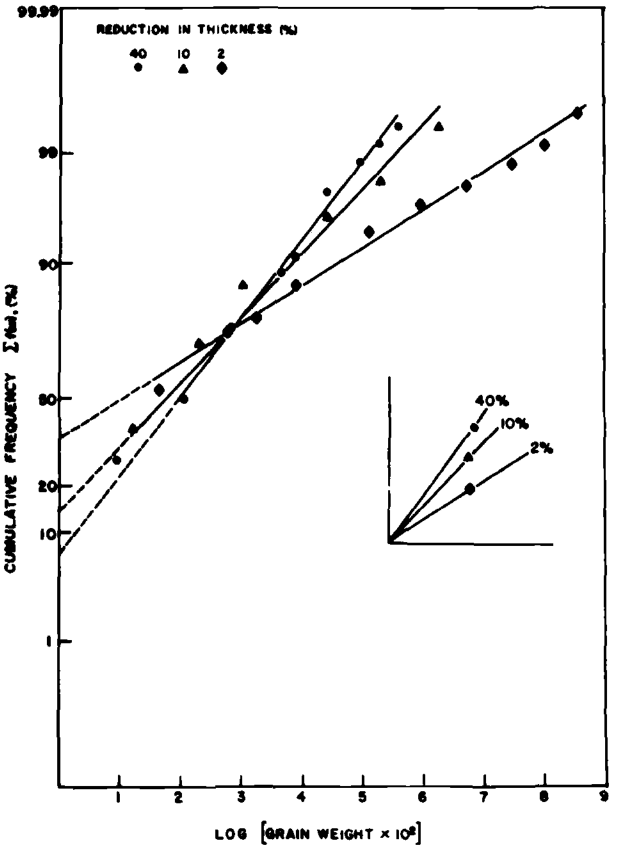

FIG. 4—*Grain size distributions in annealed aluminum, which are log normal and have widths (coefficients of variation) that vary with the amount of prior cold work (after Gokhale and Rhines [18]).*

size distribution function, which is a measure of the relative width of the distribution curve. Thus, Fig. 4 demonstrates that it is possible to vary the width of the size distribution curve independent of its mean value or average size. It was found that the width depends on the amount of prior cold work, decreasing (that is, the sizes becoming more uniform) with increasing prestrain. The grains sizes can be altered by grain growth without changing the width established by the prestrain.

Apart from the impact these observations may eventually have on the understanding of the recrystallization process, the surprising result of this work is summarized in Figs. 5 and 6. Tension tests were carried out at 77 K, and the yield and ultimate strengths were determined. The specimens chosen for analysis were in two series; within each series, the "grain size" (that is, the mean grain intercept) was the same, but the widths of the grain volume distributions were different. These results show that the values of the mechanical properties are at least as sensitive to the width of the distribution function as they are to the grain size.

The insight provided by these results is this: attempts to understand and describe the response of polycrystals to applied plastic deformation in terms of a single size parameter are fundamentally incomplete. Related experiments by the same group suggest that plastic deformation in a polycrystal starts with the largest grains in the distribution and works down through the size classes [19].

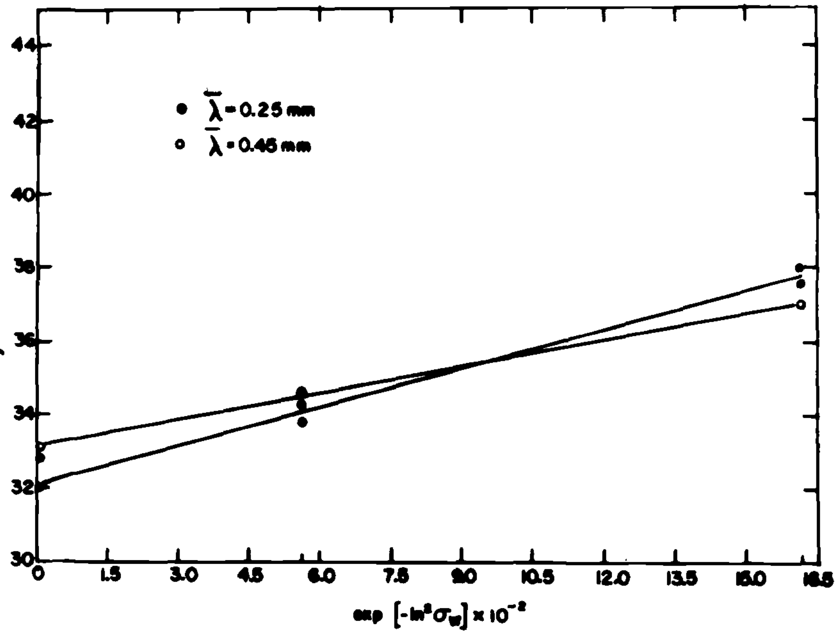

FIG. 5—*Variation of the yield strength in annealed aluminum with the mean grain size and distribution width (after Gokhale and Rhines [*18*]).*

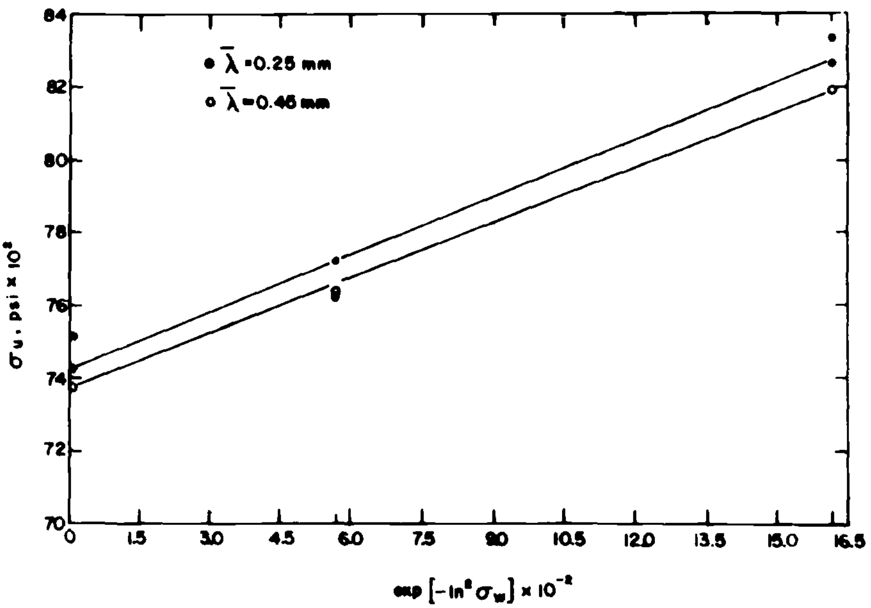

FIG. 6—*Variation of the ultimate tensile strength in annealed aluminum with the mean grain size and distribution width (after Gokhale and Rhines [18]).*

Thus, for example, yield strength, which is measured at small deformations, involves deformation of the largest grains in the distribution and might therefore be very sensitive to the width. Evidently, the description of the plastic response of polycrystals requires a more sophisticated point of view than that currently extant.

Paths of Microstructural Evolution in Sintering

In its simplest form, sintering is the response of a stack of powder to surface tension forces when it is heated to temperatures above roughly seven tenths of its melting point. Contacts between the particles weld at the outset, forming a connected solid network; the porosity is also a connected network, interlaced through the solid. Extensive literature exists on the kinetics of the process and the mechanisms that control the kinetics [*21-24*]. Existing theoretical descriptions of the various stages of the process focus on an element of the structure (interparticle necks in the first stage, isolated pores in the third) and seek to predict the geometric evolution of these elements. As is the case with many microstructural processes, however, the assertion that the behavior of the system can be described in terms of the behavior of a repeating unit is suspect when it is applied to real three-dimensional microstructures.

Stereological techniques have been applied to examine the evolution of pore geometry in loose stack sintering, as well as in pressed and sintered specimens [*25-28*]. Since sintered structures are not geometrically simple, the full utility of stereological methods can be realized because they are geometrically general.

One of the surprises discovered in the course of studies of the path of microstructural change is presented in Fig. 7, which shows the variation of the surface area of the pore/solid interface with the volume fraction of porosity during loose stack sintering and sintering after precompaction [*25,28*]. Two observations are obvious in this plot: the paths are different for these two processing conditions, and, for loose stack sintering, after an initial transient, the surface area varies linearly with the volume fraction.[3] Further, although precompaction displaces the initial geometric state away from the linear correlation, the system rebounds toward this straight line, approaching it closely at high densities.

These results make it clear that density (the volume fraction of porosity) is an insufficient descriptor of the microstructural state of the system. Pore structures evolving from the same initial powder have different surface areas, depending upon their processing history. This and similar observations may form the basis for rationalizing the variation of properties with processing history.[4]

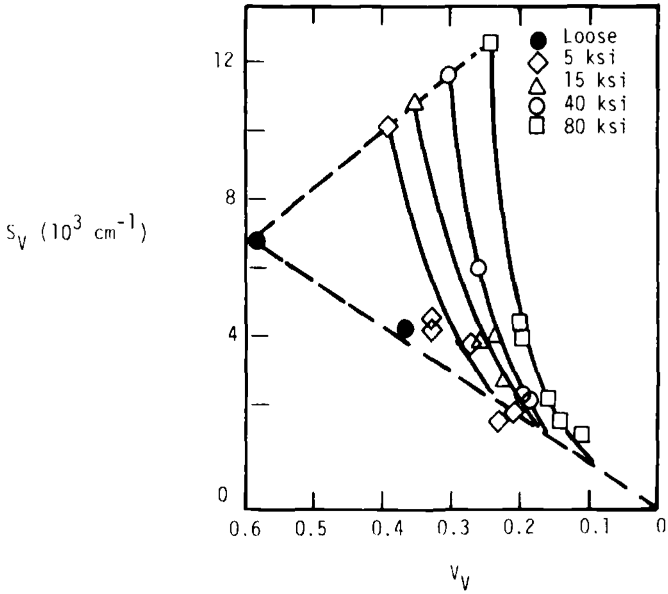

FIG. 7—*Variation of the pore surface area with the pore volume during processing of uranium dioxide powder (after Rhines et al [26]).*

---

[3] The observation that S_v varies linearly with V_v in loose stack sintering is well documented [*25-28*]. The line sketched for loose stack sintering in Fig. 7 relies on these observations in other systems.

[4] Related work [*25*] has shown in addition that it is possible to have two structures that have the same volume fraction *and* surface area of porosity, but different total curvatures and different connectivities.

The tendency for the displaced (precompacted) system to return toward the straight line relation characteristic of loose stack sintering indicates that microstructures along this line may represent an extremum in the allowable range of behavior for a given powder. It has been suggested [*26*] that this configuration represents the minimum surface area that the system may possess for the given volume fraction of porosity and connectivity of the network. Thus, if for a given connectivity and amount of porosity, the surface area is larger than this amount, the system tends to evolve toward values along the straight-line correlation.

Austenitization of a Spheroidized Steel

Stereological methods are particularly suitable for the description of microstructural evolution for dispersed particulate systems. Spheroidized microstructures are evidently relatively simple, so that the evolution of such a structure might be expected to make a good subject for illustrating the power of these methods. A detailed study of the dissolution of cementite particles in a plain carbon eutectoid steel was undertaken with this in mind [*29,30*].

In a typical experiment, quenched and tempered specimens were spheroidized at 690°C for times ranging up to one month. The resulting microstructure exhibited equiaxed carbides, with a volume fraction of 0.13 and a mean intercept length of 3 μm, dispersed in a ferrite matrix. This starting structure was then austenitized by being heated to 750°C, held for a programmed length of time, and quenched to room temperature. A time sequence of such specimens permitted examination of the evolution of the structure as the volume fraction of austenite varied from 0 to 100%.

The surprising result in this investigation is summarized in Figs. 8 and 9. The volume fraction, surface area, and integral mean curvature of the carbide particles were determined as functions of austenitization time. As the carbide and ferrite react to form austenite, it is expected that these three properties of the carbide phase should decrease with time as the carbide is consumed. This is indeed the case; the time axis is reversed in Figs. 8 and 9. It is not expected, however, that these properties should decrease *in proportion to one another*. As an equiaxed particle shrinks three-dimensionally, its volume, surface area, and total curvature are expected to vary respectively with the cube, square, and first power of its lineal dimension. Thus, they cannot change in proportion to each other.[5] Yet, this behavior was observed for all series of specimens examined.

In an attempt to clarify this behavior, specimens of the starting structures were etched to reveal the grain boundaries in the ferrite matrix. The measurements demonstrated that more than 90% of the carbide particles occupied triple points in the ferrite grain structure; further, more than 50% of the ferrite tri-

---

[5] Measurements of the size distribution of lineal intercepts, preparatory to estimation of the distribution of "sphere" diameters, showed that this size distribution did not vary with time. The total number of intercepts decreased with time, but the fraction in each size class did not change.

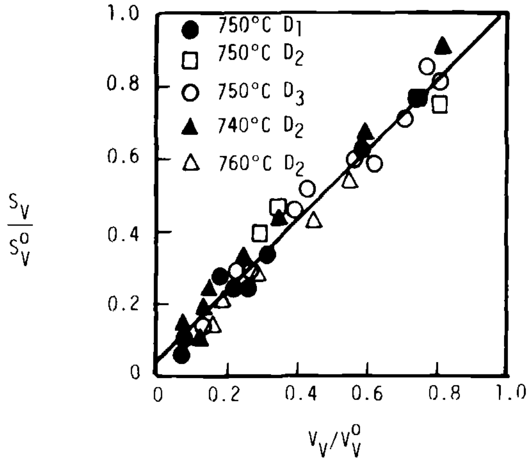

FIG. 8—*Variation of the surface area of carbides with the volume fraction during austenitization of an eutectoid steel (after Gokhale and DeHoff [30]).*

ple points were so occupied. Each triple point in a grain structure represents the intersection of a triple line (grain edge) with the plane of polish. Stereologically, the number of triple points is proportional to the length of triple line in the volume. Thus, in the starting structures the carbide particles lie along the grain edges and cover more than half of the grain edge network.

It is thus evident that a "spheroidized structure" in a eutectoid steel, rather

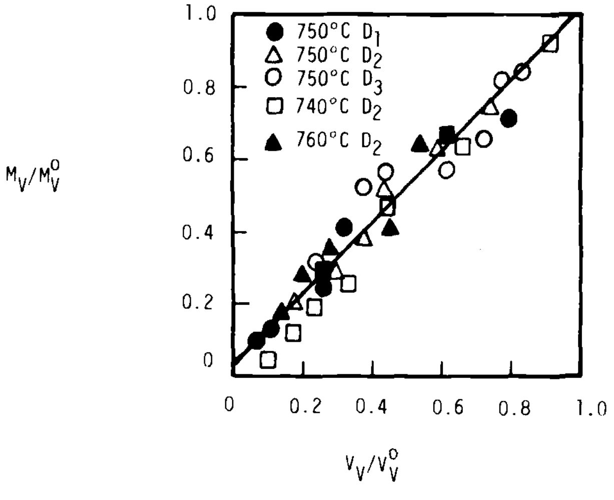

FIG. 9—*Variation of the integral mean curvature,* M_V*, with the surface area of carbides during austenitization of an eutectoid steel (after Gokhale and DeHoff [30]).*

than being a collection of equiaxed particles, is actually an incomplete grain edge network. The carbides exist as fingers lying along the triple lines in the ferrite grain structure. If it is assumed that austenite nucleates at the tips of these fingers, then the dissolution of the carbide particles occurs by shortening these fingers. Geometrically, the carbides are rods, which decrease their volume, surface area, and total curvature by decreasing their length. It is easy to show that all three geometric quantities are proportional to each other, as is displayed in Figs. 8 and 9. Thus, the microstructural evolution during austenitization is very different from that presupposed by existing theories of the process [*31,32*]; austenitization of an eutectoid steel is significantly more complex and interesting than had been postulated.

It might be expected that in a lower carbon steel, in which the volume fraction is significantly less than in the steel that was the subject of this study, the carbides might well be disconnected equiaxed particles describable as "spheroids." On the other hand, in a "spheroidized" hypereutectoid steel with a higher volume fraction, the carbides might well form a completely connected grain edge network. Thus, the geometric nature of the carbides, and hence the austenitization process, might be expected to vary significantly with the carbon content.

Summary

Application of stereology to the study of the microstructural state and its evolution in a variety of processes has produced a series of provocative surprises.

1. The peculiar kinetic behavior observed in recrystallization can be rationalized if it is assumed that recrystallized grains grow two-dimensionally.
2. The average interface velocity in a soap film model of grain growth does not behave even qualitatively in the same way that the rate of change of the mean cell size does.
3. The width of the grain size distribution can vary independent of the mean grain size, and the mechanical properties are at least as sensitive to the width as to the size.
4. The pore surface area varies linearly with the pore volume during most of the course of loose stack sintering; structures displaced from this path during processing tend to return toward it.
5. Carbides in a "spheroidized" eutectoid steel actually form an incomplete grain edge network and dissolve during austenitization by a one-dimensional (rod) shrinkage process.

These examples are representative of stereological studies. It seems evident that unexpected results are a common feature of such studies, and indeed, may be more the rule than the exception.

References

[1] Vandermeer, R. A. and Gordon, P., *Transactions of The Metallurgical Society of A.I.M.E.*, Vol. 215, 1959, pp. 577-588.

[2] English, A. T. and Backofen, W. A., *Transactions of The Metallurgical Society of A.I.M.E.*, Vol. 230, 1964, pp. 396-407.

[3] Leslie, W. C., Plecity, F. J., and Michalak, J. T., *Transactions of The Metallurgical Society of A.I.M.E.*, Vol. 221, 1961, pp. 691-700.

[4] Speich, G. R. and Fisher, R. M. in *Recrystallization, Grain Growth, and Textures*, American Society for Metals, Metals Park, Ohio, 1966, pp. 563-598.

[5] Cahn, J. W. and Hagel, W. C. in *Decomposition of Austenite by Diffusional Processes*, Interscience, New York, 1962, pp. 131-196.

[6] Gokhale, A. M., Iswaran, C. V., and DeHoff, R. T., *Metallurgical Transactions*, Vol. 10A, 1979, pp. 1239-1245.

[7] Underwood, E. E., *Quantitative Stereology*, Addison-Wesley, Reading, Mass., 1970.

[8] DeHoff, R. T. in *Proceedings*, Symposium on Structure-Property Relations, American Society for Metals, Metals Park, Ohio, in press.

[9] DeHoff, R. T. and Cone, F. P. in *Microstructural Science*, Vol. 7, I. LeMay, P. A. Fallon, and J. L. McCall, Eds., Elsevier, New York, 1979, pp. 425-432.

[10] Smith, C. S. in *Metal Interfaces*, American Society for Metals, Metals Park, Ohio, 1952, pp. 65-93.

[11] Rhines, R. N. and Craig, K. R., *Metallurgical Transactions*, Vol. 5, 1974, pp. 413-425.

[12] Steele, J. H., "A Topological Approach to the Study of Microstructure," Ph.D. dissertation, Materials Science and Engineering Department, University of Florida, 1967.

[13] Steele, J. H., *Microstructural Science*, Vol. 1, Elsevier, New York, 1973, pp. 283-295.

[14] Hall, E. O., *Proceedings of the Physical Society (London)*, Vol. 64B, 1951, pp. 747-755.

[15] Petch, N. J., *Journal of the Iron and Steel Institute*, Vol. 174, 1953, pp. 866-873.

[16] Armstrong, R. W., *Advances in Materials Research*, Vol. 4, 1969, pp. 101-167.

[17] Rhines, R. N. and Lemons, J., this publication, pp. 3-28.

[18] Gokhale, A. B. and Rhines, F. N. in *Microstructural Science*, Vol. 11, 1983, pp. 3-12.

[19] Rhines, F. N., Ellis, R. A., and Gokhale, A. B., *Scripta Metallurgica*, Vol. 15, 1981, pp. 783-785.

[20] Dallavalle, J. M., *Micromeritics*, 2nd ed., Pitman, New York, 1948.

[21] Kuczynski, G. C., *Transactions of the American Institute of Metals*, Vol. 185, 1949, pp. 169-176.

[22] Kuczynski, G. C. in *Sintering and Related Phenomena*, G. C. Kuczynski, Ed., Plenum Press, New York, 1976.

[23] Coble, R., *Journal of the American Ceramic Society*, Vol. 41, 1958, pp. 55-64.

[24] Johnson, D. L., *Journal of the American Ceramic Society*, Vol. 53, 1970, pp. 574-578.

[25] Aigeltinger, A. H. and DeHoff, R. T., *Metallurgical Transactions*, Vol. 6A, 1975, pp. 1853-1861.

[26] Rhines, F. N., DeHoff, R. T., and Kronsbein, J., "A Topological Study of Sintering," Final Report, AEC Contract AT-(40-1)-2581, Atomic Energy Commission, Washington, D.C., 1969.

[27] Whitney, E. D. and DeHoff, R. T. in *Ceramic Microstructures '76*, R. M. Fulrath and J. A. Pask, Eds., Westview Press, Boulder, Colo., 1976, pp. 81-88.

[28] Rummel, R. A., LaBuff, H. P., Rhines, F. N., and DeHoff, R. T. in *Modern Developments in Powder Metallurgy*, Vol. 1, Plenum Press, New York, 1966.

[29] Gokhale, A. M., "A Study of the Global Evolution of Microstructures," Ph.D. dissertation, University of Florida, 1977.

[30] Gokhale, A. M. and DeHoff, R. T., *Metallurgical Transactions A*, in press.

[31] Judd, R. R. and Paxton, H. W., *Transactions of The Metallurgical Society of A.I.M.E.*, Vol. 242, 1968, pp. 206-211.

[32] Speich, G. R. and Richards, M. J., *Transactions of The Metallurgical Society of A.I.M.E.*, Vol. 245, 1969, pp. 1073-1080.

Ervin E. Underwood[1]

Practical Solutions to Stereological Problems

REFERENCE: Underwood, E. E., "**Practical Solutions to Stereological Problems,**" *Practical Applications of Quantitative Metallography, ASTM STP 839,* J. L. McCall and J. H. Steele, Jr., Eds., American Society for Testing and Materials, Philadelphia, 1984, pp. 160-179.

ABSTRACT: Three microstructural topics of interest to metallurgists are considered from the standpoint of their current status. They are (1) the so-called magnification effect, in which measured microstructural quantities have different values at different magnifications; (2) the estimation of N_V, the number of particles or grains per unit volume, approximated from simple planar measurements rather than by the laborious 2-*d* to 3-*d* transform calculations; and (3) the characterization of profiles, in which five parameters are explored for their suitability in describing the average properties of irregular planar curves.

Although these stereological problems are still unsolved in the general sense, there has been considerable activity in these areas over the years. Current thoughts and approaches are summarized, with emphasis on practical applications and solutions.

KEY WORDS: quantitative metallography, profile analysis, stereology, quantitative fractography, magnification effect, volume number density

Magnification Effect

A problem that has emerged periodically over the past 30 years or so is called here the "magnification effect," in the absence of a convincing explanation of its origin. The term refers to the simple observation that measurements made on the same microstructure at different magnifications yield different results. This puzzling phenomenon is quite general—it has been noted in microstructural studies of grains in single-phase alloys, particles in alloys, slag inclusions in weld metal, nonmetallic inclusions in steels, endoplasmic reticulum of the rat, and porosity in irradiated fuel. Moreover, careful analyses of the experimental conditions have confirmed the existence of the effect even when the optical requirements for resolution have been satisfied.

---

[1] Professor of metallurgy, Fracture and Fatigue Research Laboratory, Georgia Institute of Technology, Atlanta, Ga. 30332-0102.

The author first became aware of the effect in the late 1950s, in a study of the spacings in a lamellar gold/nickel alloy.[2] Photomicrographs taken on the same specimen at different magnifications up to ×50 000 showed rapidly decreasing values of spacing at the lower (optical) magnifications, with a leveling off at higher (electron) magnifications. Figure 1 sketches the essential elements of this curve.

In general, two types of curves have been observed in plots of the microstructural quantity versus the magnification. In the direct counting type of measurement, such as the area density, or number per unit area, N_A, the density shows a relatively rapid increase at early magnifications, then levels off at higher magnifications. The other type of curve, in which a spacing, for example, is plotted versus the magnification, shows the opposite behavior. There is a relatively rapid falloff in the measured quantity at low magnifications, then a leveling off at higher magnifications.

The governing principle that seems to rationalize both types of behavior is that the investigator "sees" more at higher magnifications [*1*].[3] Thus, more grains or particles are counted at higher magnification, so the values of N_A are greater. The same is true for lamellae, but the spacings become *smaller* as more lamellae are counted.

Background

In evaluating this effect, one must ensure that all the features under examination are properly revealed, and that sufficient observations have been made to achieve a suitable precision. Furthermore, there are several optical requirements that must be satisfied [*2*]:

1. The effective numerical aperture (NA) of the objective must be known.

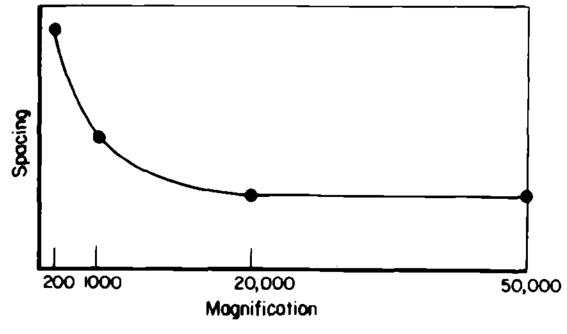

FIG. 1—*Spacings in a lamellar gold/nickel alloy versus magnification (qualitative).*[2]

---

[2] Underwood, E. E., Battelle Memorial Institute, Columbus, Ohio, unpublished research, 1958.

[3] The italic numbers in brackets refer to the list of references appended to this paper.

2. The microscope must provide for "critical illumination" of the measured features in the specimen.

3. The magnification should not be less than the "highest useful magnification" (HUM), which is equal approximately to 500 NA in optical microscopes, nor should a significant amount of empty magnification be used.

The resolving power (RP) is given by

$$\mathrm{RP} = \frac{2\mathrm{NA}}{\lambda} \tag{1}$$

where λ is the wavelength of the illuminator. The reciprocal of RP is the resolution, δ, the minimum distance that can be resolved by the objective. This equation is valid when the specimen is critically illuminated; that is, it acts as a self-luminous object. Failure to meet this requirement causes a decrease in resolution. Consequently, measured lamellar spacings, for example, would appear to be larger than their true value. On the other hand, particle densities would appear smaller than their true value.

Another factor of importance here is the HUM. For magnifications less than HUM, the full resolving power of the microscope objective lens is not being utilized. That is, detail resolved by the objective lens is not being sufficiently magnified to be resolved by the naked eye.

Examples

In 1949, Kostron [*3*] noted the effects of magnification on measurements of grain size in an aluminum/copper/magnesium alloy. He found a 23% decrease in the mean grain size between measurements taken at ×100 and ×1000, and a 30% increase in the number of grains per unit area over the same magnification range. Figure 2 shows the average values of measurements made by six observers.

These results are consistent with the postulate that the observer "sees" more at higher magnifications. More grains are counted as the magnification increases, so the curve of N_A rises. On the other hand, the mean grain area, $\bar{A}$, must decrease if more grains are counted. These trends are both observed in Fig. 2.

Measurements of the surface area per unit volume, S_V, and the volume fraction, V_V, were conducted on a rat liver structure at magnifications between ×18 000 and ×170 000 [*4*]. Examples of the results are shown in Fig. 3 for both types of measurements. In both cases there is an increase by a factor of 3 to 4 at magnifications up to ×100 000, and thereafter the curves remain virtually unchanged beyond that magnification. It is noteworthy that, although the curves are essentially parallel, two different types of measurement are involved: a point count for V_V and an intersection count for S_V.

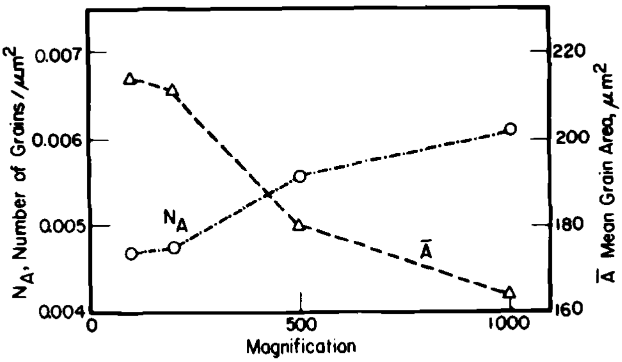

FIG. 2—*Number per unit area and mean area of grains in an aluminum/copper/magnesium alloy versus magnification* [3].

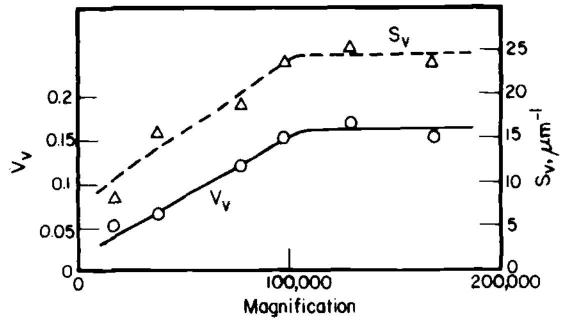

FIG. 3—*Volume fraction and surface area per unit volume in a rat liver versus magnification* [4].

As a final example of this effect, the results of a study of porosity in irradiated fuel are quoted.[4] Using square grids on clear plastic sheet, values of porosity, P_P [that is, the pore volume fraction $(V_V)_p = (P_P)_p$], were obtained on photomicrographs from the same specimen at two different magnifications. The results of the point count measurements gave 0.233 at ×100 and 0.429 at ×500, clearly establishing a strong effect due to magnification.

It can be seen that this effect is a general one. Although it has not been completely explained at this time, two choices are possible experimentally to circumvent any problems due to the magnification effect. One way is to use one (suitable) magnification for all comparative work. This choice is not always feasible, however. The other way is to use a larger magnification that falls along the level part of the curve, where changes in the magnification affect the results only slightly, if at all. In any event, the researcher should be aware of the possible effects of changing his magnifications.

---

[4] Unpublished analysis by the author.

Estimation of N_V

A perennial problem for metallurgists is the determination of N_V, the number of particles or grains per unit volume. As a "volume density," N_V is a three-dimensional parameter that is difficult to obtain accurately from two-dimensional data by conventional methods. Generally, some simple particle shape must be assumed, such as a sphere. The frequency distribution of particle section areas (or intercept lengths) is determined experimentally, which permits the calculation of the histogram of the number per unit volume versus the particle size. The total value of N_V is then obtained by summing all values from the histogram [*5,6*].

This indirect approach to the value of N_V is fraught with uncertainties caused by the oversimplified assumptions. Moreover, the calculations are laborious and time-consuming unless automatic image analysis is used, and this is not always possible unless there is sufficient contrast between the particles and matrix. As a consequence of these difficulties, many approximate relationships have been proposed that give an average value of N_V based on simple planar measurements.

General Equations [7]

In general, N_V for a system of particles is defined simply by

$$N_V = \frac{V_V}{\bar{V}} \tag{2}$$

where $\bar{V}$ is the mean particle volume. For a single-phase system of grains, $V_V = 1$, and N_V is reciprocally related to $\bar{V}$. Although V_V can be obtained readily enough, $\bar{V}$ presents problems except in unusual cases. No shape assumptions are required for Eq 2.

A statistically correct equation for a polydispersed system of convex particles is [*8*]

$$N_V = \frac{N_A}{\bar{D}} \tag{3}$$

where N_A is the number of particle sections per unit area, and $\bar{D}$ is the mean three-dimensional tangent diameter. Since N_A is obtained easily, the problem becomes one of determining $\bar{D}$. This quantity is usually difficult to obtain, except perhaps in thin foils or when particles conform to a simple shape. As a practical solution, if $\bar{D}$ can be estimated, N_V can be calculated according to Eq 3.

Convex Particles or Grains: Same Shape and Size

If we can reasonably assume that the particles or grains all have the same size and shape, then N_V can be determined either from two planar measurements or from calculated values of $\bar{D}$.

In terms of planar measurements, we can express N_V as [*9*]

$$N_V = K \frac{N_A^2}{N_L} \tag{4}$$

where N_L is the number of particles intercepted per unit length of a test line. The quantity K is a shape-dependent constant, equal to $\bar{A}'/\bar{H}'^2$, where the terms refer respectively to the mean projected area and mean projected height. Values for K are available in the literature [*10*] and are given for a few simple shapes in Table 1.

Thus, for spheres of diameter D, Eq 4 would read

$$N_V = 0.785 \frac{N_A^2}{N_L} \tag{5}$$

using the value supplied in Table 1.

The N_V value can also be determined by several other equations, provided $\bar{D}$ is known. Table 1 lists values of $\bar{D}$ for some common particle or grain shapes. When appropriate, these values can be used in Eq 3.

TABLE 1—*Values of* $\bar{D}$ *and* K *for simple particle shapes [*10*].*

Particle	$\bar{D}$	$\bar{K}$
Sphere (radius, r)	$2r$	0.785
Disk (radius, r)	$\pi r/2$	0.637
Prolate spheroid ($a = 2b$)	$2.76b$	0.703
Oblate spheroid ($a = 2b$)	$1.71a$	0.743
Cube (edge, a)	$3a/2$	0.667
Square plate (edge, a)	a	0.500
Truncated octahedron (edges, a)	$3a$	0.744
Pentagonal dodecahedron (edges, a)	$2.64a$	0.781

The value of D for a monodispersed system of spheres can also be found from simple planar measurements of the two-dimensional section diameters. In one equation we have [*11, 12*]

$$D = \frac{4}{\pi}\bar{d} \tag{6}$$

where $\bar{d}$ is the mean section diameter. From another analysis we have the relationship [*13, 14*]

$$D = \frac{\pi}{2}\left(\overline{\frac{1}{d}}\right)^{-1} = \frac{\pi}{2\bar{m}} \tag{7}$$

where $(\overline{1/d}) = \bar{m}$ is the mean value of the reciprocals of the section diameters. It would appear that D could be obtained equally well from either Eq 6 or Eq 7.

However, in a computer experiment in which a sphere was sectioned randomly many times, Loud[5] found that the calculated value of D converged to the true value much quicker using Eq 6. For instance, the value of D obtained with only 25 sections differed from the true value by less than 0.1% when using Eq 6. With Eq 7, on the other hand, 800 sections gave an estimated value of D that was off by nearly 1%. Moreover, Eqs 6 and 7 are both very sensitive to the loss of small sections, making the estimation of D less accurate than expected.

Convex Particles or Grains: Same Shape but Different Sizes

Two procedures have been described for convex objects of simple shape. In one, developed by Fullman [*15*], N_V for spheres of various diameters, D_i, is expressed by

$$N_V = \frac{2}{\pi}\bar{m}N_A \tag{8}$$

where $\bar{m}$ is the mean of the mean values of $\bar{m}_i$ for all sphere sizes (or class intervals). As indicated previously, m_i is the reciprocal of the i^{th} section diameter, $1/d_i$. This equation is also obtained by substituting Eq 3 in Eq 7.

Durand and Warren [*16*] also considered this problem, starting with Eq 4, which applies to particles of the same size and shape. If a size distribution is introduced, then it is necessary to have the first two moments of the size distribution, m_1 and m_2, averaged with respect to N_V. We then get

$$N_V = \mathrm{K}\frac{m_2 N_A^2}{m_1^2 N_L} \tag{9}$$

---

[5] Loud, A. V., New York Medical College, Valhalla, N.Y., personal communication, September 1981.

for particles of constant shape but a distribution of sizes. For a typical log-normal size distribution, (that is, skewed to the right), the value of m_2/m_1^2 is given as 1.346. Thus, for a size distribution of pentagonal dodecahedra, for example, $K = 0.781$ (from Table 1) would be substituted in Eq 9 along with the value of 1.346 for the ratio of moments. For a size distribution of spheres, Eq 9 would appear as

$$N_V = \frac{0.785(1.346)N_A^2}{N_L} \tag{10}$$

Comparison with Eq 5, for spheres of fixed shape and size, shows that values of N_V will be larger when calculated from Eq 10.

Approximate Relationships for Real Microstructures

Many relationships have been proposed for obtaining N_V in real microstructures in terms of planar quantities. However, the variations in both size and shape make the results only approximate at best.

One of the better relationships for N_V was obtained by Saltykov [*17*] for tempered carbon particles in malleable cast iron, namely

$$N_V = 2.38N_A^{1.6} \tag{11}$$

which was valid for over six orders of magnitude in N_V. Calculated values of N_V were plotted against measured values of N_A, yielding the constants given in Eq 11.

Gulliver [*18*] proposed an approximate equation for spherical particles or grains

$$N_V = 0.667N_A^{1.5} \tag{12}$$

which obviously yields smaller values of N_V than Eq 11.

Equations applicable to space-filling grains have been offered by several investigators. For example, equations couched in terms of S_V or P_L give [*19*]

$$N_V = 0.422P_L^3 \tag{13}$$

where P_L is the number of intersections of the test line, per unit length, with grain boundary traces. A more accurate representation of N_V in terms of two planar quantities was developed by Hanson using computer-generated space-filling grains [*20*]. The expression

$$N_V = \left[\left(\frac{5.8322}{N_A}\right)^{1/2} - \frac{1.4552}{N_L}\right]^{-3} \tag{14}$$

depends only on measurements of N_A and N_L. Hanson also claims that Eq 14 can be used for particulate alloys. For uniformly sized spherical inclusions, he predicts a sphere size within 3.6% of the actual size.

Comparison of Results

In order to compare the particle equations for N_V, it is necessary to have the proper planar data. Values of V_V, N_A, and N_L have been compiled for nodular graphite in cast iron[6] obtained under different cooling rates.

The results are plotted in Fig. 4 for Eqs 5, 10, and 11. Gulliver's [*18*] relationship, Eq 12, lies below these three curves but is not shown; similarly, the simple $N_V = N_A^2$ relationship proposed by Schwartz [*21*] lies above these three curves. Thus, it appears that the magnitude of the calculated value of N_V depends primarily on the exponent to N_A. But, for the purpose of assessing the various equations for N_V, it would seem that Eq 11 is probably "best," at least for equiaxed particles. Also worthy of note is Eq 9, if constant particle shape can be assumed safely.

As for the "best" N_V equation for space-filling metal grains, the two-parameter Eq 14 seems very good. Of course, one can determine the best-fitting equation for a particular microstructure by preliminary calculations using the full 2-*d* to 3-*d* transform procedure for N_V [*5*].

Determination of N$_V$ *Using Projected Quantities*

The relationships just described for N_V depend on quantities measured in the plane of polish. If transmission electron microscopy through thin foils is

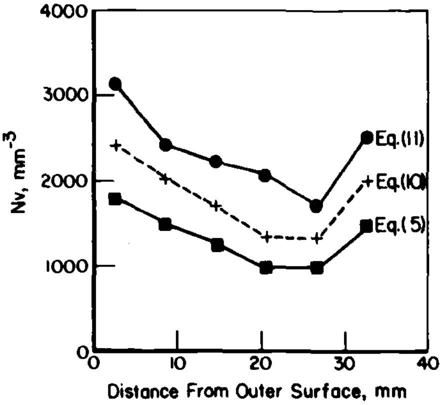

FIG. 4—*Comparison of calculated values of* N$_V$ *for nodular graphite in cast iron.*

---

[6] Unpublished research by the author, 1983.

feasible, or required, this permits other possibilities for estimating N_V. In many such cases, mixed measurements are necessary, that is, measurements from both the plane of polish and the projected image. For example, $\bar{D}$ for convex or fairly equiaxed particles can be estimated quite well in the projected image, provided V_V is low. It may then be possible to use Eq 3 to obtain N_V.

In terms of projected quantities only, a basic equation for convex particles in a thin foil of thickness t is given by [22]

$$N_V = \frac{N'_A}{t} \tag{15}$$

where N'_A is the number of particle images per unit area of the projection plane. This equation does not provide for overlap or truncation of particles at the foil surfaces.

An example of the magnitude of the corrections necessary to compensate for particle truncation and overlap in a thin foil is afforded by equiaxed particles in an aluminum alloy [23]. The quantities measured in the projection plane are $A'_A = 0.108$ (where A'_A is the area fraction of particle images in the projection plane), $N'_A = 8.47\ \mu\text{m}^{-2}$, and $\bar{D} = 0.1277\ \mu\text{m}$. The foil thickness, t, was estimated to be $0.2\ \mu\text{m}$.

The uncorrected value of N_V is given by

$$N_V = \frac{N'_A}{t} = \frac{8.47}{0.2} = 42.3 \mu\text{m}^{-3} \tag{16}$$

When truncation is allowed for, we have

$$N_V = \frac{N'_A}{\bar{D} + t} = \frac{8.47}{0.1277 + 0.2} = 25.9 \mu\text{m}^{-3} \tag{17}$$

which represents a decrease in N_V of almost 39%. Qualitatively, a decrease would be expected since the correction for truncation eliminates those particle images for particle segments whose centers do not lie within the foil.

When the corrections for both truncation and overlap are considered, the equation becomes [24]

$$N_V = \frac{N'_A + M'_A}{\bar{D} + t} \tag{18}$$

where M'_A, the number of particle images lost in the projection plane because of overlap, is given by

$$M'_A = \frac{3}{2} V_V \frac{t}{\bar{D}} N'_A \tag{19}$$

Inserting the measured values and the corrected volume fraction of $V_V = 0.0341$ in Eqs 19 and 18, we have

$$N_V = \frac{8.47 + 0.679}{0.1277 + 0.2} = 27.9 \mu\text{m}^{-3} \tag{20}$$

which represents about an 8% increase over the value obtained in Eq 17 for truncation alone. This result would be expected qualitatively since the overlap correction restores the images lost by image overlap.

If these results are representative of those found in customary alloys, then the corrections are well worth calculating. However, the assumptions and derivations of the projection equations are not as rigorous as those for planar sections, so extreme accuracy cannot be expected.

Characterization of Profiles

In many microstructural studies, the geometrical characteristics of an irregular plane curve are desired. Examples of such curves occur in the planar sections cut through rough surfaces obtained by fracture, corrosion, abrasion, or deformation, or in the silhouette of an irregular metal powder.

The geometrical and stereological quantities that can be measured from an irregular curve are rather limited. The more important ones are included in the following list:

(*a*) the true length of the curve,
(*b*) the projected length of the curve,
(*c*) the straight-line distance between endpoints of the curve,
(*d*) the x, y coordinates of points along the curve,
(*e*) the angular distribution of tangents at points along the curve,
(*f*) the length distribution of linear segments along the curve (if present), and
(*g*) the local curvature of points along the curve.

All of these quantities would not be measured at any one time, of course. Rather, a selected few would be chosen in order to relate important attributes of the curve to the investigated material properties or behavior. The measurements are most conveniently performed with semiautomatic image analysis equipment. In fact, with a suitable computer program, measurement of the coordinates alone will yield most or all of the items listed.

Parameters

Various parameters have been proposed to represent some aspect of a rough planar curve. A few of the more useful ones will be discussed briefly, and then some numerical examples will be provided.

1. The lineal roughness parameter, R_L, was defined by Pickens and Gurland [25] as the ratio

$$R_L = \frac{L_t}{L'} \tag{21}$$

where L_t is the true length of the curve, and L', the projected length, is measured along a selected reference direction. Figure 5 indicates the essential elements of this parameter. The values of R_L can vary from one (for a straight line parallel to the projection line), to a very large value (depending on the roughness of the curve). If overlap occurs, then the total projection [26], L'', may be the quantity of choice, instead of the simple apparent projection, L'.

2. Another roughness parameter, the so-called profile roughness parameter, R_P, was proposed by Behrens.[7] It is basically an averaged ratio of height to spacing (or amplitude to period) for the peaks along an undulating curve. It is defined by

$$R_P = \frac{1}{2L_T} \int_{y_1}^{y_2} P(y)dy \tag{22}$$

where y_1 and y_2 give positions of the test line, of length L_T, below and above the profile where no intersections are possible. The test line is displaced parallel to a selected reference line, at positions between y_1 and y_2. The number of intersections of the test line at each position, $P(y)$, is counted.

The working equation can be expressed as

$$R_P = \frac{\Delta y}{2L_T} \sum_i P_i \tag{23}$$

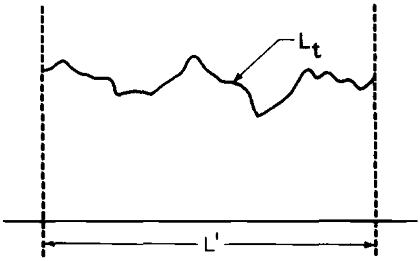

FIG. 5—*Roughness parameter* $R_L = L_t/L'$ *for an irregular planar curve* [25]: L_t *is the true length;* L' *is the projected length.*

---

[7] Behrens, E. W., Armstrong Cork Co., Lancaster, Pa., personal communication, September 1977.

where Δy is the constant displacement of the test line, and ΣP_i is the total number of intersections of the test line with the profile. Figure 6 shows the relationship of the test line and its positions to the curve. This is an excellent parameter with good physical meaning.

3. The arithmetic roughness average, $\mu(AA)$, is used in assessing the roughness of machined surfaces. It is the average vertical deviation of the curve from a central horizontal reference line, usually the mean line through the curve, although the exact location does not affect the results. It is defined by

$$\mu(AA) = \frac{1}{n} \sum_{i}^{n} |\Delta y_i| \tag{24}$$

where $|\Delta y_i|$ is the absolute value of the distance between the curve and the reference line at various positions, i, along the curve. Instead of measuring Δy_i at peak and valley positions only, it may be advantageous to measure Δy_i at regular increments along the reference line. Curves of the same shape have the same value of $\mu(AA)$, even though their sizes are different.

4. A similar parameter to the arithmetic average is the root-mean-square roughness average, μ(rms), which can be expressed by

$$\mu(\text{rms}) = \left[\frac{1}{n} \sum_{i}^{n} (\Delta y_i)^2 \right]^{1/2} \tag{25}$$

where the vertical deviations are first squared and averaged before taking the square root. This parameter is dependent on size as well as shape, since curves of the same shape but of different sizes give different values of μ(rms). The location of the reference line will affect the results, so a standard procedure must be adopted when evaluating curves.

5. The degree of orientation, Ω_{12}, of a line in a plane is a measure of the extent of alignment of the elementary (linear) segments that comprise the profile

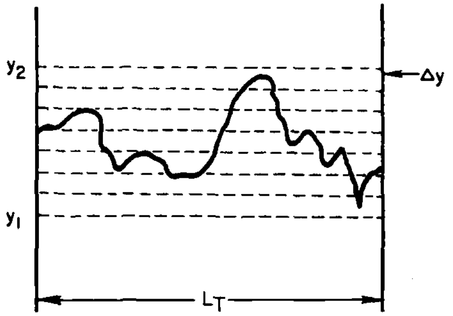

FIG. 6—*Profile roughness parameter* P_R,[7] *for an irregular planar curve. The test line positions are shown as dashed lines.*

[*27*]. In essence Ω_{12} is the ratio of the length of the segments oriented parallel to a selected reference direction, to the total line length. That is

$$\Omega_{12} = \frac{L_{\text{oriented}}}{L_{\text{total}}} \tag{26}$$

The working equation is given by

$$\Omega_{12} = \frac{(P_L)_\perp - (P_L)_\parallel}{(P_L)_\perp + 0.571(P_L)_\parallel} \tag{27}$$

where $(P_L)_\perp$ and $(P_L)_\parallel$ are the number of intersections of the profile per unit length of a test grid of parallel lines, measured in the perpendicular, $\perp$, and parallel, $\parallel$, directions, respectively, to the reference line. The values of Ω_{12} vary between *zero* (for complete absence of orientation, that is, the linear elements are completely random) to *one* (for complete orientation, that is, all the linear elements lie parallel to the reference line). Intermediate values, of course, represent partially oriented curves, with both oriented and random components.

Note that the physical interpretations of these five parameters are quite different. The R_L value is based on length comparisons, while R_P is related to mean height-to-width ratios. The terms $\mu(AA)$ and $\mu(\text{rms})$ measure the vertical deviations of the curve from a central horizontal line, while Ω_{12} expresses the ratio of oriented segment lengths to the total line length. For any particular curve, it is possible that more than one parameter, or some form of combined parameters, may be required to express its important characteristics adequately.

Examples

A selection of profiles from different sources is analyzed next, using appropriate parameters from among those just discussed. The examples include profiles (or traces) from (1) a fatigue-fractured Ti-28V alloy, (2) a cavitation-damaged surface, (3) precision matching of a fatigue crack in nickel, and (4) a particle silhouette.

Example 1—Figure 7 shows a portion of a polished and etched vertical section through the fracture surface of a fatigued Ti-28V alloy [*28*]. The surface has been coated with copper to preserve the trace details. Results have been documented for the two types of faceted regions—specifically, where multi-faceted or single-facet crack growth is observed. Table 2 gives the values obtained.

The negative changes encountered with the first four parameters in Table 2 indicate that the "roughness" decreases when proceeding from the multi-

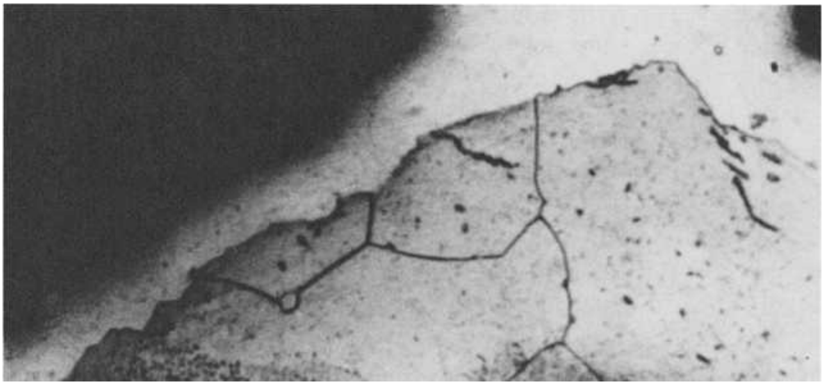

FIG. 7—*Vertical section through a fracture surface of Ti-28V alloy* [28] *(×200)*.

TABLE 2—*Profile roughness parameters for a Ti-28V alloy fracture surface (Fig. 7)* [28].

Parameter	Multifaceted Region	Single-Facet Region	Change, %
Lineal roughness parameter, R_L	1.14	1.06	−7.0
Profile roughness parameter, R_P	0.476	0.349	−26.7
Arithmetic roughness average, $\mu(AA)$	6.58	2.22	−66.3
Root-mean-square roughness average, μ(rms)	7.60	2.88	−62.1
Degree of orientation, Ω_{12}	0.419	0.553	+32.0

faceted region to the single-facet region. The positive increase in Ω_{12} also means that the "roughness" is decreasing: that is, the trace is "flatter" in the single-facet region. These are large changes, except for R_L, and in general, the parameters with the larger changes are to be preferred.

Example 2—The surface roughness traces obtained from rolled aluminum after increasing amounts of surface cavitation [*29*] are shown in Fig. 8. Two parameters were used in the roughness analysis: R_L and R_P. The results are summarized in Table 3.

Both parameters increase in a regular manner. Again the changes in R_L are not as great as those in R_P, so the latter parameter would be favored, other things being equal.

Example 3—In a rather unique fractographic study, Krasowsky and Stepanenko [*30*] obtained two pairs of matching profiles of fatigue striations in nickel using a stereoscopic method. The drawings of these four curves are reproduced here in Fig. 9, (Fig. 8 in Ref *30*), where the pairs of matching profiles are identified as I′ and II′, and I″ and II″.

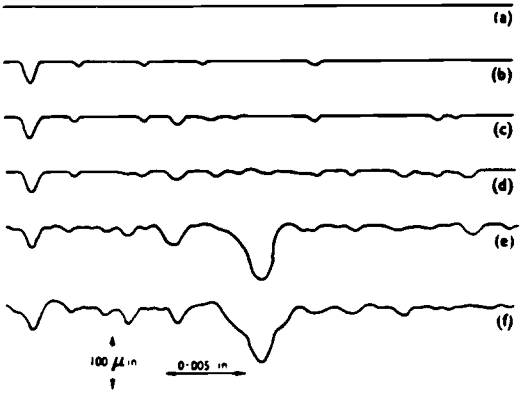

FIG. 8—*Traces obtained from a cavitated aluminum surface* [29].

TABLE 3—*Surface roughness due to cavitation (Fig. 8) [29].*

Curve[a]	Time, s	R_L	R_P
(*a*)	0	1.	0
(*b*)	10	1.062	0.065
(*c*)	20	1.065	0.086
(*d*)	30	1.069	0.127
(*e*)	60	1.245	0.287
(*f*)	120	1.278	0.340

[a] From Fig. 8.

In order to assess the degree of matching of these pairs of curves, measurements were made of R_L and R_P. The results are tabulated below in Table 4, including duplicate values for the same curves shown separately.

Of major interest is the correspondence between (ostensibly) matching fracture profile curves, that is, between I′ and II′, and between I″ and II″. The maximum differences between these pairs are about 8 and 2%, respectively, for R_L, and about 20 and 8%, respectively, for R_P. Thus, we would not label these pairs of curves as "matching," at least not in a strict geometrical sense.

Example 4—The final application of roughness parameters in this paper deals with the silhouette of a metal particle [*31*], shown in Fig. 10*a*. The polar plot of R versus θ, when replotted on cartesian coordinates, appears as in Fig. 10*b*. Four parameters were calculated for this curve, and the results are given in Table 5.

Although all these parameters appear reasonable, any one shows to best advantage when used in a comparative manner. Also, as mentioned previously, some of the numerical results depend on the scale used. It may be more useful

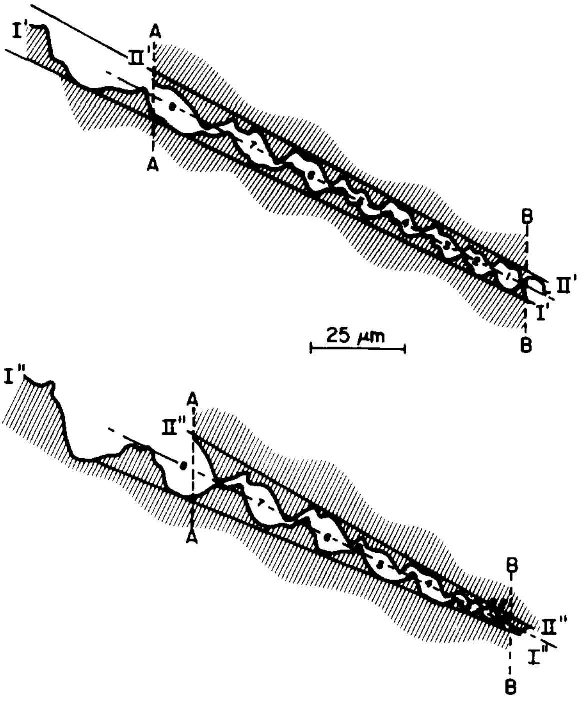

FIG. 9.—*Matching profiles of fatigue striations in nickel* [30].

TABLE 4—*Analysis of matching profiles from a fracture surface in nickel (Fig. 9) [30].*

Parameter	Profiles I′ and II′		Profiles I″ and II″	
R_L				
Figure 9	1.164	1.251	1.251	1.231
Duplicate	1.215	1.242	1.265	1.240
R_P				
Figure 9	0.330	0.392	0.347	0.340
Duplicate	0.305	0.367	0.366	0.338

to normalize the scale-dependent parameters in order to eliminate this factor as a variable.

Other parameters, not considered here, are possible. For example, the fractal dimension of an irregular curve [*32*] can be measured readily. A value of 1.05 was determined for the fracture trace illustrated in Fig. 7,[8] and additional

---

[8] Kaye, B. H., Laurentian University, Sudbury, Ontario, Canada, personal communication, 1982.

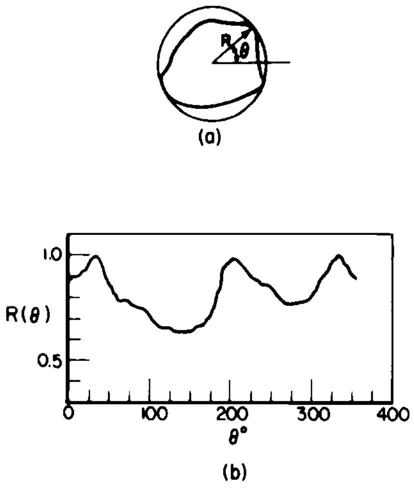

FIG. 10—*Analysis of particle profile roughness* [31]: (a) *polar plot,* (b) *rectilinear plot.*

TABLE 5—*Analysis of a particle profile (Fig. 10) [31].*

Parameter	R_L	R_P	$\mu(AA)$	μ(rms)
Value	1.487	0.444	4.53	5.11

work is being performed with this parameter. Perhaps the best application of the fractal dimension lies in the relative comparison of values determined for different curves. It also appears to be an excellent shape parameter, which subject, however, is outside the scope of this paper. Particle silhouettes have also been analyzed differently in a stereological treatment of particle characteristics [*33*].

A problem not considered specifically in this paper is how best to handle rough or irregular curves with fine detail superimposed on an undulating trace of a much greater period [*34*]. Moreover, this paper has not discussed experimental methods of obtaining the traces; the topic is a large one in its own right. And, a major problem inherent in all dimensionless ratios is that they are independent of size. One answer, of course, is to use both size-dependent and size-independent parameters to specify the rough curve completely.

The five parameters selected in this study are considered useful for describing the average properties of typical irregular planar curves. As to which parameter to use, however, the choice will depend on the characteristics of the particular curve obtained and on the important attributes to be tracked. Perhaps modified parameters or procedures will be necessary to reflect the particular changes of interest. As far as fracture is concerned, the roughness parameter, R_L, appears to play a decisive role in the quantification of fracture surfaces and the features therein [*28*].

References

[*1*] Underwood, E. E., *Transactions of the American Society for Metals*, Vol. 54, 1961, pp. 743-745.

[*2*] Gregory, B., Hall, H. T., and Bullock, G., *Transactions of the American Society for Metals*, Vol., 54, 1961, pp. 745-746.

[*3*] Kostron, H., *Archiv für Metallkunde*, Vol. 3, No. 6, 1949, pp. 193-203.

[*4*] Paumgartner, D., Losa, G., and Weibel, E. R., "The Influence of Optical Resolution on the Estimation of Stereological Parameters of Endoplasmic Reticulum and Mitochondria in Rat Hepatocytes," Paper No. 21, *Abstract Bulletin*, Fifth International Congress for Stereology, Salzburg, Austria, September 1979.

[*5*] Underwood, E. E., *Quantitative Stereology*, Addison-Wesley, Reading, Mass., 1970, Chapter 5, pp. 109-147.

[*6*] Exner, H. E., *International Metals Review*, Vol. 17, 1972, pp. 25-49.

[*7*] Underwood, E. E., *Quantitative Stereology*, Addison-Wesley, Reading, Mass., 1970, pp. 86-89.

[*8*] Underwood, E. E., *Quantitative Stereology*, Addison-Wesley, Reading, Mass., 1970, p. 96.

[*9*] Underwood, E. E., *Quantitative Stereology*, Addison-Wesley, Reading, Mass., 1970, p. 94.

[*10*] Underwood, E. E., *Quantitative Stereology*, Addison-Wesley, Reading, Mass., 1970, pp. 90-93.

[*11*] Saltykov, S. A., *Stereometrische Metallographie*, VEB Deutscher Verlag für Grundstoffindustrie, Leipzig, 1974, p. 270.

]*12*] Fullman, R. L., *Transactions of the American Institute of Mining, Metallurgical, and Petroleum Engineers*, 1953, p. 449.

[*13*] Saltykov, S. A., *Stereometrische Metallographie*, VEB Deutscher Verlag für Grundstoffindustrie, Leipzig, 1974, p. 271.

[*14*] Fullman, R. L., *Transactions of the American Institute of Mining, Metallurgical, and Petroleum Engineers*, 1953, p. 450.

[*15*] Fullman, R. L., *Transactions of the American Institute of Mining, Metallurgical, and Petroleum Engineers*, 1953, p. 450.

[*16*] Durand, M.-C. and Warren, R., *Proceedings*, Third European Symposium on Stereology, Ljubljana, Yugoslavia, 1981, pp. 109-114.

[*17*] Saltykov, S. A., *Metallurg*, Vol. 14, No. 8, 1939, p. 10 (in Russian); Brutcher Translation No. 951.

[*18*] Gulliver, G. H., *Institute of Metals, Journal*, Vol. 19, Part 1, 1918, pp. 145-148.

[*19*] Underwood, E. E., *Metals Engineering Quarterly*, Vol. 1, No. 3, 1961, pp. 70-81.

[*20*] Hanson, K. L., *Acta Metallurgica*, Vol. 27, 1979, pp. 515-521.

[*21*] Schwartz, H. A., *Metals and Alloys*, Vol. 7, No. 11, 1936, p. 278.

[*22*] Underwood, E. E., *Quantitative Stereology*, Addison-Wesley, Reading, Mass., 1970, p. 160.

[*23*] Underwood, E. E. and Starke, E. A., Jr., in *Fatigue Mechanisms, ASTM STP 675*, American Society for Testing and Materials, Philadelphia, 1979, pp. 633-682.

[*24*] Hilliard, J. E., *Transactions of the American Institute of Mining Engineers*, Vol. 224, 1962, pp. 906-917.

[*25*] Pickens, J. R. and Gurland, J., *Proceedings of the Fourth International Congress for Stereology*, E. E. Underwood, R. de Wit, and G. A. Moore, Eds., National Bureau of Standards Special Publication No. 431, National Bureau of Standards, Gaithersburg, Md., 1976, pp. 269-272.

[*26*] Underwood, E. E., *Quantitative Stereology*, Addison-Wesley, Reading, Mass., 1970, p. 175.

[*27*] Underwood, E. E., *Quantitative Stereology*, Addison-Wesley, Reading, Mass, 1970, p. 58.

[*28*] Underwood, E. E. and Chakrabortty, S. B. in *Fractography and Materials Science, ASTM STP 733*, American Society for Testing and Materials, Philadelphia, 1981, pp. 337-354.

[*29*] Butler, L. H. and Junejo, A. A., *Journal of the Institute of Metals*, Vol. 99, 1971, pp. 163-166.

[*30*] Krasowsky, A. J. and Stepanenko, V. A., *International Journal of Fracture*, Vol. 15, No. 3, 1979, pp. 203-215.

[*31*] Kaye, B. H., *Direct Characterization of Fine Particles*, Wiley, New York, 1981, p. 356.

[*32*] Mandelbrot, B. P., *Fractals: Form, Chance and Dimension*, Freeman, San Francisco, 1977, pp. 27-32.

[*33*] Underwood, E. E., "Stereological Analysis of Particle Characteristics," *Testing and Characterization of Powders and Fine Particles*, J. K. Beddow and T. P. Meloy, Eds., Heyden and Son, Philadelphia, 1980, pp. 77-96.

[*34*] Garmong, G., Paton, N. E., and Argon, A. S., *Metallurgical Transactions*, Vol. 6A, 1975, pp. 1269-1279.

Summary

The papers included in this volume are evidence of the growing number of applications of quantitative metallography. Each of the contributions is self-contained and deals either with individual applications or with practical problems involved in application of the technique.

The initial paper by Rhines and Lemons explores the linear relationship between the Brinell hardness and the area of grain boundary for a wide range of compositions of alpha brasses and for large temperature differences. These authors present an impressive and substantial amount of experimental evidence suggesting that the grain boundary hardening contribution is not a direct result of grain size, as considered from the Hall-Petch viewpoint. Their point of view, described in detail within the paper, is based on the theory that the hardening is the direct result of resistance to the passage of shear deformation (by means of dislocation movement) across a grain boundary. This approach is justified by extensive data on intercept counts, N_L, which are used to estimate the surface area per unit volume, S_V. The paper represents a significant contribution in the technical controversy over the validity of the Hall-Petch relationship for describing hardening as a function of grain size.

The contribution by Petzow, Takajo, and Kaysser discusses the use of chord (or intercept) length distributions to show that the particle coalescence theory can provide a consistent basis for understanding particle growth during liquid-phase sintering.

The paper by Krishnamurthy, Qian, and Reed-Hill provides an example of the application of point counting to estimation of the volume fraction of mechanical twins in several face-centered-cubic alloys. These estimates are used to quantify the effect of twinning on the stress-strain behavior of the alloys. Four stages are identified rather distinctly from their deformation data by changes in the work hardening rate (plotted on a $d\epsilon/d\sigma$ basis) with stress.

Gurland's paper reviews microstructural characterization of cemented carbides and the correlation between the measured parameters and the metal properties. The extent of quantitative characterization that can be obtained from point and intercept counting is an important aspect of this paper and has implications for multiphase microstructures in general.

The contribution of Vander Voort on grain size measurement provides extensive discussion of the methods for evaluating grain size.

James, in his paper, provides an example of the use of modern image analysis and image modification techniques for characterizing inclusions in sintered ferrous materials.

The paper by DeHoff discusses five excellent examples of practical applications of quantitative metallography. These examples illustrate results that have been surprising in view of the existing understanding of the following phenomena: (*a*) recrystallization, (*b*) grain growth, (*c*) mechanical properties, (*d*) sintering, and (*e*) austenitization of a spheroidized steel.

The final paper, by Underwood, addresses three separate problems that can be encountered in quantitative metallography applications:

(*a*) the tendency for magnification to affect quantitative measurements,

(*b*) the estimation of the number of particles or grains per unit volume, N_V, from equations involving simplifying assumptions about the shape and size distribution of the features under consideration, and

(*c*) quantitative characterization of profiles that are one-dimensional features produced by sectioning surfaces.

James H. Steele, Jr.

Armco Inc., Middletown, Ohio 45043; symposium cochairman and editor.

James L. McCall

Battelle Columbus Laboratories, Columbus, Ohio, 43201; symposium cochairman and editor.

Index